# New Insights from Aperiodic Variability of Young Stars

Thesis by

Krzysztof Findeisen

In Partial Fulfillment of the Requirements

for the Degree of

Doctor of Philosophy


California Institute of Technology

Pasadena, California

2015

(Defended 2014 July 29)

# Acknowledgments

This thesis would not have been possible without the help of many, many people both inside and outside Caltech. First and foremost, I would like to thank my advisor, Lynne Hillenbrand, for her guidance and support. Her mentorship made me the scientist I am today, and it was from her that I learned the valuable skills of on-site observing, photometric and spectroscopic analysis, and technical writing, among many others.

I must also thank the members of the PTF collaboration, whose tireless efforts over many years made our North America Nebula survey possible. I owe a special thanks to Eran Ofek, David Levitan, Branimir Sesar, and Russ Laher, who developed PTF's photometric data reduction pipelines and who patiently listened to both my questions and my bug reports. I am also grateful to the staff of the Palomar, Keck, and Kitt Peak observatories, for their dedication to the facilities and for their timely assistance whenever things went wrong.

I would like to thank the members of my thesis committee, John Carpenter, Lynne Hillenbrand, John Johnson, Sterl Phinney, and Charles Steidel, for their valuable feedback throughout the last three years. I also need to thank Cahill's system administrators, Patrick Shopbell, Anu Mahabal, and Jose Calderon, for helping me set up a database to manage the enormous amounts of data this thesis required, and for always being patient with my requests for more and more disk space. Many thanks also to the Cahill administrative staff for keeping everything running smoothly, and for helping me with questions about paperwork or procedures.

The YSOVAR collaboration was a great source for feedback and ideas on this research, and nearly everything I present here was vetted at YSOVAR group meetings in one form or another. I'd like to especially thank Luisa Rebull. Not only did her prior research on the North America Nebula form the foundation for my own work, she also volunteered her unpublished Spitzer photometry, created valuable data products such as spectral energy distributions, and fielded an endless stream of questions about the details of the data or their proper handling. She was amazingly helpful, and really deserves credit for *anything* in this thesis involving infrared data (any errors in those sections are, of course, entirely my own).

Additional advice and feedback came from the Time Domain Forum, where both Lynne Hillenbrand and I presented preliminary versions of this work, and from private conversations with

Nairn Baliber, Kirk Borne, John Carpenter, Ann Marie Cody, Kevin Covey, Ashish Mahabal, Adam Miller, Timothy Morton, Chad Schafer, Keivan Stassun, Matthew Stevenson, and Neal Turner. Many thanks also to Evan Kirby for his help in troubleshooting the DEIMOS pipeline software, and to Eric Black for teaching me the art of scientific record-keeping.

Graduate school is a very different experience from college, and I was lucky to have two fantastic mentors to help smooth the way. Mansi Kasliwal and Varun Bhalerao, thank you both for everything. You helped make grad school not only survivable, but fun. I'd also like to thank Varun for inspiring me to continue stargazing alongside my professional research, and for the herculean efforts he went through to save the (former) Robinson/Downs Rooftop Observatory from destruction. I'd like to thank Shriharsh Tendulkar and Mislav Baloković for being my Cahill Rooftop Observatory co-directors, Shriharsh, Scott Barenfeld, and Michael Eastwood for teaching me the way of the pundit, Jose Calderon for being patient with a softball rookie, and everyone else who made the last seven years as enjoyable as they were.

Last, but not least, a big thank you to my parents, Piotr and Joanna Findeisen, for their support all along the path to becoming an astronomer. In many ways, I am here thanks to their love and encouragement.

# Abstract

Nearly all young stars are variable, with the variability traditionally divided into two classes: periodic variables and aperiodic or "irregular" variables. Periodic variables have been studied extensively, typically using periodograms, while aperiodic variables have received much less attention due to a lack of standard statistical tools. However, aperiodic variability can serve as a powerful probe of young star accretion physics and inner circumstellar disk structure. For my dissertation, I analyzed data from a large-scale, long-term survey of the nearby North America Nebula complex, using Palomar Transient Factory photometric time series collected on a nightly or every few night cadence over several years. This survey is the most thorough exploration of variability in a sample of thousands of young stars over time baselines of days to years, revealing a rich array of lightcurve shapes, amplitudes, and timescales.

I have constrained the timescale distribution of all young variables, periodic and aperiodic, on timescales from less than a day to $\sim 100$ days. I have shown that the distribution of timescales for aperiodic variables peaks at a few days, with relatively few ($\sim 15\%$) sources dominated by variability on tens of days or longer. My constraints on aperiodic timescale distributions are based on two new tools, magnitude- vs. time-difference ($\Delta m$-$\Delta t$) plots and peak-finding plots, for describing aperiodic lightcurves; this thesis provides simulations of their performance and presents recommendations on how to apply them to aperiodic signals in other time series data sets. In addition, I have measured the error introduced into colors or SEDs from combining photometry of variable sources taken at different epochs. These are the first quantitative results to be presented on the distributions in amplitude and time scale for young aperiodic variables, particularly those varying on timescales of weeks to months.

# Contents

# List of Figures

# List of Tables

# Chapter 1

# Introduction and Background

Understanding the origins of stars and planets requires understanding the complex interplay of gravity, magnetic fields, plasma physics, radiative transport, and both gas-phase and surface-catalyzed photochemistry. Protostars and newly formed stars represent complex physical laboratories that, despite decades of work, are still incompletely understood. For example, we understand that stars form from overdensities in molecular clouds, that magnetic fields mediate the interaction between stars and circumstellar disks, and that planets are the natural end state of circumstellar disk evolution. However, we cannot yet predict how the properties of molecular clouds translate into those of new stellar populations, under what conditions does the interaction of magnetic fields with disk gas produce accretion or outflows, or what types of disks lead to what types of planetary systems.

Observational astronomy is currently undergoing a revolution with the advent of time-domain surveys such as the Optical Gravitational Lensing Experiment (OGLE), the All-Sky Automated Survey (ASAS), the Catalina Real-Time Transient Survey (CRTS), and the Palomar Transient Factory (PTF). Future projects in this direction include the Zwicky Transient Facility (ZTF) and the Large-Scale Synoptic Survey Telescope (LSST). The coming flood of optical time-domain data will enable new approaches to long-standing questions in all fields of astrophysics, including star formation – if we have the necessary tools to make full use of the data.

One of the goals of this thesis is to develop these very tools. This work presents an unprecedented characterization of a population of young stars using several years of data from the Palomar Transient Factory. The high cadence and long baseline of the data are unmatched among blind surveys of star-forming regions, and allow a variety of variability on timescales of days to years to be treated with a unified approach. To interpret the data, I create and validate new statistical tools to quantify the variability, without relying on traditional assumptions such as periodic behavior. I present preliminary conclusions, but only scratch the surface of this rich data set, let alone the richer data sets that are still to come.

## 1.1 State of Knowledge of Young Stellar Physics

### 1.1.1 Standard Model of Star Formation

It is generally accepted that stars form from the gravitational collapse of overdensities in molecular clouds (McKee & Ostriker, 2007, and references therein). As the infalling gas compresses and heats, it forms a pressure-supported protostar surrounded by a still-infalling envelope. The initial angular momentum of the system causes the envelope to evolve into a rotationally-supported circumstellar disk, from which accretion continues onto the star. Outflows of material may occur during either the envelope or the disk phase. Star formation may be taken to end when the circumstellar gas disk dissipates after a few million years, although, at least for solar- and low-mass stars, this happens before the star reaches the main sequence.

Observationally, young stars are often classified by their optical and infrared spectral energy distribution, following the scheme defined by Lada (1987) and extended by Andre et al. (1993). Class 0 objects resemble cool (several hundred K) blackbodies, and are usually undetected at optical wavelengths. Class I objects are dominated by an infrared component, but have a significant optical excess over a cool blackbody. Class II objects resemble stellar photospheres in the optical, but have a significant infrared excess compared to a warm (few thousand K) blackbody. Finally, Class III objects are dominated by stellar emission. These classes are frequently treated as synonymous with the evolutionary phases described above (e.g., identifying Class 0 objects as protostars embedded in an envelope), although in reality there is not a one-to-one correspondence. For example, Class I objects can be either newly formed stars with a significant envelope, or more evolved stars with no envelope but an edge-on disk (Masunaga & Inutsuka, 2000). The spectral energy distributions are *observational* categories only, and depend on both the physical state of the system and the angle from which we view it. However, they remain useful descriptions, and will be used throughout this thesis as a rough indicator of a star's circumstellar environment

### 1.1.2 Physics of Circumstellar Disks and Accretion

While it is accepted that circumstellar disks accrete material onto their central stars, the exact mechanism that transfers angular momentum from the inner disk outward is still unclear (Hartmann et al., 2006, and references therein). The favored model at present invokes magnetorotational instability (MRI) to generate accretion (Balbus & Hawley, 2000), but even this model faces considerable obstacles, particularly its requirement that the disk be ionized. In light of the uncertainties, many authors still use the more schematic accretion model of Shakura & Sunyaev (1973), describing the angular momentum transport by a parameter $\alpha$. Authors typically assume $\alpha \sim$ 0.01-0.1,

implying a "viscous" accretion timescale of

$$\tau_{\rm visc} \sim \frac{1}{\alpha\Omega}\left(\frac{r}{h}\right)^2 = (9,000\ {\rm yr})\left(\frac{r}{1\ {\rm AU}}\right)^{3/2}\left(\frac{0.01}{\alpha}\right)\left(\frac{0.05}{\rm h/r}\right)^2 \tag{1.1}$$

Disk evolution will typically take place on this timescale.

Both pre-main-sequence stars and protostars show evidence of strong magnetic fields (Johns-Krull et al., 1999; Imanishi et al., 2001; Donati et al., 2010) of order a few kiloGauss. These magnetic fields will interact with circumstellar gas, drastically changing how matter accretes from the circumstellar disk to the star. As we will show later, the nature of accretion from the disk to the star has a direct impact on the types of variability we expect to observe.

Circumstellar gas must be partially ionized to interact with stellar magnetic fields, but the required ionization fraction is very low, of order $10^{-5}$ (Martin, 1996). Photoionization of metals provides more than the required ionization fraction, even at low temperatures and high column densities where hydrogen cannot be efficiently ionized by either Balmer emission or Lyman-continuum emission. Assuming sufficient ionization, the stellar magnetic field will grow strong enough to redirect incoming material when

$$\frac{B^2}{8\pi} \sim \frac{1}{2}\rho v^2 \tag{1.2}$$

For disk accretion this condition is difficult to relate to fundamental parameters such as the accretion rate, because $\rho$ has a complicated dependence on the disk geometry and viscosity. However, the truncation radius $r_{\rm sph}$ can be easily derived for spherical accretion onto a magnetic dipole:

$$\begin{aligned} \rho &= \frac{\dot{M}}{4\pi r^2 v_{ff}} \\ v_{ff} &= \sqrt{\frac{2GM}{r}} \\ B(r) &= B_\star\left(\frac{r}{R_\star}\right)^{-3} \end{aligned}$$

Substituting into Equation 1.2,

$$\begin{aligned} \frac{B_\star^2}{8\pi}\left(\frac{r_{\rm sph}}{R_\star}\right)^{-6} &\sim \frac{\dot{M}v_{ff}}{8\pi r_{\rm sph}^2} \\ B_\star^2 &\sim \dot{M}\sqrt{2GM}\,r_{\rm sph}^{7/2}R_\star^{-6} \\ r_{\rm sph} &\sim B_\star^{4/7}R_\star^{12/7}\dot{M}^{-2/7}(2GM)^{-1/7} \end{aligned} \tag{1.3}$$

The magnetic truncation radius for disk accretion, based on careful modeling of the disk properties, turns out to be proportional to, and within a factor of two of, this idealized spherical radius (Ghosh & Lamb, 1979; Koenigl, 1991). For a fiducial T Tauri star ($M = 0.5\ M_\odot$, $R_\star = 2\ R_\odot$, $B_\star = 1$ kG,

| Accretion State | Definition | Accretion Rate ($M_\odot$/yr) | Expected Scenarios |
|---|---|---|---|
| Boundary Layer | $r_{\rm sph} < R_\star$ | $> 10^{-5}$ | FU Orionis outbursts |
| Magnetic Boundary Layer | $R_\star < r_{\rm sph} \lesssim 2R_\star$ | $10^{-6}$-$10^{-5}$ | Protostars |
| Funnel Accretion | $2R_\star \lesssim r_{\rm sph} < r_{\rm cor}$ | Relative-$10^{-6}$ | Classical T Tauri stars |
| Propeller Regime | $r_{\rm cor} < r_{\rm sph} < r_{\rm LC}$ | $10^{-21}$-Relative | Weakly accreting and nonaccreting stars |
| Pulsar Regime | $r_{\rm LC} < r_{\rm sph}$ | $< 10^{-21}$ | Does not occur |

**Table 1.1:** Accretion rates required to achieve each of the five accretion regimes from Romanova et al. (2008) for a fiducial T Tauri star, together with the stage(s) of early stellar evolution where each regime applies. Here, $r_{\rm sph}$ is given by Equation 1.3, $r_{\rm cor}$ is the corotation radius, and $r_{\rm LC}$ is the radius at which matter corotating with the magnetic field would need to travel faster than the speed of light. Because of disk-locking, the accretion rate that separates the funnel and propeller regime is proportional to the long-term average accretion rate for any individual star; see the text for details.

and $\dot{M} = 10^{-7}\ M_\odot$/yr), $r_{\rm sph} \sim 7\ R_\odot = 0.03$ AU.

Because matter becomes coupled to the stellar magnetic field at the truncation radius, it will transfer angular momentum to or from the star at that radius. To first order, torques between the star and the disk material will tend to make the star rotate at the Kepler period at the truncation radius. This process is called disk locking. In practice, additional torques in the system – in particular, angular momentum lost through outflows and jets – will cause the star to rotate slightly slower than material at the truncation radius. This qualitative argument has been confirmed by simulations, which predict the star should rotate at 70-80% of the disk-locked rate (Long et al., 2005). However, disk-locking is a slow process, taking $10^4$-$10^6$ years (Hartmann, 2002). It is plausible, therefore, that even if a star is disk-locked on average, fluctuations in the accretion rate will cause the *instantaneous* disk truncation radius to differ from the corotation radius.

Romanova et al. (2008) classified disk accretion onto young stars or compact objects into five regimes, based on the relative importance of the central object's magnetic field, its rotation rate, and disk accretion rate (or, more precisely, the density of the circumstellar medium). Using Equation 1.3, one can find the accretion rates at which a fiducial T Tauri star with $M = 0.5\ M_\odot$, $R = 2\ R_\odot$, $B = 1$ kG, and $P_{\rm rot} = 10$ days appears in each of these regimes. The results are summarized in Table 1.1. Since Equation 1.3 assumes the lowest possible density for an accretion flow at fixed $\dot{M}$, that provided by spherical accretion in free fall, and the weakest radial dependence of magnetic field strength, that of a dipole, it will always overestimate the truncation radius at a given accretion rate. Therefore, the accretion rates in Table 1.1 are overestimates accurate only to order of magnitude.

Disk-locked stars should fall in the funnel accretion regime because they rotate slightly more slowly than the inner disk edge ($r_{\rm sph} \lesssim r_{\rm cor}$); in effect, the rotation rate of the star adjusts itself until it lies in the funnel regime. Because the star rotates slower than the disk at the edge of the magnetosphere, gas, once loaded onto stellar magnetic field lines, will have sub-Keplerian speeds and will tend to fall toward the star. Fluctuations in the accretion rate may temporarily shift the

truncation radius beyond the corotation radius, moving the star into the propeller regime and driving more matter into outflows rather than accretion (Romanova et al., 2003).

Gas on closed magnetic field lines inside the corotation radius will concentrate into "funnels" anchored at the poles, and will approach the star at close to free-fall speed. The flow is highly supersonic, so it will shock when the ambient gas pressure exceeds the ram pressure of the accretion flow. Following Calvet & Gullbring (1998), one can parametrize the density of the accretion flow as

$$\rho_{acc} = \frac{\dot{M}}{4\pi f R^2 v_{ff}}$$

where $f$, the fraction of the star's area onto which accreting material is funneled, appears to be $\sim 0.01$ in most cases. To order of magnitude, the shock will appear at the height where

$$\begin{aligned} \frac{3}{2}nkT &= \frac{1}{2}\rho v_{ff}^2 \\ \frac{3}{2}nkT &= \frac{1}{2}\frac{\dot{M}}{4\pi f R^2}v_{ff} \\ n &= \frac{1}{3kT}\frac{\dot{M}}{4\pi f R^2}\sqrt{\frac{2GM}{R}} \end{aligned} \tag{1.4}$$

For a fiducial T Tauri star with $M = 0.5\ M_\odot$, $R = 2\ R_\odot$, $T = 4,000$ K, and $\dot{M} = 10^{-8}\ M_\odot$/yr, the critical density is $5 \times 10^{15}$ cm$^{-3}$. In the Sun, this is the density of the chromosphere (Fontenla et al., 1999). To bury the shock below the photosphere, which has a density of $\sim 10^{17}$ cm$^{-3}$ in both the Sun and pre-main-sequence stars (Fontenla et al., 1999; Siess et al., 2000), one needs an accretion rate of $\dot{M} \gtrsim 3 \times 10^{-7}\ M_\odot$ or a smaller covering fraction $f \lesssim 0.03\%$.

The temperature of the post-shock gas is given by

$$\frac{GM}{R} = \frac{3}{2}\frac{kT_{\rm shock}}{\mu m_H} \tag{1.5}$$

For the example T Tauri star above, $T_{\rm shock} \sim 2 \times 10^6$ K. The dense gas cools relatively quickly, so the post-shock region is typically only $\sim 10$ km thick (Calvet & Gullbring, 1998). For a shock formed above the photosphere, X-ray emission from the shocked gas heats the accretion flow $100 - 1,000$ km before the shock to temperatures of $\sim 2 \times 10^4$ K and the underlying photosphere to temperatures of $\sim 1 \times 10^4$ K. This "hot spot" is responsible for the excess ultraviolet and optical emission associated with accretion.

The processes associated with the circumstellar disk operate on a variety of timescales separated by several orders of magnitude. In addition to the viscous and disk-locking timescales introduced above, orbiting material may evolve on a dynamical timescale ($t_{\rm dyn} \sim \sqrt{r^3/GM}$), and the rotation period of the star may affect the behavior of the stellar magnetosphere and inner disk. A comparison of characteristic timescales for the fiducial T Tauri star of this section is presented in Table 1.2.

| Timescale | Definition | 0.03 AU | 0.1 AU | 1 AU |
|---|---|---|---|---|
| Dynamical Time | $t_{\rm dyn} \sim 2\pi\sqrt{r^3/GM}$ | 3 d | 16 d | 1.4 y |
| Rotation Period | $t_{\rm rot} \sim 2\pi/\Omega_\star$ | 10 d | | |
| Viscous Time | $t_{\rm dyn} \sim (1/\alpha\Omega)\,(r/h)^2$ | 60 y | 300 y | 9,000 y |
| Disk-Locking Time | $t_{\rm DL} \sim 0.2(M/\dot{M})(\Omega_\star/\Omega)(R_\star/r_{\rm sph})^2$ | 24,000 y | | |

**Table 1.2:** Characteristic timescales for a fiducial T Tauri star with $M = 0.5\ M_\odot$, $R_\star = 2\ R_\odot$, $B_\star = 1$ kG, $\dot{M} = 10^{-7}\ M_\odot$/yr, $P_{\rm rot} = 10$ days, $r_{\rm sph} \sim 0.03$ AU, $\alpha(r) \equiv 0.01$, and $h(r)/r \equiv 0.05$.

## 1.2 Current Knowledge and the Potential of Variability

Variability has been a known characteristic of young stars ever since their discovery; Joy (1945) first identified T Tauri stars as a class of variables decades before they were recognized as newly formed stars. We now know that accretion (Romanova et al., 2006, and references therein) and disk evolution (e.g., Turner et al., 2010) are both highly dynamic, making variability intimately linked to the processes that drive early stellar evolution. Therefore, variability in pre-main sequence stars can further our insight into physical processes associated with the formation and early evolution of both stars and planets. However, the full breadth of variable phenomena has not been explored in quantitative detail.

Optical flux variations in pre-main sequence stars depend on dynamic or radiative transfer effects that can occur on timescales ranging from hours to decades, or possibly longer. Different amplitudes and timescales can be associated with each of the postulated physical phenomena, as illustrated in Figure 1.1. In addition, the observed behavior of any individual system can be modified by orientation with respect to the line of sight, so phenomenologically distinct variables may have a common physical origin.

### 1.2.1 Major Variability Mechanisms

The wide range of plausible aperiodic behavior originates for the most part in the circumstellar environment. Variability of circumstellar origin is superposed on an underlying periodic modulation that is expected due to rotation of surface inhomogeneities, analogous to enhanced sunspots, across the projected stellar disk, as well as any short timescale chromospheric flaring.

Possible driving phenomena are listed below.

#### 1.2.1.1 Stellar Magnetic Activity

Young stars are believed to be highly active, with hot chromospheres and coronae (e.g., Costa et al., 2000) and extensive starspots (Rydgren & Vrba, 1983; Herbst et al., 2007). If starspots are unevenly distributed over the stellar surface, the star will appear to vary periodically as the starspots rotate in and out of sight. This will create periodic variability with amplitudes of a few tenths of a magnitude

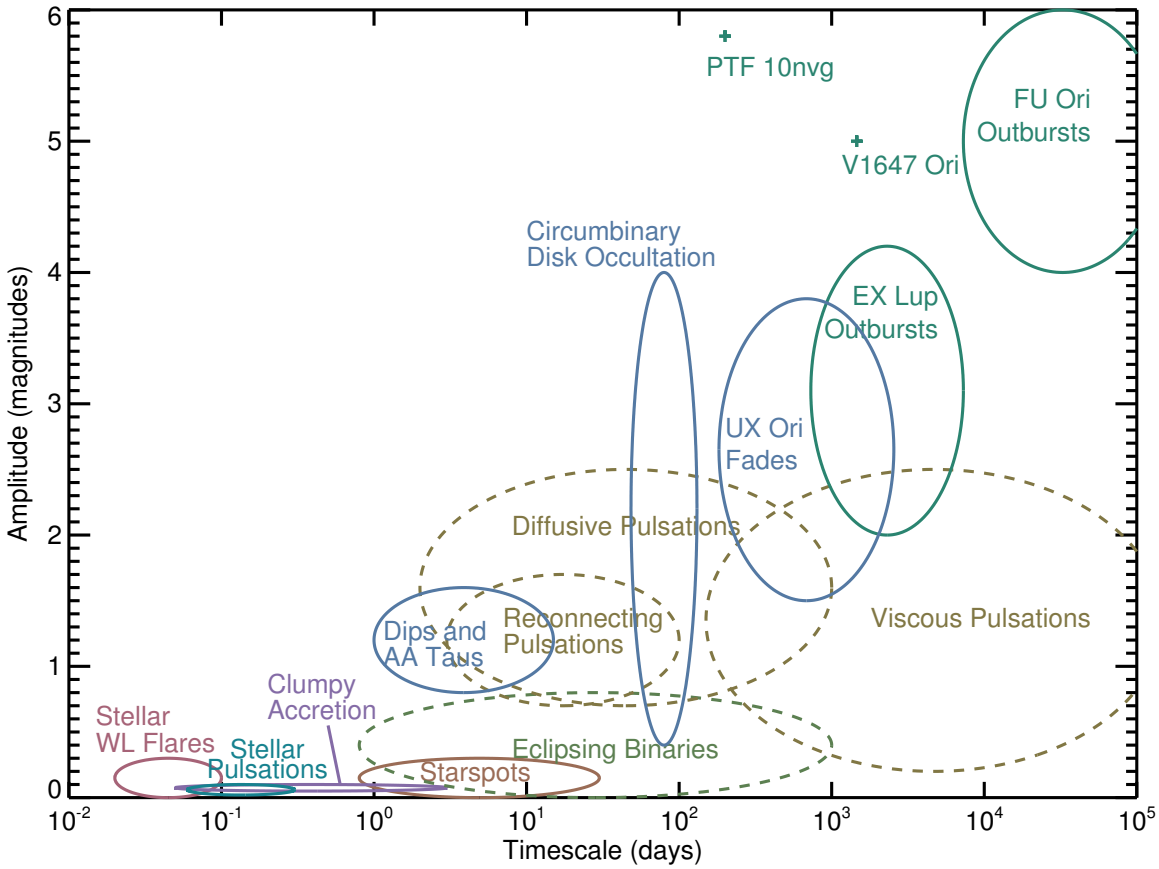


**Figure 1.1:** Schematic representation of the amplitudes and timescales expected from different types of young stellar variables. Solid ellipses take their amplitude and timescale ranges from empirical data, while dashed ellipses were placed based on theoretical work. Colors highlight related groups of variables. We expect to see an enormous dynamic range in both amplitude and timescale, with particular variability mechanisms favoring different areas of the parameter space. Generally, as expected from Table 1.2, longer-timescale variability occurs farther out in the star-disk system.

and periods of a few days, depending on the distribution of the spots, the rotation rate of the star, and the inclination of the system.

Optical flaring is also associated with magnetic activity (Kowalski et al., 2010; Kretzschmar, 2011), and so one might expect to see white-light flares (with amplitudes of up to a few tenths of a magnitude, and timescales of less than an hour) associated with the enhanced activity of pre-main-sequence stars. However, searches for such flares fail to find widespread optical flaring activity (Stassun et al., 2006).

#### 1.2.1.2 Disk-to-Star Accretion

As reviewed in subsection 1.1.2, accreting stars have not only a $10^6$ K accretion shock, but also a preshock region and postshock hot spot with temperatures of $\sim 10^4$ K. The optically thick hot spot can make a substantial contribution to the stellar flux: a hot spot with $T_{eff} \sim 8,000$ K covering 1% of a star with $T_{eff} \sim 4,000$ K will have 16% the bolometric luminosity of the undisturbed photosphere and 38% of the specific luminosity at 500 nm. The contribution of the optically thin preshock region at optical or near-infrared wavelengths is roughly an order of magnitude lower than that of the hot spot (Calvet & Gullbring, 1998), so it can be neglected.

If the accretion flow is steady, Wood et al. (1996) and Mahdavi & Kenyon (1998) showed that the star will appear to vary periodically as the hot spot rotates in and out of sight. This will create periodic variability with amplitudes of $\sim 0.5$ mag and periods of a few days, depending on the luminosity of the spot, the rotation rate of the star, and the inclination of the system.

Changes in the accretion rate are also expected to change the hot spot luminosity and produce optical variability. Since such changes are expected to be driven by disk physics, they are covered below.

#### 1.2.1.3 Magnetic Field Interaction Between the Star and the Disk

Since in general the star will not be corotating with the inner regions of its circumstellar disk, any magnetic field lines threading the disk will be stretched, distorted, and eventually reconnected as the disk and star rotate. These reconnection events may produce more powerful flares than ordinary coronal flares (Favata et al., 2005), although it is not clear whether these flares would be optically visible.

Since they fill the space between the inner disk edge and the stellar surface, stellar magnetic fields can also produce variability by modulating the accretion flow (Romanova et al., 2004b). Competition between magnetic and gas pressure can lead to cycles of accretion as the stellar magnetic field switches between a configuration that allows accretion and one that does not (Aly & Kuijpers, 1990; Romanova et al., 2004a). Amplitudes of several tenths of a magnitude are possible, and

the timescale of the variability can range from days to months depending on the specific physical mechanism invoked for the interaction.

Finally, magnetic fields can excite large-scale structures in the disk (Bouvier et al., 1999; Romanova et al., 2013). In addition to causing variable accretion flow, warps and spiral arms can cause the star to appear fainter if the system is highly inclined and the structure passes through our line of sight. Amplitudes may be up to several magnitudes, depending on the optical depth and covering fraction of the obstructing material. Stable disk structures produce periodic variability on a dynamical timescale.

#### 1.2.1.4 Differential Rotation of a Three-Dimensional Disk

Turner et al. (2010) demonstrated that circumstellar disk turbulence can create transient dust structures far from the plane of the disk. These structures evolve and disappear on timescales of a fraction of the dynamical time. If we are looking at the disk close to edge-on, these structures may intersect our line of sight to cause dimming. As noted above, the timescale of the variability may be quite short, even if the obstructing material is far from the inner edge of the disk, and due to the chaotic nature of the turbulence the lightcurve will not repeat.

#### 1.2.1.5 Envelope-to-Disk Infall

Vorobyov & Basu (2010) have shown that, when a circumstellar disk is still accreting from a surrounding envelope, the disk may grow massive enough to become gravitationally unstable. If the disk fragments, the accretion rate from the disk onto the star, and the luminosity of the system, will vary by orders of magnitude as individual fragments fall onto it, possibly producing what we observe as FU Ori and EX Lup events. This mechanism is expected to operate only during the embedded stages of star formation; once the envelope has drained onto the disk, the disk will no longer fragment.

### 1.2.2 Previous Work on Periodic Variability

Periodic variability in young stars has been well studied over the past three decades (most recently, by Grinin, 2000; Rebull et al., 2006; Herbst et al., 2007; Irwin et al., 2008; Cieza & Baliber, 2007), typically using periodograms (e.g., Lomb, 1976; Scargle, 1982) to identify the dominant period. Authors typically assume that any periodic signal reflected the rotation period of the star, whether the variability itself is from accretion hot spots or from cool starspots (Herbst et al., 1994). By invoking the disk-locking model, authors were even able to apply this assumption in cases where the variability was clearly associated with the inner disk (as in Bouvier et al., 1999).

The most common science case for studies of periodic variability was testing whether disk-locking

was common in young stellar populations (e.g., Herbst et al., 2000; Cieza & Baliber, 2007; Irwin et al., 2008). However, studies along these lines found conflicting results. Periodic variability was also used to constrain the spin-down of stars from the pre-main-sequence stage to the early main sequence (Herbst et al., 2007, and references therein). These studies form the basis of current theories of wind-driven angular momentum loss from young main sequence stars.

### 1.2.3 Previous Work on Aperiodic Variability

In contrast to the thoroughly studied periodic variability, aperiodic variability is cataloged but relatively unexplored in the literature. We know from surveys of periodic variability that roughly half to two-thirds of variable stars in star-forming regions do not have well-defined periods (e.g., Scholz & Eislöffel, 2004; Rodríguez-Ledesma et al., 2009), but these surveys usually discard aperiodic variables as irrelevant to the goal of characterizing rotation periods. As aperiodic variables constitute a large fraction of variable stars in star-forming regions, characterizing and understanding them is essential to completing our understanding of young star and disk physics.

Some variability surveys have attempted to arrange aperiodic variables into classes (Carpenter et al., 2001, 2002; Alves de Oliveira & Casali, 2008; Morales-Calderón et al., 2009; Stauffer et al., 2014). Sometimes, particularly if color variability data was available, the authors would interpret their lightcurve classes by invoking stochastically time variable disk-to-star accretion, circumstellar extinction, or both. However, these interpretations were often necessarily tentative – there was simply not enough quantifiable data to make rigorous conclusions.

Where study of aperiodic variability has made significant progress is in the study of episodic brightening or dimming events, which are usually interpreted as accretion increases or extinction increases, respectively. Examples of the former include the extreme (>2-6 mag) "outburst events" as exemplified by EX Lup and FU Ori objects (Herbig, 1977). These types of sources are interpreted as undergoing episodes of rapid mass accumulation due to an instability in the inner disk. In the context of stellar mass assembly history, the duration and frequency of such outbursts is important to establish empirically since these events are thought, based on theory, to play a determining role in setting the final mass of the star. Accretion outbursts may also determine a star's appearance to us on the so-called "birthline" in the canonical HR diagram of stellar evolution (Hartmann et al., 1997; Baraffe et al., 2009), from which stellar masses and ages are usually derived without considering the effects of accretion history.

Examples of the latter, extinction-related, variability include UX Ori stars, which undergo long-lived extinction events featuring a distinctive blueward shift in color while approaching minimum light, as well as the broader category of stars identified by, e.g., Carpenter et al. (2001, 2002) as having color-color and color-magnitude trends consistent with shorter-timescale, random variation along reddening vectors. More recently, so-called "dipper" events (e.g., Cody & Hillenbrand, 2010; Morales-

Calderón et al., 2011) are attributed to repeated sub-day or several-day circumstellar extinction enhancements. Such repeating but aperiodic flux dips or eclipse-like events have been qualitatively explained by Flaherty & Muzerolle (2010), Flaherty et al. (2012), and others using rotating non-axisymmetric disk models or by Turner et al. (2010) with a vertical disk turbulence model. Periodic versions of the dipper class are known as AA Tau stars (e.g., Bouvier et al., 1999).

## 1.3 Challenges for Variability Surveys

One of the reasons studies of periodic variables have met much more success than studies of their aperiodic counterparts is because the latter place much more stringent demands on observing programs. A periodic variable can be characterized by two numbers, an amplitude and a period, both of which can be inferred from a few tens of observations over two or three periods. Because their behavior cannot be interpolated from phased lightcurves, aperiodic variables must be monitored continuously at high time resolution (ideally, higher than the highest frequencies in the underlying lightcurve) to get equivalent information about their behavior.

In addition, aperiodic variables may have long-term as well as high-frequency variability components, or their behavior may change unpredictably over long timescales. Characterizing this behavior requires monitoring for months or even years, while periodic variability can often be fully characterized with only a month of data. Finally, placing "irregular" variables into the broader context of young stellar variability requires that the same monitoring be applied to hundreds of variables to build up a meaningful sample.

In a world of limited telescope time, real surveys have been forced to make tradeoffs between these requirements. The work of Herbst et al. (2000), for example, was able to monitor a large number of stars for over eight years because the authors had exclusive access to a small telescope. However, frequent poor weather conditions at the site meant that the survey sacrificed time resolution, and could *only* follow long term trends.

At the other extreme, Cody et al. (2013) obtained a month of minute-resolution, high precision photometry using the orbiting MOST telescope. However, they got observing time to monitor only five stars. Not only did the authors have to base their conclusion on a small sample, but they noted that a month was not enough of an observing window to see the full variability of some of their targets.

Finally, time domain spectroscopic surveys such as Johns & Basri (1995) or Choudhury et al. (2011) offer the most information at each epoch, but at the cost of *both* temporal coverage and number of stars surveyed. Most such studies have drawn their conclusions from data of a single star.

The Palomar Transient Factory North America Nebula (PTF-NAN) Survey, described in the following chapter, offers a nightly cadence over three years for thousands of stars. Although it

sacrifices some time resolution by making only nightly rather than hourly observations, its main limitation is in photometric precision when observing crowded fields. For sufficiently high amplitude sources, however, it offers a better dynamic range than either Herbst et al. (2000), who could only sample long-term variability, or Cody et al. (2013), whose work was specialized toward short-term variability.

## 1.4 Summary of Following Chapters

The primary goal of this work is to demonstrate that variability can be used to place interesting constraints on the physics of young stars and their circumstellar environments. To this end, we not only carry out a survey of variability in a nearby star-forming region, but also develop new lightcurve analysis methods and apply them to specific problems in stellar variability.

Chapter 2 presents our survey of the North America Nebula complex, including a brief overview of the Palomar Transient Factory (PTF), known characteristics of the star-forming region, and the details of the data reduction. Much of the work described in this chapter was carried out by members of the PTF collaboration, or by Rebull et al. (2011), who had carried out an infrared survey of the North America Nebula complex a few years before.

Chapter 3 presents an analysis of the lightcurves of candidate members selected by Rebull et al. (2011), concentrating on well defined brightening events ("bursts") or dimming events ("fades"). The relative simplicity of bursting or fading events, along with the scrutiny to which they had been previously subjected in the literature, makes them an excellent starting point for any study of aperiodic variability as a whole. In addition, bursting and fading have been relatively poorly studied on timescales of weeks, while our data allows us to explore these timescales very well. We find several interesting objects, including lightcurve types that have not been previously reported in the literature.

Chapter 4 and Chapter 5 are dedicated to finding a general-purpose statistic that can characterize how quickly or how slowly a lightcurve varies, regardless of lightcurve shape or sampling (a "timescale metric"). In the process, we outline a systematic method for characterizing lightcurve statistics and present a standalone program for doing so. We also identify the strengths and limitations of the two timescale metrics we identify as the best, and present recommendations for their use.

Chapter 6 applies the timescale metric selected in Chapters 4-5 to carry out a broad study of the lightcurves produced by our survey of the North America Nebula complex. We infer the timescale distribution of both periodic and aperiodic variables in the region, and look for systematic differences as a function of stars' infrared or optical spectroscopic properties. As a side application, we develop a formalism to quantify the error introduced when researchers neglect variability when comparing photometry taken at different epochs.

Finally, Chapter 7 summarizes the main findings of this dissertation, and outlines how future studies can benefit from the progress made here.

## 1.5 References


Alves de Oliveira, C., & Casali, M. 2008, A&A, 485, 155, arXiv:0804.1548

Aly, J. J., & Kuijpers, J. 1990, A&A, 227, 473

Andre, P., Ward-Thompson, D., & Barsony, M. 1993, ApJ, 406, 122

Balbus, S. A., & Hawley, J. F. 2000, Space Sci. Rev., 92, 39, arXiv:astro-ph/9906317

Baraffe, I., Chabrier, G., & Gallardo, J. 2009, ApJ, 702, L27, arXiv:0907.3886

Bouvier, J. et al. 1999, A&A, 349, 619

Calvet, N., & Gullbring, E. 1998, ApJ, 509, 802

Carpenter, J. M., Hillenbrand, L. A., & Skrutskie, M. F. 2001, AJ, 121, 3160, arXiv:astro-ph/0102446

Carpenter, J. M., Hillenbrand, L. A., Skrutskie, M. F., & Meyer, M. R. 2002, AJ, 124, 1001, arXiv:astro-ph/0204430

Choudhury, R., Bhatt, H. C., & Pandey, G. 2011, A&A, 526, A97, arXiv:1011.3412

Cieza, L., & Baliber, N. 2007, ApJ, 671, 605, arXiv:0707.4509

Cody, A. M., & Hillenbrand, L. A. 2010, ApJS, 191, 389, arXiv:1011.3539

Cody, A. M., Tayar, J., Hillenbrand, L. A., Matthews, J. M., & Kallinger, T. 2013, AJ, 145, 79, arXiv:1302.0018

Costa, V. M., Lago, M. T. V. T., Norci, L., & Meurs, E. J. A. 2000, A&A, 354, 621

Donati, J.-F. et al. 2010, MNRAS, 409, 1347, arXiv:1007.4407

Favata, F., Flaccomio, E., Reale, F., Micela, G., Sciortino, S., Shang, H., Stassun, K. G., & Feigelson, E. D. 2005, ApJS, 160, 469, arXiv:astro-ph/0506134

Flaherty, K. M., & Muzerolle, J. 2010, ApJ, 719, 1733, arXiv:1007.1249

Flaherty, K. M., Muzerolle, J., Rieke, G., Gutermuth, R., Balog, Z., Herbst, W., Megeath, S. T., & Kun, M. 2012, ApJ, 748, 71, arXiv:1202.1553

Fontenla, J., White, O. R., Fox, P. A., Avrett, E. H., & Kurucz, R. L. 1999, ApJ, 518, 480

Ghosh, P., & Lamb, F. K. 1979, ApJ, 232, 259

Grinin, V. P. 2000, in Astronomical Society of the Pacific Conference Series, Vol. 219, Disks, Planetesimals, and Planets, ed. G. Garzón, C. Eiroa, D. de Winter, & T. J. Mahoney, 216

Hartmann, L. 2002, ApJ, 566, L29

Hartmann, L., Cassen, P., & Kenyon, S. J. 1997, ApJ, 475, 770

Hartmann, L., D'Alessio, P., Calvet, N., & Muzerolle, J. 2006, ApJ, 648, 484, astro-ph/0605294

Herbig, G. H. 1977, ApJ, 217, 693

Herbst, W., Eislöffel, J., Mundt, R., & Scholz, A. 2007, Protostars and Planets V, 297, arXiv:astro-ph/0603673

Herbst, W., Herbst, D. K., Grossman, E. J., & Weinstein, D. 1994, AJ, 108, 1906

Herbst, W., Rhode, K. L., Hillenbrand, L. A., & Curran, G. 2000, AJ, 119, 261, arXiv:astro-ph/9909427

Imanishi, K., Koyama, K., & Tsuboi, Y. 2001, ApJ, 557, 747

Irwin, J., Hodgkin, S., Aigrain, S., Bouvier, J., Hebb, L., Irwin, M., & Moraux, E. 2008, MNRAS, 384, 675, arXiv:0711.2398

Johns, C. M., & Basri, G. 1995, ApJ, 449, 341

Johns-Krull, C. M., Valenti, J. A., & Koresko, C. 1999, ApJ, 516, 900

Joy, A. H. 1945, ApJ, 102, 168

Koenigl, A. 1991, ApJ, 370, L39

Kowalski, A. F., Hawley, S. L., Holtzman, J. A., Wisniewski, J. P., & Hilton, E. J. 2010, ApJ, 714, L98, arXiv:1003.3057

Kretzschmar, M. 2011, A&A, 530, A84+, arXiv:1103.3125

Lada, C. J. 1987, in IAU Symposium, Vol. 115, Star Forming Regions, ed. M. Peimbert & J. Jugaku, 1–17

Lomb, N. R. 1976, Ap&SS, 39, 447

Long, M., Romanova, M. M., & Lovelace, R. V. E. 2005, ApJ, 634, 1214, arXiv:astro-ph/0510659

Mahdavi, A., & Kenyon, S. J. 1998, ApJ, 497, 342

Martin, S. C. 1996, ApJ, 470, 537

Masunaga, H., & Inutsuka, S.-i. 2000, ApJ, 531, 350

McKee, C. F., & Ostriker, E. C. 2007, ARA&A, 45, 565, arXiv:0707.3514

Morales-Calderón, M. et al. 2011, ApJ, 733, 50, arXiv:1103.5238

——. 2009, ApJ, 702, 1507, arXiv:0907.3360

Rebull, L. M. et al. 2011, ApJS, 193, 25, arXiv:1102.0573

Rebull, L. M., Stauffer, J. R., Megeath, S. T., Hora, J. L., & Hartmann, L. 2006, ApJ, 646, 297, arXiv:astro-ph/0604104

Rodríguez-Ledesma, M. V., Mundt, R., & Eislöffel, J. 2009, A&A, 502, 883, arXiv:0906.2419

Romanova, M. M., Kulkarni, A., Long, M., Lovelace, R. V. E., Wick, J. V., Ustyugova, G. V., & Koldoba, A. V. 2006, Advances in Space Research, 38, 2887, arXiv:astro-ph/0604116

Romanova, M. M., Kulkarni, A. K., Long, M., & Lovelace, R. V. E. 2008, in American Institute of Physics Conference Series, Vol. 1068, American Institute of Physics Conference Series, ed. R. Wijnands, D. Altamirano, P. Soleri, N. Degenaar, N. Rea, P. Casella, A. Patruno, & M. Linares, 87–94, arXiv:0812.2890

Romanova, M. M., Toropina, O. D., Toropin, Y. M., & Lovelace, R. V. E. 2003, ApJ, 588, 400, arXiv:astro-ph/0209548

Romanova, M. M., Ustyugova, G. V., Koldoba, A. V., & Lovelace, R. V. E. 2004a, ApJ, 616, L151, arXiv:astro-ph/0502266

——. 2004b, ApJ, 610, 920, arXiv:astro-ph/0404496

——. 2013, MNRAS, 430, 699, arXiv:1209.1161

Rydgren, A. E., & Vrba, F. J. 1983, ApJ, 267, 191

Scargle, J. D. 1982, ApJ, 263, 835

Scholz, A., & Eislöffel, J. 2004, A&A, 419, 249, arXiv:astro-ph/0404014

Shakura, N. I., & Sunyaev, R. A. 1973, A&A, 24, 337

Siess, L., Dufour, E., & Forestini, M. 2000, A&A, 358, 593, arXiv:astro-ph/0003477

Stassun, K. G., van den Berg, M., Feigelson, E., & Flaccomio, E. 2006, ApJ, 649, 914, arXiv:astro-ph/0606079

Stauffer, J. et al. 2014, AJ, 147, 83, arXiv:1401.6600

Turner, N. J., Carballido, A., & Sano, T. 2010, ApJ, 708, 188, arXiv:0911.1533

Vorobyov, E. I., & Basu, S. 2010, ApJ, 719, 1896, arXiv:1007.2993

Wood, K., Kenyon, S. J., Whitney, B. A., & Bjorkman, J. E. 1996, ApJ, 458, L79

# Chapter 2

# Photometric and Supplementary Data

## 2.1 Introduction

This thesis describes a young star variability survey of unprecedented scope and time coverage, monitoring several thousand members of a single star-forming region for several years at (on average) nightly cadence. The thorough coverage of variability on a variety of scales has allowed for new results and new types of analysis, as described in later chapters. This chapter presents the data used for the survey as well as the target region and survey strategy.

## 2.2 Overview of PTF

The primary data set for this work was collected as part of a guest investigator program for the Palomar Transient Factory (PTF). Although PTF's primary purpose was to constrain the population of optical transients and uncover examples of new, rare, classes of transients (Rau et al., 2009), its wide field of view and flexible scheduling have also made it well-suited for studies of variable stars and AGNi. Here I briefly describe the capabilities of PTF as they relate to variable-star work in the Galactic plane.

### 2.2.1 Instruments and Main Survey

The primary survey telescope for PTF is the Samuel Oschin 48-inch telescope at Palomar, which is queue-scheduled and fully robotic. The PTF Survey Camera is a mosaic of 11 chips[1], upgraded from the CFH12K camera formerly located at the Canada-France-Hawaii Telescope. A readout time of 31 s minimizes overhead during survey operations. When mounted in the Palomar 48-inch, it covers a total area of 7.26 square degrees with $1''$ pixels, with gaps of 33-$45''$ between the individual chips

[1] The mosaic is, strictly speaking, a $2 \times 6$ array, but one of the 12 chips failed while the camera was being upgraded.

of the mosaic. The images have a FWHM of 1.5-2.0″, depending on local seeing. The standard PTF observing pattern takes exposures of 60s in either the $g'$ or Mould-$R$ bands, reaching a limiting magnitude of 21.3 and 20.6, respectively (Law et al., 2009).

A quick reduction of the data is carried out with a pipeline housed at the Lawrence Berkeley National Laboratory (LBNL), for the express purpose of identifying supernovae and other optical transients (Nugent et al., in prep.). The LBNL pipeline allows for same-night followup of promising targets using the robotic Palomar 60-inch telescope, which can observe only an 11′ field of view but can do so in multiple filters across the optical and near-infrared band. The Palomar 60-inch is tasked with generating initial lightcurves of transients while the 48-inch continues its broader survey. Additional spectroscopic follow-up is scheduled at a variety of telescopes, including the Palomar 200-inch, the Lick 3-m, the Kitt Peak 4-m, the William Herschel Telescope, and both Keck telescopes.

The LBNL pipeline is optimized for detecting sudden outbursts against background galaxies, and when applied to Galactic variable stars it is reliable to only 1 mag (Nugent et al., in prep.). We therefore used the PTF Photometric Pipeline, which performs absolute and relative photometry on a source catalog extracted from each image, but days to weeks after the observations were taken. As a result, we were unable to take advantage of PTF's rapid follow-up capabilities.

### 2.2.2 The PTF Photometric Pipeline

The PTF Photometric Pipeline (Ofek et al., 2012, Laher et al., submitted to PASP), formerly the IPAC PTF Image Processing Pipeline, provided us with the PTF photometry presented throughout this thesis. Images were debiased, flatfielded, and astrometrically calibrated. Source catalogs and photometry were generated by SExtractor (Laher et al., submitted to PASP). An absolute photometric calibration good to a systematic limit of $\sim 2\%$ was generated using SDSS sources observed throughout the night (Ofek et al., 2012). Relative photometric calibration further refined the photometry, particularly on nonphotometric nights (Levitan et al., in prep; for algorithm details see Ofek et al. (2011) and Levitan et al. (2011)). We refer to the relative photometric magnitudes produced by the pipeline as $R_{\rm PTF}$.

The PTF Photometric Pipeline photometry is typically repeatable to 0.5-1% for bright (15th mag) nonvariable sources in sparse fields on photometric nights. Photometry for typical sources in our field is less reliable, of the order of 2-3%, because nebula emission and source crowding introduce additional errors. However, we can observe to brighter magnitudes than the PTF survey reaches in normal observing. In typical PTF fields, photometric quality begins to decrease for stars brighter than $R_{\rm PTF} \lesssim 14$ (Ofek et al., 2012); because our systematic noise floor is higher, our photometry does not begin to degrade until $R_{\rm PTF} \sim 13.5$.

The pipeline flagged photometric points as bad detections if the sources were automatically

identified as part of airplane, satellite, or cosmic-ray tracks; if they fell on an area of the chip that had high dark current, was unusually noisy, or was poorly illuminated; if they fell on a chip edge; if they contained dead pixels; if they were affected by bleeding from bright stars; if they contained saturated pixels; or if they had neighbors biasing their photometry. Although flagged observations were provided to us as part of the data, we did not use them in plotting or analyzing lightcurves. We also removed any sources from our sample that were flagged in more than half the observed epochs.

## 2.3 The PTF-NAN Survey

### 2.3.1 The North America Nebula Complex

The North America Complex (W80) is a relatively nearby ($\sim 520$ pc) but incompletely characterized H II region. The Complex is contained within a highly fragmented expanding shell of molecular gas approximately 2.4° across (Bally & Scoville, 1980), or 22 pc $\left(\frac{d}{520\ \mathrm{pc}}\right)$, where $d$ is the distance to the region. The molecular shell has a kinematic age of 2 Myr $\left(\frac{d}{520\ \mathrm{pc}}\right)$, but Bally & Scoville argue both that the shell is accelerating and that it did not start expanding until the H II region was already fully developed, making the region somewhat older than its kinematic age. Part of the shell corresponds to the L935 dark cloud, which from Earth's vantage point appears to divide the complex into two optical nebulae, the North America Nebula (NGC 7000) to the east and the Pelican Nebula (IC 5070) to the west.

Because the Complex is located directly down a spiral arm from the Sun, its distance has historically been highly uncertain. The best estimate at present is from Laugalys et al. (2006), who used multi-band photometry to solve for extinctions and distances to stars towards L935 and inferred a distance to the cloud of $520 \pm 50$ pc. Since the size of the complex fits well within the uncertainties, I adopt this value as the distance to the Complex as a whole, rather than to its front face.

The stellar population of the North America Complex is only partly known. Comerón & Pasquali (2005) identified a single O5 star, 2MASS J205551.25+435224.6, as dominating the ionization of the H II region. Other known members have spectral types ranging from B to M. The largest census of the Complex available to date is from Guieu et al. (2009) and Rebull et al. (2011), who used Spitzer observations to identify $\sim 2,000$ sources with infrared excess emission consistent with circumstellar disks. This census is, however, incomplete, as an infrared excess survey is insensitive to stars that have already lost their disks. The number of stars in the region may well be double the Rebull et al. (2011) figure.

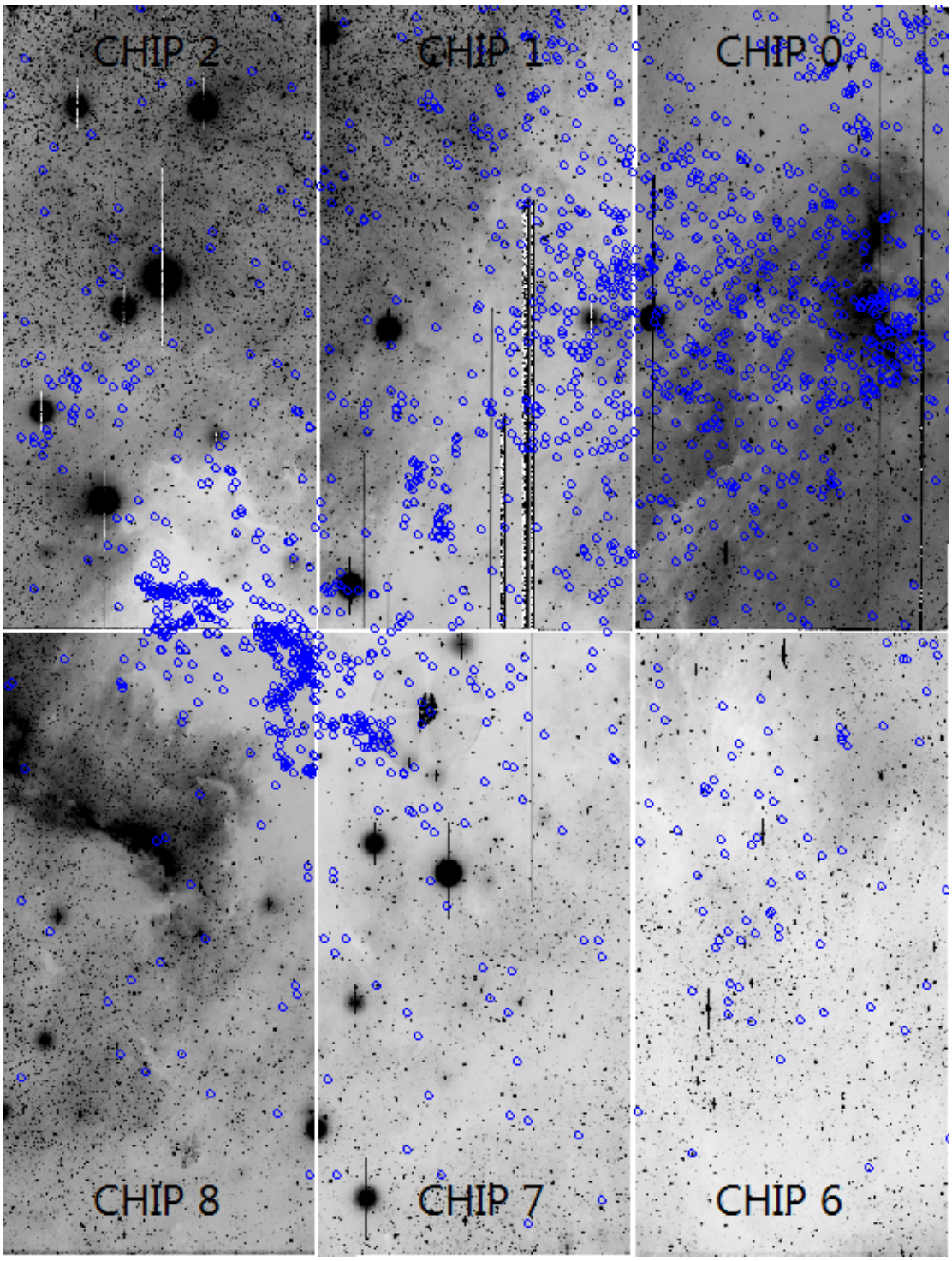


**Figure 2.1:** The North America Nebula complex, as observed by PTF in a single epoch from 2009. Only six of the 11 PTF chips are shown; the remainder, to the left of this field, were off the nebula and probed the Galactic field population. The North America Nebula proper (NGC 7000) is on the left side of the frame, while the Pelican Nebula (IC 5070) is on the upper right, with the L935 dark cloud between them. The blue circles mark the positions of candidate members selected using infrared excess by Rebull et al. (2011).

### 2.3.2 Survey Overview

We selected the North America Complex as the target for our PTF guest observer survey (the "PTF-NAN" survey) both because it is relatively nearby, allowing us to probe G-type through hotter M-type members with the typical PTF survey depth, and because we could use PTF variability data to create a membership list complementary to that of Rebull et al. (2011). As shown in Figure 2.1, almost the entire region fits in a single PTF exposure, allowing us to give the periphery and core of the region the same coverage. Because most of our targets are intrinsically red and further reddened by extinction, we conducted our survey in $R$ band.

### 2.3.3 Cadence and Time Baselines

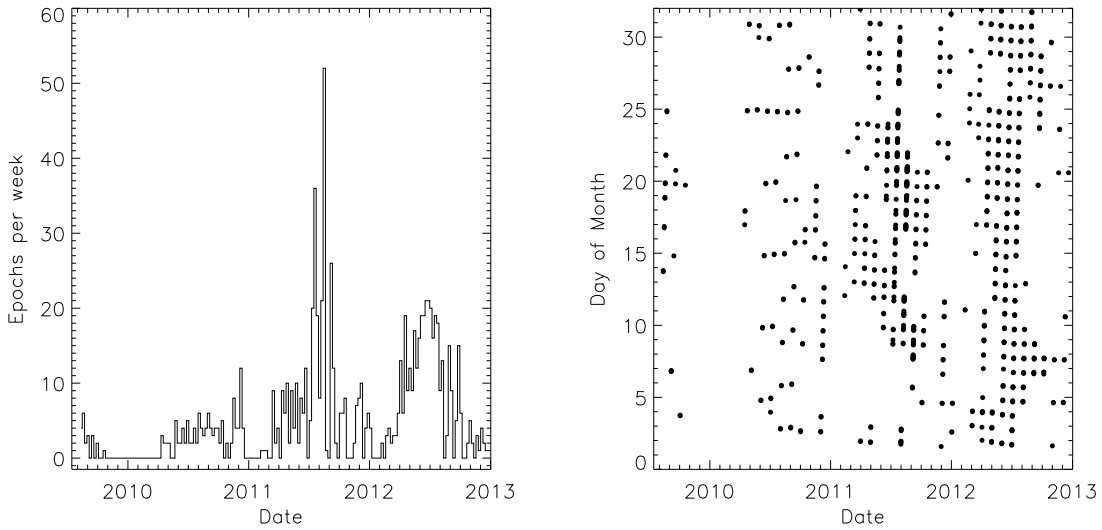


**(a)** Number of observations per week

**(b)** Individual observation times

**Figure 2.2:** The complex cadence used in the PTF North America Nebula survey. Date labels denote the beginning of each year. Figure 2.2a shows a histogram of the number of observations taken in each week of the survey. Figure 2.2b shows individual observation times of all survey epochs, with each month dispersed along the vertical axis for clarity. The period of all-night, high-cadence monitoring appears as a set of elongated points in mid-2011. The cadence in 2011-2012 was close to nightly, while observations in 2009 and 2010 were more sporadic.

Our survey cadence was complex as a result of changing operational factors. Throughout the survey, we took at least two exposures per night, separated by one hour, in case one of the measurements was corrupted by, for example, a cosmic ray. The survey started in 2009 August, continuing with observations every third night until October, when Palomar was shut down due to ash from local fires. When we started our 2010 season in April, the cadence was lowered to every fifth night. From 2010 August to October, we were able to observe every night, while the remainder of the season was hampered by poor weather. For our 2011 and 2012 seasons, from 2011 March to 2012

January and from 2012 March to 2012 December, we were able to observe every night, but only during bright time, as the PTF project had started observing exclusively with the $g'$ filter during dark time. In addition, during 2011 July and August, we obtained hourly exposures all night, in both bright and dark time. We illustrate our observing pattern in Figure 2.2.

Our survey represents one of the most uninterrupted, multi-year optical variability surveys of a star-forming region, featuring 894 epochs across 365 nights between 2009 August 13 and 2013 February 22. Our largest data gaps are the 1-3 month gaps in the winter, when the region is not visible from Palomar, and the two-week gaps during dark time in most months when the $R$ filter is not available. Aside from these regular gaps, we have two years of uninterrupted nightly coverage, except for occasional weather gaps, and another year and a half of lower-cadence data for probing long-term variability.

In addition to the data presented here, PTF continued to observe the North America Nebula region through 2013 December, although this data set has not yet been fully reduced by the PTF Photometric Pipeline. PTF will also continue to observe the North America Nebula complex, among other star-forming regions, at low cadence over the next few years as part of a separate search for very-long-term variability.

### 2.3.4 Aliasing

While the focus of our study is on aperiodic variability, we were also able to determine periods for those sources that were periodic. I analyzed the susceptibility of our cadence to aliasing following the standard window function formalism.

A series of magnitude measurements $(t_j, \hat{m}_j)$, each with negligible exposure time compared to the timescales of interest, can be expressed as the product of a continuous "real" signal $m(t)$ multiplied by an observing pattern $w(t)$, where $w(t)$ is a sum over terms $\delta(t - t_j)$ for each observation. The Fourier transform $\hat{\tilde{m}}(\nu)$ and power spectrum $\hat{P}_m(\nu)$ of the observed signal can then be expressed in terms of the Fourier transform of the observing pattern, $\tilde{w}(\nu)$ (Deeming, 1975):

$$\begin{aligned} \hat{\tilde{m}}(\nu) &= \tilde{m}(\nu) * \tilde{w}(\nu) \\ \hat{P}_m(\nu) &= P_m(\nu) * |\tilde{w}(\nu)|^2 \end{aligned}$$

The expression $\tilde{w}(\nu)$, known as the window function, convolves the true Fourier transform of the variability, $\tilde{m}(\nu)$, into the observed transform $\hat{\tilde{m}}(\nu)$ in a manner analogous to that in which the point-spread-function of an instrument convolves the true spatial distribution of incident radiation into an observed image. The window function therefore determines the quality of power spectra, periodograms, and other products of Fourier analysis in the same way that a point-spread-function determines the image quality of an instrument.

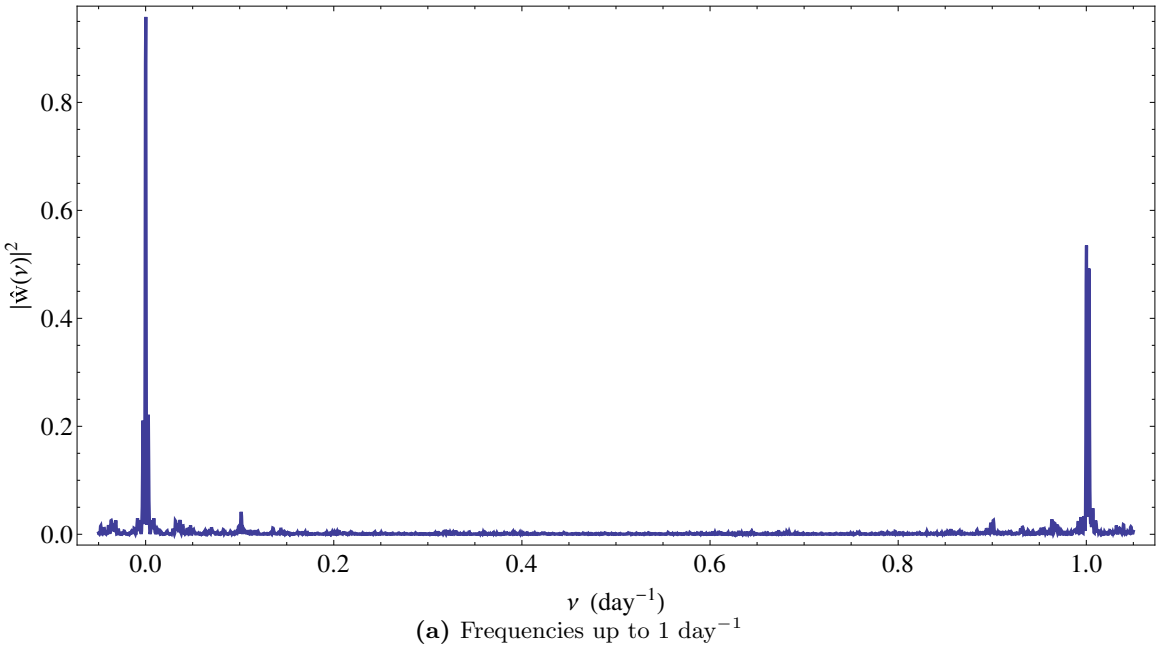


**(a)** Frequencies up to 1 day$^{-1}$

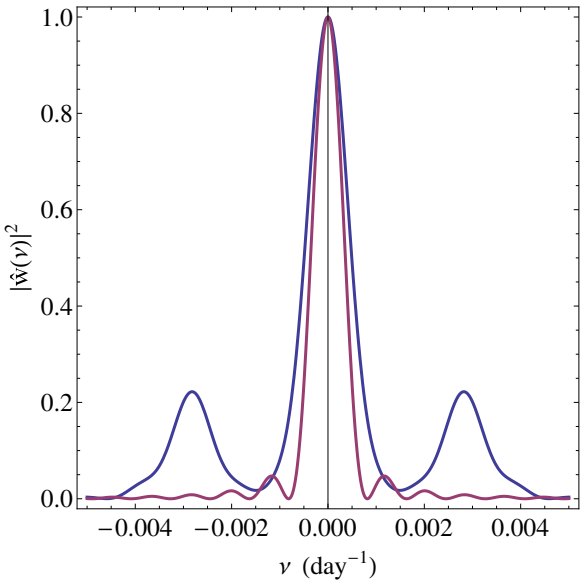


**(b)** Frequency-space convolution kernel

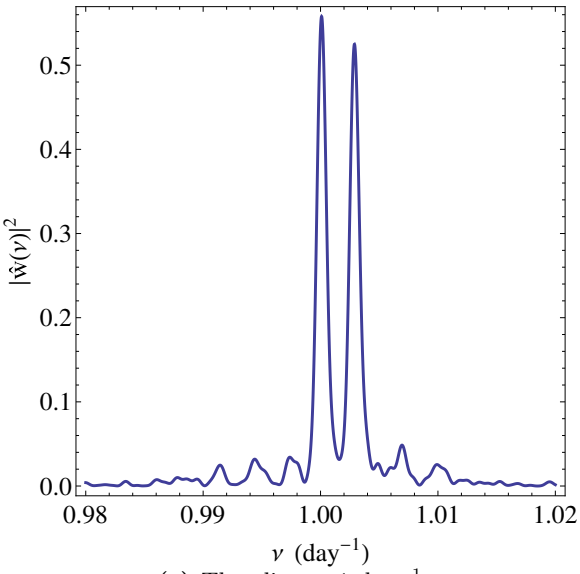


**(c)** The alias at 1 day$^{-1}$

**Figure 2.3:** The squared amplitude of the window function, $|\tilde{w}(\nu)|^2$ in the text, as a function of frequency. In all plots, the blue curve represents the window function corresponding to our PTF observations from 2009 through 2012. In Figure 2.3b, the purple curve is the window function that would be achieved in the idealized limit of continuous monitoring. The observed window function is well-behaved, with no major aliases aside from the inevitable daily alias.

If $w(t)$ has the form $\sum_j \delta(t - t_j)$ for observation times $\{t_j\}$, then the window function has the form

$$\tilde{w}(\nu) = \frac{1}{N} \sum_j e^{-2\pi i t_j \nu} \tag{2.1}$$

The squared amplitude of the window function, $|\tilde{w}(\nu)|^2$, is illustrated in Figure 2.3 for the PTF cadence from 2009 August through 2012 December. The FWHM frequency resolution of our cadence is 0.00099 day$^{-1}$, 37% larger than the resolution attainable by a continuous monitoring program over the same baseline (0.00072 day$^{-1}$). With this data we can determine 2-day periods to $\pm\frac{0.004 \text{ days}}{\sqrt{SNR}}$, but 200-day periods only to $\pm\frac{40 \text{ days}}{\sqrt{SNR}}$, where $SNR$ denotes the signal-to-noise ratio of the periodogram, not of the original measurements.

The dominant alias is a pair of peaks at 1 day$^{-1}$, which reach 56% of the primary peak at $\tilde{w}(0)$. Therefore, one expects alias peaks in a periodogram to have roughly 56% the height of the associated true peak, although the exact ratio will vary depending on coincidences with noise fluctuations or with overtones and other secondary peaks, as well as on how closely a given type of periodogram is related to Fourier analysis and the power spectrum. Our experience with phasing lightcurves in the PTF data by various trial periods confirms that, while we can frequently assume that the highest peak in a Lomb-Scargle periodogram is the true period, the true period corresponds to the second-highest peak in a fair number of cases.

The exact frequencies of the two daily aliases are 1.000 day$^{-1}$ and 1.003 day$^{-1}$. The former frequency is one per solar day, while the latter frequency is very close to one per sidereal day. We believe that, while the 1.000 day$^{-1}$ alias is the ordinary alias resulting from nightly observations, the 1.003 day$^{-1}$ alias is caused by the scheduling of observations, over the course of the year, for when the NAN Complex is highest in the sky, which results in observations separated by one sidereal day on average.

Other aliases include a yearly alias, at 0.003 day$^{-1}$ and 20% of the height of the primary peak, and an unexplained alias at 0.102 day$^{-1}$ (perhaps related to PTF's operations schedule, as it is close to one third of a synodic month) but only 4% of the height of the primary peak. In general, the window function shown in Figure 2.3 is remarkably clean, indicating that the daily alias is the main caveat in interpreting periodic variability.

### 2.3.5 Systematics

The PTF Photometric Pipeline has several limitations that must be borne in mind when analyzing our work. The most important is that, since sources were identified using SExtractor and characterized using aperture photometry, sources may be missing, misidentified, or have poor photometry in regions with substantial H$\alpha$ nebulosity. An example of a region with missing sources can be seen in Figure 2.4.

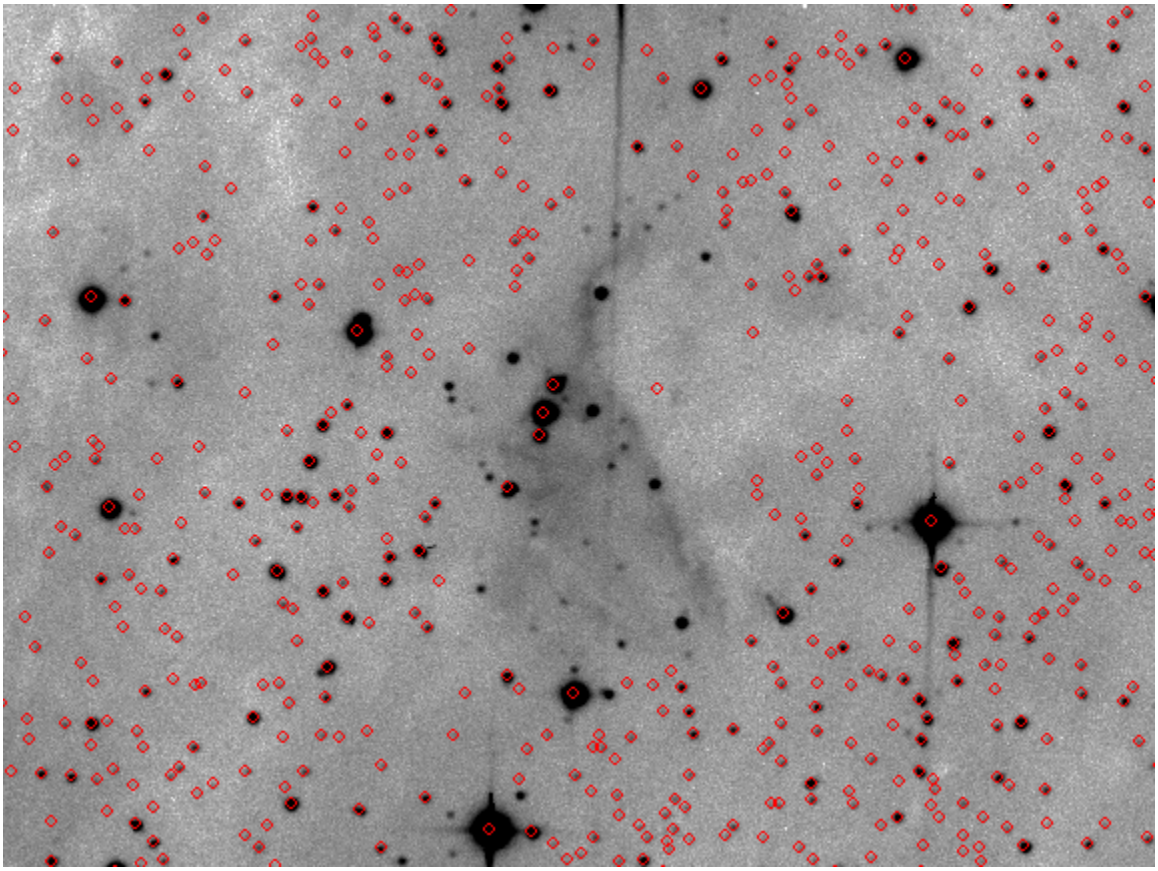

**Figure 2.4:** An example of a PTF image where not all sources were detected with SExtractor. Red circles mark the positions of SExtractor detections; most of the sources near the nebula filament in the center are *not* circled. One of the missing sources is PTF10nvg (Covey et al., 2011), which was identified by the LBNL transient pipeline.

In addition, the PTF Photometric Pipeline does not use color corrections when computing ($R_{\rm PTF}$); these terms are around 0.2 mag per magnitude of $r - i$ (Ofek et al., 2012). The lack of a color term means that sources with large color changes over the course of their variability will have their amplitudes slightly overestimated if they get redder as they get brighter, and slightly underestimated if they get redder as they get fainter. Fortunately, it will take a large color amplitude ($\Delta(r - i) \gtrsim 0.5$) to significantly affect our measured amplitudes. The color term may be a more significant issue for future work with the PTF data set, once improved reductions allow us to probe variability below amplitudes of a few tenths of a magnitude.

The pipeline also underestimates photometric errors, even after including a systematic error term (Levitan & Sesar, priv. comm. 2012).

## 2.4 Supplementary Data

### 2.4.1 Spectroscopy

We pursued optical spectroscopy both of stars with significant variability (as selected in subsection 3.2.1) and of the infrared-excess selected sample of Rebull et al. (2011) using the MMT, Keck Observatory, Palomar Observatory, and Kitt Peak National Observatory. Several of our targets were also observed by other members of the PTF collaboration as part of PTF's spectroscopic follow-up program.

We observed 257 variable infrared-excess sources in the North America Nebula using the DEIMOS multi-object spectrograph (Faber et al., 2003) at Keck on 2012 July 18-19 and 2013 July 9, using the 600 line/mm grating. PTF was monitoring the field during both 2012 nights that spectra were taken, allowing us to determine the photometric state represented by each spectrum for all stars except those varying substantially in less than a day.

The DEIMOS spectra were reduced using a modified version of the DEEP2 pipeline (Newman et al., 2013; Cooper et al., 2012), provided to us by Evan Kirby. The spectra were bias-corrected, dome-flatfielded, and wavelength-calibrated, but were not flux-calibrated. We corrected for sky and nebula emission by subtracting the off-source spectrum visible within each slit. The final spectra covered approximately the 4400-9500 Å range at 5 Å resolution, although the range covered by the spectrum of any particular star could shift by $\sim$ 500 Å in either direction depending on the position of the star's slit on the instrument mask. Many cosmic rays were left uncorrected by the pipeline, so when making the figures in Chapter 3, we cleaned the cosmic rays by hand for clarity.

194 sources selected by either variability or infrared excess were observed using the Hectospec multi-object spectrograph (Fabricant et al., 2005) on the MMT on 2012 November 3, December 4, and December 6, using the 270 lines/mm grating. The data were pipeline processed at the Harvard-Smithsonian Center for Astrophysics (Mink et al., 2007). The final spectra cover 3700-9100 Å at 6 Å

resolution. PTF observed the region on November 3 and December 6, but to interpret the December 4 spectra we had to interpolate between photometry from December 3 and December 6.

Lynne Hillenbrand had previously obtained low-resolution optical spectra of sources in the North America Nebula complex with the HYDRA multi-object spectrograph (Barden et al., 1993) on the 3.5m WIYN telescope at Kitt Peak, using the 316 line/mm grating, on six nights between 1998 June 2 and 1998 July 21. L. H. also took spectra using the (now decommissioned) Norris multi-object spectrograph (Hamilton et al., 1993) on the 5m Hale Telescope at Palomar, using the 600 line/mm grating, on 1998 August 14-15, 1999 July 21-23, and 1999 September 2-5. The HYDRA and Norris spectra do not have concurrent photometry.

The HYDRA and Norris observations were reduced for us by Gregory Herczeg using custom routines written in IDL. The routines applied corrections for bias, dome flats, cosmic rays, scattered light, and wavelength calibration. The spectra were not flux-calibrated. Sky and nebula emission were corrected by taking a shorter sky exposure offset 6-10″ from the target position, and subtracting the counts in the sky exposure from the corresponding source spectrum, after scaling to the difference in observing times. In several configurations the sky emission was scaled by an additional 10-20% to account for changes in the sky transmission. The HYDRA spectra covered 5000-10000 Å at $R \sim 1,500$, while the Norris spectra covered 6100-8750 Å at $R \sim 2,000$.

The PTF collaboration took classification spectra for 12 sources in our field: PTF09dsa, PTF09ejq, PTF09ekb, PTF09epi, PTF09fuk, PTF10gdb, PTF10geh, PTF10qpf, PTF10suh, PTF10abyb, PTF11cjr, and PTF11oyt, sometimes at multiple epochs. The PTF spectra are a heterogeneous sample. Roughly half were taken with KAST on the Lick 3-m, with the remainder divided among LRIS on Keck, RCspec on the Kitt Peak 4-m, DBSP on the Palomar 200-inch, ACAM on the William Herschel Telescope, and LRS on the Hobby-Eberly Telescope. The spectra extended from 3500-4000 Å to 8500-10000 Å at resolutions of 5-15Å.

### 2.4.2 Mid-IR Photometry

Luisa Rebull provided us with Spitzer photometry for all sources observed for Rebull et al. (2011), including unpublished photometry for sources that did not have an infrared excess. The data were reduced as described in that paper. We made use of all four IRAC channels, and the MIPS 24 $\mu$m channel, but not the MIPS 70 $\mu$m or 100 $\mu$m channels. Most of the PTF survey area was also covered by the Spitzer data (Figure 2.5).

### 2.4.3 Near-IR Photometry

We supplemented the mid-IR photometry from Spitzer with J, H, and K-band photometry from the Two-Micron All-Sky Survey (2MASS). 2MASS sources were filtered by the same quality cuts as

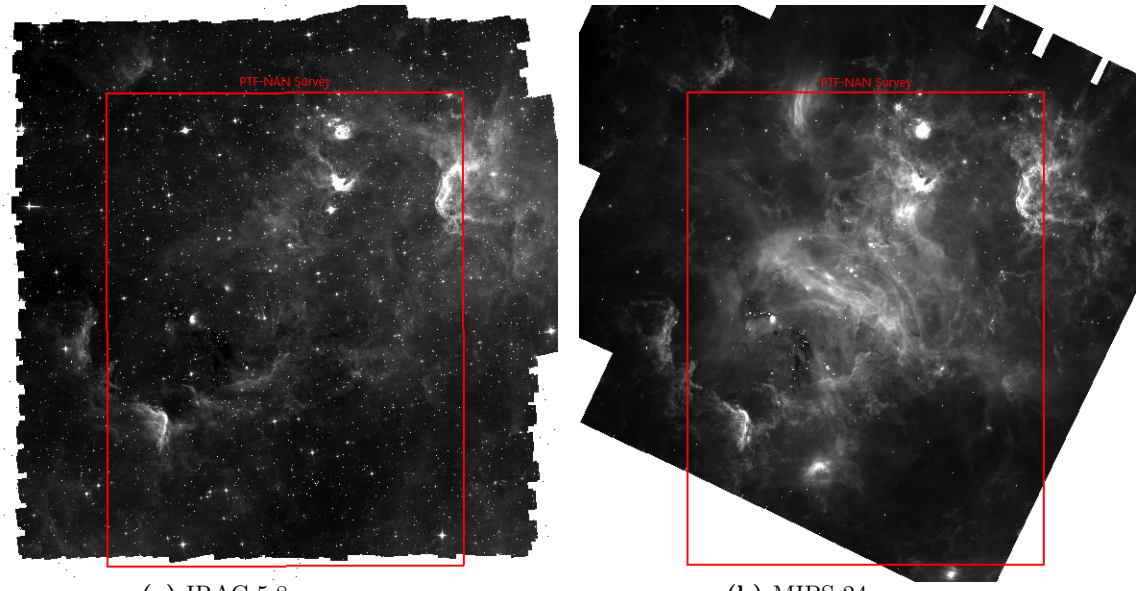


**(a)** IRAC 5.8 $\mu$m coverage **(b)** MIPS 24 $\mu$m coverage

**Figure 2.5:** The North America Nebula complex as a Spitzer mosaic (Guieu et al., 2009; Rebull et al., 2011). The red rectangle represents the area covered by Figure 2.1. We have IRAC data for nearly all sources of the survey region, and MIPS data for a majority of sources.

adopted by Guieu et al. (2009) and Rebull et al. (2011). Only photometry with band quality flags of "A", "B", "C", or "U" was considered (Rebull, priv. comm. 2014).

### 2.4.4 H$\alpha$ Fluxes

We used H$\alpha$ photometry from the INT Photometric H-alpha Survey (IPHAS; Drew et al., 2005) to characterize the fraction of sources of interest with strong accretion. Since the IPHAS initial data release appeared to have been withdrawn from publication at the time of writing[2], we instead relied on the source matching carried out by Rebull et al. (2011).

## 2.5 Summary

Thanks to PTF, we have collected, for the first time, a homogeneous long term, medium-cadence optical variability survey of the North America Nebula (NAN) complex. While the photometric precision, cadence, or time baseline have all been individually exceeded by previous surveys, the combination of factors has given us a unique perspective on pre-main-sequence stellar variability. In particular, a survey such as PTF-NAN is the only way to comprehensively study aperiodic variability, as both lower cadences and shorter baselines will miss key components of the variability.

[2] A new release was published as the thesis was being finalized (Barentsen et al., 2014), and will be incorporated into future work.

The PTF-NAN survey is supplemented by spectroscopic follow-up observations, as well as optical, near-infrared, and mid-infrared photometry collected for Rebull et al. (2011). Where available, we use H$\alpha$ fluxes from the IPHAS survey to characterize stars for which we were unable to obtain spectra.

## 2.6 References

Bally, J., & Scoville, N. Z. 1980, ApJ, 239, 121

Barden, S. C., Armandroff, T., Massey, P., Groves, L., Rudeen, A. C., Vaughnn, D., & Muller, G. 1993, in Astronomical Society of the Pacific Conference Series, Vol. 37, Fiber Optics in Astronomy II, ed. P. M. Gray, 185

Barentsen, G. et al. 2014, ArXiv e-prints, arXiv:1406.4862

Comerón, F., & Pasquali, A. 2005, A&A, 430, 541

Cooper, M. C., Newman, J. A., Davis, M., Finkbeiner, D. P., & Gerke, B. F. 2012, Astrophysics Source Code Library, ascl:1203.003

Covey, K. R. et al. 2011, AJ, 141, 40, arXiv:1011.2565

Deeming, T. J. 1975, Ap&SS, 36, 137

Drew, J. E. et al. 2005, MNRAS, 362, 753, astro-ph/0506726

Faber, S. M. et al. 2003, in Society of Photo-Optical Instrumentation Engineers (SPIE) Conference Series, Vol. 4841, Society of Photo-Optical Instrumentation Engineers (SPIE) Conference Series, ed. M. Iye & A. F. M. Moorwood, 1657–1669

Fabricant, D. et al. 2005, PASP, 117, 1411, arXiv:astro-ph/0508554

Guieu, S. et al. 2009, ApJ, 697, 787, arXiv:0904.0279

Hamilton, D., Oke, J. B., Carr, M. A., Cromer, J., Harris, F. H., Cohen, J., Emery, E., & Blakee, L. 1993, PASP, 105, 1308

Laugalys, V., Straižys, V., Vrba, F. J., Boyle, R. P., Davis Philip, A. G., & Kazlauskas, A. 2006, Baltic Astronomy, 15, 483

Law, N. M. et al. 2009, PASP, 121, 1395, arXiv:0906.5350

Levitan, D. et al. 2011, ApJ, 739, 68, arXiv:1107.1209

Mink, D. J., Wyatt, W. F., Caldwell, N., Conroy, M. A., Furesz, G., & Tokarz, S. P. 2007, in Astronomical Society of the Pacific Conference Series, Vol. 376, Astronomical Data Analysis Software and Systems XVI, ed. R. A. Shaw, F. Hill, & D. J. Bell, 249

Newman, J. A. et al. 2013, ApJS, 208, 5, arXiv:1203.3192

Ofek, E. O., Frail, D. A., Breslauer, B., Kulkarni, S. R., Chandra, P., Gal-Yam, A., Kasliwal, M. M., & Gehrels, N. 2011, ApJ, 740, 65, arXiv:1103.3010

Ofek, E. O. et al. 2012, PASP, 124, 62, arXiv:1112.4851

Rau, A. et al. 2009, PASP, 121, 1334, arXiv:0906.5355

Rebull, L. M. et al. 2011, ApJS, 193, 25, arXiv:1102.0573

# Chapter 3

# Disk-Related Bursts and Fades in Young Stars[1]

## 3.1 Introduction

The best-studied aperiodic variables at present are episodic variables: stars whose lightcurves contain one or more isolated features that can be explained as accretion or extinction events. The relative simplicity of episodic variables, along with the scrutiny to which they have already been subjected in the literature (reviewed in subsection 1.2.3), makes them an excellent starting point for any study of aperiodic variability as a whole. In addition, bursting and fading have been relatively poorly studied on timescales of weeks, while our data allows us to explore these timescales very well.

The present chapter focuses on observable optical variability among the $\sim 2,100$ known and suspected members of the North America Nebula complex cataloged by Rebull et al. (2011) based on mid-infrared selection techniques. Of these, 84% are within our monitored field. Among the wide range of behaviors exhibited by variable stars, we consider the evidence for and typical properties of bursting or fading behavior, possibly mixed with other forms of variability. In the case of bursting stars, while accretion-related instabilities having timescales of a few tens of days have been predicted by a number of theoretical studies (e.g., Aly & Kuijpers, 1990; Romanova et al., 2004), no evidence for accretion bursts produced by such instabilities has been published (Bouvier et al., 2007), although accretion bursts on both shorter (Murphy et al., 2011) and longer (Herbig, 2008) timescales have been observed. We assess, for the first time, the frequency of these intermediate timescale instabilities. For fading stars, while the existence of extinction-related variability is well-established, results vary among authors as to the frequency of young stars exhibiting such behavior, as well as the typical timescales. We also address in this study, for the first time, the ratio of bursting to fading lightcurves for a typical T Tauri star population.

The remainder of this chapter is organized as follows. In section 3.2, we present our photometric

[1]Based on work published as Findeisen et al. (2013), ApJ 768, 93. 

data and our detection thresholds for variability. Section 3.3 discusses how we defined the burster and fader populations and their key properties. In sections 3.4 and 3.5, we discuss the bursters and faders in more detail, with an emphasis on how the largest sample yet identified of such objects can constrain their underlying physics. In section 3.6, we describe several noteworthy objects in more detail. Section 3.7 summarizes our results, describes limitations of our analysis, and suggests pathways for future work.

## 3.2 Photometric Data

This study was based on PTF data collected between 2009 August and 2012 December, as described in subsection 2.3.3, and reduced by the PTF Photometric Pipeline, as described in subsection 2.2.2. The original sample selection was based on a less complete data set, through 2012 April, and some sources that were originally in our sample fell outside our selection criteria when the remaining months were included. For consistency, these sources were kept inside the sample.

### 3.2.1 Identifying the Variables

To determine which sources were variable during the observation period, we grouped all PTF detections with $14 \leq R \leq 20$ mag into half-magnitude bins on a chip-by-chip basis. The width of the bins (0.5 mag) was chosen so that the brightest and least populated bin (14-14.5 mag) had roughly 100 sources on most chips. We then computed the median RMS of all the stars in each bin, and fit the medians by an equation of the form:

$$RMS = \sqrt{a^2 + (b \times 10^{-0.4p(mag-14)})^2} \tag{3.1}$$

This equation is partly motivated as the sum of a systematic term and a flux-dependent term; the exponent of the flux-dependence $p$ was allowed to vary because the natural choice, $p = \frac{1}{2}$ (i.e., noise that scales as the square root of the flux, as expected from photon noise), was too shallow. In practice we found $p \sim \frac{2}{3}$ for most chips. We list the fit parameters in Table 3.1.

The curve found by fitting Equation 3.1 describes the locus of nonvariable stars on a given chip. We defined the boundary between variable and nonvariable stars to be 1.75 times the median RMS. This cutoff was determined empirically, rather than analytically, to avoid making assumptions about the noise properties of the data. We set the cutoff by visually inspecting lightcurves with both $R \sim 14$ and $R \sim 16$; at RMS values lower than 1.75 times the threshold the lightcurves were indistinguishable from noise, while at higher values the lightcurves were clearly structured on short timescales.

We show in Figure 3.1 plots of RMS vs. magnitude for the six chips that covered the star-forming complex, along with the median fit and the variability detection boundary for each chip. For 14th

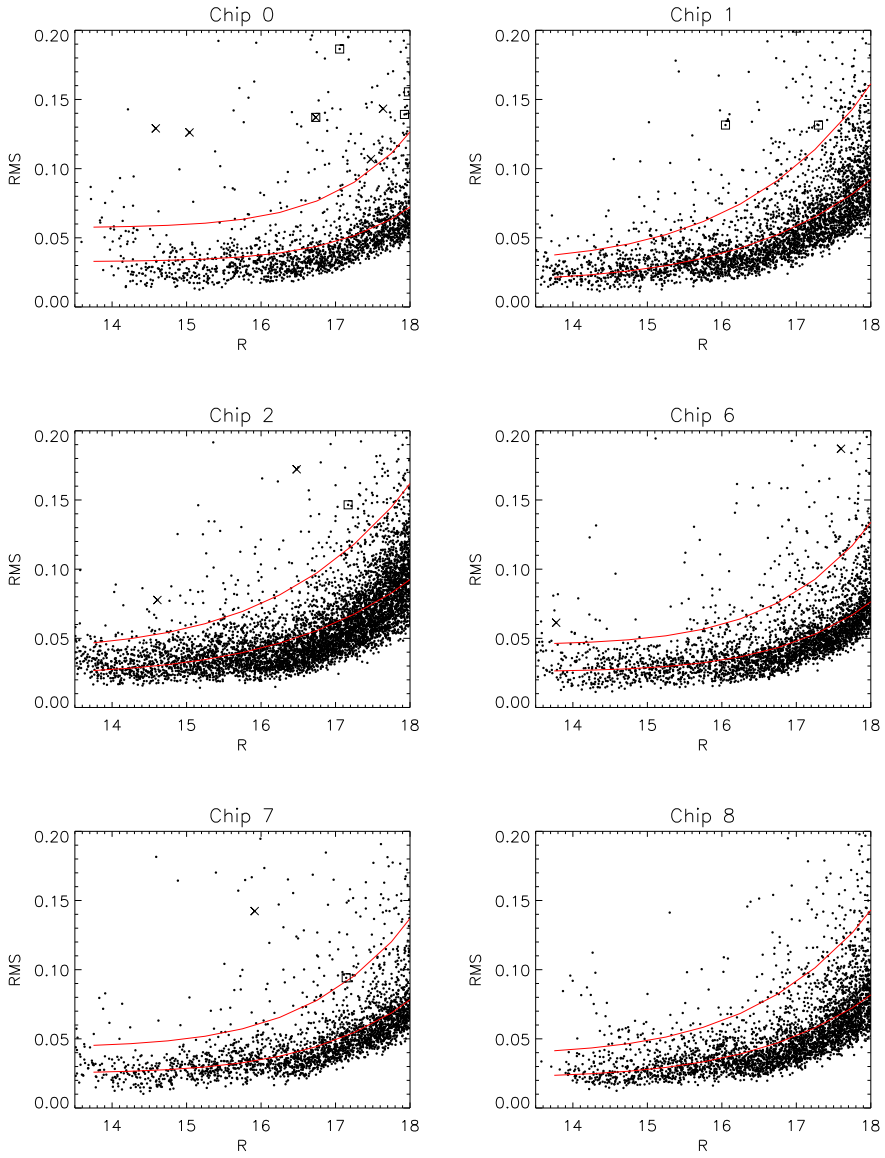


**Figure 3.1:** RMS scatter vs. median magnitude for all sources with flags (listed in subsection 2.2.2) in fewer than half the epochs. The fit to the median RMS as a function of magnitude is plotted as the lower red curve, while our variability detection threshold (1.75 times the median) is plotted as the upper red curve. X's mark candidate bursting stars from Table 3.4 while squares mark candidate fading stars. 27 high-amplitude variables are beyond the upper edge of the Chip 0 plot, 10 each above the upper edge of the Chip 1 and Chip 2 plots, and 1-5 off the upper edge of each of the others.

| Chip | $a$ | $b$ | $p$ | Total Sources | Variables |
|---|---|---|---|---|---|
| 0 | 0.033 | 0.0053 | 0.68 | 6,090 | 491 (8.1%) |
| 1 | 0.018 | 0.0130 | 0.52 | 9,330 | 490 (5.3%) |
| 2 | 0.023 | 0.0145 | 0.49 | 14,057 | 533 (3.8%) |
| 6 | 0.026 | 0.0072 | 0.62 | 11,036 | 457 (4.1%) |
| 7 | 0.025 | 0.0081 | 0.60 | 7,720 | 337 (4.4%) |
| 8 | 0.022 | 0.0105 | 0.55 | 10,393 | 397 (3.8%) |

**Table 3.1:** Best-fit values for the parameters in Equation 3.1 for each of the six target chips. The parameter $a$ can be interpreted as the systematic noise floor at bright magnitudes, and $p$ is the power-law dependence of RMS on flux at faint magnitudes. The last two columns show the total number of PTF sources on each chip as well as the number selected by making an RMS cut at 1.75 times the value given by Equation 3.1.

magnitude stars, we are sensitive to variability with an RMS amplitude of a few percent, while below 16th magnitude, we can probe only 10% flux variations. In Table 3.1, we list the number of PTF sources and the number and fraction identified as photometrically variable using the methods outlined above. Nearly 3,000 variables projected on the dark cloud and the associated nebulae are identified. Their RMS amplitudes range from 0.03 to 1.1 mag.

## 3.3 Bursting and Fading Among Infrared Excess Sources

### 3.3.1 Sample Selection

Because the North America Nebula complex is located in the plane of the Galaxy, a significant number of our high quality lightcurves are those of foreground or background field stars. In our first reconnaissance of the variability properties of the region, we therefore concentrated on variable stars among a list of candidate North America Nebula members identified by Rebull et al. (2011). Specifically, Rebull et al. used infrared colors, primarily Spitzer IRAC 3.6 $\mu$m − MIPS 24 $\mu$m, to identify stars surrounded by circumstellar dust. Additional considerations included location in various color-magnitude diagrams that help distinguish young stars from contaminating dusty sources such as extragalactic AGN and galactic late-type giants. Each source was assigned a spectral energy distribution class based on the slope of a linear fit to all available photometry between 2 and 24 $\mu$m. Class I sources have rising slopes and are interpreted as objects with not only circumstellar disks, but likely more spherically distributed envelopes as well. Flat-spectrum sources have roughly constant $\lambda F_\lambda$ over the 2-24 $\mu$m range and have a similar interpretation. Class II sources are consistent with traditional disk SEDs. Class III sources have the steepest slopes; most have no excess in the IRAC bands but were selected based on an excess at 24 $\mu$m. Only 6 of the Class III sources in Rebull et al. (2011) were not selected using either IRAC or MIPS excess criteria. Rebull et al. note that, since their primary selection is based on infrared data, they are incomplete with respect to Class III sources.

| IR Source Type | # in RGS2011 | in PTF Field | PTF Counterparts | With $R < 18$ | Flags in $< 50\%$ Epochs | High RMS |
|---|---|---|---|---|---|---|
| MIPS-Only | 25 | 25 (100%) | 0 ( 0%) | | | |
| Class I | 273 | 242 ( 89%) | 11 ( 5%) | 3 (27%) | 3 (100%) | 3 (100%) |
| Flat-Spectrum | 272 | 242 ( 89%) | 53 (22%) | 20 (38%) | 13 ( 65%) | 10 ( 77%) |
| Class II | 604 | 542 ( 90%) | 321 (59%) | 160 (50%) | 120 ( 75%) | 79 ( 66%) |
| Class III | 112 | 82 ( 73%) | 76 (93%) | 43 (53%) | 31 ( 72%) | 16 ( 52%) |
| IRAC-Only | 796 | 613 ( 77%) | 140 (23%) | 27 (19%) | 19 ( 70%) | 9 ( 47%) |
| Total | 2,082 | 1,746 ( 84%) | 601 (34%) | 253 (42%) | 186 ( 74%) | 117 ( 63%) |

**Table 3.2:** Rebull et al. (2011) gave SED classes only for sources that were detected in both IRAC and MIPS. Sources that were detected in only one or the other are listed for comparison, but were not used to estimate the incompleteness from source confusion and flux limits.

Of the 2,082 candidates from Rebull et al. (2011), 601 had a counterpart in the PTF source catalog. As we show in Table 3.2, the recovery rate by PTF depended strongly on the type of IR excess. Only 5% of the relatively red Class I sources in the PTF field had detections, while fully 93% of the relatively blue Class III sources were detected by PTF. The strong correlation between (infrared) source color and recovery rate, in the sense that redder sources are recovered less often, suggests that most of the sources we did not recover in PTF were missed because they were below our optical detection limits. However, from image inspection we also know that the PTF pipeline had difficulty identifying and extracting sources from crowded or nebulous regions. If we assume that all the Class III sources must be bright enough to detect in the optical if they are visible in the Spitzer bands even with a small infrared excess, then source extraction problems should dominate the 7% missing Class III sources. Presumably, roughly 7% of the rest of the sample also fell in regions where the PTF pipeline could not reliably identify sources. This argument assumes that Class III sources are not less likely to be in crowded or high-background regions, where the PTF pipeline is least reliable, and should be treated with caution. We note that, while the overall incompleteness does not affect our main science goals, the bias away from Class III sources in the parent sample and the bias away from Class I sources from cross-matching to PTF do limit our ability to examine how variability properties change with the degree of infrared excess.

From our sample of 601 infrared excess selected candidate members with PTF counterparts, we restricted our attention to the 253 sources brighter than a median $R_{\rm PTF} = 18$. The detailed breakdown by SED type is given in Table 3.2. We found from experience that the photometric quality for sources fainter than $R_{\rm PTF} \sim 18$ was such that, while we could determine whether a source was variable, we could not consistently assess the structure of the variability. Considering only sources whose lightcurves had bad photometry flags (see subsection 2.2.2 for a list) in fewer than half the epochs further reduced the sample to 186 stars, which are shown in Figure 3.2. The figure shows no trend with $R_{\rm PTF}$ except for more sources at fainter magnitudes, suggesting our magnitude limits avoid any substantial systematics. High-amplitude sources (RMS $\gtrsim$ 0.3-0.4 mag) tend to be associated with strong infrared excess, while low amplitudes are found in both strong- and weak-excess sources.

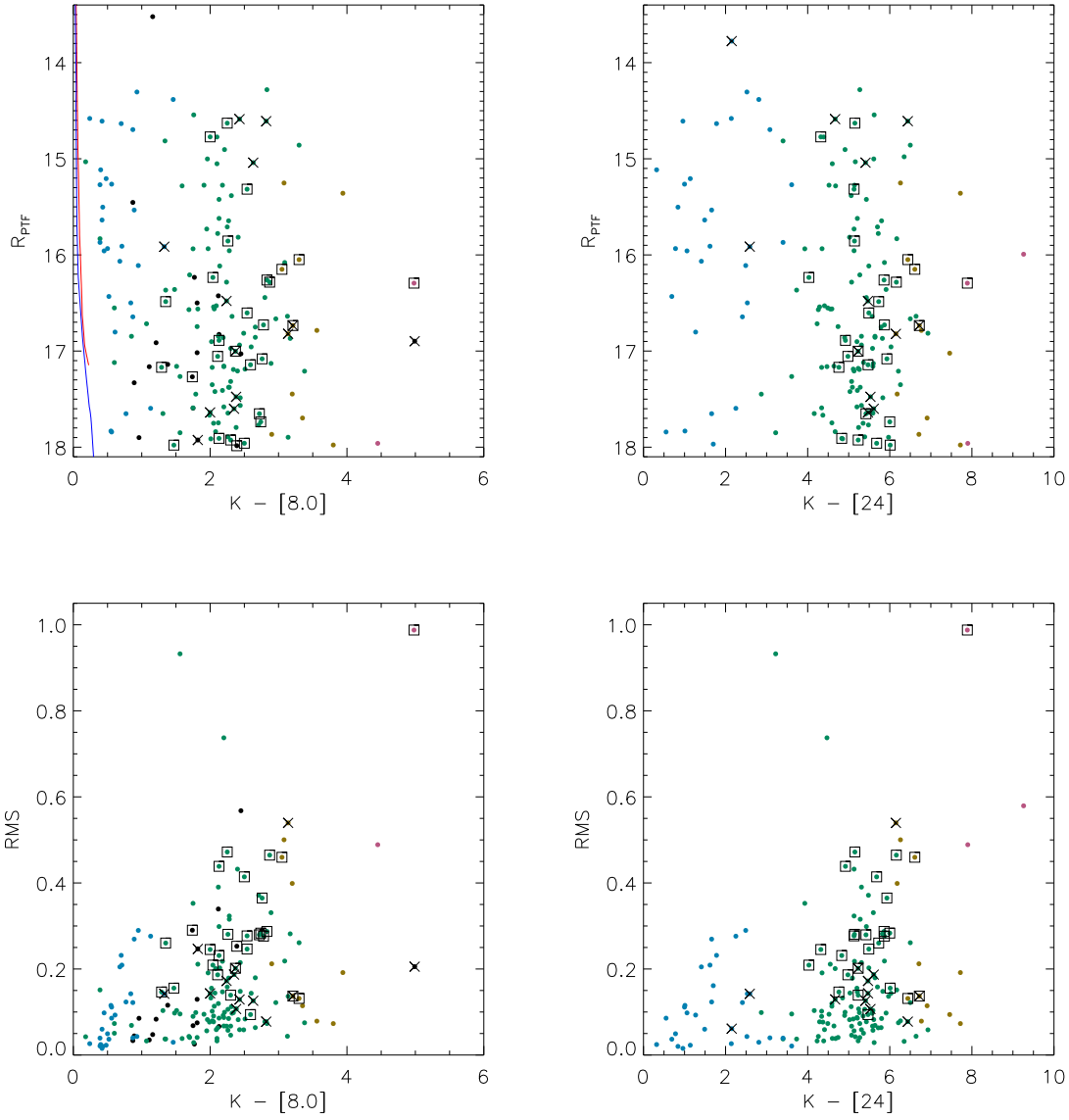


**Figure 3.2:** PTF magnitude and IR color distributions for those PTF sources that have an infrared excess from Rebull et al. (2011) and whose lightcurves have flags (listed in subsection 2.2.2) in fewer than half the epochs. The color of the dots indicates the degree of infrared excess: blue dots are class III sources, green ones class II, yellow ones have a flat IR spectrum, while magenta sources are class I sources. The black sources are those that were not detected in the Spitzer 24$\mu$m band, and so did not have an IR excess class listed in Rebull et al. (2011). Not all sources appear on both plots, as some had missing 8$\mu$m or 24$\mu$m photometry. The curves in the upper left panel show synthetic photometry of Siess et al. (2000) isochrones for ages of 2 Myr (red) and 100 Myr (blue), at a distance of 600 pc, indicating the expected colors of stars with no infrared excess at all. As in Figure 3.1, X's mark candidate bursting stars while squares mark candidate fading stars.

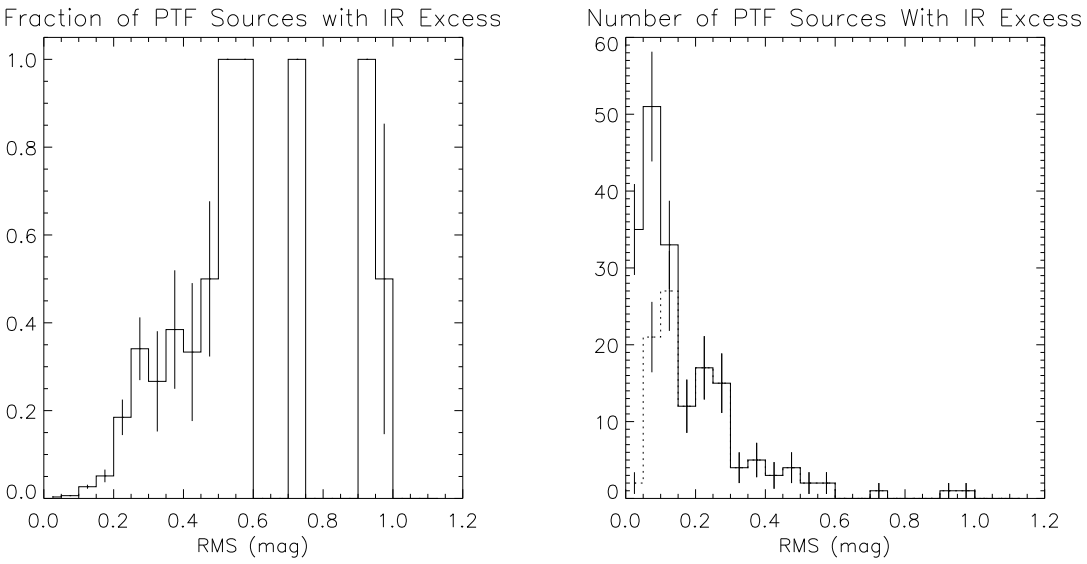


**Figure 3.3:** RMS distribution of the sample, and its correlation with the presence of Spitzer infrared excess. Left: the fraction of sources with an infrared excess out of all PTF sources with $13.5 \leq R \leq 18$ and flags (listed in subsection 2.2.2) in fewer than half the epochs. Right: the solid line denotes the distribution of RMS amplitudes for the 186 infrared excess sources from Rebull et al. (2011) whose lightcurves have flags in fewer than half the epochs. The dashed line represents the subset of 117 that lie above the variability thresholds in Figure 3.1.

From this sample of 186, we studied in more detail the 117 that showed significant variability in PTF, as defined in subsection 3.2.1. Both cuts are presented in more detail in Table 3.2. These infrared excess selected variables include most of the high amplitude variables in the field, as shown in Figure 3.3; most of the low amplitude variables in the field lack an infrared excess and are not part of our sample. The 117 infrared-excess variable sources, along with the other variables in the field, exhibit a wide range of timescales and amplitudes in their lightcurves. We sought to categorize the lightcurves and hereafter we focus on those that can be identified as bursting or fading.

When selecting sources for inclusion on the list of bursters or faders, we defined a burst in a lightcurve as a period of elevated fluxes above a (local) floor of relatively constant brightness. We did not place any explicit restriction on the length of the candidate burst. However, we tended to require elevated fluxes in multiple consecutive epochs to be certain that a brighter measurement was not a measurement error, and we required that the period of elevated fluxes be short enough that we could recognize the remainder of the lightcurve as a well-defined "quiescent" state. We defined fades analogously as a period of lowered fluxes, with the caveats that we believed the lower fluxes represented real variability and that the lower fluxes were distinct from the normal variability of the star. Both definitions were necessarily subjective, and we review possible selection effects in subsection 3.7.3.

We visually inspected all 117 lightcurves for bursting or fading activity. For comparison, we also inspected 100 randomly chosen variable PTF sources that did *not* have an infrared excess, mixing them with the sample of 117 so that we did not know whether any particular lightcurve was from the target sample or the control group. We designated a star as a burster or a fader if it had at least one bursting or fading event during the monitoring period.

### 3.3.2 Burster and Fader Statistics

We identified 14 stars with candidate bursts and 29 stars with candidate fades, with two stars showing both bursting and fading behavior. The sources are listed in Table 3.3, with their photometric behavior summarized in Table 3.4. Lightcurves of all 41 stars are available online from the PTF website[2]. The sources are also highlighted in Figures 3.1, 3.2, and 3.4.

For comparison, in the control group of 100 sources with no infrared excess, we saw only two stars that appeared to have one burst each, and no faders other than eclipsing binaries. The burst detected in one of the stars turned out to be a transient scattered light artifact we had failed to spot at the time of the original analysis. The other may also have been identified as a burster because of a systematic error in the data or in our visual inspection, or it may represent real astrophysical variability in the field. In the former case we expect $\sim 2$ of the bursters in our target sample to be mislabeled, while in the latter we expect $\sim 1$ false positives.

The stars listed in Tables 3.3 and 3.4, some of which are highlighted in Figure 3.5 and Figure 3.6, show a wide variety of behaviors. We see variability from a few tenths of a magnitude to several magnitudes. The bursts or fades last anywhere from around a day, the shortest timescale resolvable in most of our data, to hundreds of days. Events may repeat as frequently as once a week, or can appear only once in the three-year monitoring period. Nearly all the bursters and faders are aperiodic, with the exception of two faders that are discussed further in section 3.5.

### 3.3.3 Spectroscopic Characterization

We pursued optical spectroscopy of both the variable star selected sample (this paper) and the infrared-excess selected sample of Rebull et al. (2011) using the MMT, Keck Observatory, Palomar Observatory, and Kitt Peak National Observatory.

Of the spectroscopic samples described in subsection 2.4.1, the 2012 DEIMOS observations included 19 bursters or faders, and the MMT observations included 22 bursters or faders. The HYDRA and Norris spectra taken in 1998 and 1999 included 27 bursters or faders.

[2] http://www.astro.caltech.edu/ptf/

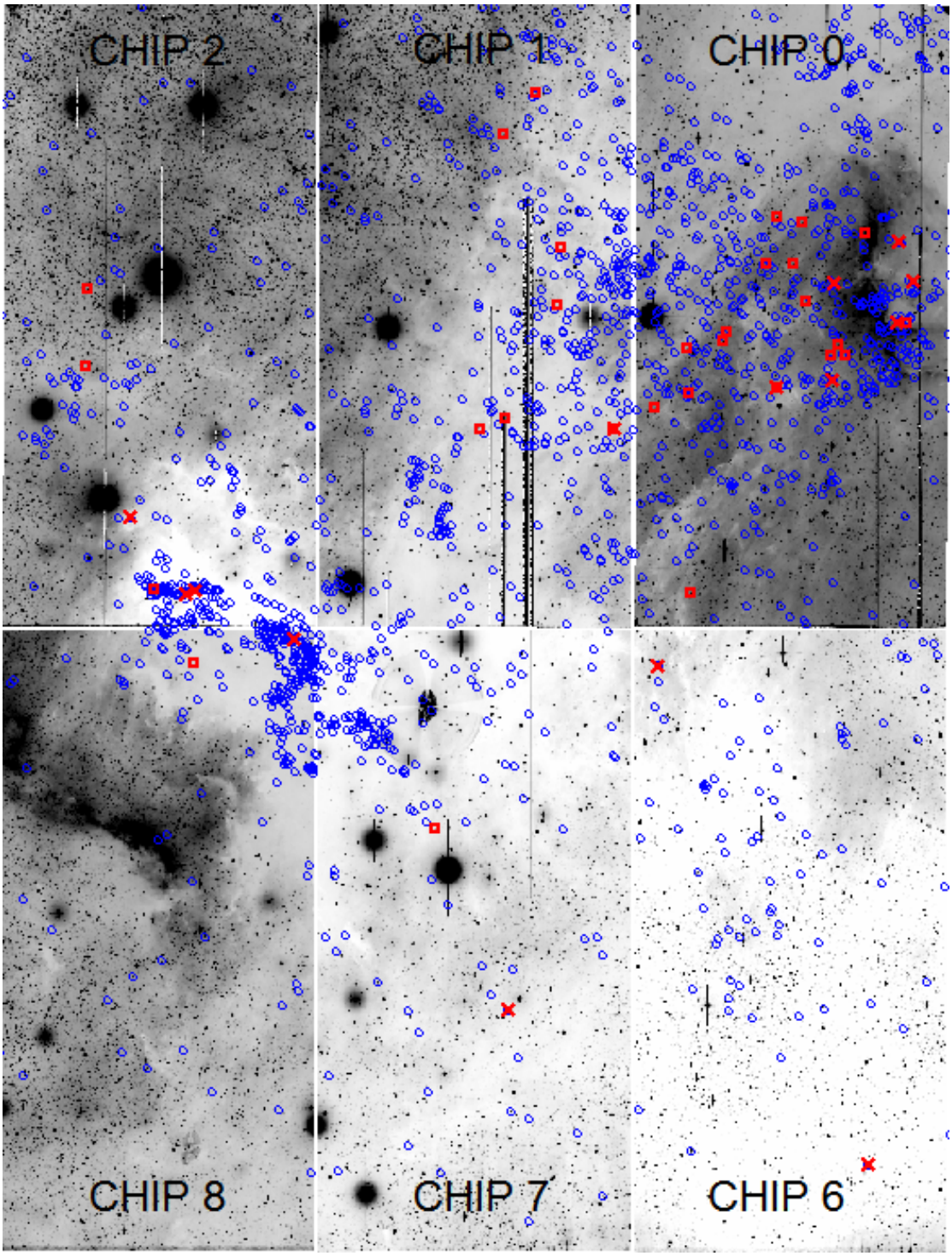


**Figure 3.4:** The North America Nebula complex, as observed by PTF in a single epoch from 2009. The blue circles mark the positions of candidate members selected using infrared excess by Rebull et al. (2011). As in Figures 3.1 and 3.2, we highlight stars with apparent bursting activity with red X's, and stars with apparent fading activity with red squares.

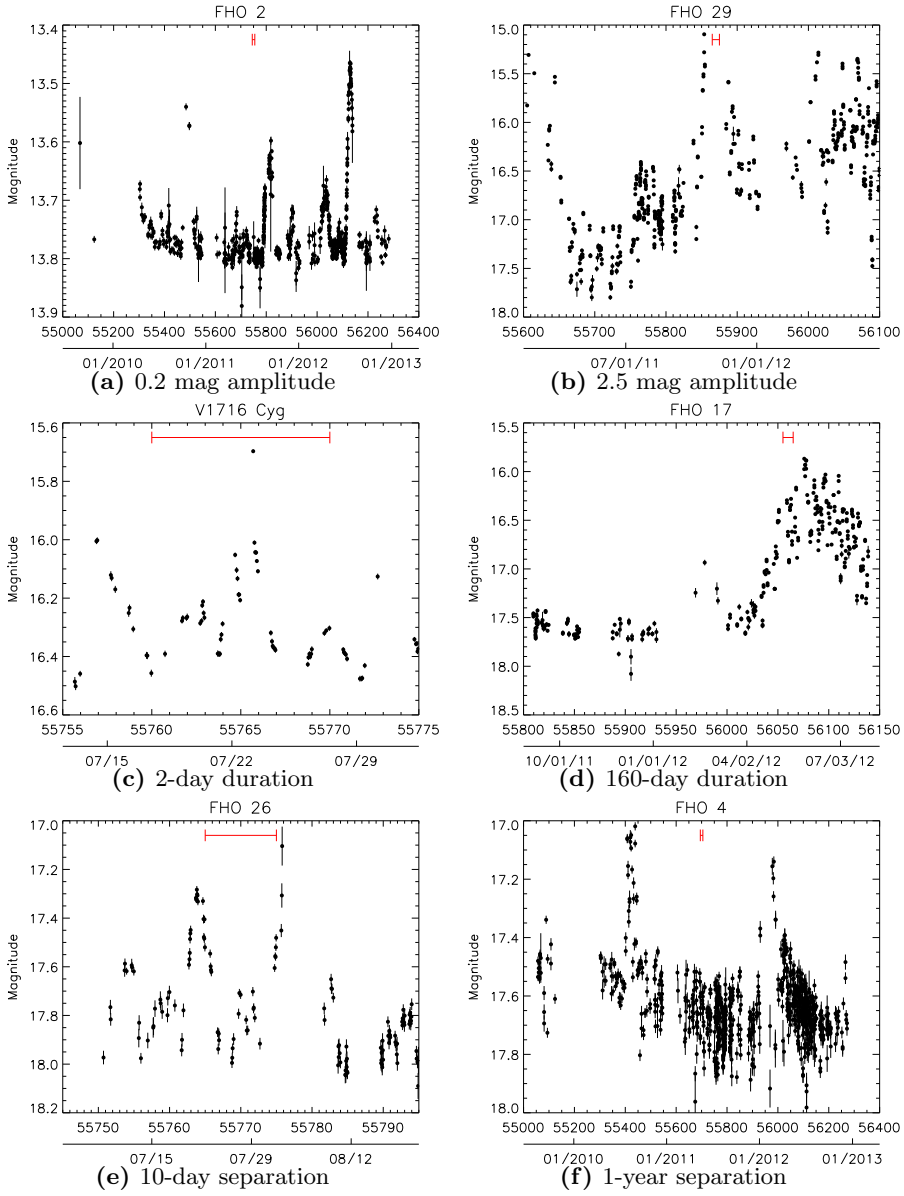


**(a)** 0.2 mag amplitude **(b)** 2.5 mag amplitude **(c)** 2-day duration **(d)** 160-day duration **(e)** 10-day separation **(f)** 1-year separation

**Figure 3.5:** Examples of the diverse behavior seen in our lightcurves for bursting stars. Variability amplitudes range from a few tenths of a magnitude to 2 magnitudes. Detected bursts can last from less than two days to over a hundred, and can be separated by anywhere from 10 days to a year. For scale, the horizontal bar near the top of each panel shows a 10 day interval. No points having any of the flags listed in subsection 2.2.2 are plotted.

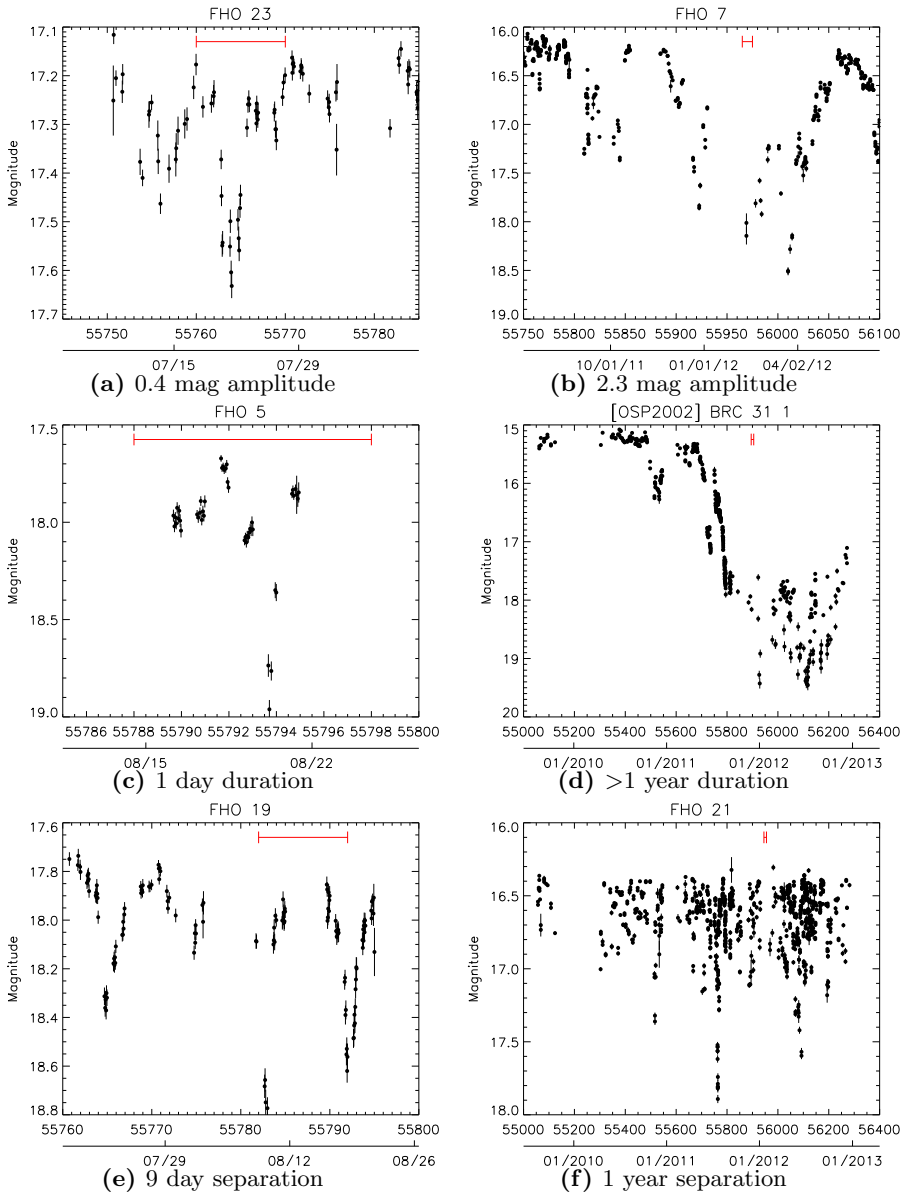


**(a)** 0.4 mag amplitude

**(b)** 2.3 mag amplitude

**(c)** 1 day duration

**(d)** >1 year duration

**(e)** 9 day separation

**(f)** 1 year separation

**Figure 3.6:** Examples of the diverse behavior seen in our lightcurves for faders. Variability amplitudes range from a few tenths of a magnitude to nearly 2 magnitudes. Fades can last anywhere from one day to over a year, and can be separated by anywhere from 9 days to over a year. For scale, the horizontal bar near the top of each panel shows a 10 day interval. No points having any of the flags listed in subsection 2.2.2 are plotted.

## 3.4 The Burster Phenomenon

### 3.4.1 Population Properties

Upward excursions in young star lightcurves traditionally have been assumed to come from one of two mechanisms. Long-lasting, several-magnitude events in young stars with circumstellar accretion disks (e.g., EX Lup, FU Ori) are interpreted as dramatic increases in the accretion rate from the disk to the star. Events lasting a few hours or less and rising by at most a few tenths of a magnitude, particularly in disk-free stars, have been assumed to be associated with magnetic flares like those seen on the young field star UV Cet or on the Sun. White light flares on the Sun last tens of minutes, while those on M dwarfs last up to several hours (e.g., Kowalski et al., 2010; Kretzschmar, 2011). As these timescales are set by the cooling times of dense chromospheric material at the base of the coronal loop, it is unlikely that magnetic flares can produce optical emission with much longer durations than observed.

Of the 14 stars that show bursting behavior, only two, [OSP2002] BRC 31 8 and FHO 1, have bursts lasting 1-2 hours, short enough to be plausible flares. The remainder must be driven by temporary increases in accretion, drops in extinction, or some other phenomenon. The bursters show a wide variety of behaviors. None are strictly periodic, although [OSP2002] BRC 31 8 and FHO 29 do show enhanced photometric activity at roughly 300-day intervals. Some bursters, like FHO 26, repeat every few weeks. Others, like LkH$\alpha$ 185 or FHO 4, show bursts only once a year or even more rarely. While [OSP2002] BRC 31 8 and FHO 1 have very short bursts, too brief to resolve outside our highest-cadence monitoring in mid-2011, FHO 17 featured a burst lasting over 100 days, and FHO 18 showed bursts with a range of lengths from a few days to two weeks.

Despite their variety, the bursters do not fall naturally into distinct subclasses, forming instead a continuum of behaviors. We show in Figure 3.7 the joint distributions of burst amplitudes, burst widths, and burst separations for all 14 bursters. To avoid systematics associated with separating a burst or fade from the surrounding, sometimes complex, variability, and to avoid complications from varying sampling from event to event, the timescales and amplitudes in Figure 3.7 were estimated by eye and should be taken as illustrative values only. There is no pattern visible in the plot aside from a rough trend where longer bursts tend to be separated by longer intervals. The absence of distinct groups of bursters suggests that the diversity of sources can be explained by continuously varying the parameters of a single common scenario, rather than by invoking different mechanisms or different configurations for short- and long-timescale bursters.

If either enhanced accretion or reduced extinction are responsible for bursting events, then stars with large infrared excess, and therefore more circumstellar material, may be more likely to show bursting behavior than stars with small infrared excess. Using the Kendall's $\tau$ statistic (Kendall, 1938), we found no evidence for a correlation between the Spitzer IRAC/MIPS [3.6] − [24] color

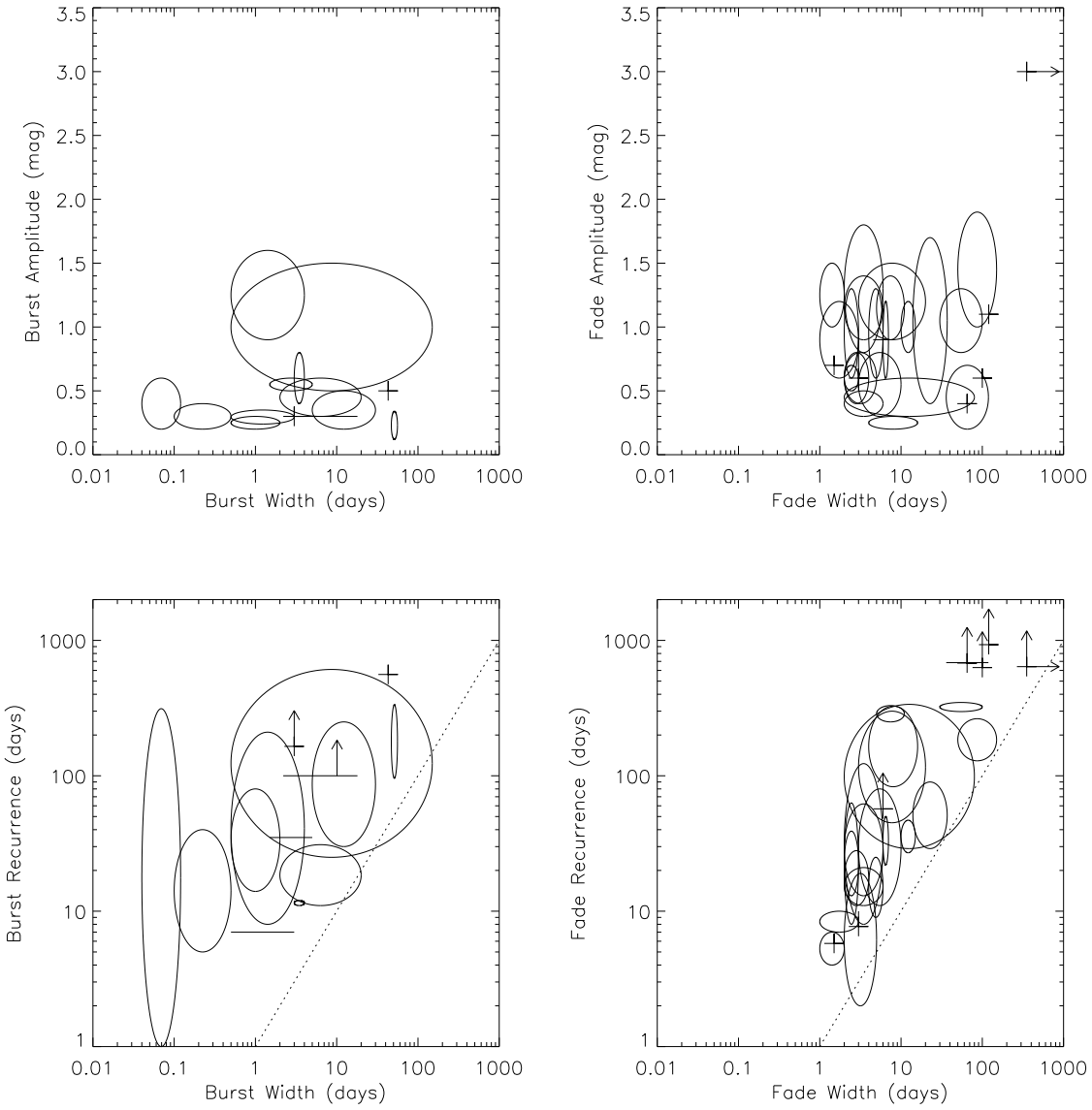


**Figure 3.7:** Plots of the characteristic amplitudes and timescales for bursters (left) and faders (right), illustrating the wide variety of observed events. The plus signs indicate sources that have either well-defined fixed values for their amplitudes and timescales (such as the two periodic AA Tau analogs in the lower left corner of the fader panels), or that have only a single measurement (such as the single-event sources in the upper right of any panel). The ellipses represent sources that have bursts or fades of varying amplitudes, varying widths, or varying separations within a single lightcurve. The area below the dotted line on the lower two figures, where events would need to overlap each other, is not allowed, though some ellipses appear there because this analysis does not consider correlations between width and separation.

(56% confidence) and the presence of bursting among our sample of 117 IR-excess sources, but we did find a marginally significant correlation (2.4% confidence) with Spitzer IRAC [3.6] − [8.0] color, in the sense that redder sources are more likely to show bursting behavior. We note that of the 14 bursters, only two, FHO 2 and FHO 24, are Class III sources. The rest have $K - [8] > 1.8$ and $K - [24] > 5$ (see Figure 3.2 for comparison to the rest of the sample). We note that since the K-band and Spitzer data are not coeval, the reported colors may be distorted by variability between the epochs of observation. However, mid-infrared variability is typically a few tenths of a magnitude or less (Espaillat et al., 2011; Morales-Calderón et al., 2011; Flaherty et al., 2012), and so should not dramatically affect a star's position in diagrams such as Figure 3.2.

While the weak correlation with [3.6] − [8.0] color suggests that bursters are associated with stronger circumstellar disks, and therefore with the possibility of enhanced accretion or reduced circumstellar extinction, the absence of a similar correlation with [3.6] − [24] color weakens this result. As noted in Table 3.3.1, however, only a limited range of infrared color is well-represented in this sample. It is also possible that any correlation is being diluted by radiative transfer effects, geometry, or other factors that determine whether any particular star shows bursting behavior. We discuss how additional data could allow more conclusive tests in subsection 3.7.3.

### 3.4.2 Constraints on Short-Term Accretion Outbursts

Magnetic or viscous instabilities acting at the boundary between the stellar magnetosphere and the circumstellar disk are expected to produce short bursts of accretion on timescales of weeks to months for certain regimes of disk properties (e.g., Aly & Kuijpers, 1990; Goodson & Winglee, 1999; Romanova et al., 2004, 2005). However, variability from such outbursts has never been observed (Bouvier et al., 2007). The consistent cadence and long time coverage of our PTF survey have allowed the most sensitive search to date for such accretion events.

Of the bursting sources in Table 3.4, FHO 2, FHO 4, and FHO 24 show multiple bursts lasting tens of days each. The separations between bursts vary: tens of days in the case of FHO 24, 100-300 days in the case of FHO 2, and $\sim 500$ days for FHO 4. We show all three sources in Figure 3.8. The timescales and shapes of these events, particularly FHO 2 and FHO 4, resemble the simulated variations in $\dot{M}$ shown in Figure 4 of Romanova et al. (2004). Although they do not stand out in the context of our sample, where burst durations vary continuously from $<$ 1-150 days, FHO 2, FHO 4, and FHO 24 are noteworthy as the first bursts reported in young stars having timescales of tens of days. To our knowledge, these lightcurves represent the first observations consistent with the predicted inner-disk instabilities.

Models predict that short-term accretion outbursts should have amplitudes of a few tenths of a magnitude. For example, scaling to a fiducial star with 0.8 $M_{\odot}$ and 2 $R_{\odot}$, the simulations of Romanova et al. (2004) predict an accretion rate of $2 \times 10^{-8}$ $M_{\odot}\mathrm{yr}^{-1}$ in quiescence and 6-

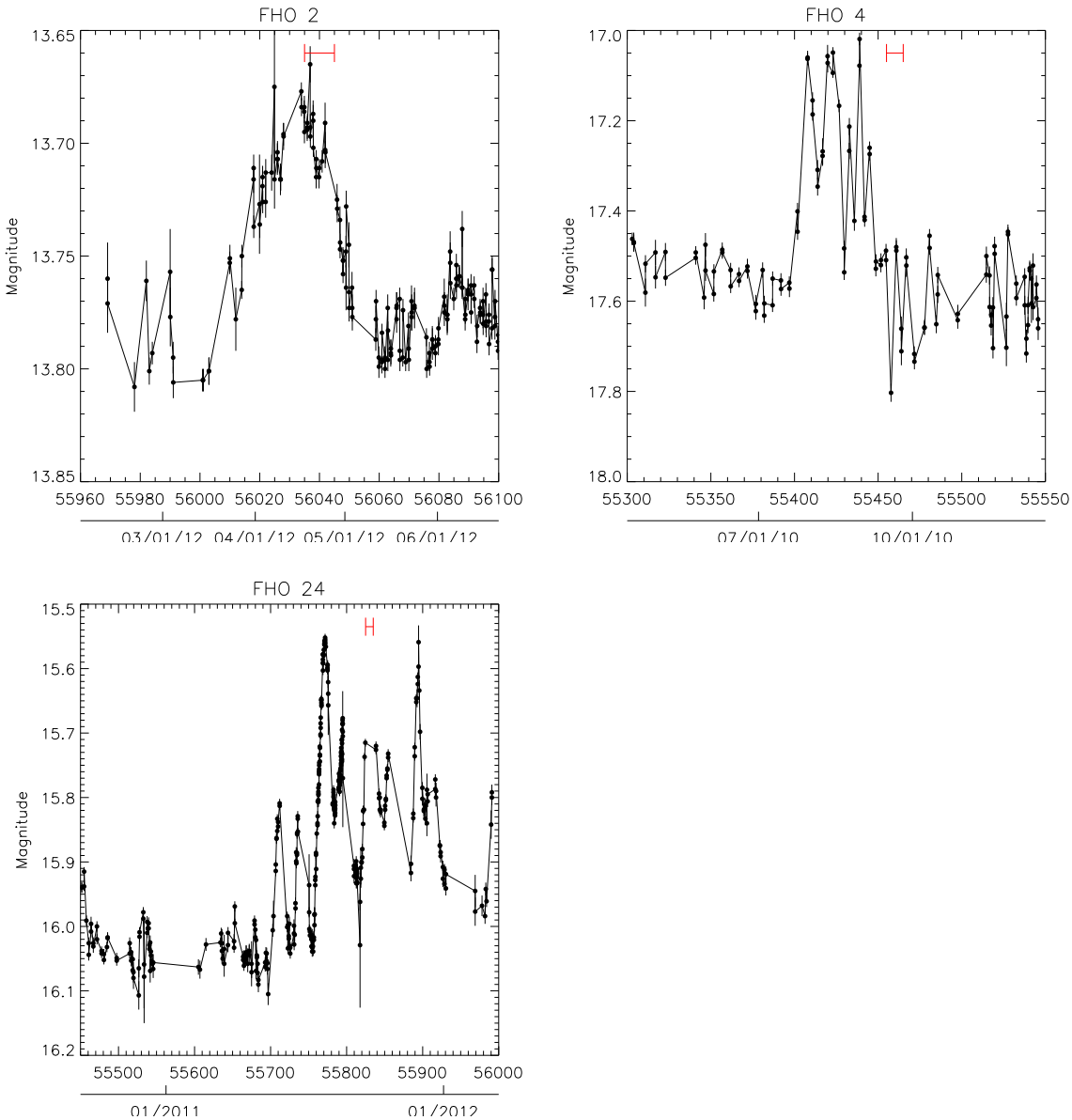


**Figure 3.8:** Burst profiles for three bursters with durations of tens of days. No points having any of the flags listed in subsection 2.2.2 are plotted. In this and subsequent plots, the points are connected by line segments to clarify the order of closely spaced observations. FHO 2 has the simplest event profile, showing a smooth rise and fall over a 20-30 day interval. The bursts of FHO 4 are longer and show a more complex profile. The lightcurve for FHO 24 shows a large number of contiguous bursts rather than a few isolated events like the other two.

$8 \times 10^{-8}$ $M_{\odot}\mathrm{yr}^{-1}$ in outburst. The fiducial star would have a luminosity of 1.14 $L_{\odot}$ (Siess et al., 2000), with quiescent and outburst accretion luminosities of 0.25 $L_{\odot}$ and 0.88 $L_{\odot}$, respectively, implying a brightening of $\sim 0.4$ magnitudes between quiescence and outburst. The three candidate stars have amplitudes between 0.2 and 0.5 mag, consistent values given star-to-star variations in star and disk parameters.

The behavior of the lightcurves is inconsistent with white-light flares analogous to those seen on the Sun. White-light flares tend to have a steep rise followed by an exponential decay. None of the three bursts show an exponential profile, and the timescales of tens of days are much longer than the minutes to hours durations observed in the Sun or in low-mass stars. A superposition of many short flares is also unlikely: FHO 2 and FHO 24 show little variability on timescales of a single day, as might be expected from a stochastic sum of shorter events. In addition, a 0.4 mag burst lasting 30 days corresponds to an energy release, depending on the (unknown) spectrum of the transient emission, of $\sim 6 \times 10^{39}$ erg for a 1.4 $L_{\odot}$ star. The entire stellar magnetic field, integrating a dipole field from an assumed $R_{\star} \sim 2$ $R_{\odot}$ to infinite radius, contains only $\sim 5 \times 10^{38}\,(B_{\mathrm{surf}}/1\ \mathrm{kG})^2$ erg. Even a 3 kG field, near the largest values observed in T Tauri stars (Bouvier et al., 2007), cannot provide enough energy to power the bursts.

The brightness enhancements for these three objects are also unlikely to be dust-clearing episodes. Only FHO 4 is a Class II source, while FHO 2 and FHO 24 are both Class III sources with excess only in the MIPS 24 $\mu$m band. It is doubtful that these two stars have enough circumstellar dust in the inner disk to allow significant extinction-driven variability. We note that stars with infrared excess only in the MIPS bands can still show ongoing accretion on the order of 0.1-0.5 $\times 10^{-8}$ $M_{\odot}$ $\mathrm{yr}^{-1}$ (Muzerolle et al., 2009; Espaillat et al., 2012), so the absence of an IRAC excess does not rule out either low-level accretion or, plausibly, brief periods of accretion at a higher rate. Extinction is a possible origin for the variability of FHO 4; color data taken over the course of one of its bursts could test this hypothesis.

## 3.5 The Fader Phenomenon

The two prototypical faders are AA Tau, which fades repeatedly by 1.4 mag over 30% of an 8.2-day cycle (Bouvier et al., 1999, 2003), and UX Ori, which fades by 3 mag for tens of days at irregular intervals (Waters & Waelkens, 1998). Both AA Tau and UX Ori are well understood as the result of recurring extinction by circumstellar material, from a warped inner disk edge in the case of AA Tau or from more irregular structures in the case of UX Ori.

Of the 29 sources that show some kind of fading behavior, only two, LkH$\alpha$ 174 and FHO 12, show the periodic modulation characteristic of AA Tau. Four more sources, LkH$\alpha$ 150, FHO 7, FHO 15, and FHO 27, show multiple fading events with durations of tens of days, as seen for

UX Ori stars. However, their typical amplitudes of 1 mag or less are much smaller than the 3-4 mag fades associated with UX Ori stars.

The remaining 23 faders do not resemble either of the previously established categories. The natural assumption is that these sources also have their variability dominated by circumstellar extinction, with different spatial scales or different geometries causing the lightcurves to behave differently.

All the sources except for the two AA Tau analogs are aperiodic, and, as illustrated in Figure 3.6, they often bear little resemblance to each other. For example, FHO 19 has narrow fades repeating every 8-10 days, but without enough coherence to be periodic. In contrast, NSV 25414 and FHO 3 both have frequent but irregular events, with the interval between adjacent fades varying by more than a factor of two. At the other extreme, FHO 21 and FHO 22 each show only one fading event per year, while LkH$\alpha$ 150 and FHO 25 fade only once in the entire survey period. Most fading events are short, but those of LkH$\alpha$ 150 and [OSP2002] BRC 31 1 last for hundreds of days. Most stars have fading events of roughly constant depth, but FHO 15 and FHO 20 have significant amplitude variability. Most fading events are symmetric, but FHO 11 and FHO 27 show strongly lopsided events.

Like the bursters, the faders do not separate naturally into sources with distinct timescales. We show in Figure 3.7 the joint distributions of fade amplitudes, fade widths, and fade separations for all 29 faders. The absence of gaps in the plot suggests that, as with the bursters, short- and long-timescale faders have a common origin.

As with the bursters, we tested for a correlation with the presence of circumstellar material. Using the Kendall's $\tau$ statistic, we found no evidence for a correlation between the Spitzer IRAC $[3.6]-[8.0]$ or IRAC/MIPS $[3.6]-[24]$ colors and the presence of fading among our sample of 117 IR-excess variables at 20% and 18% confidence, respectively. However, we did not find a single example of a fader among Class III sources (i.e., significant excess only at 24 $\mu$m), as would be expected if circumstellar material near the star is needed for fading events to occur.

To test whether the fading events could instead be the result of variable foreground extinction, we searched for a correlation between stars' near-infrared color, where we can avoid variability-induced systematic errors through the use of coeval 2MASS photometry, and the presence or absence of fading behavior. Since unreddened M dwarfs have $J-K \lesssim 1$, stars with $1 \lesssim J-K \lesssim 3$ must have significant extinction, while stars with $J-K < 1$ may have only moderate extinction. If fading events are caused by foreground dust, we might expect fading to be more prevalent among the reddest stars. Using the Kendall's $\tau$ statistic, we found no evidence for a correlation between the $J-K$ color and the presence of fading among our sample of 117 IR-excess variables at 26% confidence.

While we find that neither the degree of infrared excess nor proxies for near-infrared reddening

are good predictors for the presence of fading behavior, the absence of faders among the Class III sources is consistent with fading events requiring the presence of inner disk dust and therefore the possibility of occasionally enhanced extinction along the line of sight. We discuss how additional data could allow more conclusive tests in subsection 3.7.3.

## 3.6 Individual Sources of Interest

In section 3.4 and section 3.5 we examined the 41 burster or fader candidates as an ensemble. However, many of the sources have a character of their own. While we present brief descriptions of all the sources in Table 3.4, in this section we focus on a small number of stars whose behavior seems particularly difficult to explain. We present the available data on each and challenge interested readers to develop models for these sources.

### 3.6.1 FHO 26

FHO 26 showed several-day-long, $\sim$ 0.7 mag bursts in 2010 and 2011 (see upper right panel of Figure 3.9) but became quiescent in late 2011. In 2012, except for two brief bursts, it has shown only a 0.2 mag, 5.6-day periodic modulation. The 2010-2011 bursts do not phase up under the 2012 period. FHO 26 has a modest infrared excess, as shown in the lower left panel of Figure 3.9.

We show in the lower right panel a spectrum of the source taken in 2012 July, well into the quiescent phase and near the peak of the periodic variability. The spectrum shows an M4.5 photosphere with emission from H$\alpha$ (-13 Å equivalent width).

### 3.6.2 [OSP2002] BRC 31 1

[OSP2002] BRC 31 1 grew fainter by nearly three magnitudes between 2011 April and August but showed relatively little variability before the fade, as shown in the upper left panel of Figure 3.10. Our spectrum, taken during the star's faint state, shows a forest of emission lines including H$\alpha$, Ca II, [O I], [Fe II], [S II], [Ni II], Fe II, and many others. A spectrum of [OSP2002] BRC 31 1 from 1998 shows only H$\alpha$, Ca II, and Fe II at the same strength as in 2012, plus much weaker [O I] and [Fe II] lines. We see few absorption lines in the spectrum in either epoch.

The 1998 and 2012 spectra are similar to high- and low-state spectra, respectively, of the long-term variable PTF10nvg (Hillenbrand et al., 2013). Since BRC 31 1, like PTF10nvg, is a Class I infrared excess source, it is possible that BRC 31 1 is a similar system: a high-inclination source with circumstellar material obscuring the inner disk, stellar photosphere, and accretion zone, but not obscuring a spatially extended jet. We note the lightcurve resembles that of V1184 Tau presented by Grinin et al. (2008).

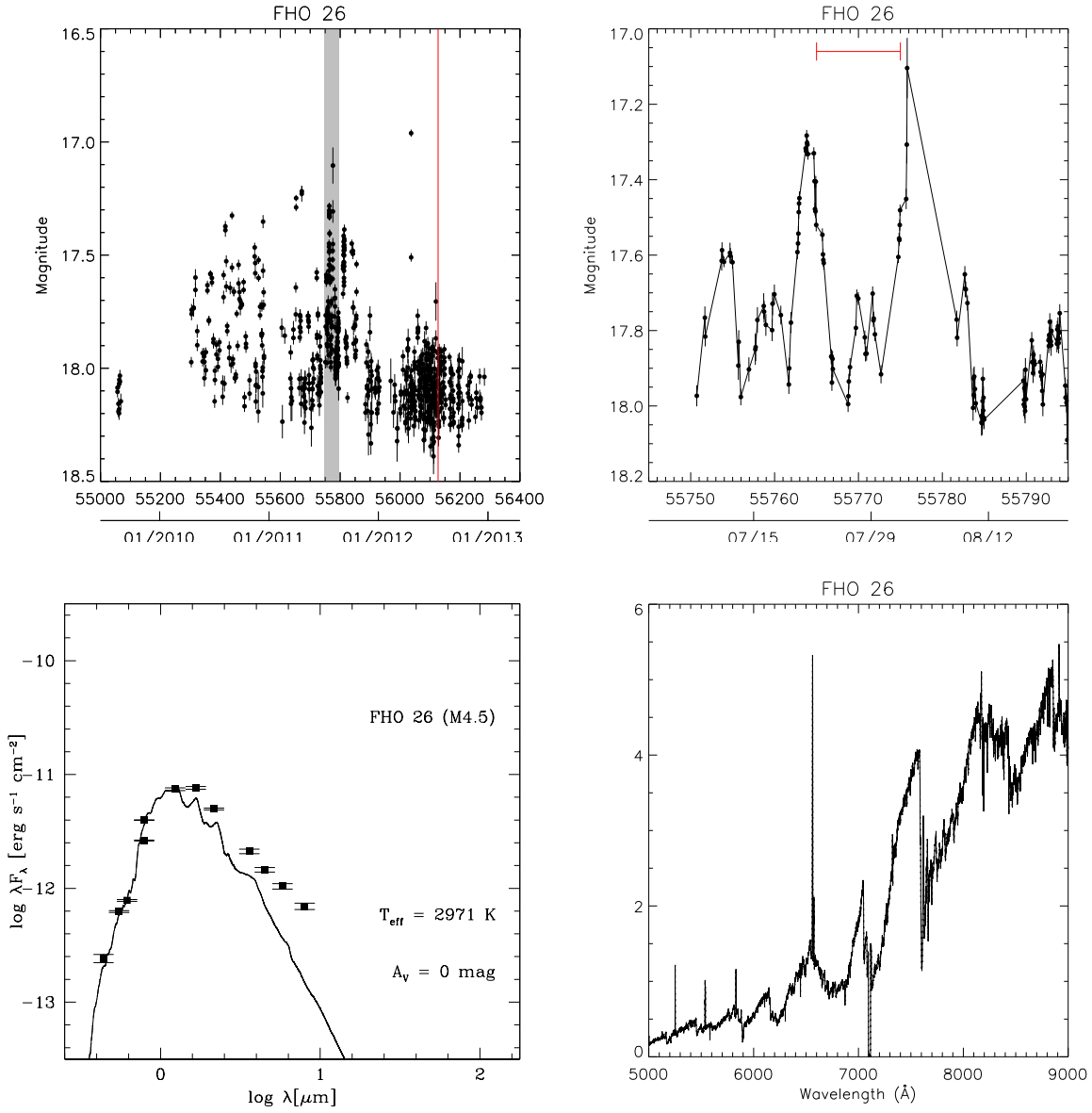


**Figure 3.9:** A star whose regular bursting activity stopped at the end of 2011. The upper left panel shows the full 3-year lightcurve, with the shaded period expanded in the upper right panel to illustrate typical bursts for this source and the vertical red line marking the time at which the 2012 July spectrum in the lower right panel was taken. The red scale bar represents a 10-day interval. No points having any of the flags listed in subsection 2.2.2 are plotted. The lower left panel shows the spectral energy distribution for this source. The points are taken from non-simultaneous optical, near-infrared, and Spitzer photometry. The solid curve is a reddened NextGen model atmosphere (Hauschildt et al., 1999) with temperature corresponding to the star's spectral type, matched to the optical through $J$-band fluxes.

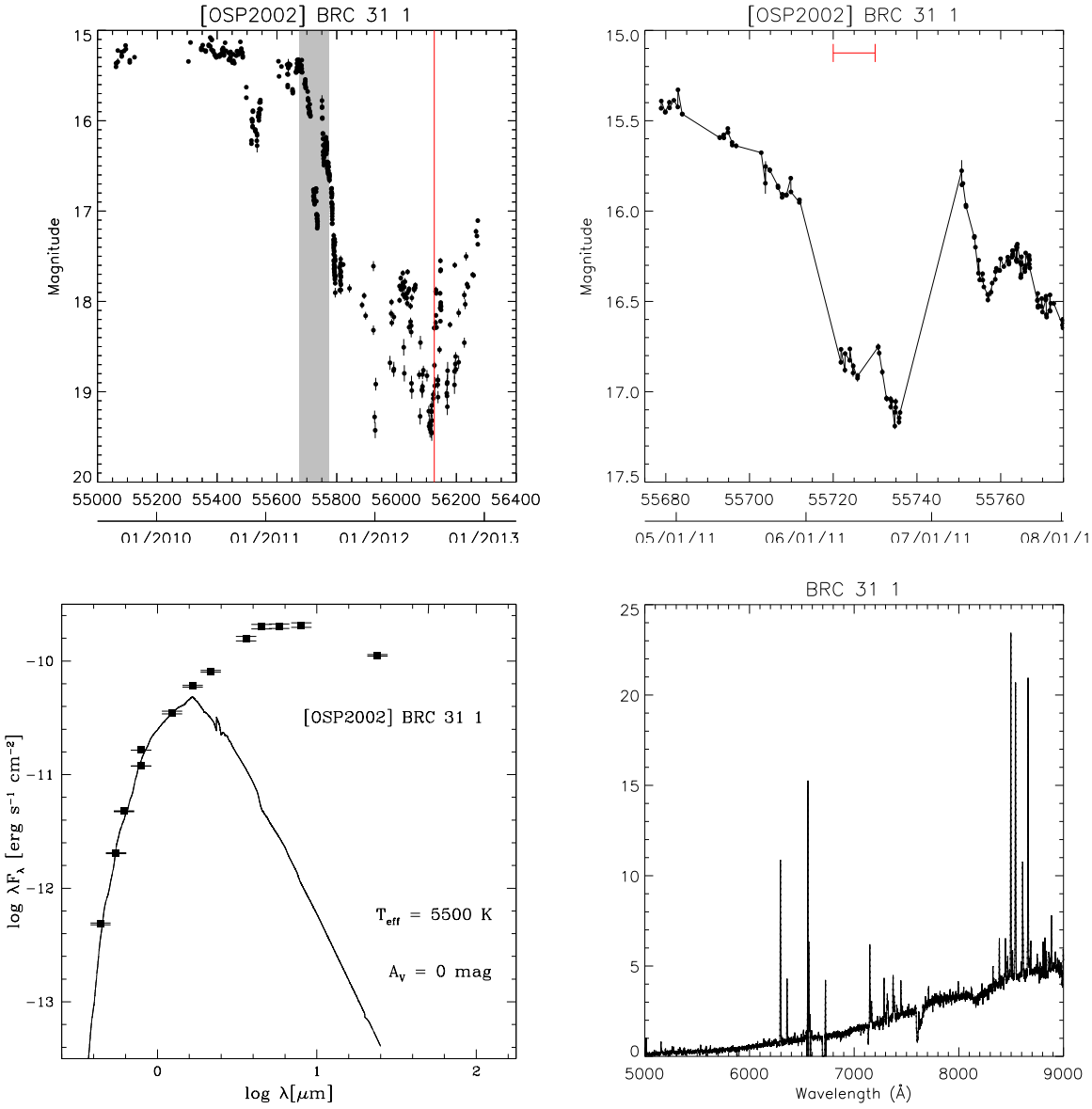


**Figure 3.10:** Same as Figure 3.9, but for a star showing a sudden decline in 2011. The star was not detected in roughly half the epochs in 2012; the non-detections are not shown. The upper right panel highlights the decline, including a temporary dip that interrupted it. Since we could not determine a spectral type for this source, the photosphere shown in the lower left panel is for an assumed effective temperature.

### 3.6.3 FHO 18

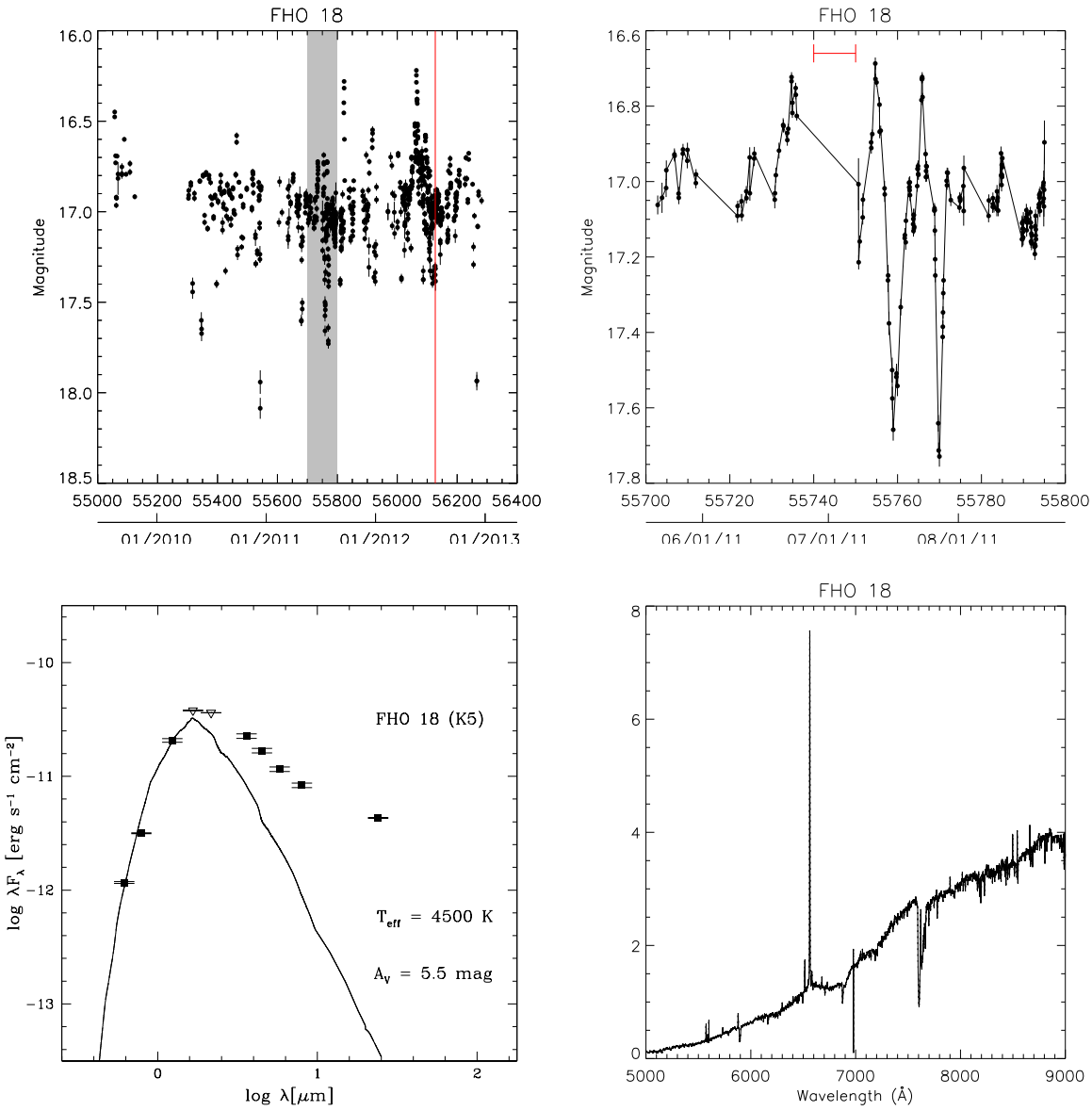


**Figure 3.11:** Same as Figure 3.9, but for a star showing an odd combination of bursting and fading. The upper right panel shows the fades and their precursor bursts.

FHO 18, shown in the upper panels of Figure 3.11, faded twice by 0.6 mag in quick succession in 2011. Immediately before each fading event, it brightened by 0.3 mag (upper right panel). This behavior was not repeated for other fading events during our monitoring period. Aside from these two fades and their precursor bursts, FHO 18 appears to be a typical Class II young star.

Our DEIMOS spectrum of FHO 18 was taken during a 0.4 mag fade. The spectrum shows a K5 star with H$\alpha$ emission (-23 Å equivalent width) as well as weaker Ca II and He I emission. However,

as this fade was *not* preceded by a burst the spectrum does not directly constrain the star's unusual behavior in mid-2011.

### 3.6.4 FHO 27

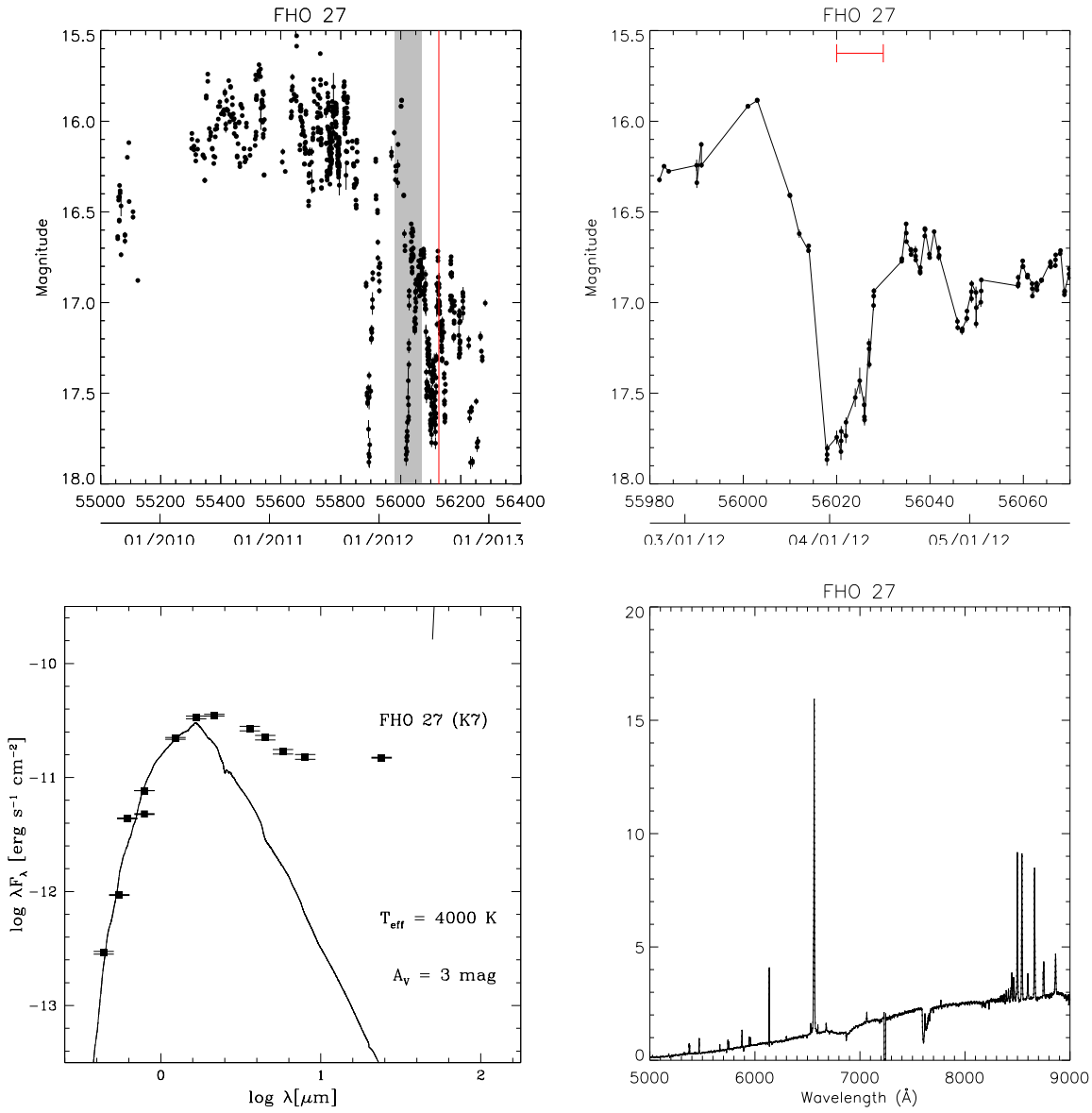


**Figure 3.12:** Same as Figure 3.9, but for a star showing a series of fades superimposed on a year-long decay. The upper right panel highlights the asymmetric profile of one of the fades.

FHO 27 had only 0.5-0.6 mag variability with a roughly constant or slightly rising mean magnitude throughout 2009-2010, but then began to show deep (up to 2 mag) fading events from late 2011 onward. At the same time, the upper envelope of the lightcurve began to gradually dim, leveling off

in mid-2012 after a total decrease of roughly 0.8-0.9 mag. The minimum magnitude reached during each fading event rose from 17.9 in the first fade to 17.3 in late 2012, so that the most recent fades have only a few tenths of a magnitude depth.

While the fading events repeat every 30-90 days, they are not periodic. In addition, each fade has a dramatically different profile from those before and after, with many of the profiles showing strong asymmetries (Figure 3.12, upper right panel), and some fades being much shallower than the rest (e.g., a 0.3 mag fade in late 2012 April was sandwiched between a 1.1 mag and a 0.6 mag fade).

The spectral energy distribution of the source, shown in the lower left panel of Figure 3.12, has a strong infrared excess; Rebull et al. (2011) classify FHO 27 as a flat-spectrum source.

We acquired one spectrum of FHO 27 in 2012 July, during the star's long-term low state but between the deeper fading events. The K7 spectrum in the lower right panel of Figure 3.12 shows strong H$\alpha$ (-80 Å equivalent width), Paschen series, and Ca II emission. Weaker lines in the spectrum include He I, [O I], and O I.

### 3.6.5 FHO 28

Like FHO 27, FHO 28 was dominated by 0.6 mag irregular variability in the first few years of our survey, interrupted by occasional 1 mag fades. Then, in early 2012, it began showing rapid variability with the same maximum brightness, but with a much higher amplitude of 2 mag. The high-amplitude variability lasted 130 days before the star returned to its earlier behavior. Since the source was not strictly periodic during its high-amplitude phase, it is not clear whether the variability has been fully resolved at our daily cadence, in which case the fades are roughly 9 days apart, or whether we are seeing a strobing effect of a more rapid 23-hour variation. The lightcurve is shown on the top two panels of Figure 3.13.

The spectral energy distribution, shown in the lower left panel of Figure 3.13, shows a Class II infrared excess. A spectrum of FHO 28 (Figure 3.13, lower right panel), taken during its strongly varying phase, shows an M3 star with strong H$\alpha$ emission (-60 Å equivalent width) and weak Ca II lines. An older spectrum shows that H$\alpha$ was much weaker (-20 Å) in 1998, although since we don't know the photometric state of FHO 28 at the time, it is not clear whether the difference between the two spectra is related to the star's increased activity in 2012.

FHO 28 is yet another example of how the photometric behavior of young stars can change abruptly from one year to the next. This source would *not* be classified as a fader if we had only data from its active phase, as the photometry shows no preference between high and low magnitudes (Figure 3.13, upper right panel). It is the comparison to previous years that allows us to establish that the brighter magnitudes represent the unperturbed state of the star.

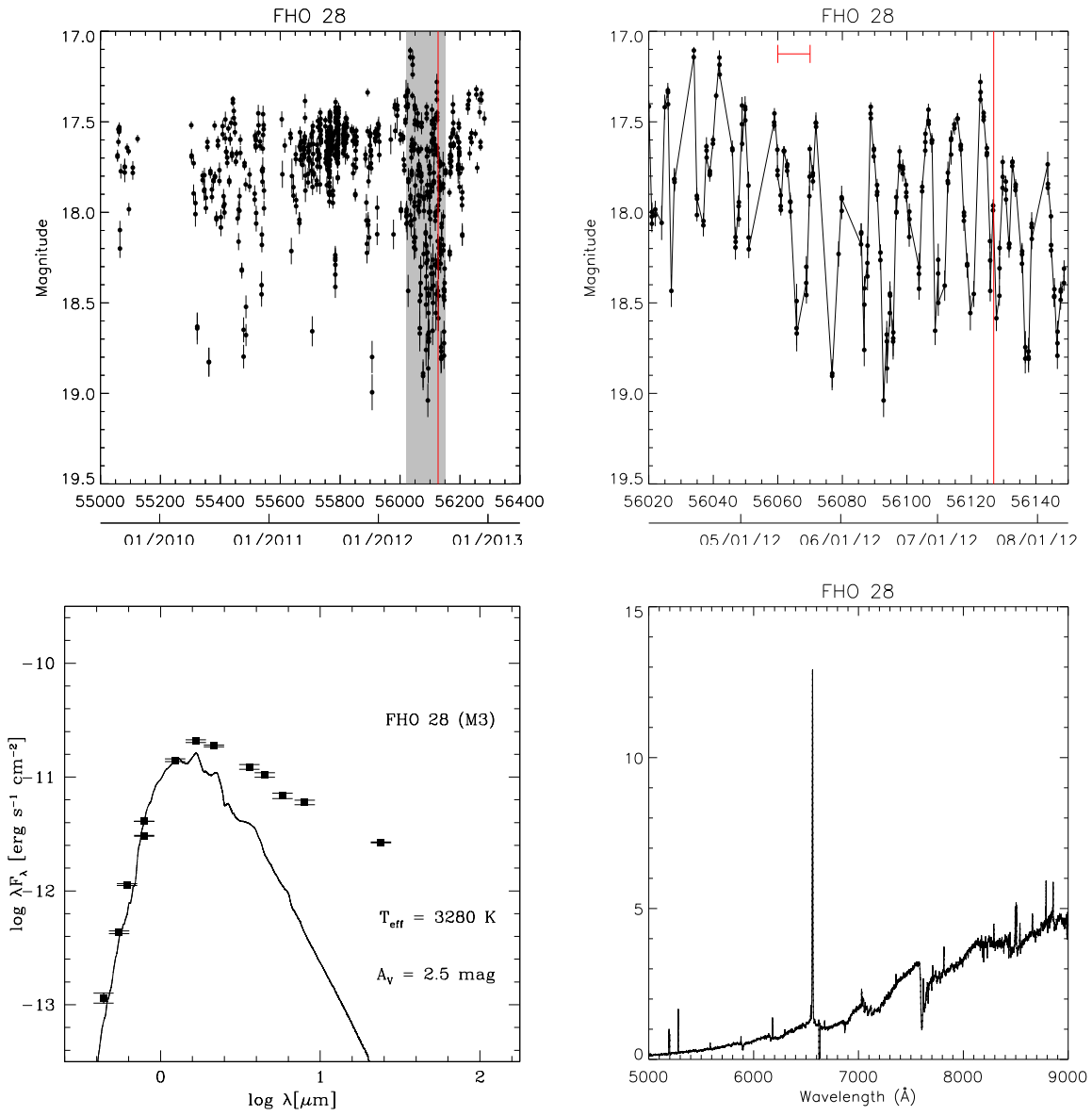


**Figure 3.13:** Same as Figure 3.9, but for a star showing an increased frequency of fades in 2012. The upper right panel illustrates that the fades in the more active phase were nearly superimposed.

## 3.7 Summary and Discussion

### 3.7.1 Key Results

We have presented first results from a new variability survey of young stars that probes a large dynamic range of timescales, from roughly a day to roughly a year. We have used this new data set to uniformly identify stars with episodic variability, regardless of whether the episodes had day-scale, month-scale, or year-scale durations and regardless of whether the episodes were periodic. From a sample of 186 candidate members of the North America Nebula complex, we have identified 14 that showed episodes of brightening ("bursters") and 29 that showed episodes of dimming ("faders"), sometimes mixed with more erratic variability. Two stars showed both bursting and fading at separate epochs. We have presented basic photometric and spectroscopic properties of both bursters and faders.

We have found that:

1. Most high-amplitude variables have a strong infrared excess, while low-amplitude variables may or may not have a strong excess. While similar correlations have been noted before, i.e., that classical T Tauri stars tend to have higher amplitudes than weak-lined T Tauri stars, we show here that a correlation between degree of infrared excess and variability amplitude also holds among stars with infrared excess.

2. Even within the individual burster and fader classes, we see a wide variety of timescales, amplitudes, and burst or fade profiles. This includes events that occur only once or twice in our three-year monitoring period, and would be missed in a shorter survey. It is not clear whether these varied behaviors imply varied underlying mechanisms. We find no gap separating groups of bursters or faders with different amplitudes or timescales (Figure 3.7), suggesting that they are all members of a single population, but in-depth study of representative objects will be needed to settle the issue.

3. We identify three bursters whose photometric and spectroscopic characteristics are consistent with published models of accretion driven by instabilities at the boundary between the stellar magnetosphere and the circumstellar disk. To our knowledge, this is the first time candidate objects corresponding to these models have been identified.

4. A substantial number of sources show variability over long timescales. Among other examples, FHO 14 and FHO 28 showed enhanced fading activity in an interval 100-200 days long. [OSP2002] BRC 31 1 changed from a 15th magnitude star in 2010 to a 18-19th magnitude star in 2012. [OSP2002] BRC 31 8 and FHO 29 both showed bursting modulated by a timescale of roughly 300 days. Except for the sudden decay of [OSP2002] BRC 31 1, these are behaviors

that have not been associated with bursting or fading activity before, for lack of sufficient sampling.

### 3.7.2 Comparison to Previous Work

While much previous time domain work on young stars has focused on finding and characterizing periodic variables, there have been some studies of more general variability. Here we discuss whether our population statistics are consistent with the existing literature.

We see bursting behavior in 14 sources, or $12 \pm 3\%$ of the $R < 18$ mag variables with an infrared excess. To the best of our knowledge, no one has reported a short-term optical burst fraction for pre-main-sequence stars, so we have no published results to which to compare this figure.

We see fading behavior in 29 sources, or $25 \pm 4\%$ of the variables with an infrared excess and $16 \pm 3\%$ of all sources with a good PTF lightcurve and an infrared excess. For comparison, Alencar et al. (2010) found that 28% of stars selected from X-ray or H$\alpha$ emission, all variables, showed periodic fading behavior in unfiltered optical light. Morales-Calderón et al. (2011) found fades (periodic or not) in the mid-infrared in 5% of variables and 3% of their total sample, selected by proper motion, X-ray or H$\alpha$ emission, or infrared excess. Finally, Cody & Hillenbrand (2010) found I-band fading behavior in 6% of their variables and 5% of their total sample, selected by kinematics, H$\alpha$ emission, forbidden line emission, lithium absorption, or infrared excess. Each of these surveys was a few weeks in duration, shorter than our survey, but had higher cadence by factors of 10-200.

To test whether our results are consistent with previous work after accounting for differences in our observing strategies, we clipped our lightcurves to a 30-day period of high-cadence observations, up to eight per night, between JD 2455765.5 and 2455795.5. This allowed us to compare our data to Morales-Calderón et al. (2011), who observed their field for a month at roughly a 2-hour cadence. We found that 12 of our faders (LkH$\alpha$ 174, V1701 Cyg, and FHO 3, 5, 14, 16, 18, 19, 20, 21, 22, and 28) were recognizable as such during the 30-day period, indicating that with only a month of high-cadence data we would have reported a $10 \pm 3\%$ fader fraction out of the variables in our sample or $6 \pm 2\%$ of the infrared-selected sample. This is slightly higher than, though consistent with, the Morales-Calderón et al. results. Since our ground-based survey had more data gaps than the Spitzer observations of Morales-Calderón et al., however, our fader rate had we observed with their exact cadence may have been higher. On the other hand, it is possible that we are overestimating our recovery rate, since we had already identified these stars as faders using the full data set and were aware of their nature while examining the clipped lightcurves, introducing hindsight bias.

### 3.7.3 Limitations of the Present Work

We were careful to identify bursting and fading events using only the lightcurves themselves, and not any ancillary data such as SEDs or spectra, to avoid psychological biases in interpreting ambiguous cases. However, we could not eliminate all ambiguity: the qualitative nature of event identification inevitably made some kinds of events easier to detect than others. The easiest events to identify were either those where the event lasted for several days, so that the lightcurve resolved the event profile, or those where the event repeated many times over our observing baseline, so that we could be confident that a high or low point represented real variability rather than a statistical fluke or an isolated error in the data reduction. We tried to confirm, using thumbnail images, whether isolated high or low points represented brief but real changes in the stellar flux, but image inspection allowed us to verify only high-amplitude events. We therefore may be incomplete to variability on timescales of a few hours.

We also had difficulty identifying bursts or fades lasting longer than several months, particularly if they were superimposed on other variability. Some stars in our sample showed erratic variability on timescales of months, and it is not always clear from only three years of data whether a star that spent several months in a high (or low) state had undergone an anomalous change in brightness, or whether we were merely seeing an extreme in a continuous series of brightness fluctuations. We chose to err on the side of caution, and only counted sources where the lightcurve apart from the candidate burst or fade had much lower-amplitude variability. However, this introduced a bias against mixed variability modes.

There are at least two sources in the North America Nebula complex that, while they meet our definition of bursters, are absent from our sample. PTF10qpf (Miller et al., 2011) was an $R = 16.5$ star at the beginning of the survey that brightened to $R \sim 12.5$ in mid-2010 and has remained there since. The source was disqualified from this paper's sample because it failed three criteria in the photometry produced by the PTF Photometric Pipeline: it was flagged as blended with nearby stars at nearly all epochs, it was flagged as saturated in nearly all epochs after the outburst, and its median magnitude of 12.9 was well above our flux limits. PTF10nvg (Covey et al., 2011) did not rise past PTF's saturation limits; however, as noted in Table 3.3.1, the PTF Photometric Pipeline had difficulty identifying sources around nebulosity. PTF10nvg is located just off a bright nebula filament, and neither it nor any other nearby sources were extracted. These two omissions illustrate key sources of incompleteness in this work: crowding, nebula contamination, and a limited magnitude range. Fortunately, these problems do not apply to the majority of sources in the Spitzer-selected sample, which are well-separated, in low-background regions, and of less than one magnitude amplitude.

This work is based primarily on a long-term, single-band photometric survey, which has allowed us to identify and characterize new types of bursters and faders. However, the data we have presented

here cannot identify without ambiguity the physics behind each kind of bursting or fading variability, or even whether all bursters or all faders represent different cases of a common variability mechanism. The following additional data would provide more insight into the nature of bursters or faders:

- Time series color information would help test whether all of the faders are caused by variable extinction along the line of sight to the star. Color data would also help us interpret bursters by providing color constraints to better estimate the energy released in the burst. We plan to present a color analysis of our bursters and faders in future work.

- Spectroscopic monitoring, especially at high dispersion, would allow us to compare accretion and wind indicators in a star's high and low states, allowing us to distinguish which events are accretion-powered, which represent partial or total obscuration of the photosphere, and which are driven by something else entirely.

- Polarimetry would help identify which bursts or fades are associated with changes in the obscuration of the star, as it probes what fraction of the measured flux comes from the photosphere and what fraction is scattered from the disk (e.g., Grinin, 1992; Bouvier et al., 1999). In particular, it could be used to directly test the hypothesis that all fades are obscuration events — if they are, then they should all show stronger polarization at minimum light.

We have shown, using the unprecedented PTF data set, that the class of faders is far broader than previously appreciated, and that bursters, while fewer in number, show a comparable diversity. We have identified new phenomenology within both classes. These objects can serve as prototypes for future study of particular forms of bursting or fading activity.

| [RGS2011] ID | Short Name | SED Class | $\bar{R}$ (mag) | $R_{med}$ (mag) | RMS (mag) | $\Delta R$ (mag) | Total Detections | Unflagged Detections |
|---|---|---|---|---|---|---|---|---|
| 205032.32+442617.4 | FHO 1 | II | 17.4 | 17.5 | 0.13 | 1.12 | 873 | 870 |
| 205036.93+442140.8 | [OSP2002] BRC 31 1 | I | 16.8 | 16.6 | 1.24 | 4.94 | 750 | 505 |
| 205040.29+443049.0 | LkH$\alpha$ 139 | II | 14.6 | 14.6 | 0.13 | 0.92 | 883 | 778 |
| 205042.78+442155.8 | [OSP2002] BRC 31 8 | | 16.9 | 16.9 | 0.18 | 1.97 | 877 | 872 |
| 205100.90+443149.8 | V1701 Cyg | II | 15.5 | 15.4 | 0.36 | 1.89 | 769 | 629 |
| 205114.80+424819.8 | FHO 2 | III | 13.8 | 13.8 | 0.075 | 0.91 | 857 | 750 |
| 205115.14+441817.4 | LkH$\alpha$ 150 | II | 16.4 | 16.3 | 0.29 | 2.22 | 879 | 833 |
| 205119.43+441930.5 | FHO 3 | II | 17.1 | 17.0 | 0.48 | 2.74 | 873 | 865 |
| 205120.99+442619.6 | LkH$\alpha$ 153 | II | 15.1 | 15.1 | 0.13 | 0.80 | 882 | 866 |
| 205123.59+441542.5 | FHO 4 | II | 17.6 | 17.6 | 0.13 | 1.13 | 875 | 875 |
| 205124.70+441818.5 | FHO 5 | II | 18.0 | 17.9 | 0.24 | 2.06 | 872 | 839 |
| 205139.26+442428.0 | FHO 6 | II | 14.8 | 14.7 | 0.26 | 1.49 | 884 | 872 |
| 205139.93+443314.1 | FHO 7 | II | 16.7 | 16.5 | 0.53 | 2.66 | 879 | 877 |
| 205145.99+442835.1 | FHO 8 | II | 17.8 | 17.7 | 0.27 | 2.71 | 874 | 870 |
| 205155.70+443352.6 | FHO 9 | II | 15.9 | 15.8 | 0.26 | 1.76 | 881 | 865 |
| 205158.63+441456.7 | FHO 10 | Flat | 16.7 | 16.7 | 0.12 | 0.90 | 879 | 825 |
| 205203.65+442838.1 | FHO 11 | II | 18.0 | 17.9 | 0.13 | 0.98 | 870 | 836 |
| 205228.33+442114.7 | FHO 12 | II | 16.5 | 16.4 | 0.26 | 1.71 | 878 | 863 |
| 205230.89+442011.3 | LkH$\alpha$ 174 | II | 16.7 | 16.7 | 0.28 | 1.51 | 878 | 878 |
| 205252.48+441424.9 | FHO 13 | II | 18.1 | 18.1[a] | 0.42 | 2.63 | 874 | 795 |
| 205253.43+441936.3 | FHO 14 | II | 18.0 | 17.9 | 0.14 | 1.11 | 873 | 853 |
| 205254.30+435216.3 | FHO 15 | II | 17.1 | 17.0 | 0.34 | 2.01 | 877 | 785 |
| 205314.00+441257.8 | FHO 16 | II | 17.1 | 17.0 | 0.18 | 1.21 | 877 | 877 |
| 205315.62+434422.8 | FHO 17 | II | 17.3 | 17.5 | 0.49 | 2.21 | 848 | 720 |
| 205340.13+441045.6 | FHO 18 | II | 17.0 | 17.0 | 0.21 | 1.87 | 875 | 875 |
| 205410.15+443103.0 | FHO 19 | | 18.0 | 17.9 | 0.24 | 1.88 | 869 | 867 |
| 205413.74+442432.4 | FHO 20 | II | 16.3 | 16.2 | 0.21 | 2.36 | 876 | 876 |
| 205424.41+444817.3 | FHO 21 | II | 16.7 | 16.6 | 0.24 | 1.59 | 876 | 876 |
| 205445.66+444341.8 | FHO 22 | | 17.4 | 17.3 | 0.31 | 2.99 | 874 | 872 |
| 205446.61+441205.7 | FHO 23 | II | 17.4 | 17.3 | 0.16 | 0.87 | 763 | 665 |
| 205451.27+430622.6 | FHO 24 | III | 15.9 | 15.8 | 0.13 | 0.70 | 860 | 860 |
| 205503.01+441051.9 | FHO 25 | Flat | 16.1 | 16.1 | 0.12 | 1.31 | 876 | 872 |
| 205534.30+432637.1 | [CP2005] 17 | II | 17.2 | 17.2 | 0.10 | 0.88 | 850 | 850 |
| 205659.32+434752.9 | FHO 26 | | 18.0 | 18.0[a] | 0.23 | 1.72 | 861 | 827 |
| 205759.84+435326.5 | LkH$\alpha$ 185 | II | 14.6 | 14.6 | 0.074 | 0.70 | 884 | 884 |
| 205801.36+434520.5 | FHO 27 | Flat | 16.6 | 16.3 | 0.61 | 2.35 | 878 | 866 |
| 205806.10+435301.4 | V1716 Cyg | II | 16.5 | 16.5 | 0.16 | 1.10 | 879 | 879 |
| 205825.55+435328.6 | FHO 28 | II | 17.8 | 17.7 | 0.40 | 2.40 | 874 | 871 |
| 205839.73+440132.8 | FHO 29 | Flat | 16.7 | 16.8 | 0.59 | 3.17 | 879 | 877 |
| 205905.98+442655.9 | NSV 25414 | II | 14.7 | 14.6 | 0.45 | 2.21 | 884 | 823 |
| 205906.69+441823.7 | FHO 30 | II | 17.2 | 17.2 | 0.14 | 1.23 | 872 | 869 |

**Table 3.3:** $\bar{R}$ denotes the mean PTF magnitude, $R_{med}$ the median PTF magnitude, and $\Delta R$ the peak-to-peak amplitude.

[a] While this star is fainter than $R_{med} = 18$ in the 2012 December data release, the target selection was done using the 2012 April release, at which time the source had $R_{med} < 18$.

| [RGS2011] ID | Short Name | $R_{med}$ (mag) | Event | Lightcurve Notes | Spectrum Notes |
|---|---|---|---|---|---|
| 205032.32+442617.4 | FHO 1 | 17.5 | Burster | Several bursts, each lasting only 1-2 hours. | |
| 205036.93+442140.8 | [OSP2002] BRC 31 1 | 16.3 | Fader | Faded in mid-2011, still at minimum. See subsection 3.6.2. | Spectrum dominated by emission lines in both 1998 and 2012. Both epochs show H$\alpha$, Ca II, Paschen series, and Fe II emission; 2012 also has [O I], [Fe II], [S II], and [Ni II]. |
| 205040.29+443049.0 | LkH$\alpha$ 139 | 14.6 | Burster | One burst lasting 3 days in 2011. | |
| 205042.78+442155.8 | [OSP2002] BRC 31 8 | 16.9 | Burster | 300-day modulation, with daily 1-2 hour bursts near maximum of the modulation. | |
| 205100.90+443149.8 | V1701 Cyg | 15.3 | Fader | Fades lasting several days, roughly once a month. | |
| 205114.80+424819.8 | FHO 2 | 13.8 | Burster | Bursts lasting $\sim$ 50 days, every 100-300 days. See subsection 3.4.2. | |
| 205115.14+441817.4 | LkH$\alpha$ 150 | 16.3 | Fader | Faded by 1 mag in early 2012 for 3-4 months. Long rise with $\pm$0.4 mag variations during recovery. | |
| 205119.43+441930.5 | FHO 3 | 16.9 | Fader | 2-day fades at intervals from 4 to 7 days. | |
| 205120.99+442619.6 | LkH$\alpha$ 153 | 15.0 | Burster | One burst lasting 2-15 days, and several lasting less than 1 day each | |
| 205123.59+441542.5 | FHO 4 | 17.6 | Burster | Two bursts lasting $\sim$ 60 days, separated by 350 days. More complex profile than FHO 2. See subsection 3.4.2. | M2 star with H$\alpha$, He I, [N II], Ca II emission. H$\alpha$ and Ca II half as strong in 2012 as in 1998. |
| 205124.70+441818.5 | FHO 5 | 17.9 | Fader | Many short 1 mag fades lasting $\sim$ 1 day, mixed with some longer ($\sim$ 3 day) but shallower ($\sim$ 0.6 mag) fades. | |
| 205139.26+442428.0 | FHO 6 | 14.8 | Fader | Many short fades lasting $\sim$ 4 days, separated by 20-50 days, superimposed on lower-amplitude erratic variability. | |

**Table 3.4:** Phenomenology of candidate bursters and faders. $R_{med}$ denotes the median PTF magnitude. Lightcurves for all these sources are available online from the PTF website.

| [RGS2011] ID | Short Name | $R_{med}$ (mag) | Event | Lightcurve Notes | Spectrum Notes |
|---|---|---|---|---|---|
| 205139.93+443314.1 | FHO 7 | 16.3 | Fader | Three fading events, 50, 150, and > 180 days long, each with complex bursts in their cores; one additional event, lasting < 70 days, started at the end of the 2010 season. Decline seen over 2012, though not as pronounced as in FHO 27. | K5 star with H$\alpha$ and Ca II emission. |
| 205145.99+442835.1 | FHO 8 | 17.7 | Fader | One 0.5 mag fading event lasting 100 days. | |
| 205155.70+443352.6 | FHO 9 | 15.9 | Fader | One 0.6 mag fading event lasting $\sim$ 6 days in 2011 July. 4-day, 0.6 mag, fading events separated by 10-20 days throughout rest of lightcurve. | |
| 205158.63+441456.7 | FHO 10 | 16.7 | Fader | Two fades $\sim$ 0.3 mag deep lasting 4-5 days, and one lasting < 10 days. Events separated by several months. Mixed with erratic variability of $\sim$ 0.2 mag. | |
| | | | Burster | Two bursts $\sim$ 0.4 mag high lasting < 3 days each, separated by 7 days. Mixed with erratic variability of $\sim$ 0.2 mag. | |
| 205203.65+442838.1 | FHO 11 | 17.9 | Fader | Slow decay over $\sim$ 100 days followed by a rapid rise in $\sim$ 30 days. Weaker, shorter fade 2 years before had a fast decay followed by a slow rise. | |
| 205228.33+442114.7 | FHO 12 | 16.5 | Fader | 1.5-day fading events repeating every 5.8 days. | K7 star with strong H$\alpha$ emission, as well as He I and [O I] emission. |
| 205230.89+442011.3 | LkH$\alpha$ 174 | 16.7 | Fader | Fading events lasting 3 days, repeating every 7.7 days. Roughly 1/3 of the cycles do not have a fade. | K5 star with H$\alpha$, Ca II, and He I emission. |
| 205252.48+441424.9 | FHO 13 | 18.0 | Fader | Fades lasting several days, every 10-20 days. Most fades have depths of $\sim$ 1 mag; roughly every $\sim$ 200 days a fade is deeper, $\sim$ 1.4 mag. | |

**Table 3.4:** Phenomenology of candidate bursters and faders. $R_{med}$ denotes the median PTF magnitude. Lightcurves for all these sources are available online from the PTF website.

| [RGS2011] ID | Short Name | $R_{med}$ (mag) | Event | Lightcurve Notes | Spectrum Notes |
|---|---|---|---|---|---|
| 205253.43+441936.3 | FHO 14 | 18.0 | Fader | 0.4-0.7 mag fading events lasting 6-12 days every 20-30 days. One 0.2 mag, 150-day fading event with several of the shorter fades within it. | |
| 205254.30+435216.3 | FHO 15 | 17.1 | Fader | Three low states lasting 100, 30, and 70 days, in order, separated by one year; all three show high variability at minimum. First two fades 1.3 mag deep, third only 0.8 mag. | K8 with H$\alpha$, He I, and O I emission. |
| 205314.00+441257.8 | FHO 16 | 17.1 | Fader | Combination of 0.6 mag fades, lasting 2-4 days, and 0.3 mag fades, lasting 60-80 days. | |
| 205315.62+434422.8 | FHO 17 | 17.6 | Burster | Several 0.4 mag bursts lasting 1-3 days, followed by a quiescent period, followed by a 1.5 mag burst lasting 150 days. | |
| 205340.13+441045.6 | FHO 18 | 17.0 | Fader | Two 0.4 mag fades lasting 5 and 3 days, 11 days apart. Both fades immediately preceded by 0.3 mag bursts. See subsection 3.6.3. | K5 star with H$\alpha$, He I, Ca II, and [N II] emission. |
| | | | Burster | Two 0.8 mag bursts lasting 10 and 7 days, 240 days apart. Several 0.3 mag bursts separated by tens of days. | |
| 205410.15+443103.0 | FHO 19 | 18.0 | Fader | Several fades lasting 3 days each, repeating every 8-10 days. Fade depth varies between 0.5 and 0.9 mag. | |
| 205413.74+442432.4 | FHO 20 | 16.2 | Fader | 2-5 day fading events; longer events tend to be deeper. | |
| 205424.41+444817.3 | FHO 21 | 16.6 | Fader | Three fades, lasting $\sim$ 10 days (first part not observed), 5 days, and 11 days, separated by 250 and 330 days. | |
| 205445.66+444341.8 | FHO 22 | 17.3 | Fader | Complex fades lasting 6-20 days, separated by 230 and 300 days. Hints of a double profile for each event. One additional 3-day fade 50 days after the third main fade. | |

**Table 3.4:** Phenomenology of candidate bursters and faders. $R_{med}$ denotes the median PTF magnitude. Lightcurves for all these sources are available online from the PTF website.

| [RGS2011] ID | Short Name | $R_{med}$ (mag) | Event | Lightcurve Notes | Spectrum Notes |
|---|---|---|---|---|---|
| 205446.61+441205.7 | FHO 23 | 17.3 | Fader | Several fades lasting 2-6 days, separated by a few weeks. Fades range from 0.6 mag to 0.3 mag, the level of the underlying erratic variability. | |
| 205451.27+430622.6 | FHO 24 | 15.9 | Burster | 0.2 mag burst lasting $\sim$ 15 days in 2010, followed by a series of 0.5 mag bursts in 2012 lasting 15-40 days each. See subsection 3.4.2. | |
| 205503.01+441051.9 | FHO 25 | 16.0 | Fader | One $\sim$ 5-10-day fade in late 2010 | |
| 205534.30+432637.1 | [CP2005] 17 | 17.1 | Fader | One 65-day fade in 2010. | |
| 205659.32+434752.9 | FHO 26 | 17.9 | Burster | Several bursts in 2010-2011, lasting 4-5 days each and separated by 10-30 days. No activity in 2012. See subsection 3.6.1. | M4.5 star with H$\alpha$ emission. |
| 205759.84+435326.5 | LkH$\alpha$ 185 | 14.6 | Burster | First half of a 0.3 mag burst before a data gap in mid-2011. Rise time 2 days. | |
| 205801.36+434520.5 | FHO 27 | 16.1 | Fader | Multiple fading events lasting 15-40 days and separated by intervals ranging from 30-60 days. Events superimposed on a steep decline over the course of 2012, more extreme than in FHO 7. Fading events get shallower over the course of the decline. See subsection 3.6.4. | K7 star with strong H$\alpha$, Ca II, Paschen series, and He I emission, and weaker lines of [O I] and O I. |
| 205806.10+435301.4 | V1716 Cyg | 16.5 | Burster | Two bursts, the first lasting 5-20 days and the second 3 days, separated by 35 days. Complex profiles. | |

**Table 3.4:** Phenomenology of candidate bursters and faders. $R_{med}$ denotes the median PTF magnitude. Lightcurves for all these sources are available online from the PTF website.

| [RGS2011] ID | Short Name | $R_{med}$ (mag) | Event | Lightcurve Notes | Spectrum Notes |
|---|---|---|---|---|---|
| 205825.55+435328.6 | FHO 28 | 17.7 | Fader | 130-day interval of repeated 8-day fading events in 2012; only 5, well-separated events each in 2010 and 2011. 2011 fades were typically only 2 days long, while 2010 events were too sparsely sampled to constrain their length. See subsection 3.6.5. | M3 star with H$\alpha$ emission in both 1998 and 2012, though the line is stronger in 2012. The 2012 spectrum also has weak emission of Ca II, [N II], He I. |
| 205839.73+440132.8 | FHO 29 | 16.8 | Burster | High states in early 2010, early 2011, late 2011, and entire first half of 2012. 2010-2011 bursts repeat roughly every 270-300 days, but 2012 behavior does not fit the period. | |
| 205905.98+442655.9 | NSV 25414 | 14.6 | Fader | 1 mag fading events lasting 10-15 days, with $\pm$0.5 mag variability at minimum. Fades repeat every $\sim$ 30 days. | |
| 205906.69+441823.7 | FHO 30 | 17.2 | Fader | Short 0.6 mag fades, typically 2 days or less, separated by between 10 and 60 days. Two 0.15 mag fades lasting 30 days each in mid-2011 and late 2012. All fades are superimposed on 0.4 mag erratic variability. | |

**Table 3.4:** Phenomenology of candidate bursters and faders. $R_{med}$ denotes the median PTF magnitude. Lightcurves for all these sources are available online from the PTF website.

## 3.8 References

Alencar, S. H. P. et al. 2010, A&A, 519, A88+, arXiv:1005.4384

Aly, J. J., & Kuijpers, J. 1990, A&A, 227, 473

Bouvier, J., Alencar, S. H. P., Harries, T. J., Johns-Krull, C. M., & Romanova, M. M. 2007, Protostars and Planets V, 479, arXiv:astro-ph/0603498

Bouvier, J. et al. 1999, A&A, 349, 619

——. 2003, A&A, 409, 169, arXiv:astro-ph/0306551

Cody, A. M., & Hillenbrand, L. A. 2010, ApJS, 191, 389, arXiv:1011.3539

Covey, K. R. et al. 2011, AJ, 141, 40, arXiv:1011.2565

Espaillat, C., Furlan, E., D'Alessio, P., Sargent, B., Nagel, E., Calvet, N., Watson, D. M., & Muzerolle, J. 2011, ApJ, 728, 49, arXiv:1012.3500

Espaillat, C. et al. 2012, ApJ, 747, 103, arXiv:1201.1518

Flaherty, K. M., Muzerolle, J., Rieke, G., Gutermuth, R., Balog, Z., Herbst, W., Megeath, S. T., & Kun, M. 2012, ApJ, 748, 71, arXiv:1202.1553

Goodson, A. P., & Winglee, R. M. 1999, ApJ, 524, 159

Grinin, V. P. 1992, Astronomical and Astrophysical Transactions, 3, 17

Grinin, V. P., Barsunova, O. Y., Shugarov, S. Y., Kroll, P., & Sergeev, S. G. 2008, Astrophysics, 51, 1

Hauschildt, P. H., Allard, F., & Baron, E. 1999, ApJ, 512, 377, arXiv:astro-ph/9807286

Herbig, G. H. 2008, AJ, 135, 637

Hillenbrand, L. A. et al. 2013, AJ, 145, 59, arXiv:1208.2066

Kendall, M. 1938, Biometrika, 30, 81

Kowalski, A. F., Hawley, S. L., Holtzman, J. A., Wisniewski, J. P., & Hilton, E. J. 2010, ApJ, 714, L98, arXiv:1003.3057

Kretzschmar, M. 2011, A&A, 530, A84+, arXiv:1103.3125

Miller, A. A. et al. 2011, ApJ, 730, 80, arXiv:1011.2063

Morales-Calderón, M. et al. 2011, ApJ, 733, 50, arXiv:1103.5238

Murphy, S. J., Lawson, W. A., Bessell, M. S., & Bayliss, D. D. R. 2011, MNRAS, 411, L51, arXiv:1011.3816

Muzerolle, J. et al. 2009, ApJ, 704, L15, arXiv:0909.5201

Rebull, L. M. et al. 2011, ApJS, 193, 25, arXiv:1102.0573

Romanova, M. M., Ustyugova, G. V., Koldoba, A. V., & Lovelace, R. V. E. 2004, ApJ, 616, L151, arXiv:astro-ph/0502266

——. 2005, ApJ, 635, L165, arXiv:astro-ph/0511600

Siess, L., Dufour, E., & Forestini, M. 2000, A&A, 358, 593, arXiv:astro-ph/0003477

Waters, L. B. F. M., & Waelkens, C. 1998, ARA&A, 36, 233

# Chapter 4

# Theoretical Performance of Timescale Metrics

## 4.1 Introduction

Periodic lightcurves can be easily characterized by their period, and a number of standard methods exist in the literature for determining the period of a lightcurve (e.g., Scargle, 1982; Lenz & Breger, 2005). No analogous metric exists for characterizing aperiodic signals. However, as argued in subsection 1.2.1, the timescale is a key observational characteristic that can discriminate between variability associated with different regions of a young star-disk system. Therefore, I attempt to find a robust metric for characterizing the variability timescale of aperiodic variables and quantitatively distinguishing rapidly- from slowly-varying signals.

I define a good timescale metric as one that meets the following criteria:

**Universal:** it is defined for any lightcurve with any sampling, provided some minimum number of data points are present. In particular, it should not require evenly spaced samples, nor should it place preconditions on the properties of the underlying signal.

**Data-Driven:** it does not require hand-tuning, but is determined entirely by the data.

**Versatile:** it gives consistent results across lightcurves having different shapes or characteristic behaviors.

**Accurate:** it correlates with the "true" timescale of a lightcurve.

**Precise:** it has a low statistical variance.

**Dependable:** it gives consistent results across different noise levels or cadences.

**Robust:** it changes little if a small number of data points are added or removed, even if those points are outliers.

**Well-Characterized:** it offers a way to determine the significance of the detected timescale.

As an illustrative example, the popular Lomb-Scargle periodogram (Lomb, 1976; Scargle, 1982) is versatile (in the sense that non-sinusoids will give the correct period, albeit at lower significance than a sinusoid of the same period and amplitude would), accurate, precise, and well-characterized. It is not universal (it works well only for sources dominated by a single periodic component), nor data driven (the analyst must choose an appropriate frequency grid), nor dependable (many real cadences will introduce aliases, sidelobes, or other artifacts), nor robust (each observation contributes equally to each point in the periodogram, allowing combinations of outliers to create false peaks at particular frequencies). There may never be a timescale metric that meets all these criteria, but they help guide an objective comparison of competing metrics with each other. As the example with the periodogram shows, even a metric that fails several criteria can still be very valuable in the right applications.

This chapter describes algebraic calculations directed toward identifying a good aperiodic timescale metric. To my knowledge, these calculations have not been done before in this context. Numerical simulations toward the same goal are presented in Chapter 5.

### 4.1.1 Motivation for an Analytic Treatment

Numerical simulations allow a timescale metric to be tested under a range of lightcurve parameters, observing strategies, and signal-to-noise ratios. However, they cannot address every issue. An assessment of timescale metrics based entirely on simulations would have three key limitations:

- the number of simulations needed to capture the full range of lightcurve behaviors would be difficult to determine. This is particularly a problem for long-timescale stochastic lightcurves, where the behavior in any individual lightcurve can deviate far from the ensemble average. Results based on too-few simulations, even if formally significant, could have undetected biases, while ensuring that there are enough simulations would carry a steep computational cost.

- while a simulation can characterize the behavior of a timescale metric for any assumed observing strategy, it offers little guidance on how to generalize the results. Since the space of possible cadences is too large to cover effectively, it can be difficult to distinguish which simulation results are a general property of a timescale metric and which are specific to the cadences that have been tried.

- a simulation cannot be used to test the bias or consistency of a timescale metric, because it does not provide the true value being estimated by the metric. Even if a simulation can show that the value of a timescale metric converges as the duration or cadence of a lightcurve increases, it will not show whether the limit of convergence is in fact the correct value of the statistic.

The analytical work described in this chapter provides supporting information to address all three concerns. By concentrating on the average behavior of a particular timescale metric on a lightcurve, a theoretical analysis is immune to "cosmic variance" from individual lightcurves (but, conversely, it cannot constrain the amount of error introduced by individual lightcurve variation in a real analysis). The work in this chapter distinguishes between cadence-dependent and cadence-independent properties of a timescale metric by working in terms of the functions underlying a particular lightcurve, without reference to a specific cadence. Finally, by working with the underlying function rather than simulated observations of limited cadence or length, the analysis in this chapter establishes the baseline needed for characterizations of the bias or consistency of a timescale metric.

### 4.1.2 Conventions in this Chapter

In keeping with typical statistical conventions, I use $P()$ to denote probabilities, $F()$ to denote cumulative distributions, and $f$ to denote probability densities throughout this chapter. $E()$ denotes an expectation value, and $V()$ a variance. The covariance of $X$ and $Y$ may be denoted either $V(X,Y)$, or, for clarity, $\mathrm{cov}(X,Y)$. The correlation coefficient will be denoted $\rho(X,Y)$. To avoid confusion in calculations that contain absolute values, I use a semicolon rather than the more typical vertical bar to denote conditional probabilities or densities, i.e., the probability of $A$ given $B$ will be denoted $P(A;B)$ rather than $P(A|B)$.

When describing specific lightcurve models, $m(t)$ denotes the source magnitude as a function of time $t$. When analyzing stochastic models, the source magnitude may be denoted $M$ rather than $m$ to emphasize its interpretation as a random variable, but the meaning is otherwise unchanged. Many models require an arbitrary reference time, denoted $t_0$. $m_0$ denotes a reference magnitude, usually, but not always, the mean of the lightcurve model. $A$ denotes an amplitude parameter for deterministic models, and $\sigma_m$ an amplitude parameter for stochastic models; the latter can usually be interpreted as an RMS amplitude. Finally, the timescale for periodic models is represented by $\omega = 2\pi/P$, where $P$ is the period, while the timescale for aperiodic models is denoted $\tau$.

This chapter contains a large number of equations. For clarity, only equations describing key results are numbered. Equations representing intermediate steps in derivations are not numbered.

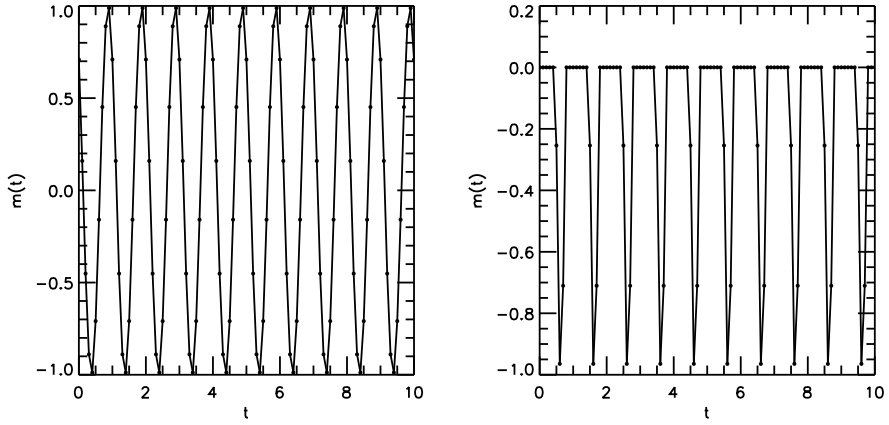


**(a)** Sinusoid




**(b)** AA Tau

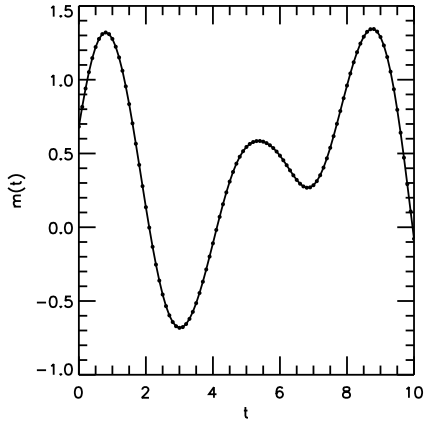


**(c)** Squared Exponential GP

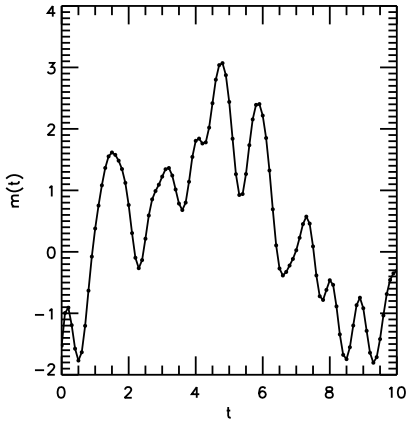


**(d)** Two-Timescale GP

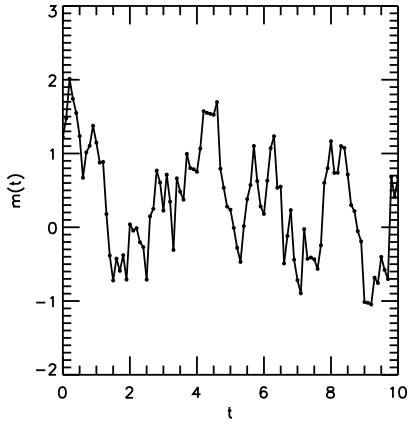


**(e)** Damped Random Walk

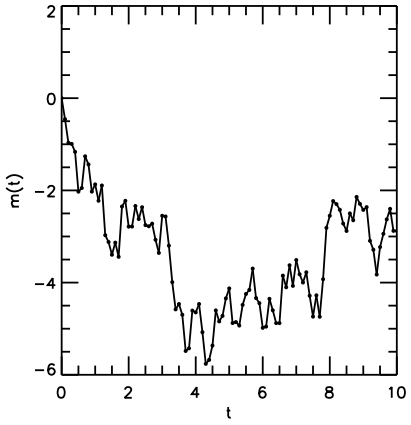


**(f)** Random Walk

**Figure 4.1:** Examples of the lightcurves discussed in this section, in arbitrary units. The two-timescale Gaussian process has components with equal amplitudes and timescales of 1 and 0.3 units. The random walk has no characteristic timescale, but has a diffusion constant equal to that of the damped random walk. All other lightcurves have a characteristic timescale of 1 unit.

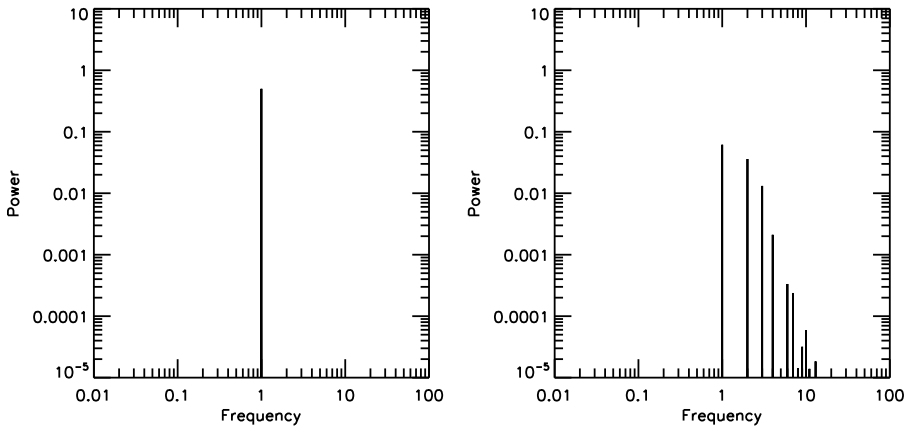


**(a)** Sinusoid




**(b)** AA Tau

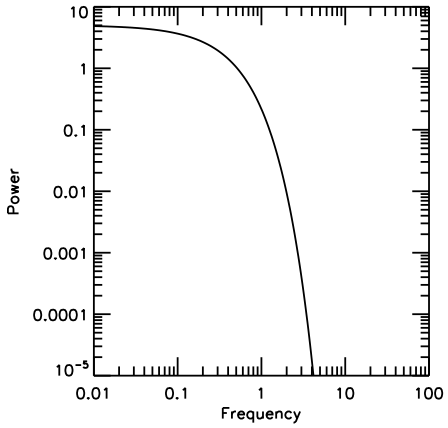


**(c)** Squared Exponential GP

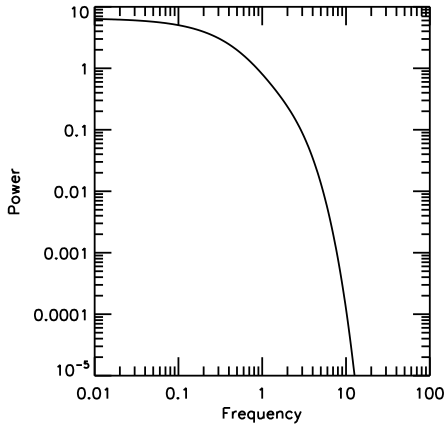


**(d)** Two-Timescale GP

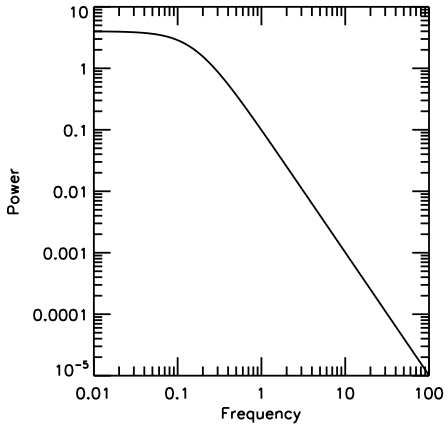


**(e)** Damped Random Walk

Power spectrum does not exist

**(f)** Random Walk

**Figure 4.2:** Theoretical power spectra for the lightcurves discussed in this section, in arbitrary units. A frequency of 1 unit corresponds to a time separation of 1 unit in Figure 4.1. Lightcurve model parameters are as in Figure 4.1.

## 4.2 Test Signals

### 4.2.1 Sinusoid

As the archetypal periodic function, a sinusoidal signal serves as a good reference point for comparison to aperiodic functions. For all calculations, I adopt the form

$$m(t) = m_0 + A\sin\left(\omega(t - t_0)\right) \tag{4.1}$$

Note that in this convention, $A$ is the half-amplitude, not the peak-to-peak amplitude. The 5-95% amplitude of a sine is $2A\cos\left(\frac{\pi}{2}(0.10)\right) = 1.975A$. The RMS amplitude is $A\sqrt{\pi}$.

The power spectral density of a sinusoid, following the Fourier transform convention of Gillespie (1996), is the well-known result

$$S(\nu) = \frac{1}{2}A^2\left(\delta(\nu - \frac{1}{P}) + \delta(\nu + \frac{1}{P})\right)$$

where $\delta$ denotes the Dirac delta function. By definition, a sinusoid has only a single frequency component.

### 4.2.2 AA Tau

For a periodic function less well-behaved than the sine, I adopt an abstraction of an AA Tau variable, i.e., a lightcurve with periodic dips. For the dip profile I assume a half-sine waveform. This profile adequately represents the fact that most dips have smooth walls and lack a flat bottom (Cody, priv. comm. 2012; McGinniss et al., in prep.).

The adopted form is

$$\begin{aligned} m(t) &= \begin{cases} m_0 - A\cos\left(\frac{\pi}{2}\frac{\phi}{\delta\phi}\right) & \text{if } |\phi| < \delta\phi \\ m_0 & \text{otherwise} \end{cases} \\ \text{where } \phi &= \text{frac}\left(\frac{\omega}{2\pi}(t - t_0)\right) - \frac{1}{2} \end{aligned} \tag{4.2}$$

where the convention that $-\frac{1}{2} \leq \phi < \frac{1}{2}$ is adopted for convenience. $\delta\phi$ is the half-width of the dip in units of the period, and can range from 0 to $\frac{1}{2}$. The 5-95% amplitude for an AA Tau lightcurve is

$$\begin{cases} 0 & \text{if } 2\delta\phi < 0.05 \\ A\cos\left(\frac{0.05\pi}{4\delta\phi}\right) & \text{if } 0.05 < 2\delta\phi < 0.95 \\ A\cos\left(\frac{0.05\pi}{4\delta\phi}\right) - A\cos\left(\frac{0.95\pi}{4\delta\phi}\right) & \text{if } 0.95 < \delta\phi \end{cases}$$

The RMS amplitude is

$$\frac{A}{\pi\sqrt{2}}\sqrt{2\delta\phi\left(8\delta\phi\cos\left(\frac{\pi}{2\delta\phi}\right)+\pi\sin\left(\frac{\pi}{2\delta\phi}\right)\right)+\pi^2-(4\delta\phi)^2}$$

The power spectral density of an AA Tau lightcurve, following the Fourier transform convention of Gillespie (1996), is approximately

$$\begin{aligned}S(\nu) &= A^2\left(0.0365+0.0615\left(\delta(\nu-\frac{1}{P})+\delta(\nu+\frac{1}{P})\right)+0.0360\left(\delta(\nu-\frac{2}{P})+\delta(\nu+\frac{2}{P})\right)\right.\\ &\quad +0.0132\left(\delta(\nu-\frac{3}{P})+\delta(\nu+\frac{3}{P})\right)+0.0021\left(\delta(\nu-\frac{4}{P})+\delta(\nu+\frac{4}{P})\right)\\ &\quad \left.+0.0003\left(\delta(\nu-\frac{6}{P})+\delta(\nu+\frac{6}{P})\right)+0.0002\left(\delta(\nu-\frac{7}{P})+\delta(\nu+\frac{7}{P})\right)+\ldots\right)\end{aligned}$$

and follows from the Fourier series of Equation 4.2.

### 4.2.3 White Noise

A white noise process is a probabilistic model where magnitudes are drawn from a Gaussian distribution, and are independent of the magnitudes at all other times. I adopt the notation

$$\begin{aligned}E(m(t)) &= m_0\\ V(m(t)) &= \sigma_m^2\\ \mathrm{cov}\left(m(t_i),m(t_j)\right) &= \sigma_m^2\delta(t_i,t_j)\end{aligned} \tag{4.3}$$

where $\delta$ denotes the Kronecker delta, not the Dirac delta, and $\mathrm{cov}(X,Y)$ denotes the covariance of random variables $X$ and $Y$. $\sigma_m$ can be interpreted as the RMS amplitude of the white noise process. The 5-95% amplitude for a white noise process is $2\sigma_m\sqrt{2}\ \mathrm{erf}^{-1}0.90 = 3.291\sigma_m$.

The power spectral density of a white noise process, following Gillespie (1996), is

$$S(\nu) = 2\sigma_m^2$$

By definition, a white noise process has a uniform power spectrum.

### 4.2.4 Squared Exponential Gaussian Process

The squared exponential Gaussian process is a probabilistic model where magnitudes are drawn from a Gaussian distribution, and the correlation between magnitudes at any two times follows a

Gaussian function of the difference between them. I use the form

$$\begin{aligned} E(m(t)) &= m_0 \\ V(m(t)) &= \sigma_m^2 \\ \mathrm{cov}\left(m(t_i), m(t_j)\right) &= \sigma_m^2 e^{-(t_i - t_j)^2/2\tau^2} \end{aligned} \tag{4.4}$$

Again, $\sigma_m$ denotes the RMS amplitude of the squared exponential Gaussian process. The 5-95% amplitude for a squared exponential Gaussian process is $2\sigma_m\sqrt{2}\ \mathrm{erf}^{-1}\,0.90 = 3.291\sigma_m$.

The power spectral density of a squared exponential Gaussian process, following the Fourier transform convention of Gillespie (1996), is

$$S(\nu) = 2\sqrt{2\pi}\tau\sigma_m^2 e^{-(2\pi\tau\nu)^2/2}$$

The power spectrum is flat for $\nu \lesssim 1/\tau$, but has almost no power at higher frequencies (Figure 4.2c).

### 4.2.5 Two-Timescale Gaussian Process

To test how well different timescale measures work with lightcurves that have multiple components, I consider an extension of the squared exponential Gaussian process that decays on two different timescales, following

$$\begin{aligned} E(m(t)) &= m_0 \\ V(m(t)) &= \sigma_1^2 + \sigma_2^2 \\ \mathrm{cov}\left(m(t_i), m(t_j)\right) &= \sigma_1^2 e^{-(t_i - t_j)^2/2\tau_1^2} + \sigma_2^2 e^{-(t_i - t_j)^2/2\tau_2^2} \end{aligned} \tag{4.5}$$

where $\sigma_1$ and $\tau_1$ are the RMS amplitude and timescale of the first component, and $\sigma_2$ and $\tau_2$ are those of the second component. I assume, with no loss of generality, that $\tau_1 < \tau_2$. The 5-95% amplitude for a two-timescale Gaussian process is $2\sqrt{2\sigma_1^2 + 2\sigma_2^2}\,\mathrm{erf}^{-1}\,0.90 = 3.291\sqrt{\sigma_1^2 + \sigma_2^2}$. The RMS amplitude is $\sqrt{\sigma_1^2 + \sigma_2^2}$.

The power spectral density of a two-timescale Gaussian process, following the Fourier transform convention of Gillespie (1996), is

$$S(\nu) = 2\sqrt{2\pi}\left(\tau_1\sigma_1^2 e^{-(2\pi\tau_1\nu)^2/2} + \tau_2\sigma_2^2 e^{-(2\pi\tau_2\nu)^2/2}\right)$$

There is a lot of power for $\nu \lesssim 1/\tau_1$, but almost none at higher frequencies (Figure 4.2d).

### 4.2.6 Damped Random Walk

Although a damped random walk, or more formally an Ornstein-Uhlenbeck process, is normally defined in terms of a stochastic differential equation, it can be shown that the samples $X(t_i)$ of a

damped random walk are jointly normally distributed (Doob, 1942). Therefore, a damped random walk is a Gaussian process and can be described with the same formalism as the white noise and squared exponential Gaussian process cases. If $(m(t) - m_0)$ follows an Ornstein-Uhlenbeck process (I subtract $m_0$ because I follow the formalism of Gillespie (1996), who defines the process to have mean zero), then

$$\begin{aligned} E(m(t)) &= m_0 + x_0 e^{-(t-t_0)/\tau} \\ V(m(t)) &= \tfrac{D\tau}{2}\left(1 - e^{-2(t-t_0)/\tau}\right) \\ \operatorname{cov}\left(m(t_i), m(t_j)\right) &= \tfrac{D\tau}{2} e^{-(t_2-t_1)/\tau}\left(1 - e^{-2(t-t_0)/\tau}\right) \end{aligned}$$

where $D$ is the diffusion constant, $\tau$ is the damping time, the random walk begins at $m(t_0) - m_0 = x_0$, and $t_1$ and $t_2$ denote the order of the times $t_i$ and $t_j$ such that $t_0 \leq t_1 \leq t_2$. The case of interest for an astrophysical lightcurve is when $t - t_0 \gg \tau$, so that the initial conditions are irrelevant and the lightcurve can be described as a stationary process:

$$\begin{aligned} E(m(t)) &= m_0 \\ V(m(t)) &= \tfrac{D\tau}{2} \\ \operatorname{cov}\left(m(t_i), m(t_j)\right) &= \tfrac{D\tau}{2} e^{-(t_2-t_1)/\tau} \\ &= \tfrac{D\tau}{2} e^{-|t_i-t_j|/\tau} \end{aligned} \tag{4.6}$$

In the last line, I've used the fact that $t_1 = \min\{t_i, t_j\}$ and $t_2 = \max\{t_i, t_j\}$.

The 5-95% amplitude for a damped random walk in the stationary limit is $2\sqrt{D\tau}\ \operatorname{erf}^{-1} 0.90 = 2.327\sqrt{D\tau}$. The RMS amplitude is $\sqrt{\frac{D\tau}{2}}$.

The power spectral density of a damped random walk, following Gillespie (1996), is

$$S(\nu) = \frac{4\tau\sigma_m^2}{1 + (2\pi\tau\nu)^2}$$

The power spectral density is flat for $\nu \lesssim 1/\tau$, but decays as $1/\nu^2$ at higher frequencies (Figure 4.2e).

### 4.2.7 Undamped Random Walk

The random walk, or, more formally, a Wiener process, is the limit of a damped random walk when the damping time $\tau$ becomes infinite. Following Gillespie (1996), the mean and variance are

$$\begin{aligned} E(m(t)) &= m_0 \\ V(m(t)) &= D(t - t_0) \end{aligned} \tag{4.7}$$

Given the relationship between the damped and undamped random walks, the covariance of the latter is

$$\mathrm{cov}(m_i, m_j) = \lim_{\tau\to\infty} \frac{D\tau}{2} e^{-(t_2-t_1)/\tau} \left(1 - e^{-2(t_1-t_0)/\tau}\right)$$

Changing variables to $x = 1/\tau$ to make the expansions easier,

$$\begin{aligned}
\mathrm{cov}(m_i, m_j) &= \lim_{x\to 0} \frac{D}{2x} e^{-x(t_2-t_1)} \left(1 - e^{-2x(t_1-t_0)}\right) \\
&= \lim_{x\to 0} \frac{D}{2x} \left(1 - x(t_2-t_1) + O(x^2)\right) \left(2x(t_1-t_0) + O(x^2)\right) \\
&= \lim_{x\to 0} \frac{D}{2x} \left(2x(t_1-t_0) + O(x^2)\right) \\
&= \lim_{x\to 0} \frac{D}{2} \left(2(t_1-t_0) + O(x)\right) \\
&= D(t_1 - t_0) \qquad (4.8)
\end{aligned}$$

The covariance between two measurements is the variance of the earlier measurement.

Note that, since the variance and covariance increase without bound as one gets farther and farther from the initial time $t_0$, a random walk is not a (weak-sense) stationary process and many results concerning the properties of stochastic processes do not apply. In particular, a random walk does not have a well-defined power spectral density (Gillespie, 1996), although some authors incorrectly state it has a $1/\nu^2$ spectrum.

## 4.3 Overview of the Chapter

The remainder of this chapter is organized as follows. Each of sections 4.4 through 4.6 introduces a specific timescale metric (in order, structure functions, autocovariance functions, and $\Delta m$-$\Delta t$ plots), then examines the behavior of that metric on each lightcurve model presented in section 4.2. Having examined the performance of the timescale metric across a variety of lightcurve forms, each section ends with an assessment of the fitness or unfitness of the metric. Each assessment includes a table (Table 4.1, Table 4.2, or Table 4.3, respectively) containing the theoretical timescales for each lightcurve. We provide a higher-level summary of the results in section 4.7, which compares the three metrics with each other, and evaluates which meet four of the criteria introduced above: whether the metric is universal, data-driven, versatile, or accurate. The remaining criteria must be tested against specific data sets, and are studied using numerical simulations in the following chapter.

For each combination of timescale metric and lightcurve model, I first derive a functional form for the timescale metric, then evaluate the function at several key values to obtain a scalar timescale. All three timescale metrics include at least one parameter such as a cutoff value; I carry out the analysis for several representative values of the parameter(s), and explain my choices at the start of

that metric's section.

Wherever the definition of a timescale metric requires an amplitude for the lightcurve, I adopted the range between the 5th and 95th percentiles of the magnitudes. This definition can be applied consistently to both deterministic and stochastic lightcurve models, and it is also a valuable way to characterize real data to minimize the effect of outliers. As a result, this definition allows easy conversion between analytical work and real data.

## 4.4 Structure Functions

In this section I calculate the ideal behavior of a structure function for each lightcurve model introduced in section 4.2. The (first-order) structure function is an estimate of the expected value of $(m(t) - m(t + \Delta t))^2$ as a function of $\Delta t$, and therefore represents the "typical" degree of variability seen in observations separated by a timescale $\Delta t$. In practice the estimate is often done by binning the observations onto a grid of $\Delta t$ values (Paltani et al., 1997, e.g.,), but this need not be the only algorithm for evaluating structure functions.

In general, at very short timescales, where the lightcurve can be approximated as linear, the structure function scales as $\Delta t^2$. For incoherent sources, the structure function approaches an asymptotic value of $2V(m)$ at very long timescales (Simonetti et al., 1985). For periodic sources, the structure function approaches zero at integer multiples of the period, since (by definition) $m(t) - m(t + P) \approx 0$.

In the limit of infinite cadence, the structure function can be evaluated directly by computing the expectation value of $(m(t) - m(t + \Delta t))^2$ from the definition of $m(t)$. For Gaussian processes, in particular, the structure function can be expressed entirely in terms of the autocovariance function that defines them.

I consider converting a structure function into a scalar timescale by finding the first $\Delta t$ at which the structure function crosses one ninth, one quarter, or one half of the squared amplitude. These values were selected on the basis of intuition: the first two correspond to variations of one third and one half the lightcurve amplitude, respectively, while the last was adopted to better probe the structure function on longer timescales.

I begin tests of the structure function with a sinusoidal lightcurve, as a straightforward periodic signal, before moving to more complex periodic signals and to aperiodic signals.

### 4.4.1 Sinusoid

If $m(t) = m_0 + A\sin(\omega(t-t_0))$, then

$$\begin{aligned} SF(\Delta t) &= E((m(t)-m(t+\Delta t))^2) \\ &= \frac{\omega}{2\pi}\int_{t_0}^{t_0+2\pi/\omega} \left(A\sin(\omega(t-t_0)) - A\sin(\omega(t+\Delta t-t_0))\right)^2 dt \end{aligned}$$

Let $x = \frac{\omega}{2\pi}(t-t_0)$ and let $\Delta x = \frac{\omega}{2\pi}\Delta t$. Then

$$\begin{aligned} SF(\Delta t) &= A^2\int_0^1 \left(\sin 2\pi x - \sin(2\pi(x+\Delta x))\right)^2 dx \\ &= A^2(1-\cos(2\pi\Delta x)) \\ &= A^2(1-\cos(\omega\Delta t)) \end{aligned} \tag{4.9}$$

This function is shown in Figure 4.3a.

The scalar timescales calculated from the structure function for a sinusoidal signal are listed in Table 4.1.

### 4.4.2 AA Tau

If

$$m(t) = \begin{cases} m_0 - A\cos\left(\frac{\pi}{2}\frac{\phi}{\delta\phi}\right) & \text{if } |\phi| < \delta\phi \\ m_0 & \text{otherwise} \end{cases}$$

then the integrand in the expression $E((m(t)-m(t+\Delta t))^2)$ can assume one of four forms:

$$\begin{aligned} SF(\Delta t) &= \int_{|\phi|>\delta\phi \,\wedge\, |\phi+\Delta\phi|>\delta\phi} (m_0-m_0)^2\, d\phi \\ &+ \int_{|\phi|>\delta\phi \,\wedge\, |\phi+\Delta\phi|<\delta\phi} \left(m_0 - m_0 + A\cos\left(\frac{\pi}{2}\frac{\phi+\Delta\phi}{\delta\phi}\right)\right)^2 d\phi \\ &+ \int_{|\phi|<\delta\phi \,\wedge\, |\phi+\Delta\phi|<\delta\phi} \left(m_0 - A\cos\left(\frac{\pi}{2}\frac{\phi}{\delta\phi}\right) - m_0 + A\cos\left(\frac{\pi}{2}\frac{\phi+\Delta\phi}{\delta\phi}\right)\right)^2 d\phi \\ &+ \int_{|\phi|<\delta\phi \,\wedge\, |\phi+\Delta\phi|>\delta\phi} \left(m_0 - A\cos\left(\frac{\pi}{2}\frac{\phi}{\delta\phi}\right) - m_0\right)^2 d\phi \end{aligned}$$

depending on whether neither, either, or both the lightcurve at time $t$ (or phase $\phi$) and time $t+\Delta t$ ($\phi+\Delta\phi$) are in a dip. Here, $\Delta\phi = \mathrm{frac}\left(\frac{\omega}{2\pi}\Delta t\right) \in [0,1)$ is the time lag in phase units, and it is implied that $\phi$ and $\phi+\Delta\phi$ are wrapped to stay in the interval $[-1/2, 1/2)$ across the domain of each integral. This expression cannot be directly simplified using symbolic mathematics packages such as Mathematica, because the combined logic of keeping the phases straight and testing where the lightcurve is in or out of dip is too complex for them to handle. I therefore break up the sum into

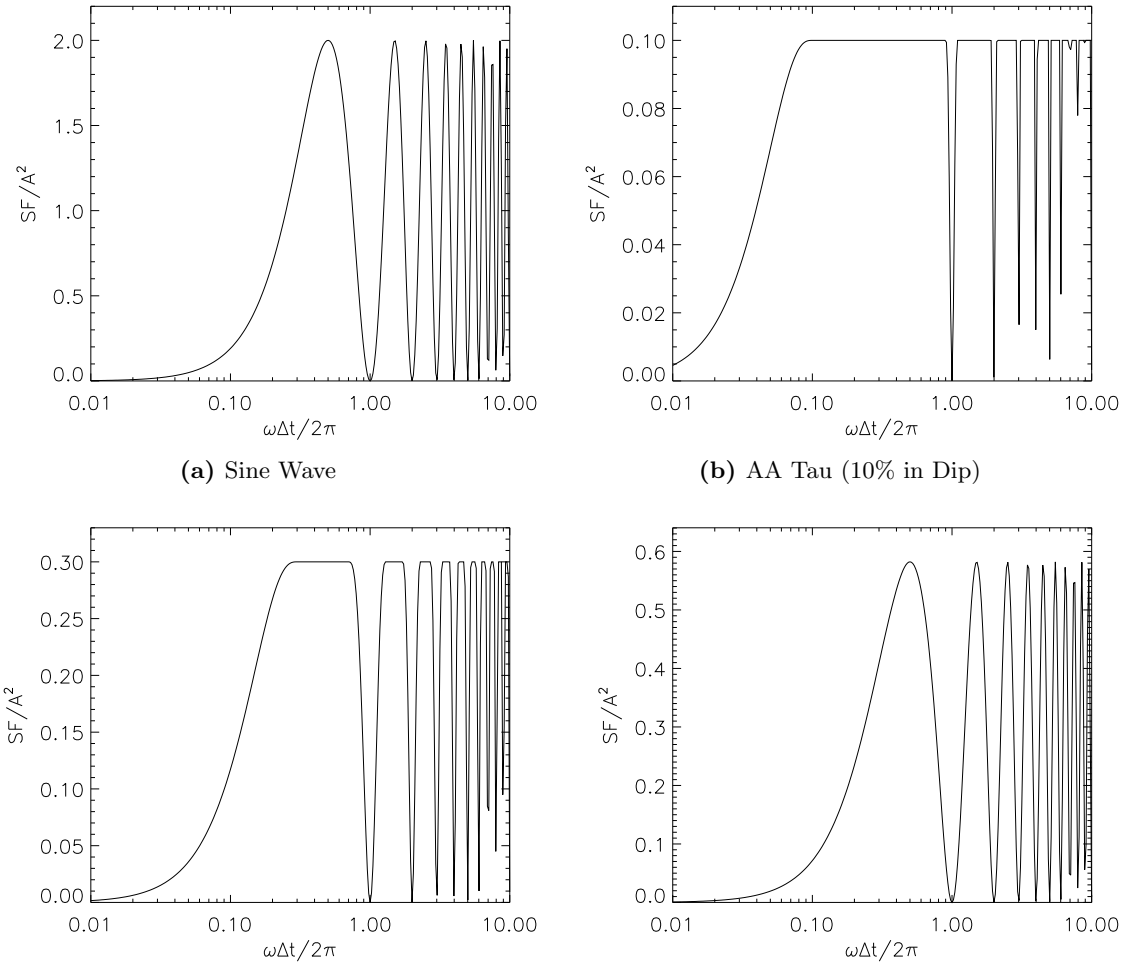


**(a)** Sine Wave

**(b)** AA Tau (10% in Dip)

**(c)** AA Tau (30% in Dip)

**(d)** AA Tau (60% in Dip)

**Figure 4.3:** Normalized structure functions for a sinusoidal signal, and an AA Tau-like signal spending 10%, 30%, and 60% of each cycle in a dip ($\delta\phi = 0.05$, $\delta\phi = 0.15$, and $\delta\phi = 0.30$, respectively). For all plots, the time lag is plotted in units of the period.

individual cases where the limits are well-defined, and evaluate each separately.

In general, the limits of integration depend on the values of $\delta\phi$, the half-width of the dip, and $\Delta\phi$, the time lag. For a given lightcurve shape, i.e., a fixed $\delta\phi$, there are four values of $\Delta\phi$ where limits may qualitatively change:

- if $\Delta\phi = 2\delta\phi$, then when $m(\phi)$ is at the beginning of a dip $m(\phi + \Delta\phi)$ will be at the end. For smaller values of $\Delta\phi$ it is possible for $m(\phi)$ and $m(\phi + \Delta\phi)$ to both be in the dip for the same value of $\phi$, while for larger values it is not.
- if $\Delta\phi = 1 - 2\delta\phi$, then when $m(\phi)$ is at the end of a dip $m(\phi + \Delta\phi)$ will be at the beginning (after wraparound). For larger values of $\Delta\phi$ it is possible for $m(\phi)$ and $m(\phi + \Delta\phi)$ to both be in the dip for the same value of $\phi$, while for smaller values it is not.
- if $\Delta\phi = 1/2 + \delta\phi$, then when $m(\phi)$ is at the beginning of a dip $(\phi + \Delta\phi)$ reaches $+1/2$ and needs to be wrapped to $-1/2$. For smaller $\Delta\phi$ the wraparound occurs while $m(\phi)$ is in the dip, while for larger $\Delta\phi$ the wraparound occurs while $m(\phi)$ is not in the dip.
- if $\Delta\phi = 1/2 - \delta\phi$, then when $m(\phi)$ is at the end of a dip $(\phi + \Delta\phi)$ reaches $+1/2$ and needs to be wrapped to $-1/2$. For larger $\Delta\phi$ the wraparound occurs while $m(\phi)$ is in the dip, while for smaller $\Delta\phi$ the wraparound occurs while $m(\phi)$ is not in the dip.

These four critical values of $\Delta\phi$ divide the integration into five different cases. In addition, the order of the critical values changes when $\delta\phi = 1/6$ and $\delta\phi = 1/4$, creating three regimes of $\delta\phi$ for a total of fifteen cases. Fortunately, most of the cases only affect the forms of the integrals, and not their results; the final answer can be merged into only four cases. The fifteen cases are illustrated in Figure 4.4.

In each of the following cases, each integral is over an interval of positive length, i.e., the upper limit is strictly greater than the lower limit.

**Case I** $0 < \delta\phi < 1/6 \ \wedge \ 0 < \Delta\phi < 2\delta\phi < 1/2 - \delta\phi < 1/2 + \delta\phi < 1 - 2\delta\phi$

In this case the time lag $\Delta\phi$ is so small that the integral doesn't "skip" any combinations of integrands:

$$\begin{aligned} SF(\Delta t) &= \int_{-1/2}^{-\delta\phi-\Delta\phi} (0)d\phi + \int_{-\delta\phi-\Delta\phi}^{-\delta\phi} \left(A\cos\left(\frac{\pi}{2}\frac{\phi+\Delta\phi}{\delta\phi}\right)\right)^2 d\phi \\ &\quad + \int_{-\delta\phi}^{\delta\phi-\Delta\phi} \left(A\cos\left(\frac{\pi}{2}\frac{\phi+\Delta\phi}{\delta\phi}\right) - A\cos\left(\frac{\pi}{2}\frac{\phi}{\delta\phi}\right)\right)^2 d\phi \\ &\quad + \int_{\delta\phi-\Delta\phi}^{\delta\phi} \left(A\cos\left(\frac{\pi}{2}\frac{\phi}{\delta\phi}\right)\right)^2 d\phi + \int_{\delta\phi}^{1/2} (0)d\phi \\ &= \frac{A^2}{\pi}\left(\pi(\Delta\phi - 2\delta\phi)\cos\left(\frac{\pi\Delta\phi}{2\delta\phi}\right) + 2\delta\phi\left(\pi - \sin\left(\frac{\pi\Delta\phi}{2\delta\phi}\right)\right)\right) \end{aligned}$$

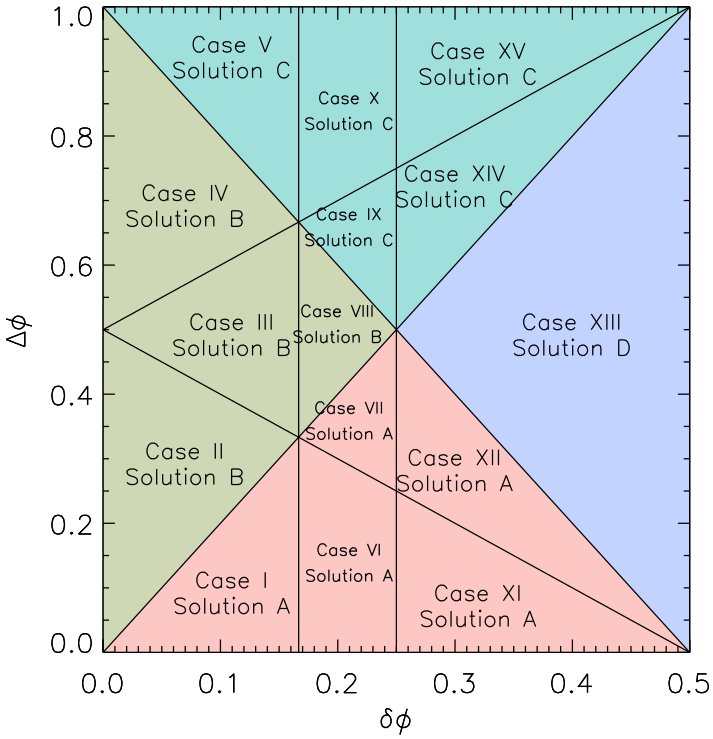


**Figure 4.4:** The fifteen cases described in subsection 4.4.2, plotted as a function of the dip half-width $\delta\phi$ and the time lag in phase units $\Delta\phi$. Colors highlight the regions where each of the branches of Equation 4.10 holds.

Call this formula for $SF(\Delta t)$ "Solution A."

**Case II** $0 < \delta\phi < 1/6 \ \wedge \ 2\delta\phi < \Delta\phi < 1/2 - \delta\phi < 1/2 + \delta\phi < 1 - 2\delta\phi$

In this case the gaps $\delta\phi$ are narrow enough, and the time lag $\Delta\phi$ large enough, that at no point in the integral will both $m(\phi)$ and $m(\phi + \Delta\phi)$ be in a dip:

$$\begin{aligned} SF(\Delta t) &= \int_{-1/2}^{-\delta\phi-\Delta\phi} (0) d\phi + \int_{-\delta\phi-\Delta\phi}^{\delta\phi-\Delta\phi} \left( A \cos\left( \frac{\pi}{2} \frac{\phi + \Delta\phi}{\delta\phi} \right) \right)^2 d\phi + \int_{\delta\phi-\Delta\phi}^{-\delta\phi} (0) d\phi \\ &\quad + \int_{-\delta\phi}^{\delta\phi} \left( A \cos\left( \frac{\pi}{2} \frac{\phi}{\delta\phi} \right) \right)^2 d\phi + \int_{\delta\phi}^{1/2} (0) d\phi \\ &= 2A^2 \delta\phi \end{aligned}$$

Call this formula for $SF(\Delta t)$ "Solution B."

**Case III** $0 < \delta\phi < 1/6 \ \wedge \ 2\delta\phi < 1/2 - \delta\phi < \Delta\phi < 1/2 + \delta\phi < 1 - 2\delta\phi$

This case is identical to Case II, except that the order of integration has changed:

$$\begin{aligned} SF(\Delta t) &= \int_{-1/2}^{\delta\phi-\Delta\phi} \left( A \cos\left( \frac{\pi}{2} \frac{\phi + \Delta\phi}{\delta\phi} \right) \right)^2 d\phi + \int_{\delta\phi-\Delta\phi}^{-\delta\phi} (0) d\phi + \int_{-\delta\phi}^{\delta\phi} \left( A \cos\left( \frac{\pi}{2} \frac{\phi}{\delta\phi} \right) \right)^2 d\phi \\ &\quad + \int_{\delta\phi}^{1-\delta\phi-\Delta\phi} (0) d\phi + \int_{1-\delta\phi-\Delta\phi}^{1/2} \left( A \cos\left( \frac{\pi}{2} \frac{\phi + \Delta\phi - 1}{\delta\phi} \right) \right)^2 d\phi \\ &= 2A^2 \delta\phi \\ &= \text{Solution B} \end{aligned}$$

Note the substitution of $\phi + \Delta\phi - 1$ for $\phi + \Delta\phi$ in the final integrand to wrap the expression back into the interval $[-1/2, 1/2)$. The same expression will appear in later cases, where appropriate.

**Case IV** $0 < \delta\phi < 1/6 \ \wedge \ 2\delta\phi < 1/2 - \delta\phi < 1/2 + \delta\phi < \Delta\phi < 1 - 2\delta\phi$

This case is identical to Case II, except that the order of integration has changed:

$$\begin{aligned} SF(\Delta t) &= \int_{-1/2}^{-\delta\phi} (0) d\phi + \int_{-\delta\phi}^{\delta\phi} \left( A \cos\left( \frac{\pi}{2} \frac{\phi}{\delta\phi} \right) \right)^2 d\phi + \int_{\delta\phi}^{1-\delta\phi-\Delta\phi} (0) d\phi \\ &\quad + \int_{1-\delta\phi-\Delta\phi}^{1+\delta\phi-\Delta\phi} \left( A \cos\left( \frac{\pi}{2} \frac{\phi + \Delta\phi - 1}{\delta\phi} \right) \right)^2 d\phi + \int_{1+\delta\phi-\Delta\phi}^{1/2} (0) d\phi \\ &= 2A^2 \delta\phi \\ &= \text{Solution B} \end{aligned}$$

**Case V** $0 < \delta\phi < 1/6 \ \wedge \ 2\delta\phi < 1/2 - \delta\phi < 1/2 + \delta\phi < 1 - 2\delta\phi < \Delta\phi < 1$

This case is identical to Case IV, except that $\Delta\phi$ is now larger than the phase difference between the end of one dip and the beginning of the following dip. Therefore, there are once again values of

$\phi$ where $m(\phi)$ will be in one dip and $m(\phi+\Delta\phi)$ will be in the next dip:

$$\begin{aligned} SF(\Delta t) &= \int_{-1/2}^{-\delta\phi}(0)d\phi + \int_{-\delta\phi}^{1-\delta\phi-\Delta\phi}\left(A\cos\left(\frac{\pi}{2}\frac{\phi}{\delta\phi}\right)\right)^2 d\phi \\ &\quad + \int_{1-\delta\phi-\Delta\phi}^{\delta\phi}\left(A\cos\left(\frac{\pi}{2}\frac{\phi+\Delta\phi-1}{\delta\phi}\right) - A\cos\left(\frac{\pi}{2}\frac{\phi}{\delta\phi}\right)\right)^2 d\phi \\ &\quad + \int_{\delta\phi}^{1+\delta\phi-\Delta\phi}\left(A\cos\left(\frac{\pi}{2}\frac{\phi+\Delta\phi-1}{\delta\phi}\right)\right)^2 d\phi + \int_{1+\delta\phi-\Delta\phi}^{1/2}(0)d\phi \\ &= \frac{A^2}{\pi}\left(\pi(1-\Delta\phi-2\delta\phi)\cos\left(\frac{\pi(1-\Delta\phi)}{2\delta\phi}\right) + 2\delta\phi\left(\pi - \sin\left(\frac{\pi(1-\Delta\phi)}{2\delta\phi}\right)\right)\right) \end{aligned}$$

Call this formula for $SF(\Delta t)$ "Solution C."

**Case VI** $1/6 < \delta\phi < 1/4 \ \wedge\ 0 < \Delta\phi < 1/2 - \delta\phi < 2\delta\phi < 1 - 2\delta\phi < 1/2 + \delta\phi$

This case is identical to Case I. The time lag $\Delta\phi$ is so small that the integral doesn't "skip" any combinations of integrands:

$$\begin{aligned} SF(\Delta t) &= \int_{-1/2}^{-\delta\phi-\Delta\phi}(0)d\phi + \int_{-\delta\phi-\Delta\phi}^{-\delta\phi}\left(A\cos\left(\frac{\pi}{2}\frac{\phi+\Delta\phi}{\delta\phi}\right)\right)^2 d\phi \\ &\quad + \int_{-\delta\phi}^{\delta\phi-\Delta\phi}\left(A\cos\left(\frac{\pi}{2}\frac{\phi+\Delta\phi}{\delta\phi}\right) - A\cos\left(\frac{\pi}{2}\frac{\phi}{\delta\phi}\right)\right)^2 d\phi \\ &\quad + \int_{\delta\phi-\Delta\phi}^{\delta\phi}\left(A\cos\left(\frac{\pi}{2}\frac{\phi}{\delta\phi}\right)\right)^2 d\phi + \int_{\delta\phi}^{1/2}(0)d\phi \\ &= \frac{A^2}{\pi}\left(\pi(\Delta\phi-2\delta\phi)\cos\left(\frac{\pi\Delta\phi}{2\delta\phi}\right) + 2\delta\phi\left(\pi - \sin\left(\frac{\pi\Delta\phi}{2\delta\phi}\right)\right)\right) \\ &= \text{Solution A} \end{aligned}$$

**Case VII** $1/6 < \delta\phi < 1/4 \ \wedge\ 1/2 - \delta\phi < \Delta\phi < 2\delta\phi < 1 - 2\delta\phi < 1/2 + \delta\phi$

This case is identical to Case II, except that the order of integration has changed:

$$\begin{aligned} SF(\Delta t) &= \int_{-1/2}^{-\delta\phi}\left(A\cos\left(\frac{\pi}{2}\frac{\phi+\Delta\phi}{\delta\phi}\right)\right)^2 d\phi + \int_{-\delta\phi}^{\delta\phi-\Delta\phi}\left(A\cos\left(\frac{\pi}{2}\frac{\phi+\Delta\phi}{\delta\phi}\right) - A\cos\left(\frac{\pi}{2}\frac{\phi}{\delta\phi}\right)\right)^2 d\phi \\ &\quad + \int_{\delta\phi-\Delta\phi}^{\delta\phi}\left(A\cos\left(\frac{\pi}{2}\frac{\phi}{\delta\phi}\right)\right)^2 d\phi + \int_{\delta\phi}^{1-\delta\phi-\Delta\phi}(0)d\phi + \int_{1-\delta\phi-\Delta\phi}^{1/2}\left(A\cos\left(\frac{\pi}{2}\frac{\phi+\Delta\phi-1}{\delta\phi}\right)\right)^2 d\phi \\ &= \frac{A^2}{\pi}\left(\pi(\Delta\phi-2\delta\phi)\cos\left(\frac{\pi\Delta\phi}{2\delta\phi}\right) + 2\delta\phi\left(\pi - \sin\left(\frac{\pi\Delta\phi}{2\delta\phi}\right)\right)\right) \\ &= \text{Solution A} \end{aligned}$$

**Case VIII** $1/6 < \delta\phi < 1/4 \ \wedge\ 1/2 - \delta\phi < 2\delta\phi < \Delta\phi < 1 - 2\delta\phi < 1/2 + \delta\phi$

This case is identical to Case III. It differs from Case VII in that there is no value of $\phi$ where

$m(\phi)$ and $m(\phi+\Delta\phi)$ are both in a dip.

$$\begin{aligned} SF(\Delta t) &= \int_{-1/2}^{\delta\phi-\Delta\phi}\left(A\cos\left(\frac{\pi}{2}\frac{\phi+\Delta\phi}{\delta\phi}\right)\right)^2 d\phi + \int_{\delta\phi-\Delta\phi}^{-\delta\phi}(0)d\phi + \int_{-\delta\phi}^{\delta\phi}\left(A\cos\left(\frac{\pi}{2}\frac{\phi}{\delta\phi}\right)\right)^2 d\phi \\ &\quad + \int_{\delta\phi}^{1-\delta\phi-\Delta\phi}(0)d\phi + \int_{1-\delta\phi-\Delta\phi}^{1/2}\left(A\cos\left(\frac{\pi}{2}\frac{\phi+\Delta\phi-1}{\delta\phi}\right)\right)^2 d\phi \\ &= 2A^2\delta\phi \\ &= \text{Solution B} \end{aligned}$$

**Case IX** $1/6 < \delta\phi < 1/4 \ \wedge\ 1/2-\delta\phi < 2\delta\phi < 1-2\delta\phi < \Delta\phi < 1/2+\delta\phi$

This case differs from Case VIII in that, for some values of $\phi$, $m(\phi)$ will be in one dip and $m(\phi+\Delta\phi)$ will be in the next dip.

$$\begin{aligned} SF(\Delta t) &= \int_{-1/2}^{\delta\phi-\Delta\phi}\left(A\cos\left(\frac{\pi}{2}\frac{\phi+\Delta\phi}{\delta\phi}\right)\right)^2 d\phi + \int_{\delta\phi-\Delta\phi}^{-\delta\phi}(0)d\phi + \int_{-\delta\phi}^{1-\delta\phi-\Delta\phi}\left(A\cos\left(\frac{\pi}{2}\frac{\phi}{\delta\phi}\right)\right)^2 d\phi \\ &\quad + \int_{1-\delta\phi-\Delta\phi}^{\delta\phi}\left(A\cos\left(\frac{\pi}{2}\frac{\phi+\Delta\phi-1}{\delta\phi}\right)-A\cos\left(\frac{\pi}{2}\frac{\phi}{\delta\phi}\right)\right)^2 d\phi \\ &\quad + \int_{\delta\phi}^{1/2}\left(A\cos\left(\frac{\pi}{2}\frac{\phi+\Delta\phi-1}{\delta\phi}\right)\right)^2 d\phi \\ &= \frac{A^2}{\pi}\left(\pi(1-\Delta\phi-2\delta\phi)\cos\left(\frac{\pi(1-\Delta\phi)}{2\delta\phi}\right)+2\delta\phi\left(\pi-\sin\left(\frac{\pi(1-\Delta\phi)}{2\delta\phi}\right)\right)\right) \\ &= \text{Solution C} \end{aligned}$$

**Case X** $1/6 < \delta\phi < 1/4 \ \wedge\ 1/2-\delta\phi < 2\delta\phi < 1-2\delta\phi < 1/2+\delta\phi < \Delta\phi < 1$

This case is identical to Case V. It differs from case IX only in the order of integration:

$$\begin{aligned} SF(\Delta t) &= \int_{-1/2}^{-\delta\phi}(0)d\phi + \int_{-\delta\phi}^{1-\delta\phi-\Delta\phi}\left(A\cos\left(\frac{\pi}{2}\frac{\phi}{\delta\phi}\right)\right)^2 d\phi \\ &\quad + \int_{1-\delta\phi-\Delta\phi}^{\delta\phi}\left(A\cos\left(\frac{\pi}{2}\frac{\phi+\Delta\phi-1}{\delta\phi}\right)-A\cos\left(\frac{\pi}{2}\frac{\phi}{\delta\phi}\right)\right)^2 d\phi \\ &\quad + \int_{\delta\phi}^{1+\delta\phi-\Delta\phi}\left(A\cos\left(\frac{\pi}{2}\frac{\phi+\Delta\phi-1}{\delta\phi}\right)\right)^2 d\phi + \int_{1+\delta\phi-\Delta\phi}^{1/2}(0)d\phi \\ &= \frac{A^2}{\pi}\left(\pi(1-\Delta\phi-2\delta\phi)\cos\left(\frac{\pi(1-\Delta\phi)}{2\delta\phi}\right)+2\delta\phi\left(\pi-\sin\left(\frac{\pi(1-\Delta\phi)}{2\delta\phi}\right)\right)\right) \\ &= \text{Solution C} \end{aligned}$$

**Case XI** $1/4 < \delta\phi < 1/2 \ \wedge\ 0 < \Delta\phi < 1/2-\delta\phi < 1-2\delta\phi < 2\delta\phi < 1/2+\delta\phi$

This case is identical to Case I. The time lag $\Delta\phi$ is so small that the integral doesn't "skip" any

combinations of integrands:

$$\begin{aligned} SF(\Delta t) &= \int_{-1/2}^{-\delta\phi-\Delta\phi}(0)d\phi + \int_{-\delta\phi-\Delta\phi}^{-\delta\phi}\left(A\cos\left(\frac{\pi}{2}\frac{\phi+\Delta\phi}{\delta\phi}\right)\right)^2 d\phi \\ &\quad + \int_{-\delta\phi}^{\delta\phi-\Delta\phi}\left(A\cos\left(\frac{\pi}{2}\frac{\phi+\Delta\phi}{\delta\phi}\right) - A\cos\left(\frac{\pi}{2}\frac{\phi}{\delta\phi}\right)\right)^2 d\phi \\ &\quad + \int_{\delta\phi-\Delta\phi}^{\delta\phi}\left(A\cos\left(\frac{\pi}{2}\frac{\phi}{\delta\phi}\right)\right)^2 d\phi + \int_{\delta\phi}^{1/2}(0)d\phi \\ &= \frac{A^2}{\pi}\left(\pi(\Delta\phi-2\delta\phi)\cos\left(\frac{\pi\Delta\phi}{2\delta\phi}\right) + 2\delta\phi\left(\pi - \sin\left(\frac{\pi\Delta\phi}{2\delta\phi}\right)\right)\right) \\ &= \text{Solution A} \end{aligned}$$

**Case XII** $1/4 < \delta\phi < 1/2 \ \wedge\ 1/2 - \delta\phi < \Delta\phi < 1 - 2\delta\phi < 2\delta\phi < 1/2 + \delta\phi$

This case is identical to Case VII. It differs from case XI only in the order of integration:

$$\begin{aligned} SF(\Delta t) &= \int_{-1/2}^{-\delta\phi}\left(A\cos\left(\frac{\pi}{2}\frac{\phi+\Delta\phi}{\delta\phi}\right)\right)^2 d\phi + \int_{-\delta\phi}^{\delta\phi-\Delta\phi}\left(A\cos\left(\frac{\pi}{2}\frac{\phi+\Delta\phi}{\delta\phi}\right) - A\cos\left(\frac{\pi}{2}\frac{\phi}{\delta\phi}\right)\right)^2 d\phi \\ &\quad + \int_{\delta\phi-\Delta\phi}^{\delta\phi}\left(A\cos\left(\frac{\pi}{2}\frac{\phi}{\delta\phi}\right)\right)^2 d\phi + \int_{\delta\phi}^{1-\delta\phi-\Delta\phi}(0)d\phi + \int_{1-\delta\phi-\Delta\phi}^{1/2}\left(A\cos\left(\frac{\pi}{2}\frac{\phi+\Delta\phi-1}{\delta\phi}\right)\right)^2 d\phi \\ &= \frac{A^2}{\pi}\left(\pi(\Delta\phi-2\delta\phi)\cos\left(\frac{\pi\Delta\phi}{2\delta\phi}\right) + 2\delta\phi\left(\pi - \sin\left(\frac{\pi\Delta\phi}{2\delta\phi}\right)\right)\right) \\ &= \text{Solution A} \end{aligned}$$

**Case XIII** $1/4 < \delta\phi < 1/2 \ \wedge\ 1/2 - \delta\phi < 1 - 2\delta\phi < \Delta\phi < 2\delta\phi < 1/2 + \delta\phi$

This unique case allows $m(\phi)$ and $m(\phi+\Delta\phi)$ to simultaneously appear in a dip during two distinct intervals of $\phi$. One interval corresponds to $m(\phi)$ and $m(\phi+\Delta\phi)$ both being found within the same dip, while the other corresponds to $m(\phi)$ being in one dip and $m(\phi+\Delta\phi)$ being in the next dip.

$$\begin{aligned} SF(\Delta t) &= \int_{-1/2}^{-\delta\phi}\left(A\cos\left(\frac{\pi}{2}\frac{\phi+\Delta\phi}{\delta\phi}\right)\right)^2 d\phi + \int_{-\delta\phi}^{\delta\phi-\Delta\phi}\left(A\cos\left(\frac{\pi}{2}\frac{\phi+\Delta\phi}{\delta\phi}\right) - A\cos\left(\frac{\pi}{2}\frac{\phi}{\delta\phi}\right)\right)^2 d\phi \\ &\quad + \int_{\delta\phi-\Delta\phi}^{1-\delta\phi-\Delta\phi}\left(A\cos\left(\frac{\pi}{2}\frac{\phi}{\delta\phi}\right)\right)^2 d\phi + \int_{1-\delta\phi-\Delta\phi}^{\delta\phi}\left(A\cos\left(\frac{\pi}{2}\frac{\phi+\Delta\phi-1}{\delta\phi}\right) - A\cos\left(\frac{\pi}{2}\frac{\phi}{\delta\phi}\right)\right)^2 d\phi \\ &\quad + \int_{\delta\phi}^{1/2}\left(A\cos\left(\frac{\pi}{2}\frac{\phi+\Delta\phi-1}{\delta\phi}\right)\right)^2 d\phi \\ &= \frac{A^2}{\pi}\left(\pi(1-\Delta\phi-2\delta\phi)\cos\left(\frac{\pi(1-\Delta\phi)}{2\delta\phi}\right) + 2\delta\phi\left(\pi - \sin\left(\frac{\pi\Delta\phi}{2\delta\phi}\right) + \sin\left(\frac{\pi(1-\Delta\phi-2\delta\phi)}{2\delta\phi}\right)\right)\right. \\ &\qquad \left. + \pi(\Delta\phi-2\delta\phi)\cos\left(\frac{\pi\Delta\phi}{2\delta\phi}\right)\right) \end{aligned}$$

Call this solution for $SF(\Delta t)$ "Solution D."

**Case XIV** $1/4 < \delta\phi < 1/2 \ \wedge \ 1/2 - \delta\phi < 1 - 2\delta\phi < 2\delta\phi < \Delta\phi < 1/2 + \delta\phi$

This case is identical to Case XI. For some values of $\phi$, $m(\phi)$ will be in one dip and $m(\phi + \Delta\phi)$ will be in the next dip, but $m(\phi)$ and $m(\phi + \Delta\phi$ will never be in the same dip.

$$\begin{aligned}
SF(\Delta t) &= \int_{-1/2}^{\delta\phi-\Delta\phi} \left(A\cos\left(\frac{\pi}{2}\frac{\phi+\Delta\phi}{\delta\phi}\right)\right)^2 d\phi + \int_{\delta\phi-\Delta\phi}^{-\delta\phi}(0)d\phi + \int_{-\delta\phi}^{1-\delta\phi-\Delta\phi}\left(A\cos\left(\frac{\pi}{2}\frac{\phi}{\delta\phi}\right)\right)^2 d\phi \\
&\quad + \int_{1-\delta\phi-\Delta\phi}^{\delta\phi}\left(A\cos\left(\frac{\pi}{2}\frac{\phi+\Delta\phi-1}{\delta\phi}\right) - A\cos\left(\frac{\pi}{2}\frac{\phi}{\delta\phi}\right)\right)^2 d\phi \\
&\quad + \int_{\delta\phi}^{1/2}\left(A\cos\left(\frac{\pi}{2}\frac{\phi+\Delta\phi-1}{\delta\phi}\right)\right)^2 d\phi \\
&= \frac{A^2}{\pi}\left(\pi(1-\Delta\phi-2\delta\phi)\cos\left(\frac{\pi(1-\Delta\phi)}{2\delta\phi}\right) + 2\delta\phi\left(\pi - \sin\left(\frac{\pi(1-\Delta\phi)}{2\delta\phi}\right)\right)\right) \\
&= \text{Solution C}
\end{aligned}$$

**Case XV** $1/4 < \delta\phi < 1/2 \ \wedge \ 1/2 - \delta\phi < 1 - 2\delta\phi < 2\delta\phi < 1/2 + \delta\phi < \Delta\phi < 1$

This case is identical to Case V. It differs from case XIV only in the order of integration:

$$\begin{aligned}
SF(\Delta t) &= \int_{-1/2}^{-\delta\phi}(0)d\phi + \int_{-\delta\phi}^{1-\delta\phi-\Delta\phi}\left(A\cos\left(\frac{\pi}{2}\frac{\phi}{\delta\phi}\right)\right)^2 d\phi \\
&\quad + \int_{1-\delta\phi-\Delta\phi}^{\delta\phi}\left(A\cos\left(\frac{\pi}{2}\frac{\phi+\Delta\phi-1}{\delta\phi}\right) - A\cos\left(\frac{\pi}{2}\frac{\phi}{\delta\phi}\right)\right)^2 d\phi \\
&\quad + \int_{\delta\phi}^{1+\delta\phi-\Delta\phi}\left(A\cos\left(\frac{\pi}{2}\frac{\phi+\Delta\phi-1}{\delta\phi}\right)\right)^2 d\phi + \int_{1+\delta\phi-\Delta\phi}^{1/2}(0)d\phi \\
&= \frac{A^2}{\pi}\left(\pi(1-\Delta\phi-2\delta\phi)\cos\left(\frac{\pi(1-\Delta\phi)}{2\delta\phi}\right) + 2\delta\phi\left(\pi - \sin\left(\frac{\pi(1-\Delta\phi)}{2\delta\phi}\right)\right)\right) \\
&= \text{Solution C}
\end{aligned}$$

I summarize the fifteen cases in Figure 4.4. The four solutions appear in regions with simple boundaries, so the structure function may be written

$$SF(\Delta t) = \begin{cases}
\frac{A^2}{\pi}\left(\pi(\Delta\phi-2\delta\phi)\cos\left(\frac{\pi\Delta\phi}{2\delta\phi}\right) + 2\delta\phi\left(\pi - \sin\left(\frac{\pi\Delta\phi}{2\delta\phi}\right)\right)\right) & \text{if } \Delta\phi < 2\delta\phi \text{ and } \Delta\phi < 1-2\delta\phi \\
2A^2\delta\phi & \text{if } \Delta\phi > 2\delta\phi \text{ and } \Delta\phi < 1-2\delta\phi \\
\frac{A^2}{\pi}\left(\pi(1-\Delta\phi-2\delta\phi)\cos\left(\frac{\pi(1-\Delta\phi)}{2\delta\phi}\right)\right. & \\
\quad \left. + 2\delta\phi\left(\pi - \sin\left(\frac{\pi(1-\Delta\phi)}{2\delta\phi}\right)\right)\right) & \text{if } \Delta\phi > 2\delta\phi \text{ and } \Delta\phi > 1-2\delta\phi \\
\frac{A^2}{\pi}\left(\pi(1-\Delta\phi-2\delta\phi)\cos\left(\frac{\pi(1-\Delta\phi)}{2\delta\phi}\right)\right. & \\
\quad + 2\delta\phi\left(\pi - \sin\left(\frac{\pi\Delta\phi}{2\delta\phi}\right) + \sin\left(\frac{\pi(1-\Delta\phi-2\delta\phi)}{2\delta\phi}\right)\right) & \\
\quad \left. + \pi(\Delta\phi-2\delta\phi)\cos\left(\frac{\pi\Delta\phi}{2\delta\phi}\right)\right) & \text{if } \Delta\phi < 2\delta\phi \text{ and } \Delta\phi > 1-2\delta\phi
\end{cases} \tag{4.10}$$

where $\Delta\phi = \text{frac}\left(\frac{\omega}{2\pi}\Delta t\right)$.

The four expressions match up along the boundaries $\Delta\phi = 2\delta\phi$ and $\Delta\phi = 1 - 2\delta\phi$. If $\Delta\phi = 2\delta\phi$,

then

$$SF(\Delta t) = \begin{cases} \frac{A^2}{\pi}(2\pi\delta\phi) & \text{if } \Delta\phi < 1 - 2\delta\phi \\ 2A^2\delta\phi & \text{if } \Delta\phi < 1 - 2\delta\phi \\ \frac{A^2}{\pi}\left(\pi(1-4\delta\phi)\cos\left(\frac{\pi(1-2\delta\phi)}{2\delta\phi}\right)\right. & \\ \quad \left. + 2\delta\phi\left(\pi - \sin\left(\frac{\pi(1-2\delta\phi)}{2\delta\phi}\right)\right)\right) & \text{if } \Delta\phi > 1 - 2\delta\phi \\ \frac{A^2}{\pi}\left(\pi(1-4\delta\phi)\cos\left(\frac{\pi(1-2\delta\phi)}{2\delta\phi}\right)\right. & \\ \quad \left. + 2\delta\phi\left(\pi + \sin\left(\frac{\pi(1-2\delta\phi)}{2\delta\phi} - \pi\right)\right)\right) & \text{if } \Delta\phi > 1 - 2\delta\phi \end{cases}$$

If $\Delta\phi = 1 - 2\delta\phi$, then

$$SF(\Delta t) = \begin{cases} \frac{A^2}{\pi}\left(\pi(1-4\delta\phi)\cos\left(\frac{\pi(1-2\delta\phi)}{2\delta\phi}\right) + 2\delta\phi\left(\pi - \sin\left(\frac{\pi(1-2\delta\phi)}{2\delta\phi}\right)\right)\right) & \text{if } \Delta\phi < 2\delta\phi \\ 2A^2\delta\phi & \text{if } \Delta\phi > 2\delta\phi \\ \frac{A^2}{\pi}(2\pi\delta\phi) & \text{if } \Delta\phi > 2\delta\phi \\ \frac{A^2}{\pi}\left(2\delta\phi\left(\pi - \sin\left(\frac{\pi(1-2\delta\phi)}{2\delta\phi}\right)\right)\right. & \\ \quad \left. + \pi(1-4\delta\phi)\cos\left(\frac{\pi(1-2\delta\phi)}{2\delta\phi}\right)\right) & \text{if } \Delta\phi < 2\delta\phi \end{cases}$$

The structure function given by Equation 4.10 is shown in Figure 4.3 for $\delta\phi = 0.05$, $\delta\phi = 0.15$, and $\delta\phi = 0.30$.

The scalar timescales calculated from the structure function for an AA Tau-like lightcurve are listed in Table 4.1.

### 4.4.3 Gaussian Processes

Since the Gaussian process models differ only in their covariance function, the behavior of the structure function can be covered with a common formalism. For any random signal $M(t)$,

$$\begin{aligned} SF(\Delta t) &= E((M(t) - M(t+\Delta t))^2) \\ &= E((M(t))^2) - 2E(M(t)M(t+\Delta t)) + E((M(t+\Delta t))^2) \\ &= V(M(t)) - (E(M(t)))^2 - 2\operatorname{cov}(M(t), M(t+\Delta t)) + 2E(M(t))E(M(t+\Delta t)) \\ &\quad + V(M(t+\Delta t)) - (E(M(t+\Delta t)))^2 \end{aligned} \tag{4.11}$$

If, in addition, $M(t)$ has constant mean,

$$\begin{aligned} SF(\Delta t) &= V(M(t)) - (E(M))^2 - 2\operatorname{cov}(M(t), M(t+\Delta t)) + 2(E(M))^2 + V(M(t+\Delta t)) - (E(M))^2 \\ &= V(M(t)) - 2\operatorname{cov}(M(t), M(t+\Delta t)) + V(M(t+\Delta t)) \end{aligned} \tag{4.12}$$

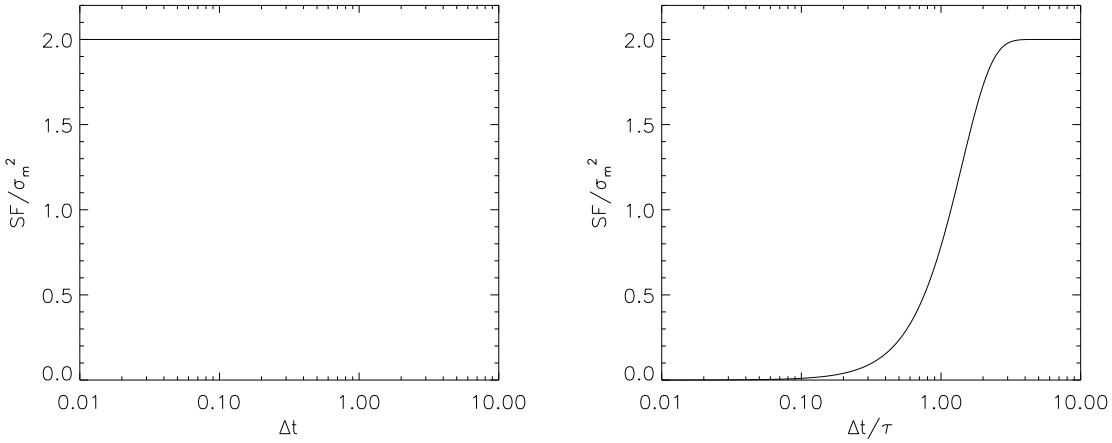


**(a)** The normalized structure function for a white noise process. The discontinuous value $SF(0) = 0$ is not shown.

**(b)** The normalized structure function for a squared exponential Gaussian process. The time is plotted in units of the coherence time, $\tau$.

**Figure 4.5**

If, in addition, $M(t)$ has constant variance,

$$\begin{aligned} SF(\Delta t) &= V(M) - 2\,\mathrm{cov}\,(M(t), M(t+\Delta t)) + V(M) \\ &= 2V(M) - 2\,\mathrm{cov}\,(M(t), M(t+\Delta t)) \\ &= 2V(M)(1 - \rho(\Delta t)) \end{aligned} \tag{4.13}$$

#### 4.4.3.1 White Noise

Substituting $\rho = \delta(t, t+\Delta t)$ into Equation 4.13,

$$SF(\Delta t) = \begin{cases} 0 & \text{if } \Delta t = 0 \\ 2\sigma_m^2 & \text{if } \Delta t \neq 0 \end{cases} \tag{4.14}$$

This function is plotted in Figure 4.5a.

The structure function crosses 1/9 amplitude$^2$ at an infinitesimal value of $\Delta t$, and never crosses 1/4 amplitude$^2$ or 1/2 amplitude$^2$.

#### 4.4.3.2 Squared Exponential Gaussian Process

Substituting $\rho = e^{-\Delta t^2/2\tau^2}$ into Equation 4.13,

$$SF(\Delta t) = 2\sigma_m^2 \left(1 - e^{-\Delta t^2/2\tau^2}\right) \tag{4.15}$$

The corresponding plot is shown in Figure 4.5b.

The scalar timescales calculated from the structure function are listed in Table 4.1.

#### 4.4.3.3 Two-Timescale Gaussian Process

Since the correlation coefficient $\rho$ has a somewhat complicated form, the variance in Equation 4.5 is easiest to use with Equation 4.12:

$$\begin{aligned} SF(\Delta t) &= \sigma_1^2 + \sigma_2^2 - 2\sigma_1^2 e^{-\Delta t^2/2\tau_1^2} - 2\sigma_2^2 e^{-\Delta t^2/2\tau_2^2} + \sigma_1^2 + \sigma_2^2 \\ &= 2\sigma_1^2 \left(1 - e^{-\Delta t^2/2\tau_1^2}\right) + 2\sigma_2^2 \left(1 - e^{-\Delta t^2/2\tau_2^2}\right) \end{aligned} \tag{4.16}$$

The corresponding plots are shown in Figure 4.6, for different regimes of $\sigma_1/\sigma_2$ and $\tau_1/\tau_2$.

The scalar timescales calculated from the structure function for a two-timescale Gaussian process are listed in Table 4.1.

#### 4.4.3.4 Damped Random Walk

Substituting $\rho = e^{-|\Delta t|/\tau}$ into Equation 4.13,

$$SF(\Delta t) = D\tau \left(1 - e^{-|\Delta t|/\tau}\right) \tag{4.17}$$

The corresponding distribution is shown in Figure 4.7a.

The scalar timescales calculated from the structure function for a damped random walk are listed in Table 4.1.

#### 4.4.3.5 Random Walk

Substituting the formulas in Equations 4.7 and 4.8 into Equation 4.11 (note that, since the variance is not constant, Equation 4.13 does not apply),

$$\begin{aligned} SF(\Delta t) &= D(t - t_0) - m_0^2 - 2D(t_1 - t_0) + 2m_0^2 + D(t + \Delta t - t_0) - m_0^2 \\ &= \begin{cases} D(t - t_0) - 2D(t - t_0) + D(t + \Delta t - t_0) & \text{if } \Delta t > 0 \\ D(t - t_0) - 2D(t + \Delta t - t_0) + D(t + \Delta t - t_0) & \text{if } \Delta t < 0 \end{cases} \\ &= \begin{cases} D(\Delta t) & \text{if } \Delta t > 0 \\ D(-\Delta t) & \text{if } \Delta t < 0 \end{cases} \\ &= D|\Delta t| \end{aligned} \tag{4.18}$$

While both the variance and the covariance of a random walk depend on the starting time $t_0$, the structure function does not. It is shown in Figure 4.7b.

While the structure function is well defined, the lightcurve amplitude grows without bound. As

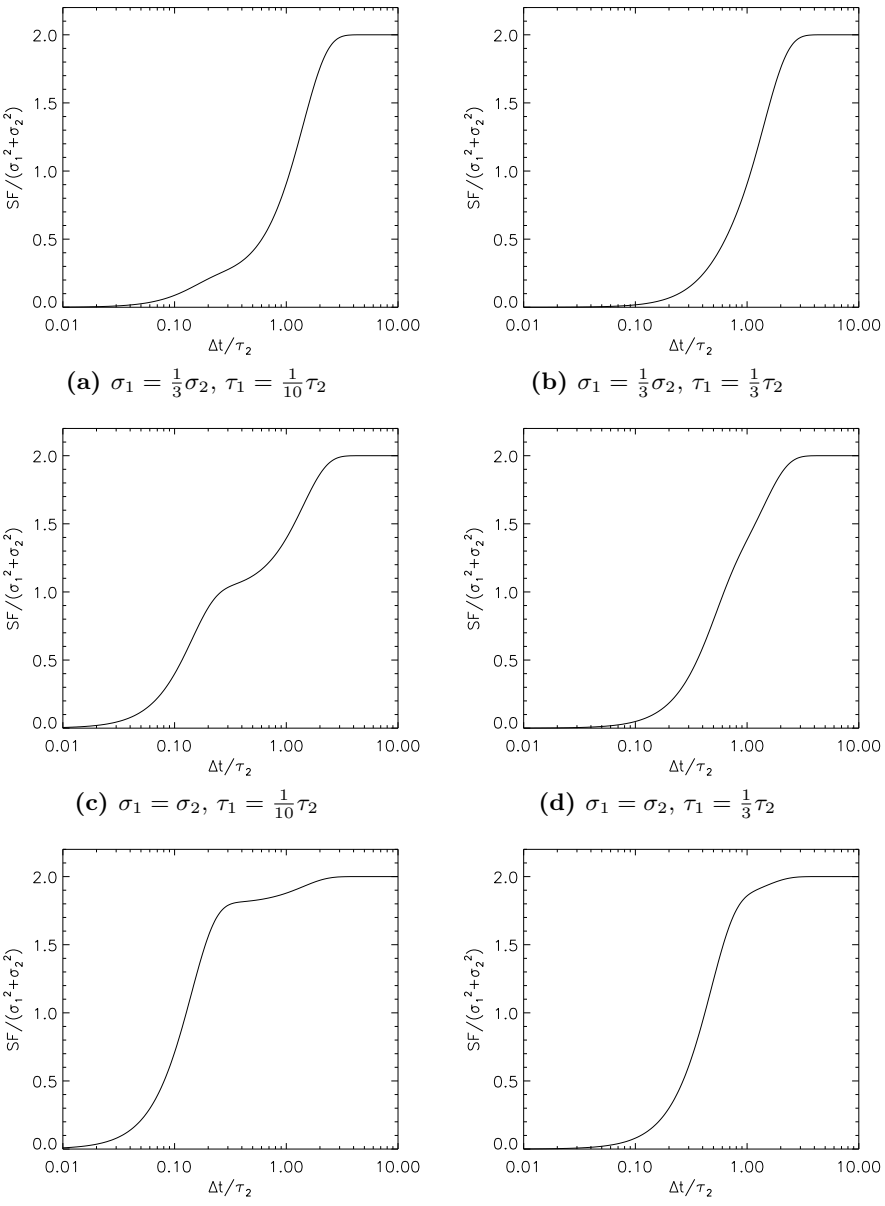


**(a)** $\sigma_1 = \frac{1}{3}\sigma_2$, $\tau_1 = \frac{1}{10}\tau_2$ **(b)** $\sigma_1 = \frac{1}{3}\sigma_2$, $\tau_1 = \frac{1}{3}\tau_2$

**(c)** $\sigma_1 = \sigma_2$, $\tau_1 = \frac{1}{10}\tau_2$ **(d)** $\sigma_1 = \sigma_2$, $\tau_1 = \frac{1}{3}\tau_2$

**(e)** $\sigma_1 = 3\sigma_2$, $\tau_1 = \frac{1}{10}\tau_2$ **(f)** $\sigma_1 = 3\sigma_2$, $\tau_1 = \frac{1}{3}\tau_2$

**Figure 4.6:** The normalized structure function for a Gaussian process with two incoherent variability components. Each panel adopts different assumptions about the relative amplitudes and timescales of the fast component (1) and the slow component (2). The time is plotted in units of the coherence time for the slower component, $\tau_2$.

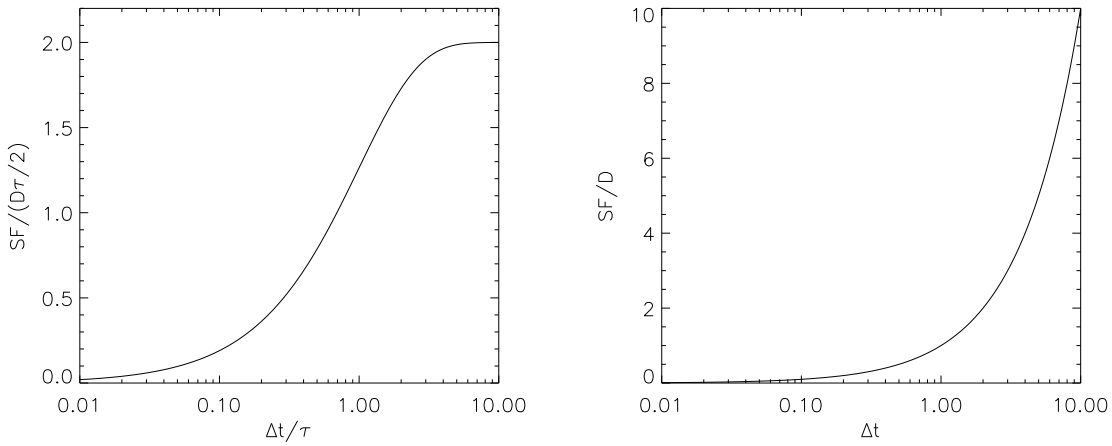


**(a)** The normalized structure function for a damped random walk. The time is plotted in units of the damping time, $\tau$.

**(b)** The normalized structure function for a random walk.

**Figure 4.7**

a result, the exercise of defining the timescale as the point where the structure function exceeds some fraction of the (infinite) amplitude squared becomes meaningless. I have no scalar timescales to present for the random walk in Table 4.1.

### 4.4.4 Summary

I present, in Table 4.1, the timescale measures for all lightcurve types considered in this section. Among the periodic variables, the ratio of the structure function timescale to the period depends strongly on the shape of the lightcurve: the timescales for AA Tau lightcurves are always lower than the corresponding timescales for sinusoidal lightcurves, and they vary strongly with the width of the dip. The structure function timescale can in principle be used to constrain the width of the dip ($2P\delta\phi$ in my notation), but without a phased lightcurve the conversion factor is known only to a factor of two, and if a phased lightcurve is available the dip width can be measured directly.

Among the aperiodic timescales, the ratio of the structure function timescale to the underlying timescale differs by 40% between the squared exponential Gaussian process and the damped random walk. If the statistical properties of the lightcurve are not known *a priori*, the uncertain lightcurve properties may introduce some systematic error into the result. As will be shown in the next chapter, this 40% systematic error is comparable to the scatter most timescale metrics face from different realizations of the same type of lightcurve, so the structure function is adequately robust to variations in lightcurve properties.

The behavior of the structure function when applied to the two-timescale Gaussian process is qualitatively reasonable – in particular, it approaches the result for a squared exponential Gaussian process when one component has a higher amplitude than the other. However, there is no indication

from the analysis that there is more than one component, or that the inferred timescale is effectively a weighted average of the two real components. While the presence of two components could be inferred from modeling the shape of the structure function (in particular, from features such as the prominent "shoulder" in the middle row of Figure 4.6), such modeling would require making assumptions about the lightcurve structure, contrary to the intent of the analysis presented here.

| Model | SF crosses $\frac{1}{9}$ amp$^2$ | SF crosses $\frac{1}{4}$ amp$^2$ | SF crosses $\frac{1}{2}$ amp$^2$ |
|---|---|---|---|
| Sinusoid | $0.154P$ | $0.246P$ | $0.450P$ |
| AA Tau (10% Dip) | $0.0425P = 0.85P\delta\phi$ | Never | Never |
| AA Tau (30% Dip) | $0.0924P = 0.616P\delta\phi$ | $0.170P = 1.133P\delta\phi$ | Never |
| AA Tau (60% Dip) | $0.127P = 0.423P\delta\phi$ | $0.206P = 0.687P\delta\phi$ | $0.359P = 1.197P\delta\phi$ |
| White Noise | 0 | Never | Never |
| Squared Exponential GP | $1.356\tau$ | Never | Never |
| Two-Timescale GP ($\sigma_1 = \frac{1}{3}\sigma_2$, $\tau_1 = \frac{1}{10}\tau_2$) | $12.759\tau_1 = 1.276\tau_2$ | Never | Never |
| Two-Timescale GP ($\sigma_1 = \frac{1}{3}\sigma_2$, $\tau_1 = \frac{1}{3}\tau_2$) | $3.828\tau_1 = 1.276\tau_2$ | Never | Never |
| Two-Timescale GP ($\sigma_1 = \sigma_2$, $\tau_1 = \frac{1}{10}\tau_2$) | $6.726\tau_1 = 0.673\tau_2$ | Never | Never |
| Two-Timescale GP ($\sigma_1 = \sigma_2$, $\tau_1 = \frac{1}{3}\tau_2$) | $2.354\tau_1 = 0.785\tau_2$ | Never | Never |
| Two-Timescale GP ($\sigma_1 = 3\sigma_2$, $\tau_1 = \frac{1}{10}\tau_2$) | $1.483\tau_1 = 0.149\tau_2$ | Never | Never |
| Two-Timescale GP ($\sigma_1 = 3\sigma_2$, $\tau_1 = \frac{1}{3}\tau_2$) | $1.460\tau_1 = 0.487\tau_2$ | Never | Never |
| Damped Random Walk | $0.919\tau$ | Never | Never |
| Random Walk | | Infinite Amplitude | |

**Table 4.1:** Trial scalar timescale measures, based on the structure function, for each of the lightcurve models introduced in section 4.2. Timescales are given in units of the period, $P$, for periodic sources and the characteristic timescale, $\tau$, for aperiodic sources. For the two-timescale Gaussian process the results are expressed in terms of both the timescale of the shorter component, $\tau_1$, and that of the longer component, $\tau_2$. For the AA Tau lightcurve the results are expressed in terms of both the period, $P$, and the half-width of the lightcurve's periodic dip, $P\delta\phi$.

## 4.5 Autocovariance Functions

Having presented, in the previous section, the behavior of structure functions for each lightcurve model introduced in section 4.2, in this section I calculate the ideal behavior of an autocovariance function for the same set of models. The autocovariance function of a random signal $M(t)$ is defined as $ACF(\Delta t) = E(M(t)M(t+\Delta t))$, and can be seen as a measure of how well the magnitude at time $t$ predicts the magnitude at time $t + \Delta t$. Absolute values close to the variance $V(M)$ mean that the magnitude at $t + \Delta t$ is tightly constrained.

The autocovariance can be related to the covariance function of $M(t)$ by:

$$\begin{aligned} ACF(\Delta t) &= E(M(t)M(t+\Delta t)) \\ &= \text{cov}\left(M(t), M(t+\Delta t)\right) + E(M(t))E(M(t+\Delta t)) \end{aligned} \tag{4.19}$$

If $M(t)$ has constant mean, then

$$ACF(\Delta t) = \text{cov}\left(M(t), M(t+\Delta t)\right) + (E(M))^2 \tag{4.20}$$

The autocovariance function can also be related to the structure function by noting that both depend on $\mathrm{cov}\,(M(t), M(t+\Delta t))$:

$$\begin{aligned} ACF(\Delta t) &= \mathrm{cov}\,(M(t), M(t+\Delta t)) + E(M(t))E(M(t+\Delta t)) \\ SF(\Delta t) &= V(M(t)) - (E(M(t)))^2 - 2\,\mathrm{cov}\,(M(t), M(t+\Delta t)) + 2E(M(t))E(M(t+\Delta t)) \\ &\quad + V(M(t+\Delta t)) - (E(M(t+\Delta t)))^2 \\ ACF(\Delta t) &= -\frac{1}{2}SF(\Delta t) + \frac{1}{2}V(M(t)) - \frac{1}{2}(E(M(t)))^2 + 2E(M(t))E(M(t+\Delta t)) \\ &\quad + \frac{1}{2}V(M(t+\Delta t)) - \frac{1}{2}(E(M(t+\Delta t)))^2 \end{aligned} \tag{4.21}$$

where I obtain the last expression by substituting for $\mathrm{cov}\,(M(t), M(t+\Delta t))$. If $M(t)$ has constant mean, then

$$ACF(\Delta t) = -\frac{1}{2}SF(\Delta t) + \frac{1}{2}V(M(t)) + E(M)^2 + \frac{1}{2}V(M(t+\Delta t)) \tag{4.22}$$

If $M(t)$ also has constant variance, then

$$ACF(\Delta t) = -\frac{1}{2}SF(\Delta t) + V(M) + E(M)^2 \tag{4.23}$$

Autocovariance has a growing presence in the literature, most often as a robust alternative to periodograms (e.g., McQuillan et al., 2013). The most popular approach to autocovariances involves taking bins of $\Delta t$ values (Edelson & Krolik, 1988), although some authors instead interpolate the lightcurve to a regular grid (e.g., McQuillan et al., 2013). Note that many papers prefer the autocorrelation function, $ACF(\Delta t)/V(M)$, to the autocovariance function, and use $ACF$ to denote autocorrelation. The analysis of this section is expressed more simply in terms of the autocovariance function, but my results for autocovariance can be converted into autocorrelation functions by normalizing by $ACF(0)$.

Autocovariance and autocorrelation functions of periodic sources tend to show a number of evenly spaced peaks at integer multiples of the period; these peaks persist even in the presence of outliers or systematic trends, which can introduce an overall slope in the ACF but do not create localized artifacts (McQuillan et al., 2013).

For aperiodic sources the ACF typically shows a smooth downward trend from perfect correlation at $\Delta t = 0$ to values near zero. Many authors have adopted the first $\Delta t$ where the ACF equals zero as a timescale measure (e.g., Abdo et al., 2010), arguing that it represents a transition from correlated to anticorrelated behavior. As I show below, for many aperiodic sources, the ACF approaches zero without crossing it, i.e., it shows a transition directly from correlated to *uncorrelated* behavior. In such cases, the location of the zero crossing may instead be dominated by noise in the ACF. A more subtle problem is that a nonzero mean in the lightcurve will introduce an offset in the ACF (note

the dependence on $m_0$ in the examples that follow). While lightcurves are normally shifted to zero mean before the ACF is calculated, any error in estimating the mean will produce a residual offset that can create the appearance of correlated and anticorrelated regions in the ACF.

I evaluate converting an autocovariance function into a scalar timescale by finding the first $\Delta t$ at which the ACF crosses one ninth, one quarter, or one half of its value at zero time lag. These values were selected on the basis of intuition: since the autocovariance has dimensions of squared magnitudes, the first two thresholds correspond to variations of one third and one half the lightcurve amplitude, respectively, while the last is midway between ACF(0) and a value of 0, which for Gaussian process models represents a long-term asymptote (i.e., two signals measured a long time apart are nearly uncorrelated).

As in the previous section, I first establish the behavior of the autocovariance function for a sinusoidal signal, then for the other lightcurve models.

### 4.5.1 Sinusoid

If $m(t) = m_0 + A\sin(\omega(t - t_0))$, then

$$\begin{aligned} ACF(\Delta t) &= E(m(t)m(t+\Delta t)) \\ &= \frac{\omega}{2\pi}\int_{t_0}^{t_0+2\pi/\omega} (m_0 + A\sin(\omega(t-t_0)))\,(m_0 + A\sin(\omega(t+\Delta t-t_0)))\,dt \end{aligned}$$

Let $x = \frac{\omega}{2\pi}(t - t_0)$ and let $\Delta x = \frac{\omega}{2\pi}\Delta t$. Then

$$\begin{aligned} ACF(\Delta t) &= \int_0^1 (m_0 + A\sin 2\pi x)\,(m_0 + A\sin(2\pi(x+\Delta x)))\,dx \\ &= m_0^2 + \frac{1}{2}A^2\cos(2\pi\Delta x) \\ &= m_0^2 + \frac{1}{2}A^2\cos(\omega\Delta t) \end{aligned} \tag{4.24}$$

The autocovariance function is shown in Figure 4.8a.

The scalar timescales calculated from the autocovariance function for a sine are listed in Table 4.2.

### 4.5.2 AA Tau

If

$$m(t) = \begin{cases} m_0 - A\cos\left(\frac{\pi}{2}\frac{\phi}{\delta\phi}\right) & \text{if } |\phi| < \delta\phi \\ m_0 & \text{otherwise} \end{cases}$$

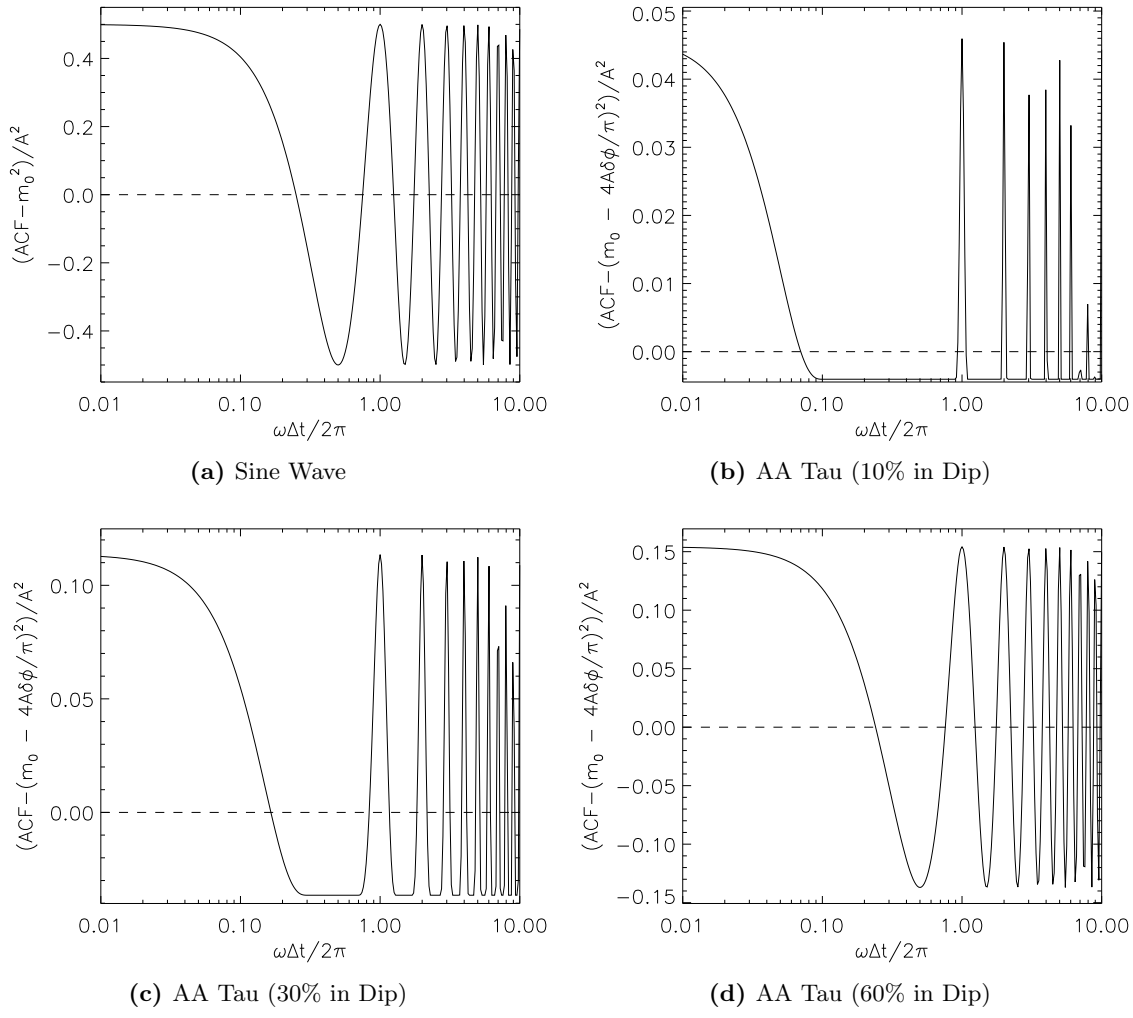


**(a)** Sine Wave

**(b)** AA Tau (10% in Dip)

**(c)** AA Tau (30% in Dip)

**(d)** AA Tau (60% in Dip)

**Figure 4.8:** Mean-subtracted and normalized autocovariance functions for a sinusoidal signal, and an AA Tau-like signal spending 10%, 30%, and 60% of each cycle in a dip ($\delta\phi = 0.05$, $\delta\phi = 0.15$, and $\delta\phi = 0.30$, respectively). For all plots, the time lag is plotted in units of the period.

then the mean and variance of the signal are:

$$\begin{aligned} E(m) &= \int_{-1/2}^{1/2} m(\phi)d\phi \\ &= m_0 - \frac{4A}{\pi}\delta\phi \\ V(m) &= \int_{-1/2}^{1/2} (m(\phi) - E(m))^2 d\phi \\ &= A^2\delta\phi\left(1 - \frac{16}{\pi^2}\delta\phi\right) \end{aligned}$$

Substituting into Equation 4.23,

$$\begin{aligned} ACF(\Delta t) &= m_0^2 - \frac{8A}{\pi}m_0\delta\phi \\ &- \begin{cases} \frac{A^2}{2\pi}\left(\pi(\Delta\phi - 2\delta\phi)\cos\left(\frac{\pi\Delta\phi}{2\delta\phi}\right) - 2\delta\phi\sin\left(\frac{\pi\Delta\phi}{2\delta\phi}\right)\right) & \text{if } \Delta\phi < 2\delta\phi \text{ and } \Delta\phi < 1 - 2\delta\phi \\ 0 & \text{if } \Delta\phi > 2\delta\phi \text{ and } \Delta\phi < 1 - 2\delta\phi \\ \frac{A^2}{2\pi}\left(\pi(1 - \Delta\phi - 2\delta\phi)\cos\left(\frac{\pi(1-\Delta\phi)}{2\delta\phi}\right)\right. & \\ \quad \left. - 2\delta\phi\sin\left(\frac{\pi(1-\Delta\phi)}{2\delta\phi}\right)\right) & \text{if } \Delta\phi > 2\delta\phi \text{ and } \Delta\phi > 1 - 2\delta\phi \\ \frac{A^2}{2\pi}\left(\pi(1 - \Delta\phi - 2\delta\phi)\cos\left(\frac{\pi(1-\Delta\phi)}{2\delta\phi}\right)\right. & \\ \quad - 2\delta\phi\left(\sin\left(\frac{\pi\Delta\phi}{2\delta\phi}\right) - \sin\left(\frac{\pi(1-\Delta\phi-2\delta\phi)}{2\delta\phi}\right)\right) & \\ \quad \left. + \pi(\Delta\phi - 2\delta\phi)\cos\left(\frac{\pi\Delta\phi}{2\delta\phi}\right)\right) & \text{if } \Delta\phi < 2\delta\phi \text{ and } \Delta\phi > 1 - 2\delta\phi \end{cases} \\ \text{where } \Delta\phi &= \text{frac}\left(\frac{\omega}{2\pi}\Delta t\right) \end{aligned} \tag{4.25}$$

The autocovariance function is shown in Figure 4.8.

The scalar timescales calculated from the autocovariance function for an AA Tau are listed in Table 4.2.

### 4.5.3 Gaussian Processes

#### 4.5.3.1 White Noise

Substituting into Equation 4.20,

$$ACF(\Delta t) = \begin{cases} \sigma_m^2 + m_0^2 & \text{if } \Delta t = 0 \\ m_0^2 & \text{if } \Delta t \neq 0 \end{cases} \tag{4.26}$$

The autocovariance function is shown in Figure 4.9.

The ACF for a white noise process falls from ACF(0) to 0 at an infinitesimal value of $\Delta t$, so the timescale is effectively 0.

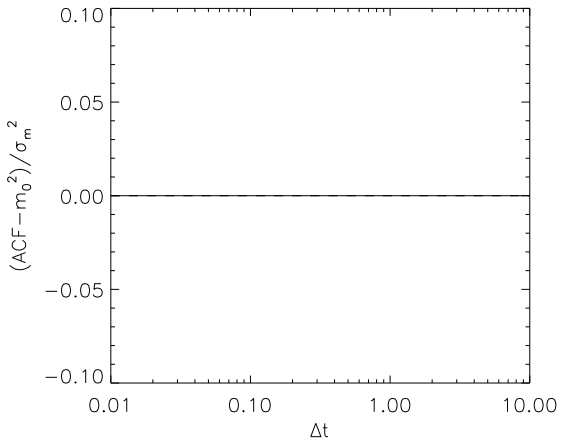


**Figure 4.9:** The mean-subtracted and normalized autocovariance function for a white noise process. The discontinuous value $ACF(0) - m_0^2 = \sigma_m^2$ is not shown.

#### 4.5.3.2 Squared Exponential Gaussian Process

Substituting into Equation 4.20,

$$ACF(\Delta t) = \sigma_m^2 e^{-(\Delta t)^2/2\tau^2} + m_0^2 \tag{4.27}$$

The autocovariance function is shown in Figure 4.10a.

The scalar timescales calculated from the autocovariance function for a squared exponential Gaussian process are listed in Table 4.2.

#### 4.5.3.3 Two-Timescale Gaussian Process

Substituting into Equation 4.20,

$$ACF(\Delta t) = \sigma_1^2 e^{-\Delta t^2/2\tau_1^2} + \sigma_2^2 e^{-\Delta t^2/2\tau_2^2} + m_0^2 \tag{4.28}$$

The autocovariance function is shown in Figure 4.11.

The scalar timescales calculated from the autocovariance function for a two-timescale Gaussian process are listed in Table 4.2.

#### 4.5.3.4 Damped Random Walk

Substituting into Equation 4.20,

$$ACF(\Delta t) = \frac{D\tau}{2} e^{-|\Delta t|/\tau} + m_0^2 \tag{4.29}$$

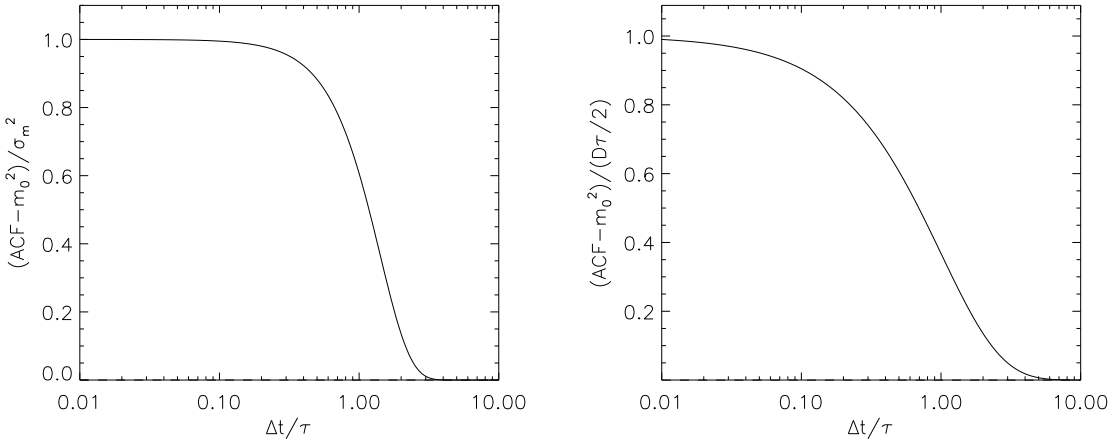


**(a)** The mean-subtracted and normalized autocovariance function for a squared exponential Gaussian process. The time is plotted in units of the coherence time, $\tau$.

**(b)** The mean-subtracted and normalized autocovariance function for a damped random walk. The time is plotted in units of the damping time, $\tau$.

**Figure 4.10**

The autocovariance function is shown in Figure 4.10b.

The scalar timescales calculated from the autocovariance function for a damped random walk are listed in Table 4.2.

#### 4.5.3.5 Random Walk

Substituting into Equation 4.20,

$$ACF(\Delta t) = D\,(t_1 - t_0) + m_0^2 \tag{4.30}$$

where $t_1$ is the smaller of the two times separated by $\Delta t$. The same formula can be derived, with a bit more work, using Equation 4.22. Since $t_1 - t_0$ grows without bound as one observes a random walk for longer periods of time, the ACF is likewise unlimited for an undamped random walk.

### 4.5.4 Summary

I present, in Table 4.2, the timescale measures for all lightcurve types considered in this section. Among the periodic variables, the ratio of the ACF timescale to the period depends strongly on the shape of the lightcurve: the timescales for AA Tau lightcurves are always lower than the corresponding timescales for sinusoidal lightcurves. The timescales appear to be set by the periodic dips, as the ratio of the ACF timescale to the width of the dip ($2P\delta\phi$ in my notation) varies by at most 40%. However, characterizing the dip with this method is an extremely roundabout way of doing so: if a source is already known to be an AA Tau analog, it must have a known period, and the dip

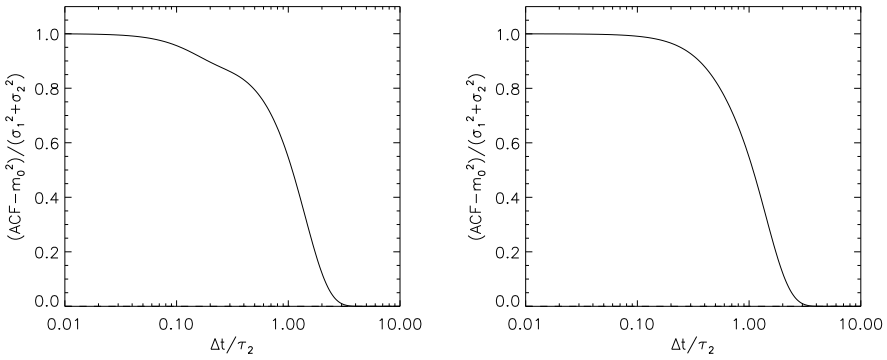


**(a)** $\sigma_1 = \frac{1}{3}\sigma_2$, $\tau_1 = \frac{1}{10}\tau_2$




**(b)** $\sigma_1 = \frac{1}{3}\sigma_2$, $\tau_1 = \frac{1}{3}\tau_2$

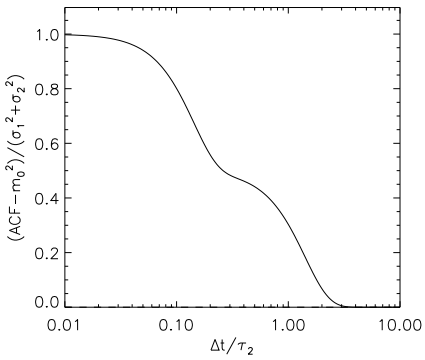


**(c)** $\sigma_1 = \sigma_2$, $\tau_1 = \frac{1}{10}\tau_2$

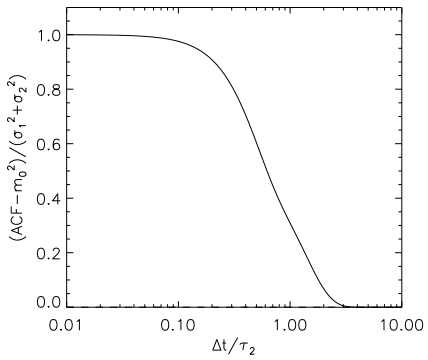


**(d)** $\sigma_1 = \sigma_2$, $\tau_1 = \frac{1}{3}\tau_2$

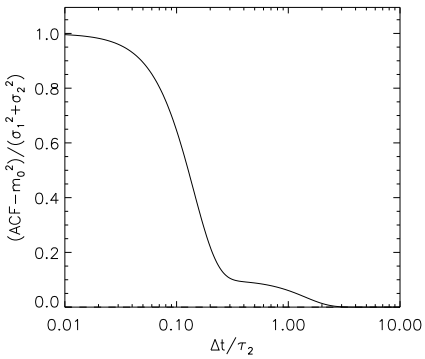


**(e)** $\sigma_1 = 3\sigma_2$, $\tau_1 = \frac{1}{10}\tau_2$

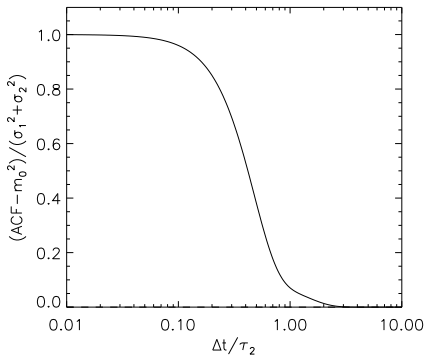


**(f)** $\sigma_1 = 3\sigma_2$, $\tau_1 = \frac{1}{3}\tau_2$

**Figure 4.11:** The mean-subtracted and normalized autocovariance function for a Gaussian process with two incoherent variability components. Each panel adopts different assumptions about the relative amplitudes and timescales of the fast component (1) and the slow component (2). The time is plotted in units of the coherence time for the slower component, $\tau_2$.

width can be measured directly from the phased lightcurve.

Among the aperiodic timescales, the ratio of the ACF timescale to the underlying timescale differs by 60% between the squared exponential Gaussian process and the damped random walk if the time at which the ACF equals half its peak is taken as the timescale; it differs by at most 20% for the lower thresholds. If the statistical properties of the lightcurve are not known *a priori*, the uncertain lightcurve properties may introduce some systematic error into the result. As will be shown in the next chapter, the scatter most timescale metrics face from different realizations of the same type of lightcurve is typically 40% or more, so a 20% systematic error is quite acceptable.

As for the structure function, the behavior of the ACF when applied to the two-timescale Gaussian process has the expected asymptotic behaviors but gives no indication that there is more than one component. Again, more detailed modeling, with specific assumptions about the lightcurve structure, would be needed to separate the components.

| Model | ACF crosses $\frac{1}{9}$ | ACF crosses $\frac{1}{4}$ | ACF crosses $\frac{1}{2}$ |
|---|---|---|---|
| Sinusoid | $0.232P$ | $0.210P$ | $0.167P$ |
| AA Tau (10% Dip) | $0.0597P = 1.194P\delta\phi$ | $0.0505P = 1.010P\delta\phi$ | $0.0371P = 0.742P\delta\phi$ |
| AA Tau (30% Dip) | $0.148P = 0.987P\delta\phi$ | $0.129P = 0.860P\delta\phi$ | $0.0979P = 0.653P\delta\phi$ |
| AA Tau (60% Dip) | $0.222P = 0.740P\delta\phi$ | $0.198P = 0.660P\delta\phi$ | $0.154P = 0.513P\delta\phi$ |
| White Noise | 0 | 0 | 0 |
| Squared Exponential GP | $2.096\tau$ | $1.665\tau$ | $1.177\tau$ |
| Two-Timescale GP ($\sigma_1 = \frac{1}{3}\sigma_2$, $\tau_1 = \frac{1}{10}\tau_2$) | $20.454\tau_1 = 2.045\tau_2$ | $16.006\tau_1 = 1.601\tau_2$ | $10.842\tau_1 = 1.084\tau_2$ |
| Two-Timescale GP ($\sigma_1 = \frac{1}{3}\sigma_2$, $\tau_1 = \frac{1}{3}\tau_2$) | $6.136\tau_1 = 2.045\tau_2$ | $4.802\tau_1 = 1.601\tau_2$ | $3.255\tau_1 = 1.085\tau_2$ |
| Two-Timescale GP ($\sigma_1 = \sigma_2$, $\tau_1 = \frac{1}{10}\tau_2$) | $17.344\tau_1 = 1.734\tau_2$ | $11.774\tau_1 = 1.177\tau_2$ | $2.607\tau_1 = 0.261\tau_2$ |
| Two-Timescale GP ($\sigma_1 = \sigma_2$, $\tau_1 = \frac{1}{3}\tau_2$) | $5.203\tau_1 = 1.734\tau_2$ | $3.542\tau_1 = 1.181\tau_2$ | $1.865\tau_1 = 0.622\tau_2$ |
| Two-Timescale GP ($\sigma_1 = 3\sigma_2$, $\tau_1 = \frac{1}{10}\tau_2$) | $2.859\tau_1 = 0.286\tau_2$ | $1.887\tau_1 = 0.189\tau_2$ | $1.272\tau_1 = 0.127\tau_2$ |
| Two-Timescale GP ($\sigma_1 = 3\sigma_2$, $\tau_1 = \frac{1}{3}\tau_2$) | $2.492\tau_1 = 0.831\tau_2$ | $1.835\tau_1 = 0.612\tau_2$ | $1.257\tau_1 = 0.419\tau_2$ |
| Damped Random Walk | $2.197\tau$ | $1.386\tau$ | $0.693\tau$ |
| Random Walk | | ACF Undefined | |

**Table 4.2:** Trial scalar timescale measures, based on the autocovariance function, for each of the lightcurve models introduced in section 4.2. Timescales are given in units of the period, $P$, for periodic sources and the characteristic timescale, $\tau$, for aperiodic sources. For the two-timescale Gaussian process the results are expressed in terms of both the timescale of the shorter component, $\tau_1$, and that of the longer component, $\tau_2$. For the AA Tau lightcurve the results are expressed in terms of both the period, $P$, and the half-width of the lightcurve's periodic dip, $P\delta\phi$.

## 4.6 $\Delta m$-$\Delta t$ Plots

In the previous two sections I studied structure functions and autocovariance functions, both well-established tools for analyzing time series data. In this section I calculate the ideal behavior of a new tool I developed, the $\Delta m$-$\Delta t$ plot, for each lightcurve model introduced in section 4.2.

The $\Delta m$-$\Delta t$ plot is a nonparametric representation of a lightcurve that describes the frequency with which a particular degree of variability is observed on a particular timescale. In some ways it resembles the self-correlation analysis of Percy et al. (2003, 2010), although it preserves more information about the lightcurve's behavior and thus allows a broader range of analysis techniques.

It is defined by pairing up all observations $m_i(t_i)$ of a lightcurve, and recording only the time and magnitude differences:

$$\begin{aligned} \Delta m_{ij} &= |m_i - m_j| \quad (i > j) \\ \Delta t_{ij} &= |t_i - t_j| \quad (i > j) \end{aligned}$$

where the restriction $i > j$ is to ensure each pair is considered only once. If the original lightcurve had $N$ data points, the corresponding $\Delta m$-$\Delta t$ plot has $N(N-1)/2$ pairs of $(\Delta t, \Delta m)$ values. The $\Delta m$-$\Delta t$ plot is closely related to the structure function, as $SF(\Delta t) = E(\Delta m^2)$.

Since the lightcurves from the PTF-NAN survey through 2012 December have up to 884 epochs, their $\Delta m$-$\Delta t$ plots may have up to 390,286 unique pairs of points. A plot with this many points is difficult to interpret, as nearly all the points simply blend together. Therefore, another layer of abstraction, such as a histogram or a density estimator, may be used to present a $\Delta m$-$\Delta t$ plot.

In general, different timescales will be sampled to different degrees by a $\Delta m$-$\Delta t$ plot. For example, consider a time series consisting of N points uniformly spaced by an interval $\delta t$. The allowed values of $\Delta t$ will have the form $\Delta t = n\delta t$, with $1 \leq n \leq N-1$, and the number of pairs with each value will be $N - n$. The shortest timescales will be by far the best-sampled, with the median value of $\Delta t$ being approximately $0.3N\delta t$ in the limit $N \gg 1$. Data gaps and other complexities can lead to other bias patterns.

Any method of analyzing $\Delta m$-$\Delta t$ plots, whether qualitative or formal, must correct for the differing number of pairs at different timescales, because the relative number of pairs at different timescales is a property of the experimental setup rather than of the source(s) being studied. At present, I am binning the pairs in $\log \Delta t$, and describing the $\Delta m$-$\Delta t$ plots in terms of summary statistics on $\Delta m$ within each time bin. This representation removes the biases associated with variable sampling, though (as with all histograms) the results will tend to converge slowly to the true distribution as the number of observations increases, and the results may be biased by changes in the $\Delta m$ distribution across the width of an individual bin. In addition, the shortest timescale bins, being the narrowest, are poorly populated, introducing sampling noise into the results.

At present I use four statistics within each $\Delta t$ bin: the 10% quantile, 50% quantile (or median), and 90% quantile of the $\Delta m$ values in each bin, and the fraction of $\Delta m$ values exceeding half the amplitude of the lightcurve. These statistics, particularly the first three, provide a reasonably good representation of how the $\Delta m$ distribution changes with timescale. The half-amplitude fraction, while easier to interpret in terms of a timescale on which the star is varying, tends to be more noisy than the $\Delta m$ quantiles.

In general, all four statistics increase monotonically with timescale. This behavior is easy to understand if the star is varying incoherently: the amount by which the star changes brightness in, for example, 100 days cannot be less than the amount by which it changes brightness in 10 days because it has had the opportunity to undergo a 10-day change within the 100-day period. In

particular, if the star has no variability mechanisms operating on timescales longer than 10 days, then the 100-day brightness change will simply be the (incoherent) sum of 10 10-day changes. A flattening in the $\Delta m$ vs. $\Delta t$ curve therefore means that all the variability occurs on shorter timescales.

In the limits of infinite observing interval, infinite cadence, and noise-free measurements, the discrete points of a $\Delta m$-$\Delta t$ plot merge into a continuous distribution: every timescale is sampled an infinite number of times, and the density of pairs is given by a probability density function $f(\Delta m; \Delta t)$. The $Q$th quantile of $\Delta m$ is the solution of $F(\Delta m; \Delta t) = Q$ for $\Delta m$ at fixed $\Delta t$, where $F$ is the cumulative distribution function. The half-amplitude fraction is simply $1 - F(\frac{1}{2}A; \Delta t)$. To allow a full range of analysis, for each trial lightcurve I find both $f(\Delta m; \Delta t)$ and $F(\Delta m; \Delta t)$.

I convert a $\Delta m$-$\Delta t$ plot into a scalar timescale by finding the first $\Delta t$ at which the median or 90% quantile crosses one third or one half of the amplitude. Both thresholds were chosen on the basis of intuition: the median should represent the "typical" variability, and the 90% quantile the "upper envelope," while either one third or one half the total amplitude is a plausible definition of significant variability. The high-amplitude fraction is redundant with the quantiles in this analysis: the time at which $Q$ of the pairs of $\Delta m$ values exceed $F$ of the amplitude, where $Q$ and $F$ are arbitrary fractions, is the time at which the $(1 - Q)$ quantile equals $F$ of the amplitude.

As in the previous two sections, I first compute the $\Delta m$-$\Delta t$ plot for a simple sinusoidal signal, then consider more complex lightcurve models.

### 4.6.1 Sinusoid

If $m(t) = m_0 + A \sin(\omega(t - t_0))$, then

$$\begin{aligned} |\Delta m| &= |A \sin(\omega(t_j - t_0)) - A \sin(\omega(t_i - t_0))| \\ &= \left| 2A \cos\left(\frac{1}{2}\omega(t_i + t_j - 2t_0)\right) \sin\left(\frac{1}{2}\omega(t_j - t_i)\right) \right| \end{aligned}$$

Let $x_i = \frac{\omega}{2\pi}(t_i - t_0)$ and let $\Delta x = x_i - x_j = \frac{\omega}{2\pi}\Delta t$. Then

$$\begin{aligned} |\Delta m| &= 2A|\cos(\pi(x_i + x_j))||\sin(\pi\Delta x)| \\ &= 2A|\sin(\pi\Delta x)||\cos(\pi(2x_i - \Delta x))| \end{aligned}$$

If $\Delta t$, and therefore $\Delta x$, is held constant, the value of $\Delta m$ is determined entirely by the phase $x_i$ at which one of the points is observed. The distribution function of $\Delta m$ is therefore

$$\begin{aligned} F(|\Delta m|; \Delta t) &= P(2A|\sin(\pi\Delta x)||\cos(\pi(2x_i - \Delta x))| \le |\Delta m|) \\ &= P\left(|\cos(\pi(2x_i - \Delta x))| \le \frac{|\Delta m|}{2A|\sin(\pi\Delta x)|}\right) \end{aligned}$$

If $\frac{|\Delta m|}{2A|\sin(\pi\Delta x)|} > 1$, this probability is trivially 1. Otherwise, I note that $|\cos(\pi(2x_i - \Delta x))|$ is periodic with period 1, and that for continuous observations the phase of $x_i$ should be uniformly distributed over the interval $[0, 1)$. For convenience, I shift the phase convention, by a constant, to the interval $[\frac{1}{2}\Delta x - \frac{1}{2}, \frac{1}{2}\Delta x + \frac{1}{2})$. Then the probability becomes

$$\begin{aligned} P(|\cos(\pi(2x_i - \Delta x))| \le u; 0 \le u \le 1) &= \int_{\frac{1}{2}\Delta x - \frac{1}{2}}^{\frac{1}{2}\Delta x + \frac{1}{2}} \Theta(x_i; u) f(x_i) dx_i \\ \Theta(x_i; u) &= \begin{cases} 1 & \text{if } |\cos(\pi(2x_i - \Delta x))| \le u \\ 0 & \text{otherwise} \end{cases} \end{aligned}$$

where $f(x_i) = 1$ is the probability density function of $x_i$. Changing variables,

$$\begin{aligned} P(|\cos(\pi(2x_i - \Delta x))| \le u) &= \int_{-\frac{1}{2}}^{\frac{1}{2}} \Theta(y_i; u) f(y_i) dy_i \\ \Theta(y_i; u) &= \begin{cases} 1 & \text{if } |\cos(2\pi y_i)| \le u \\ 0 & \text{otherwise} \end{cases} \end{aligned}$$

This last integral is easy to evaluate:

$$\begin{aligned} P(|\cos(\pi(2x_i - \Delta x))| \le u) &= \int_{-\frac{1}{2}}^{-\frac{1}{\pi}\cos^{-1} u} (1) f(y_i) dy_i + \int_{-\frac{1}{\pi}\cos^{-1} u}^{\frac{1}{\pi}\cos^{-1} u} (0) f(y_i) dy_i + \int_{\frac{1}{\pi}\cos^{-1} u}^{\frac{1}{2}} (1) f(y_i) dy_i \\ &= 1 - \frac{2}{\pi}\cos^{-1} u \\ &= \frac{2}{\pi}\sin^{-1} u \end{aligned}$$

Substituting for the dummy variable $u$,

$$\begin{aligned} F(|\Delta m|; \Delta t) &= P\left(|\cos(\pi(2x_i - \Delta x))| \le \frac{|\Delta m|}{2A|\sin(\pi\Delta x)|}\right) \\ &= \begin{cases} 1 & \text{if } 2A|\sin(\frac{1}{2}\omega\Delta t)| < |\Delta m| \\ \frac{2}{\pi}\sin^{-1}\left(\frac{|\Delta m|}{2A|\sin(\frac{1}{2}\omega\Delta t)|}\right) & \text{if } 0 \le |\Delta m| \le 2A|\sin(\frac{1}{2}\omega\Delta t)| \\ 0 & \text{if } |\Delta m| < 0 \end{cases} \end{aligned} \tag{4.31}$$

Differentiating to get the probability density function,

$$f(|\Delta m|; \Delta t) = \begin{cases} 0 & \text{if } 2A|\sin(\frac{1}{2}\omega\Delta t)| < |\Delta m| \\ \frac{1}{\pi A|\sin(\frac{1}{2}\omega\Delta t)|} \frac{1}{\sqrt{1 - \left(\frac{|\Delta m|}{2A|\sin(\frac{1}{2}\omega\Delta t)|}\right)^2}} & \text{if } 0 \le |\Delta m| < 2A|\sin(\frac{1}{2}\omega\Delta t)| \\ 0 & \text{if } |\Delta m| < 0 \end{cases} \tag{4.32}$$

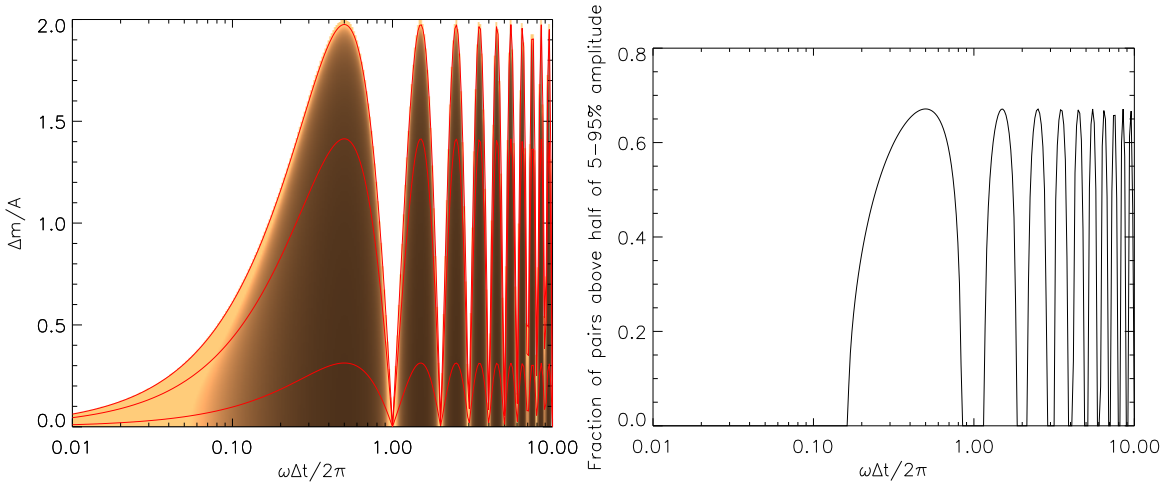


**Figure 4.12:** Normalized $\Delta m$-$\Delta t$ plot for a sinusoidal signal. The left panel shows the density function of $\Delta m$ as increasingly lighter shading, with 10th, 50th, and 90th percentiles of $\Delta m$ shown in red. The right panel shows the fraction of $\Delta m$ pairs exceeding half the amplitude. For both plots, $\Delta t$ is plotted in units of the period.

This density increases without bound as $|\Delta m|$ approaches its maximum value $2A|\sin\left(\frac{1}{2}\omega\Delta t\right)|$. The distribution of $\Delta m$ as a function of $\Delta t$ is shown in Figure 4.12, as are the corresponding quantiles and high-amplitude fractions.

The scalar timescales calculated from the $\Delta m$-$\Delta t$ plot for a sine are listed in Table 4.3.

### 4.6.2 AA Tau

If

$$m(t) = \begin{cases} m_0 - A\cos\left(\frac{\pi}{2}\frac{\phi}{\delta\phi}\right) & \text{if } |\phi| < \delta\phi \\ m_0 & \text{otherwise} \end{cases}$$

then the signed magnitude difference $\Delta m$ can assume one of four forms:

$$\Delta m = \begin{cases} m_0 - m_0 & \text{if } |\phi| > \delta\phi \ \wedge \ |\phi + \Delta\phi| > \delta\phi \\ m_0 - A\cos\left(\frac{\pi}{2}\frac{\phi}{\delta\phi}\right) - m_0 & \text{if } |\phi| < \delta\phi \ \wedge \ |\phi + \Delta\phi| > \delta\phi \\ m_0 - m_0 + A\cos\left(\frac{\pi}{2}\frac{\phi+\Delta\phi}{\delta\phi}\right) & \text{if } |\phi| > \delta\phi \ \wedge \ |\phi + \Delta\phi| < \delta\phi \\ m_0 - A\cos\left(\frac{\pi}{2}\frac{\phi}{\delta\phi}\right) - m_0 + A\cos\left(\frac{\pi}{2}\frac{\phi+\Delta\phi}{\delta\phi}\right) & \text{if } |\phi| < \delta\phi \ \wedge \ |\phi + \Delta\phi| < \delta\phi \end{cases}$$

depending on whether neither, either, or both the lightcurve at time $t$ and time $t + \Delta t$ are in a dip. Here, $\Delta\phi = \text{frac}\left(\frac{\omega}{2\pi}\Delta t\right) - \frac{1}{2} \in [-1/2, 1/2)$ is the time lag in phase units, and it is implied that $\phi$ and $\phi + \Delta\phi$ are wrapped to stay in the interval $[-1/2, 1/2)$ across the domain of each integral. Note that the phase convention for $\Delta\phi$ is different from that adopted in subsection 4.4.2, because I am no longer looking at an explicit integration problem.

The probability distribution over these four cases cannot be directly treated using symbolic

mathematics packages such as Mathematica, because the combined logic of keeping the phases straight and testing where the lightcurve is in or out of dip is too complex for them to handle. I therefore evaluate each branch of the expression for $\Delta m$ separately, and then find the probability of being in each case given $\Delta\phi$ and $\Delta\phi$. The cumulative distribution function will then be given by

$$\begin{aligned} F(|\Delta m|;|\Delta t|) = & \quad F(|\Delta m|;|\Delta t| \ \wedge \ \text{Case A})P(\text{Case A};|\Delta t|) \\ & + \quad F(|\Delta m|;|\Delta t| \ \wedge \ \text{Case B})P(\text{Case B};|\Delta t|) \\ & + \quad F(|\Delta m|;|\Delta t| \ \wedge \ \text{Case C})P(\text{Case C};|\Delta t|) \\ & + \quad F(|\Delta m|;|\Delta t| \ \wedge \ \text{Case D})P(\text{Case D};|\Delta t|) \end{aligned} \tag{4.33}$$

and the probability density function will be given by an analogous decomposition.

#### 4.6.2.1 Piecewise Probability Density and Distribution Functions

**Case A** $|\phi| > \delta\phi \ \wedge \ |\phi + \Delta\phi| < \delta\phi$

In this case, $\Delta m$ is identically 0. In terms of probability distributions,

$$f(|\Delta m|;|\Delta t| \ \wedge \ \text{Case A}) = \delta(\Delta m) \tag{4.34}$$

$$F(|\Delta m|;|\Delta t| \ \wedge \ \text{Case A}) = \begin{cases} 1 & \text{if } |\Delta m| > 0 \\ 0 & \text{if } |\Delta m| < 0 \end{cases} \tag{4.35}$$

where $\delta(x)$ denotes the Dirac delta function. Note that the cumulative distribution function $F(|\Delta m|)$ is undefined at zero.

**Case B** $|\phi| < \delta\phi \ \wedge \ |\phi + \Delta\phi| > \delta\phi$

The magnitude difference is

$$\begin{aligned} |\Delta m| &= A\left|\cos\left(\frac{\pi}{2}\frac{\phi}{\delta\phi}\right)\right| \\ &= A|\cos(\pi x)| \end{aligned}$$

where $x = \frac{\phi}{2\delta\phi} \in [-1/2, 1/2]$ measures the position of phase $\phi$ relative to the dip. Since this case assumes that $\phi + \Delta\phi$ is *not* in the dip, the allowed range of $x$ depends on the value of $\Delta x = \frac{\Delta\phi}{2\delta\phi}$. Specifically,

$$x \in \begin{cases} [-1/2, 1/2] & \text{if } |\Delta x| > 1 \\ [1/2 - \Delta x, 1/2] & \text{if } 0 < \Delta x < 1 \\ [-1/2, -1/2 - \Delta x] & \text{if } -1 < \Delta x < 0 \end{cases}$$

The cumulative distribution function for $|\Delta m|$ is therefore

$$\begin{aligned}
F(|\Delta m|; |\Delta t| \ \wedge \ \text{Case B}) &= P(A|cos(\pi x)| \leq |\Delta m|) \\
&= P(|cos(\pi x)| \leq \frac{|\Delta m|}{A}) \\
&= \begin{cases}
1 & \text{if } \frac{|\Delta m|}{A} > 1 \\
1 - \int_{-\frac{1}{\pi}\cos^{-1}|\Delta m|/A}^{\frac{1}{\pi}\cos^{-1}|\Delta m|/A} dx & \text{if } 0 < \frac{|\Delta m|}{A} < 1 \ \wedge \ |\Delta x| > 1 \\
1 - \frac{1}{\Delta x}\int_{\max\left\{-\frac{1}{\pi}\cos^{-1}|\Delta m|/A, 1/2-\Delta x\right\}}^{\max\left\{\frac{1}{\pi}\cos^{-1}|\Delta m|/A, 1/2-\Delta x\right\}} dx & \text{if } 0 < \frac{|\Delta m|}{A} < 1 \ \wedge \ 0 < \Delta x < 1 \\
1 - \frac{1}{\Delta x}\int_{\min\left\{-\frac{1}{\pi}\cos^{-1}|\Delta m|/A, -1/2-\Delta x\right\}}^{\min\left\{\frac{1}{\pi}\cos^{-1}|\Delta m|/A, -1/2-\Delta x\right\}} dx & \text{if } 0 < \frac{|\Delta m|}{A} < 1 \ \wedge \ -1 < \Delta x < 0 \\
0 & \text{if } \frac{|\Delta m|}{A} < 0
\end{cases}
\end{aligned}$$

Note that for sufficiently large $|\Delta x|$ the integrals may be over an interval of zero length. This happens when $x$ is forced to be near the edges of the dip, and $|\cos(\pi x)| \leq \frac{|\Delta m|}{A}$ for all allowed $x$.

Since the integrands are trivial and only the limits depend on $\Delta x$, the above equation may be integrated on a case-by-case basis to give

$$F(|\Delta m|; |\Delta t| \wedge \text{Case B}) = \begin{cases}
1 & \text{if } \frac{|\Delta m|}{A} > 1 \\
1 - \frac{2}{\pi}\cos^{-1}\left(\frac{|\Delta m|}{A}\right) & \text{if } \frac{|\Delta m|}{A} < 1 \ \wedge \ |\Delta x| > 1 \\
1 - \frac{2}{\pi|\Delta x|}\cos^{-1}\left(\frac{|\Delta m|}{A}\right) & \text{if } \sin(\pi|\Delta x|) < \frac{|\Delta m|}{A} < 1 \ \wedge \ 1/2 < |\Delta x| < 1 \\
1 & \text{if } \sin(\pi|\Delta x|) < \frac{|\Delta m|}{A} < 1 \ \wedge \ 0 < |\Delta x| < 1/2 \\
1 - \frac{1}{|\Delta x|}\left(\frac{1}{\pi}\cos^{-1}\left(\frac{|\Delta m|}{A}\right) + |\Delta x| - 1/2\right) & \text{if } 0 < \frac{|\Delta m|}{A} < \sin(\pi|\Delta x|) \ \wedge \ |\Delta x| < 1 \\
0 & \text{if } \frac{|\Delta m|}{A} < 0
\end{cases} \tag{4.36}$$

Differentiating to get the density function,

$$f(|\Delta m|; |\Delta t| \ \wedge \ \text{Case B}) = \begin{cases}
0 & \text{if } \frac{|\Delta m|}{A} > 1 \\
\frac{2}{\pi A}\frac{1}{\sqrt{1-\left(\frac{|\Delta m|}{A}\right)^2}} & \text{if } \frac{|\Delta m|}{A} < 1 \ \wedge \ |\Delta x| > 1 \\
\frac{2}{\pi A|\Delta x|}\frac{1}{\sqrt{1-\left(\frac{|\Delta m|}{A}\right)^2}} & \text{if } \sin(\pi|\Delta x|) < \frac{|\Delta m|}{A} < 1 \ \wedge \ 1/2 < |\Delta x| < 1 \\
0 & \text{if } \sin(\pi|\Delta x|) < \frac{|\Delta m|}{A} < 1 \ \wedge \ 0 < |\Delta x| < 1/2 \\
\frac{1}{\pi A|\Delta x|}\frac{1}{\sqrt{1-\left(\frac{|\Delta m|}{A}\right)^2}} & \text{if } 0 < \frac{|\Delta m|}{A} < \sin(\pi|\Delta x|) \ \wedge \ |\Delta x| < 1 \\
0 & \text{if } \frac{|\Delta m|}{A} < 0
\end{cases} \tag{4.37}$$

**Case C** $|\phi| > \delta\phi \ \wedge \ |\phi + \Delta\phi| < \delta\phi$

Since this case is Case B with $\phi$ and $(\phi + \Delta\phi)$ interchanged, the solution is the same as for Case B.

**Case D** $|\phi| < \delta\phi \ \wedge \ |\phi + \Delta\phi| < \delta\phi$

The magnitude difference is

$$\begin{aligned} |\Delta m| &= \left| A\cos\left(\frac{\pi}{2}\frac{\phi}{\delta\phi}\right) - A\cos\left(\frac{\pi}{2}\frac{\phi+\Delta\phi}{\delta\phi}\right)\right| \\ &= 2A\left|\sin\left(\frac{\pi}{4}\frac{2\phi+\Delta\phi}{\delta\phi}\right)\right|\left|\sin\left(\frac{\pi}{4}\frac{\Delta\phi}{\delta\phi}\right)\right| \\ &= 2A\left|\sin\left(\frac{\pi}{2}(2x+\Delta x)\right)\right|\left|\sin\left(\frac{\pi}{2}\Delta x\right)\right| \end{aligned}$$

where, as before, $x = \frac{\phi}{2\delta\phi} \in [-1/2, 1/2]$ and $\Delta x = \frac{\Delta\phi}{2\delta\phi}$. The values of $x$ allowed by the constraint that both $x$ and $x + \Delta x$ fall in the dip are

$$x \in \begin{cases} [\Delta x - 1/2, 1/2] & \text{if } 0 < \Delta x < 1 \\ [-1/2, \Delta x + 1/2] & \text{if } -1 < \Delta x < 0 \end{cases}$$

The case $|\Delta x| > 1$ is incompatible with the assumption that both $x$ and $x + \Delta x$ are in the dip, since the dip has width 1 in the units of $x$ and $\Delta x$.

It follows that the expression $\frac{1}{2}(2x + \Delta x)$ that appears in the expression for $|\Delta m|$ falls in the range

$$\frac{1}{2}(2x+\Delta x) \in \begin{cases} [\frac{1}{2}\Delta x - \frac{1}{2}, \frac{1}{2} - \frac{1}{2}\Delta x] & \text{if } 0 < \Delta x < 1 \\ [-\frac{1}{2} - \frac{1}{2}\Delta x, \frac{1}{2}\Delta x + \frac{1}{2}] & \text{if } -1 < \Delta x < 0 \end{cases}$$

The cumulative distribution function for $|\Delta m|$ is therefore

$$\begin{aligned} F(|\Delta m|; |\Delta t| \ \wedge \ \text{Case D}) &= P\left(2A\left|\sin\left(\frac{\pi}{2}(2x+\Delta x)\right)\right|\left|\sin\left(\frac{\pi}{2}\Delta x\right)\right| \le |\Delta m|\right) \\ &= P\left(\left|\sin\left(\frac{\pi}{2}(2x+\Delta x)\right)\right| \le \frac{|\Delta m|}{2A\left|\sin\left(\frac{\pi}{2}\Delta x\right)\right|}\right) \\ &= P\left(|\sin(\pi y)| \le u\right) \\ &= \begin{cases} \frac{1}{1-\Delta x}\int_{\max\left\{-\frac{1}{\pi}\sin^{-1}u, \frac{1}{2}\Delta x - \frac{1}{2}\right\}}^{\min\left\{\frac{1}{\pi}\sin^{-1}u, \frac{1}{2}-\frac{1}{2}\Delta x\right\}} dy & \text{if } 0 < \Delta x < 1 \\ \frac{1}{1+\Delta x}\int_{\max\left\{-\frac{1}{\pi}\sin^{-1}u, -\frac{1}{2}\Delta x - \frac{1}{2}\right\}}^{\min\left\{\frac{1}{\pi}\sin^{-1}u, \frac{1}{2}-\frac{1}{2}\Delta x\right\}} dy & \text{if } -1 < \Delta x < 0 \end{cases} \end{aligned}$$

Since the integrands are trivial and only the limits depend on $\Delta x$, the above equation may be integrated on a case-by-case basis to give

$$F(|\Delta m|; |\Delta t| \wedge \text{Case D}) = \begin{cases} 1 & \text{if } \frac{|\Delta m|}{2A\left|\sin\left(\frac{\pi}{2}\Delta x\right)\right|} > \sin\left(\frac{\pi}{2} - \frac{\pi}{2}|\Delta x|\right) \\ \frac{2}{\pi(1-|\Delta x|)}\sin^{-1}\left(\frac{|\Delta m|}{2A\left|\sin\left(\frac{\pi}{2}\Delta x\right)\right|}\right) & \text{if } 0 < \frac{|\Delta m|}{2A\left|\sin\left(\frac{\pi}{2}\Delta x\right)\right|} < \sin\left(\frac{\pi}{2} - \frac{\pi}{2}|\Delta x|\right) \\ 0 & \text{if } \frac{|\Delta m|}{2A\left|\sin\left(\frac{\pi}{2}\Delta x\right)\right|} < 0 \end{cases} \tag{4.38}$$

Differentiating to get the density function,

$$f(|\Delta m|; |\Delta t| \wedge \text{Case D}) = \begin{cases} 0 & \text{if } \frac{|\Delta m|}{2A\left|\sin\left(\frac{\pi}{2}\Delta x\right)\right|} > \sin\left(\frac{\pi}{2} - \frac{\pi}{2}|\Delta x|\right) \\ \frac{1}{\pi(1-|\Delta x|)A\left|\sin\left(\frac{\pi}{2}\Delta x\right)\right|} \frac{1}{\sqrt{1-\left(\frac{|\Delta m|}{2A\left|\sin\left(\frac{\pi}{2}\Delta x\right)\right|}\right)^2}} & \text{if } 0 < \frac{|\Delta m|}{2A\left|\sin\left(\frac{\pi}{2}\Delta x\right)\right|} < \sin\left(\frac{\pi}{2} - \frac{\pi}{2}|\Delta x|\right) \\ 0 & \text{if } \frac{|\Delta m|}{2A\left|\sin\left(\frac{\pi}{2}\Delta x\right)\right|} < 0 \end{cases} \tag{4.39}$$

#### 4.6.2.2 Probabilities of the Cases

In general, the probabilities of the four cases in Equation 4.33 depend on the values of $\delta\phi$, the half-width of the dip, and $\Delta\phi$, the time lag. For a given lightcurve shape, i.e., a fixed $\delta\phi$, there are six values of $\Delta\phi$ where the probabilities may change discontinuously:

- if $|\Delta\phi| = 2\delta\phi$, then when one of $m(\phi)$ and $m(\phi + \Delta\phi)$ is at the beginning of a dip the other will be at the end. For smaller values of $\Delta\phi$ it is possible for $m(\phi)$ and $m(\phi + \Delta\phi)$ to both be in the same dip at the same value of $\phi$, while for larger values it is not.
- if $|\Delta\phi| = 1 - 2\delta\phi$, then when one of $m(\phi)$ and $m(\phi + \Delta\phi)$ is at the end of a dip the other will be at the beginning of the next dip. For larger values of $\Delta\phi$ it is possible for $m(\phi)$ and $m(\phi + \Delta\phi)$ to both be in a dip at the same value of $\phi$, while for smaller values it is not.
- if $|\Delta\phi| = 1/2 - \delta\phi$, then when one of $m(\phi)$ and $(\phi + \Delta\phi)$ is at the end of a dip the other reaches $\pm 1/2$ and needs to be wrapped around. For larger $\Delta\phi$ the wraparound occurs while one function is in the dip, while for smaller $\Delta\phi$ the wraparound occurs while neither function is in a dip. The complementary case, $|\Delta\phi| = 1/2 + \delta\phi$, does not occur for $\Delta\phi \in [-1/2, 1/2)$.

These six critical values of $\Delta\phi$ divide the parameter space into five different cases, as illustrated in Figure 4.13a.

**Case I** $\quad |\Delta\phi| < 2\delta\phi \ \wedge \ |\Delta\phi| < 1/2 - \delta\phi$

This situation is shown in Figure 4.13b, where the diagonal line — the set of allowed combinations of $\phi$ and $\phi + \Delta\phi$ — can find itself in any of the four cases A-D. Noting that the intercept of the

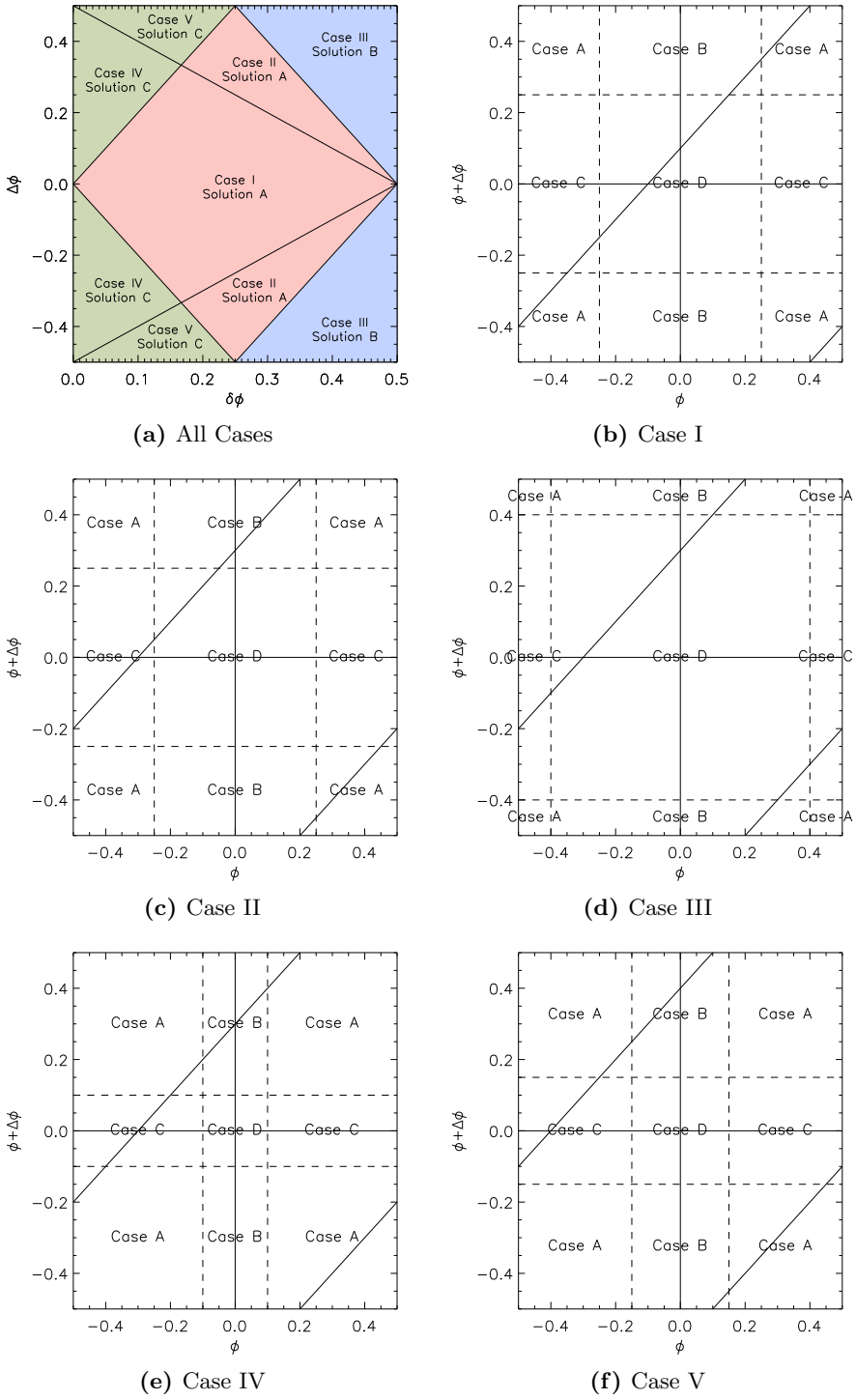


**(a)** All Cases

**(b)** Case I

**(c)** Case II

**(d)** Case III

**(e)** Case IV

**(f)** Case V

**Figure 4.13:** a): the five cases described in subsubsection 4.6.2.2, plotted as a function of the dip half-width $\delta\phi$ and the time lag in phase units $\Delta\phi$. Colors highlight the regions where each of the branches of Equation 4.33 holds. Other panels: plots of the allowed combinations of $\phi$ and $\phi + \Delta\phi$ over the course of a full period. Dashed lines are at $\pm\delta\phi$, and divide cases A, B, C, and D (see subsubsection 4.6.2.1) from each other.

diagonal line is $\Delta\phi$, the fraction of phases spent in each case is:

$$\begin{aligned} P(\text{Case A}; |\Delta t|) &= 1 - 2\delta\phi - \Delta\phi \\ P(\text{Case B}; |\Delta t|) &= \Delta\phi \\ P(\text{Case C}; |\Delta t|) &= \Delta\phi \\ P(\text{Case D}; |\Delta t|) &= 2\delta\phi - \Delta\phi \end{aligned}$$

Call these probabilities "Solution A."

**Case II** $|\Delta\phi| < 2\delta\phi \ \wedge \ 1/2 - \delta\phi < |\Delta\phi| < 1 - 2\delta\phi$

This situation, shown in Figure 4.13c, differs from Case I only in the location of the phase wraparound relative to the boundaries between Cases A, B, and C. The fraction of phases spent in each case is:

$$\begin{aligned} P(\text{Case A}; |\Delta t|) &= 1 - 2\delta\phi - \Delta\phi \\ P(\text{Case B}; |\Delta t|) &= \Delta\phi \\ P(\text{Case C}; |\Delta t|) &= \Delta\phi \\ P(\text{Case D}; |\Delta t|) &= 2\delta\phi - \Delta\phi \end{aligned}$$

These are also Solution A.

**Case III** $|\Delta\phi| < 2\delta\phi \ \wedge \ 1 - 2\delta\phi < |\Delta\phi|$

In this case, shown in Figure 4.13d, the spacing $\Delta\phi$ between the two observations is larger than the amount of time between the end of one dip and the beginning of the next. Therefore, Case A is impossible. From the plot, the probabilities can be seen to be

$$\begin{aligned} P(\text{Case A}; |\Delta t|) &= 0 \\ P(\text{Case B}; |\Delta t|) &= 1 - 2\delta\phi \\ P(\text{Case C}; |\Delta t|) &= 1 - 2\delta\phi \\ P(\text{Case D}; |\Delta t|) &= 4\delta\phi - 1 \end{aligned}$$

Call these probabilities "Solution B."

**Case IV** $|\Delta\phi| > 2\delta\phi \ \wedge \ |\Delta\phi| < 1/2 - \delta\phi$

In this case, shown in Figure 4.13d, the spacing $\Delta\phi$ between the two observations is larger than the width of the dip. Therefore, Case D is impossible. From the plot, the probabilities can be seen to be

$$\begin{aligned} P(\text{Case A}; |\Delta t|) &= 1 - 4\delta\phi \\ P(\text{Case B}; |\Delta t|) &= 2\delta\phi \\ P(\text{Case C}; |\Delta t|) &= 2\delta\phi \\ P(\text{Case D}; |\Delta t|) &= 0 \end{aligned}$$

Call these probabilities "Solution C."

**Case V** $|\Delta\phi| > 2\delta\phi \ \wedge \ 1/2 - \delta\phi < |\Delta\phi| < 1 - 2\delta\phi$

This situation, shown in Figure 4.13c, differs from Case IV only in the location of the phase wraparound relative to the boundaries between Cases A, B, and C. The fraction of phases spent in each case is:

$$\begin{aligned} P(\text{Case A}; |\Delta t|) &= 1 - 4\delta\phi \\ P(\text{Case B}; |\Delta t|) &= 2\delta\phi \\ P(\text{Case C}; |\Delta t|) &= 2\delta\phi \\ P(\text{Case D}; |\Delta t|) &= 0 \end{aligned}$$

These are also Solution C.

Equation 4.33 may now be used to find $F(|\Delta m|)$ and $f(|\Delta m|)$ for any value of $\Delta\phi = \text{frac}\left(\frac{\omega}{2\pi}\Delta t\right) - \frac{1}{2}$. The resulting expressions are evaluated in Figure 4.14.

The scalar timescales calculated from the $\Delta m$-$\Delta t$ plot for an AA Tau-like lightcurve are listed in Table 4.3.

### 4.6.3 Gaussian Processes

By definition, the magnitude measurements $M(t)$ sampled from a Gaussian process are jointly normally distributed random variables. Therefore, their signed difference $\Delta m$ is itself a normal

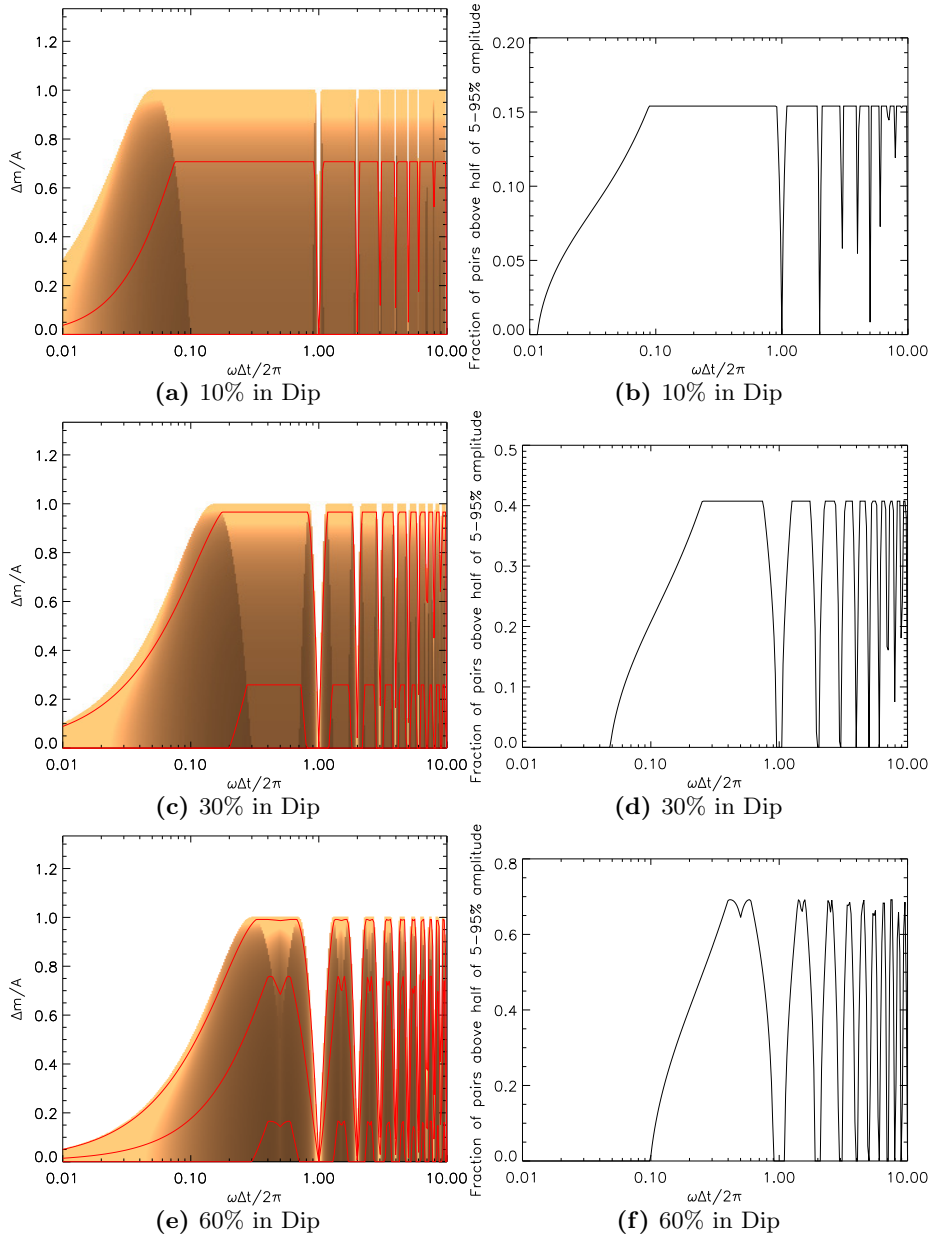


**(a)** 10% in Dip **(b)** 10% in Dip

**(c)** 30% in Dip **(d)** 30% in Dip

**(e)** 60% in Dip **(f)** 60% in Dip

**Figure 4.14:** Normalized $\Delta m$-$\Delta t$ plots for an AA Tau-like signal spending 10%, 30%, and 60% of each cycle in a dip ($\delta\phi = 0.05$, $\delta\phi = 0.15$, and $\delta\phi = 0.30$, respectively). The left panel shows the density function of $\Delta m$ as increasingly lighter shading, with 10th, 50th, and 90th percentiles of $\Delta m$ shown in red. Note that the 10th and 50th percentiles are often zero, reflecting the large number of pairs of points where both observations in the pair were taken outside a dip. The right panel shows the fraction of $\Delta m$ pairs exceeding half the amplitude. For all plots, $\Delta t$ is plotted in units of the period.

random variable with mean

$$\begin{aligned} E(\Delta m) &= E(M(t+\Delta t) - M(t)) \\ &= E(M(t+\Delta t)) - E(M(t)) \end{aligned}$$

If $M(t)$ has constant mean, then $E(\Delta m) = E(M) - E(M) = 0$.

The variance is:

$$\begin{aligned} V(\Delta m) &= E((M(t+\Delta t) - M(t))^2) - (E(M(t+\Delta t) - M(t)))^2 \\ &= E((M(t+\Delta t))^2) - 2E(M(t+\Delta t)M(t)) + E((M(t))^2) - (E(M(t+\Delta t)))^2 \\ &\quad +2E(M(t+\Delta t))E(M(t)) - (E(M(t)))^2 \\ &= V(M(t+\Delta t)) - 2\operatorname{cov}(M(t+\Delta t), M(t)) + V(M(t)) \end{aligned} \tag{4.40}$$

If $M(t)$ has constant variance, then

$$\begin{aligned} V(\Delta m) &= V(M) - 2\operatorname{cov}(M(t+\Delta t), M(t)) + V(M) \\ &= 2V(M) - 2\operatorname{cov}(M(t+\Delta t), M(t)) \\ &= 2\sigma_m^2(1 - \rho(\Delta t)) \end{aligned} \tag{4.41}$$

The absolute magnitude difference $|\Delta m|$ follows not a Gaussian distribution, but a half-Gaussian. Letting $\sigma_\Delta^2(\Delta t) = V(\Delta m(\Delta t))$, the complete probability distribution is

$$f(|\Delta m|; |\Delta t|) = \begin{cases} \frac{1}{\sigma_\Delta}\sqrt{\frac{2}{\pi}} e^{-\Delta m^2/2\sigma_\Delta^2} & \text{if } |\Delta m| \geq 0 \\ 0 & \text{if } |\Delta m| < 0 \end{cases} \tag{4.42}$$

$$F(|\Delta m|; |\Delta t|) = \begin{cases} \operatorname{erf}\left(\frac{|\Delta m|}{\sigma_\Delta \sqrt{2}}\right) & \text{if } |\Delta m| \geq 0 \\ 0 & \text{if } |\Delta m| < 0 \end{cases} \tag{4.43}$$

#### 4.6.3.1 White Noise

Substituting $\rho = \delta(t_i, t_j)$ into Equation 4.41,

$$\sigma_\Delta^2(\Delta t) = \begin{cases} 0 & \text{if } \Delta t = 0 \\ 2\sigma_m^2 & \text{if } \Delta t \neq 0 \end{cases} \tag{4.44}$$

In Figure 4.15, I show plots of Equation 4.42 and Equation 4.43 after substituting Equation 4.44.

The median value of $\Delta m$ never exceeds 1/3 or 1/2 the amplitude, while the 90% quantile crosses both thresholds at an infinitesimal value of $\Delta t$.

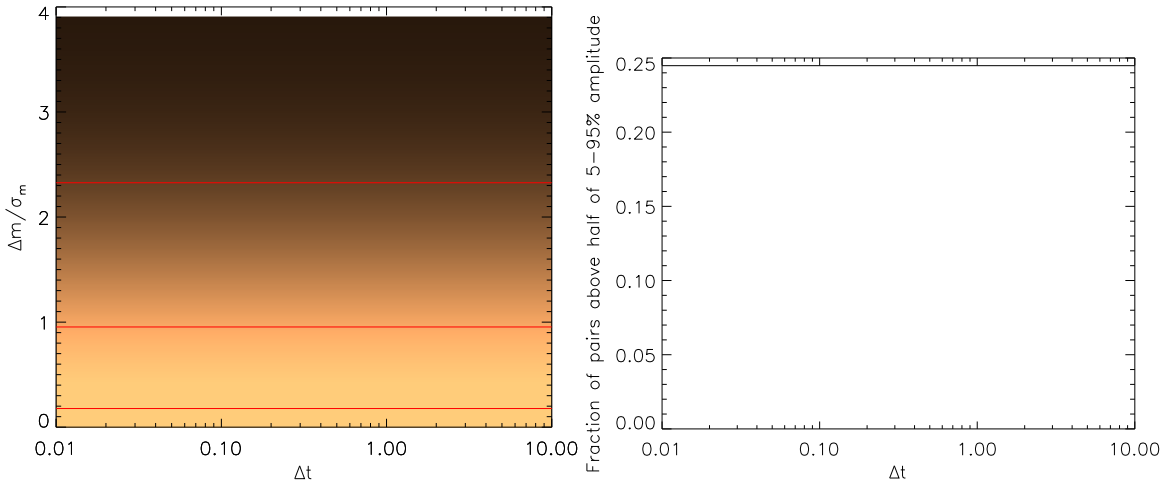


**Figure 4.15:** Normalized $\Delta m$-$\Delta t$ plot for a white noise process. The left panel shows the density function of $\Delta m$ as increasingly lighter shading, with quantiles of $\Delta m$ shown in red. The discontinuity at $\Delta t = 0$ is not shown. The right panel shows the fraction of $\Delta m$ pairs exceeding half the amplitude.

#### 4.6.3.2 Squared Exponential Gaussian Process

Substituting $\rho = e^{-\Delta t^2/2\tau^2}$ into Equation 4.41,

$$\sigma_\Delta^2(\Delta t) = 2\sigma_m^2 \left(1 - e^{-\Delta t^2/2\tau^2}\right) \tag{4.45}$$

The corresponding plots are shown in Figure 4.16. The scalar timescales calculated from the $\Delta m$-$\Delta t$ plot for a squared exponential Gaussian process are listed in Table 4.3.

#### 4.6.3.3 Two-Timescale Gaussian Process

The variance in Equation 4.5 is easiest to use with Equation 4.40:

$$\begin{aligned} \sigma_\Delta^2(\Delta t) &= \sigma_1^2 + \sigma_2^2 - 2\sigma_1^2 e^{-\Delta t^2/2\tau_1^2} + \sigma_2^2 e^{-\Delta t^2/2\tau_2^2} + \sigma_1^2 + \sigma_2^2 \\ &= 2(\sigma_1^2 + \sigma_2^2) - 2\sigma_1^2 e^{-\Delta t^2/2\tau_1^2} - 2\sigma_2^2 e^{-\Delta t^2/2\tau_2^2} \end{aligned} \tag{4.46}$$

The corresponding plots are shown in Figures 4.17 and 4.18, for different regimes of $\sigma_1/\sigma_2$ and $\tau_1/\tau_2$.

The scalar timescales calculated from the $\Delta m$-$\Delta t$ plot for a two-timescale Gaussian process are listed in Table 4.3.

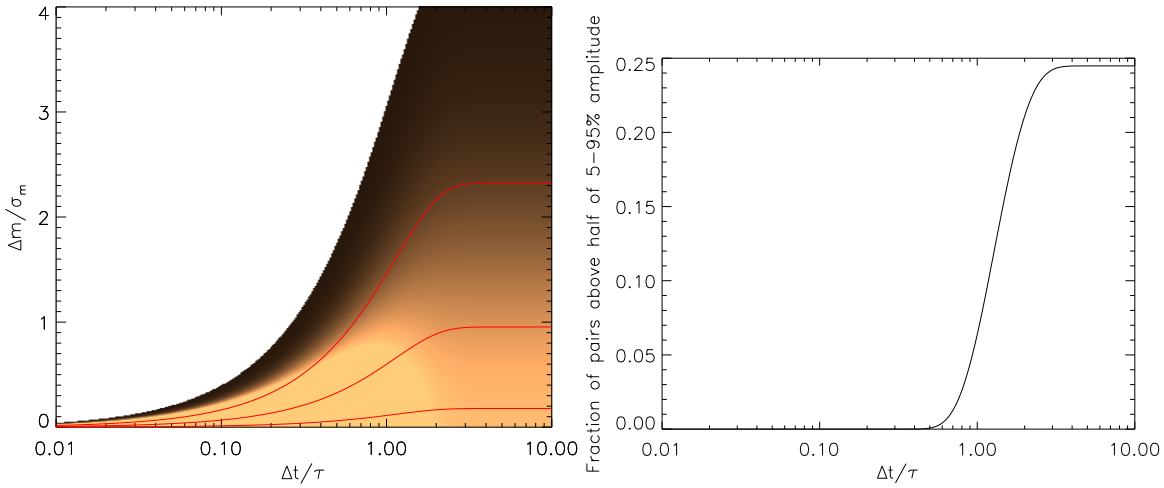


**Figure 4.16:** Normalized $\Delta m$-$\Delta t$ plot for a squared exponential Gaussian process. The left panel shows the density function of $\Delta m$ as increasingly lighter shading, with quantiles of $\Delta m$ shown in red. The right panel shows the fraction of $\Delta m$ pairs exceeding half the amplitude. For both plots, $\Delta t$ is plotted in units of the correlation time.

#### 4.6.3.4 Damped Random Walk

Substituting $\rho = e^{-|t_i - t_j|/\tau}$ into Equation 4.41,

$$\sigma^2_\Delta(\Delta t) \quad = \quad D\tau\left(1 - e^{-|\Delta t|/\tau}\right) \tag{4.47}$$

The corresponding distribution is shown in Figure 4.19. The scalar timescales calculated from the $\Delta m$-$\Delta t$ plot for a damped random walk are listed in Table 4.3.

#### 4.6.3.5 Random Walk

Substituting the formulas in Equations 4.7 and Equation 4.8 into Equation 4.40 (note that, since the variance is not constant, Equation 4.41 does not apply),

$$\begin{aligned}
\sigma^2_\Delta(\Delta t) &= D(t_i - t_0) - 2D(t_1 - t_0) + D(t_j - t_0) \\
&= \begin{cases} D(t_i - t_0) - 2D(t_i - t_0) + D(t_j - t_0) & \text{if } t_i < t_j \\ D(t_i - t_0) - 2D(t_j - t_0) + D(t_j - t_0) & \text{if } t_i > t_j \end{cases} \\
&= \begin{cases} D(t_j - t_i) & \text{if } t_i < t_j \\ D(t_i - t_j) & \text{if } t_i > t_j \end{cases} \\
&= D|\Delta t|
\end{aligned} \tag{4.48}$$

While both the variance and the covariance of a random walk depend on the starting time $t_0$, the distribution of $\Delta m$ as a function of $\Delta t$ does not. The distribution is shown in Figure 4.20.

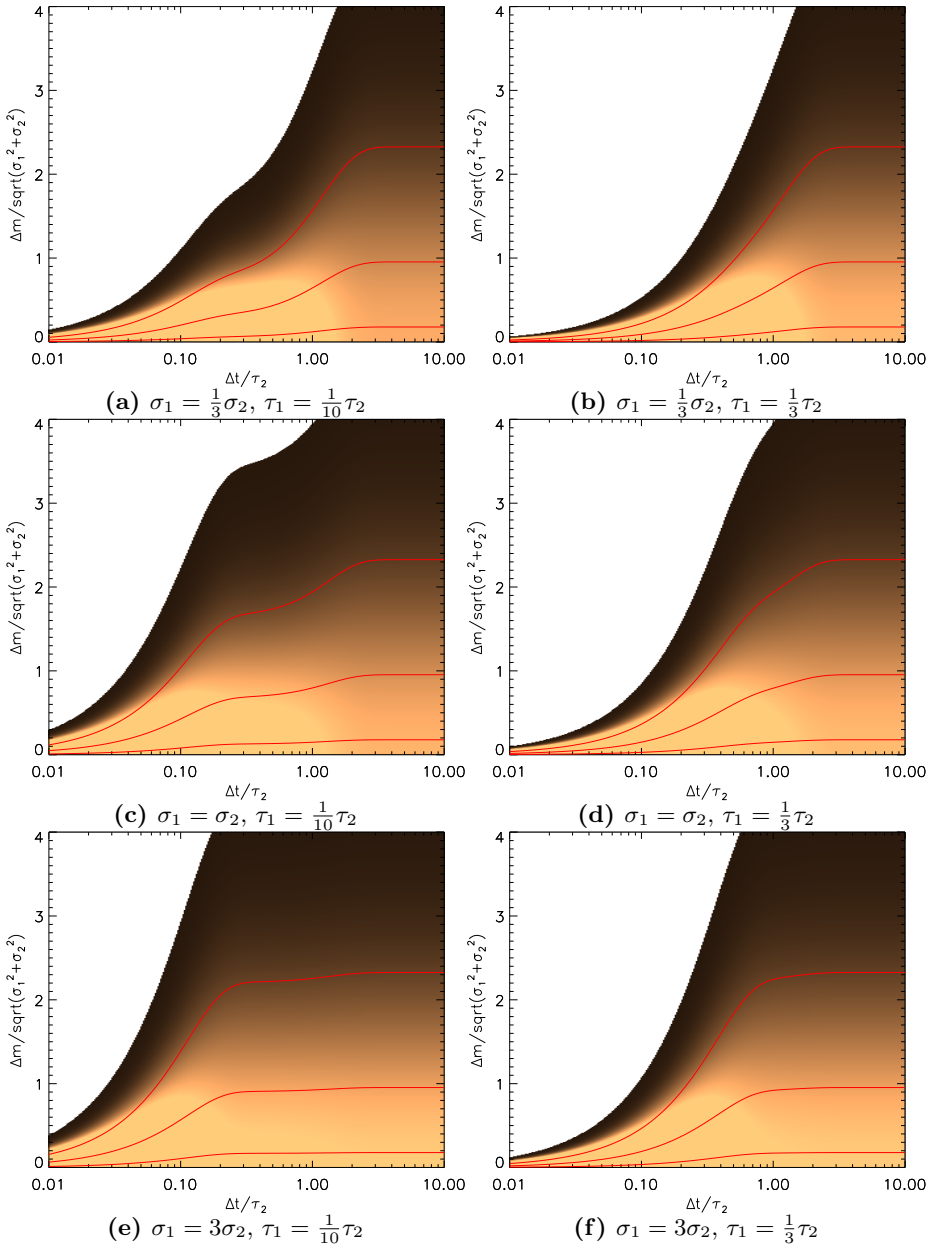


**(a)** $\sigma_1 = \frac{1}{3}\sigma_2$, $\tau_1 = \frac{1}{10}\tau_2$ **(b)** $\sigma_1 = \frac{1}{3}\sigma_2$, $\tau_1 = \frac{1}{3}\tau_2$

**(c)** $\sigma_1 = \sigma_2$, $\tau_1 = \frac{1}{10}\tau_2$ **(d)** $\sigma_1 = \sigma_2$, $\tau_1 = \frac{1}{3}\tau_2$

**(e)** $\sigma_1 = 3\sigma_2$, $\tau_1 = \frac{1}{10}\tau_2$ **(f)** $\sigma_1 = 3\sigma_2$, $\tau_1 = \frac{1}{3}\tau_2$

**Figure 4.17:** Normalized $\Delta m$-$\Delta t$ plot for a two-timescale Gaussian process. The density function of $\Delta m$ is indicated by increasingly lighter shading, with quantiles of $\Delta m$ shown in red. Each panel adopts different assumptions about the relative amplitudes and timescales of the fast component (1) and the slow component (2). The time is plotted in units of the coherence time for the slower component, $\tau_2$.

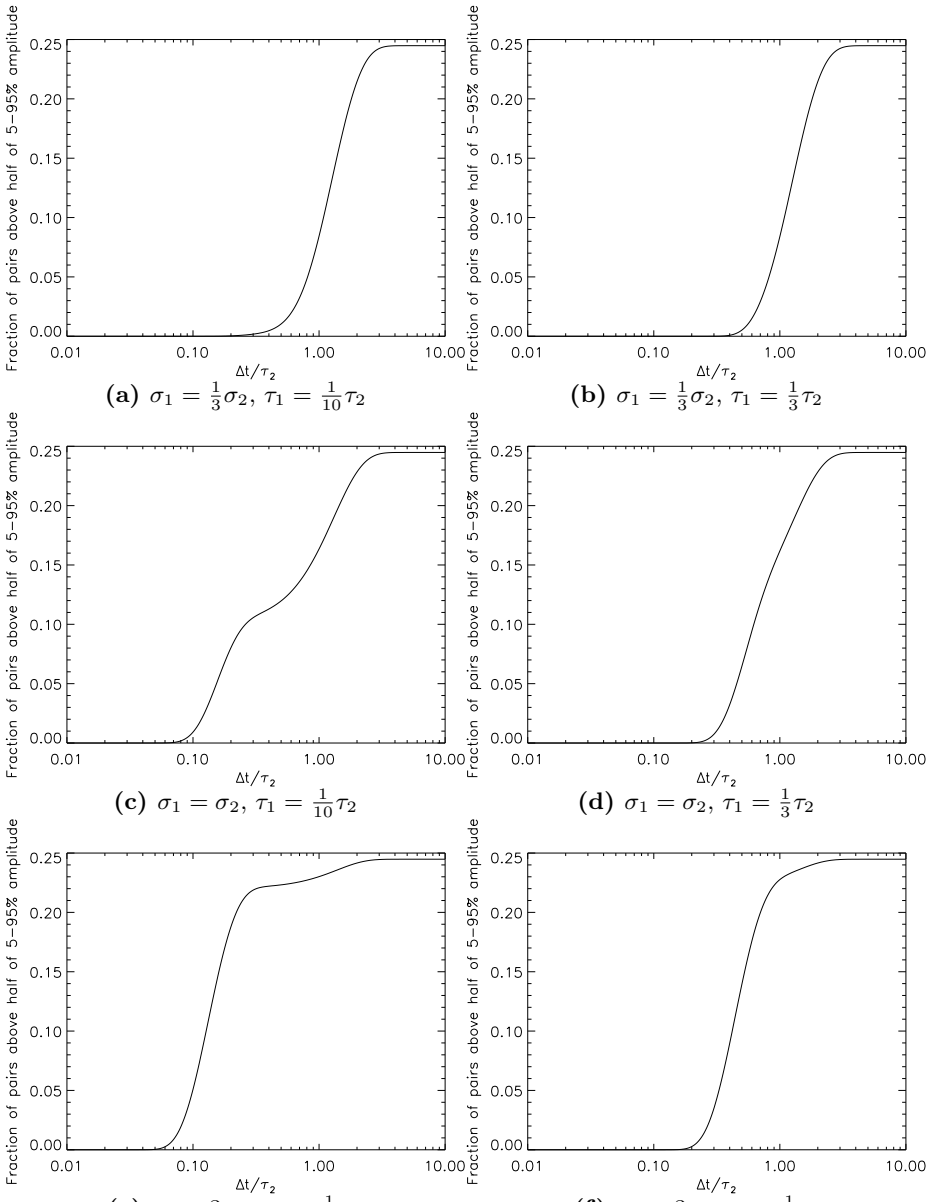


**(a)** $\sigma_1 = \frac{1}{3}\sigma_2$, $\tau_1 = \frac{1}{10}\tau_2$ **(b)** $\sigma_1 = \frac{1}{3}\sigma_2$, $\tau_1 = \frac{1}{3}\tau_2$

**(c)** $\sigma_1 = \sigma_2$, $\tau_1 = \frac{1}{10}\tau_2$ **(d)** $\sigma_1 = \sigma_2$, $\tau_1 = \frac{1}{3}\tau_2$

**(e)** $\sigma_1 = 3\sigma_2$, $\tau_1 = \frac{1}{10}\tau_2$ **(f)** $\sigma_1 = 3\sigma_2$, $\tau_1 = \frac{1}{3}\tau_2$

**Figure 4.18:** Fraction of $\Delta m$ pairs exceeding half the amplitude for a two-timescale Gaussian process. Each panel adopts different assumptions about the relative amplitudes and timescales of the fast component (1) and the slow component (2). The time is plotted in units of the coherence time for the slower component, $\tau_2$.

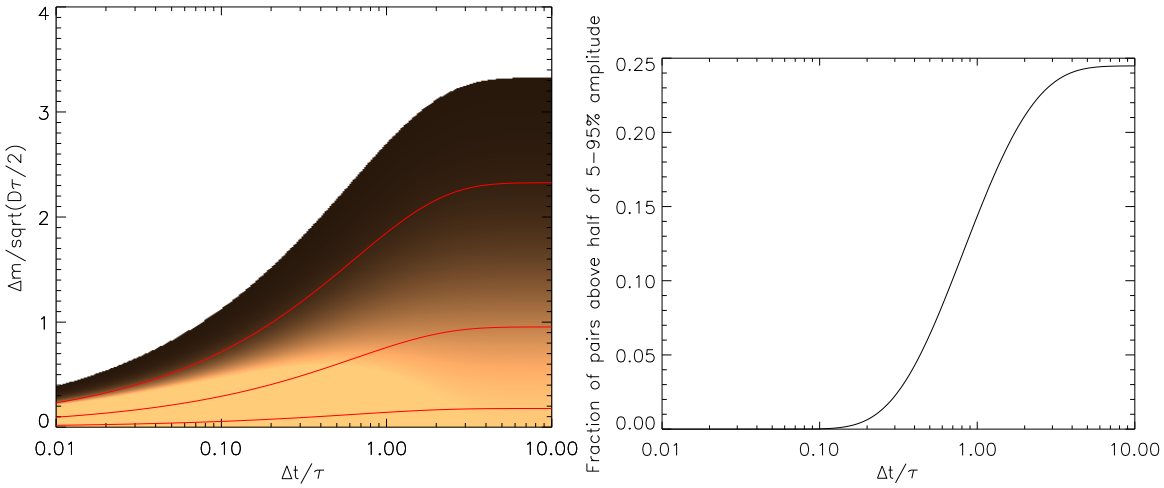


**Figure 4.19:** Normalized $\Delta m$-$\Delta t$ plot for a damped random walk. The left panel shows the density function of $\Delta m$ as increasingly lighter shading, with quantiles of $\Delta m$ shown in red. The right panel shows the fraction of $\Delta m$ pairs exceeding half the amplitude. For both plots, $\Delta t$ is plotted in units of the damping time.

While the $\Delta m$-$\Delta t$ plot is well defined, the lightcurve amplitude is not, so there is no way to set a threshold for the $\Delta m$-$\Delta t$ quantiles to cross. There is therefore no timescale associated with the $\Delta m$-$\Delta t$ analysis.

### 4.6.4 Summary

I present, in Table 4.3, the timescale measures for all lightcurve types considered in this section. Among the periodic variables, the ratio of the structure function timescale to the period depends strongly on the shape of the lightcurve: the timescales for AA Tau lightcurves are always lower than the corresponding timescales for sinusoidal lightcurves, and they vary strongly with the width of the dip. However, the timescale is not proportional to the width of the dip, and cannot be used to characterize it.

Among the aperiodic timescales, the ratio of the $\Delta m$-$\Delta t$ timescale to the underlying timescale differs by a factor of two to three between the squared exponential Gaussian process and the damped random walk. If the statistical properties of the lightcurve are not known *a priori*, the uncertain lightcurve properties may introduce a systematic error of a factor of two or more into the result.

As with the structure function and the autocovariance function, the behavior of $\Delta m$-$\Delta t$ plots when applied to the two-timescale Gaussian process has the expected asymptotic behaviors but gives no indication that there is more than one component. Again, more detailed modeling, with specific assumptions about the lightcurve structure, would be needed to separate the components.

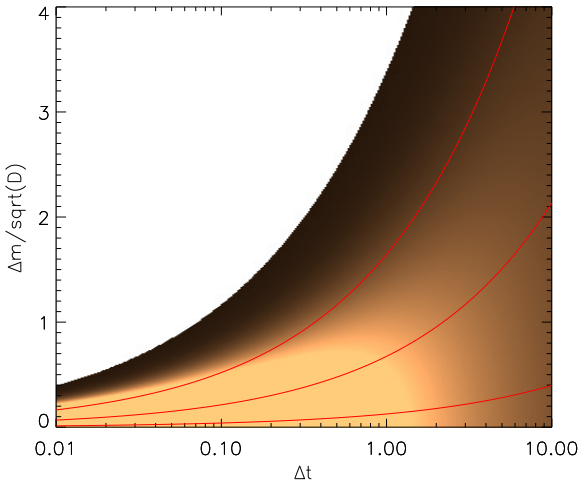


**Figure 4.20:** Normalized $\Delta m$-$\Delta t$ plot for a random walk. The density function of $\Delta m$ is indicated by increasingly lighter shading, with quantiles of $\Delta m$ shown in red.

| Model | Median crosses $\frac{1}{3}$ amp | Median crosses $\frac{1}{2}$ amp | 90% quantile crosses $\frac{1}{3}$ amp | 90% quantile crosses $\frac{1}{2}$ amp |
|---|---|---|---|---|
| Sinusoid | $0.154P$ | $0.246P$ | $0.108P$ | $0.167P$ |
| AA Tau (10% Dip) | Never | Never | $0.0312P = 0.624P\delta\phi$ | $0.0417P = 0.834P\delta\phi$ |
| AA Tau (30% Dip) | Never | Never | $0.0388P = 0.257P\delta\phi$ | $0.0616P = 0.411P\delta\phi$ |
| AA Tau (60% Dip) | $0.175P = 0.583P\delta\phi$ | $0.255P = 0.850P\delta\phi$ | $0.0694P = 0.231P\delta\phi$ | $0.109P = 0.363P\delta\phi$ |
| White Noise | Never | Never | 0 | 0 |
| Squared Exponential GP | Never | Never | $0.709\tau$ | $1.178\tau$ |
| Two-Timescale GP ($\sigma_1 = \frac{1}{3}\sigma_2$, $\tau_1 = \frac{1}{10}\tau_2$) | Never | Never | $5.403\tau_1 = 0.540\tau_2$ | $10.842\tau_1 = 1.084\tau_2$ |
| Two-Timescale GP ($\sigma_1 = \frac{1}{3}\sigma_2$, $\tau_1 = \frac{1}{3}\tau_2$) | Never | Never | $1.766\tau_1 = 0.589\tau_2$ | $3.255\tau_1 = 1.085\tau_2$ |
| Two-Timescale GP ($\sigma_1 = \sigma_2$, $\tau_1 = \frac{1}{10}\tau_2$) | Never | Never | $1.075\tau_1 = 0.107\tau_2$ | $2.607\tau_1 = 0.261\tau_2$ |
| Two-Timescale GP ($\sigma_1 = \sigma_2$, $\tau_1 = \frac{1}{3}\tau_2$) | Never | Never | $0.996\tau_1 = 0.332\tau_2$ | $1.865\tau_1 = 0.622\tau_2$ |
| Two-Timescale GP ($\sigma_1 = 3\sigma_2$, $\tau_1 = \frac{1}{10}\tau_2$) | Never | Never | $0.753\tau_1 = 0.0753\tau_2$ | $1.272\tau_1 = 0.127\tau_2$ |
| Two-Timescale GP ($\sigma_1 = 3\sigma_2$, $\tau_1 = \frac{1}{3}\tau_2$) | Never | Never | $0.747\tau_1 = 0.249\tau_2$ | $1.257\tau_1 = 0.419\tau_2$ |
| Damped Random Walk | Never | Never | $0.251\tau$ | $0.693\tau$ |
| Random Walk | Infinite Amplitude | | | |

**Table 4.3:** Trial scalar timescale measures, based on the $\Delta m$-$\Delta t$ plot, for each of the lightcurve models introduced in section 4.2. Timescales are given in units of the period, $P$, for periodic sources and the characteristic timescale, $\tau$, for aperiodic sources. For the two-timescale Gaussian process the results are expressed in terms of both the timescale of the shorter component, $\tau_1$, and that of the longer component, $\tau_2$. For the AA Tau lightcurve the results are expressed in terms of both the period, $P$, and the half-width of the lightcurve's periodic dip, $P\delta\phi$.

## 4.7 Summary of Theoretical Results

In this chapter I've tested, under highly idealized conditions, three candidate timescale metrics (structure functions, autocovariance functions, and $\Delta m$-$\Delta t$ plots) on six types of lightcurve models: a sine, a periodic "dipper" like AA Tau, a squared exponential Gaussian process, a variant of the squared exponential Gaussian process having two components with different timescales, a damped random walk, and an (undamped) random walk. By testing each timescale metric on a variety of lightcurve models, I was able to determine how well each metric adapts to different lightcurves and also ensure that the analysis was not biased by a single model on which a particular metric performs unusually well or poorly. To my knowledge, this is the first such analysis of timescale metrics, and in particular the first to attempt to characterize performance without reference to an assumed

lightcurve model.

| Criterion | Structure Function | Autocovariance Function | $\Delta m$-$\Delta t$ Plot |
|---|---|---|---|
| Universal | Yes | Yes | Yes |
| Data-driven | May require binning/interpolation | May require binning/interpolation | May require binning |
| Versatile | to $\sim 40\%$ | to $\sim 20\%$ | to factor of 2 |
| Accurate | Yes | Yes | Yes |

**Table 4.4:** Performance of three candidate timescale metrics with respect to the criteria introduced in section 4.1. An entry beginning with "May require" means that, while the timescale metric itself satisfies the criterion, a specific algorithm for calculating the metric may not.

The performance of each metric across the various lightcurves was described in detail in sections 4.4 through 4.6. A summary of the results, in terms of the criteria introduced in section 4.1, is presented in Table 4.4. All three metrics are universal, by construction. They are likewise accurate except when applied to the two lightcurve models that had more parameters than a single timescale, namely AA Tau lightcurves and two-timescale Gaussian processes. This behavior appears to be a problem with the models, rather than with the timescale metrics: the concept of "the timescale of the lightcurve" is ill-defined in the context of either model. As a result, neither model will be considered further.

The three metrics differ primarily by how well they handle a variety of lightcurves, particularly the aperiodic lightcurves for which the metrics are intended. Autocovariance functions are the most reliable by this criterion, with variation in the lightcurve function affecting the conversion to underlying timescale by only 20%. $\Delta m$-$\Delta t$ plots are most affected by changes to the statistical properties of the lightcurve; the additional small-scale structure in a damped random walk produces an estimated timescale at most half that for a squared exponential Gaussian process with the same characteristic timescale. This is a significant limitation to $\Delta m$-$\Delta t$ plots compared to the other two metrics.

Autocovariance functions and $\Delta m$-$\Delta t$ plots are tested further in the next chapter, using numerical simulations. Due to time constraints, I was unable to test an implementation of a structure function on simulated data.

## 4.8 References

Abdo, A. A. et al. 2010, ApJ, 722, 520, arXiv:1004.0348

Doob, J. L. 1942, Annals of Mathematics, 43, 351

Edelson, R. A., & Krolik, J. H. 1988, ApJ, 333, 646

Gillespie, D. T. 1996, American Journal of Physics, 64, 225

Lenz, P., & Breger, M. 2005, Communications in Asteroseismology, 146, 53

Lomb, N. R. 1976, Ap&SS, 39, 447

McQuillan, A., Aigrain, S., & Mazeh, T. 2013, MNRAS, 432, 1203, arXiv:1303.6787

Paltani, S., Courvoisier, T. J.-L., Blecha, A., & Bratschi, P. 1997, A&A, 327, 539, astro-ph/9706203

Percy, J. R., Grynko, S., Seneviratne, R., & Herbst, W. 2010, PASP, 122, 753

Percy, J. R., Hosick, J., & Leigh, N. W. C. 2003, PASP, 115, 59

Scargle, J. D. 1982, ApJ, 263, 835

Simonetti, J. H., Cordes, J. M., & Heeschen, D. S. 1985, ApJ, 296, 46

# Chapter 5

# Numerical Performance of Timescale Metrics

## 5.1 Introduction

This chapter continues the search for a practical aperiodic timescale definition started in Chapter 4. There, I defined a good aperiodic timescale metric as one that is:

**Universal:** it is defined for any lightcurve with any sampling, provided some minimum number of data points are present. In particular, it should not require evenly spaced samples, nor should it place preconditions on the properties of the underlying signal.

**Data-Driven:** it does not require hand-tuning, but is determined entirely by the data.

**Versatile:** it gives consistent results across lightcurves having different shapes or characteristic behaviors

**Accurate:** it correlates with the "true" timescale of a lightcurve

**Precise:** it has a low statistical variance

**Dependable:** it gives consistent results across different noise levels or cadences

**Robust:** it changes little if a small number of data points are added or removed, even if those points are outliers

**Well-Characterized:** it offers a way to determine the significance of the detected timescale

The definition of a timescale metric determines whether it is universal or data driven, so these criteria do not require testing. The previous chapter derived analytical expressions for timescale metrics as applied in the hypothetical case of perfect knowledge of the lightcurve, allowing me to rank timescale metrics based on their versatility and, to a lesser degree, their accuracy. The remaining criteria cannot be evaluated without realistic, or, in other words, imperfect, test data.

To determine the impact of measurement noise, limited cadence, and finite observing windows on lightcurve analysis, I simulated observations of the family of signals defined in section 4.2 at several key cadences. By determining how the precision and accuracy of timescale estimates depend on noise, cadence, and outliers, I can evaluate how each timescale metric performs by the above criteria. This is the first systematic attempt to use simulations to identify the best timescale metric for aperiodic lightcurves.

### 5.1.1 LightcurveMC: an extensible lightcurve simulation program

I have developed a program to generate random lightcurves and to perform automated statistical analysis of each lightcurve. LightcurveMC is designed to be highly modular, allowing new lightcurve types or new analysis tools to be introduced without excessive development overhead. The statistical tools are completely agnostic to how the lightcurve data is generated, and the lightcurve generators are completely agnostic to how the data will be analyzed. The use of fixed random seeds throughout guarantees that the program generates consistent results from run to run.

All figures and results in this chapter were generated using LightcurveMC 2.3.0. It is available, with documentation, from the Astrophysics Source Code Library as ascl:1408.012 (Findeisen, 2014). For the simulation runs presented here, the program was built using GCC 4.4.7-3 on Red Hat Enterprise Linux 6.4 and linked against kpfutils[1] 1.0.0, Timescales[2] 1.0.0, Boost[3] 1.41.0, GSL[4] 1.10, TCLAP[5] 1.2.1, R[6] 2.15.1, Rcpp[7] 0.10.3, RInside[8] 0.2.10, gptk[9] 1.06, and numDeriv[10] 2012.9-1. The random generation of squared exponential and two-timescale Gaussian processes is sensitive to the version of GSL, but otherwise the program output reported here should be reproducible regardless of compiler, interpreter, or library version.

### 5.1.2 Input Cadences

I tested timescale metrics on four observing cadences, representing different young star monitoring programs recently carried out at Caltech and the Infrared Processing and Analysis Facility. The cadences, presented in Table 5.1, were selected to probe different observing regimes. The PTF-NAN Full cadence is the cadence at which we observed the North America Nebula with the Palomar Transient Factory from 2009 August to 2012 December. The PTF-NAN 2010 cadence is the subset of these observations that were taken in 2010. The YSOVAR 2010 cadence represents a month

[1] https://github.com/kfindeisen/kpfutils
[2] https://github.com/kfindeisen/Timescales
[3] http://www.boost.org/
[4] http://www.gnu.org/software/gsl/
[5] http://tclap.sourceforge.net/
[6] http://www.r-project.org/
[7] http://dirk.eddelbuettel.com/code/rcpp.html
[8] http://dirk.eddelbuettel.com/code/rinside.html
[9] http://cran.r-project.org/web/packages/gptk/
[10] http://cran.r-project.org/web/packages/numDeriv/

of Spitzer observations for the Young Stellar Object Variability survey (Morales-Calderón et al., 2011) to represent a higher-cadence and shorter-baseline monitoring program than either of the two PTF-NAN cadences. Finally, the CoRoT cadence represents a month of high-frequency observations taken by Cody et al. (2014) to probe the extremes of both very high cadence and very large number of points.

| Cadence | Size | Baseline (days) | Char. Cadence (days) | Median Gap (days) | Longest Gap (days) | Regularity |
|---|---|---|---|---|---|---|
| PTF-NAN Full | 910 | 1,224.9 | 0.21 | 0.048 | 179.3 | 0.811 |
| PTF-NAN 2010 | 126 | 252.7 | 1.98 | 0.91 | 17.0 | 0.973 |
| YSOVAR 2010 | 39 | 35.7 | 1.26 | 0.91 | 2.5 | 0.954 |
| CoRoT | 6,307 | 38.7 | 0.012 | 0.0059 | 0.78 | 0.997 |

**Table 5.1:** Key properties of the observing cadences considered in this chapter. Characteristic cadence is a measure of the "typical" spacing between observations and is defined in the text. The median gap is the typical separation between two consecutive observations, and is mainly shown to illustrate the contrast between it and characteristic cadence, which tends to agree more with intuitive descriptions of the cadence. The longest gap is the maximum interval, within the lightcurve, containing no observations, while the regularity is a measure of how closely the cadence approaches even spacing. Most realistic cadences have regularities of 0.7 or higher; only the most pathological examples have regularities approaching 0.

I characterize each cadence by its baseline, by its characteristic cadence, by the length of the longest gap in the data, and by how closely it resembles a uniform time series. To define a characteristic cadence for an irregularly sampled time series, I note that a regular time series of $N$ observations spaced by $\delta t$ probes timescales from $\delta t$ to $(N-1)\delta t$. Specifically, if one finds the set of separations between any two points in the lightcurve, $\{\Delta t\}$, there are $N-1$ pairs of points separated by $\delta t$, $N-2$ pairs separated by $2\delta t$, and so on, for a total of $N(N-1)/2$ pairs of points. Since the first $N-1$ of these $N(N-1)/2$ pairs are equal to the cadence, the cadence is the $2/N$th quantile of the set $\{\Delta t\}$.

Reasoning that the set $\{\Delta t\}$ is a complete characterization of which timescales get probed with what degree of redundancy by a data set, I define the characteristic cadence of *any* time series to be the $2/N$th quantile of $\{\Delta t\}$. This definition works moderately well for simple generalizations of a regular time series. For example, if pairs of observations separated by a small interval $\tau$ are themselves separated by a larger interval $\delta t \gg \tau$, the characteristic cadence can be shown to be $\delta t - \tau$, the interval between the last observation of one pair and the first observation of the next pair. For triplets and longer subsequences of observations, on the other hand, the characteristic cadence is $2\tau$.

I characterize the regularity of a cadence by comparing the cumulative distribution function of $\{\Delta t\}$ with the corresponding distribution function of an evenly sampled cadence with the same time baseline and number of points. The maximum difference $0 \leq \Delta < 1$ between the two distribution functions characterizes how strongly the $\{\Delta t\}$ distribution deviates from the linear case (this is the

same statistic used in the one-sample Kolmogorov-Smirnov test). I define the regularity of a cadence to be $1 - \Delta$.

## 5.2 Simulation Strategy

| List of Timescale Metrics | List of Lightcurve Models |
|---|---|
| Interpolated Autocorrelation Function | Sinusoid |
| Scargle Autocorrelation Function | Squared Exponential Gaussian Process |
| $\Delta m$-$\Delta t$ Plot | Two-Timescale Gaussian Process |
| Peak-Finding | Damped Random Walk |
| Gaussian Process Fitting | Random Walk |

**Table 5.2:** Timescale metrics explored in this chapter, and the simulated lightcurves used to test them.

### 5.2.1 Simulations

For the simulations I generated lightcurves from sinusoidal, squared exponential Gaussian process, damped random walk, and random walk models over a grid of lightcurve parameters. The models are described in more detail in section 4.2, and the parameter grid is described below. Figure 4.1 shows a sample of the program output for a regular test cadence.

I tested amplitudes of 1 mag, 0.5 mag, 0.25 mag, and 0.1 mag, measured between the 5th and 95th percentiles ("5-95% amplitude" in the remainder of this chapter). The formulas from the previous chapter were used to transform these amplitudes into model parameters. For example, since the 5-95% amplitude for a sine wave is $1.975A$, I selected $A = 1/1.975 = 0.506$ mag to generate a 1 mag sinusoidal signal.

I added Gaussian white noise to each lightcurve, in flux space, at signal-to-noise ratios of 20, 10, and 4, measured with respect to the theoretical median flux of the lightcurve. I also had a corresponding run with no noise (for Gaussian process models, since the fits cannot converge if there is exactly zero noise, I instead adopted a signal-to-noise ratio of 300). Points that had negative flux after adding noise were counted as nondetections and removed from the analysis, but I did not simulate detection limits explicitly.

I tested the full PTF cadence, the 2010-only PTF cadence, and the YSOVAR cadence from Table 5.1. I did not test all 48 combinations of amplitude, signal-to-noise, and cadence; instead, I tested each amplitude at a signal-to-noise of 20 and full PTF cadence, each signal-to-noise at an amplitude of 0.5 mag and PTF cadence, and each cadence at a signal-to-noise of 20 and amplitude of 0.5 mag, for a total of 9 combinations.

For simulations using either PTF cadence, I tested lightcurve timescales of 0.5 days, 2 days, 5 days, 16 days, 64 days, and 256 days at all 9 combinations of amplitude, signal-to-noise, and

cadence. For simulations using the YSOVAR cadence, I tested timescales of 0.1 days, 1 day, 2 days, 5 days, 20 days, and 40 days.

At each grid point I generated 1,000 lightcurves of each type, giving them the appropriate amplitude and timescale. Since a random walk does not have a well-defined amplitude or timescale, I assigned it a diffusion constant $D = \frac{2\sigma^2}{\tau}$, where $\sigma$ and $\tau$ were the amplitude and timescale adopted for the damped random walk. This convention for $D$ gave the damped and undamped random walks at the same grid point equal diffusion constants for ease of comparison. I also generated 1,000 white noise lightcurves at each combination of amplitude, signal-to-noise, and cadence to compare to the structured lightcurves. The final tally was 225,000 simulated lightcurves. Each timescale metric was tested on each of the lightcurves, with one exception. To keep running times down, the much slower Gaussian process fitting was tested on only the first 30 lightcurves of each set of 1,000.

### 5.2.2 Timescale Characterization

Section 5.3 through section 5.7 present the simulation results for each of four timescale metrics: interpolated autocorrelation functions, $\Delta m$-$\Delta t$ plots, peak-finding plots, and Gaussian process fitting. In each section, I address first the details of how each metric was calculated from the simulated data, followed by representative results for sinusoidal and damped random walk lightcurves, followed by qualitative patterns in the metric's behavior.

Following the qualitative description, I rank each timescale metric by the following criteria:

**Precision:** characterized by the relative scatter across each set of 1,000 identical runs. This is a probe of precision in the sense used in section 5.1.

**Discriminatory power:** the smallest difference in underlying timescales that can be distinguished using the timescale metric, characterized by the ratio of the scatter in output timescale to the slope of the dependence of output timescale on input timescale. This is an indirect probe of accuracy in the sense used in section 5.1.

**Sensitivity to noise:** characterized by the rate at which the precision and discrimination deteriorate as the noise level increases. This is a partial probe of dependability in the sense used in section 5.1.

**Sensitivity to cadence:** characterized by the bias with respect to theoretical performance, and by the range of timescales having optimal precision and discrimination at each cadence. This is a partial probe of dependability in the sense used in section 5.1.

**Sensitivity to incomplete data:** characterized by the difference in output timescale between the PTF 2010-only and full lightcurves. This is a partial probe of robustness in the sense used in section 5.1.

At the end of each section, I summarize the performance of the corresponding timescale metric as illustrated by the simulations.

## 5.3 Interpolated Autocorrelation Functions

The interpolated autocorrelation function is calculated by interpolating the lightcurve to a regular time grid with spacing narrower than the smallest gap between two observations. Any standard autocorrelation algorithm can be applied to the resulting regular time series. Timescales are derived by finding the first lag at which the autocorrelation falls below 1/2, 1/4, or 1/9. An example of both an autocorrelation function and the corresponding timescale is shown in Figure 5.1.

In the analysis presented here, the autocorrelation function was calculated over a linear grid of time lags ranging from 0 to the full lightcurve baseline, in steps of 0.1 days. This choice of bins oversampled the data without leading to prohibitive running times.

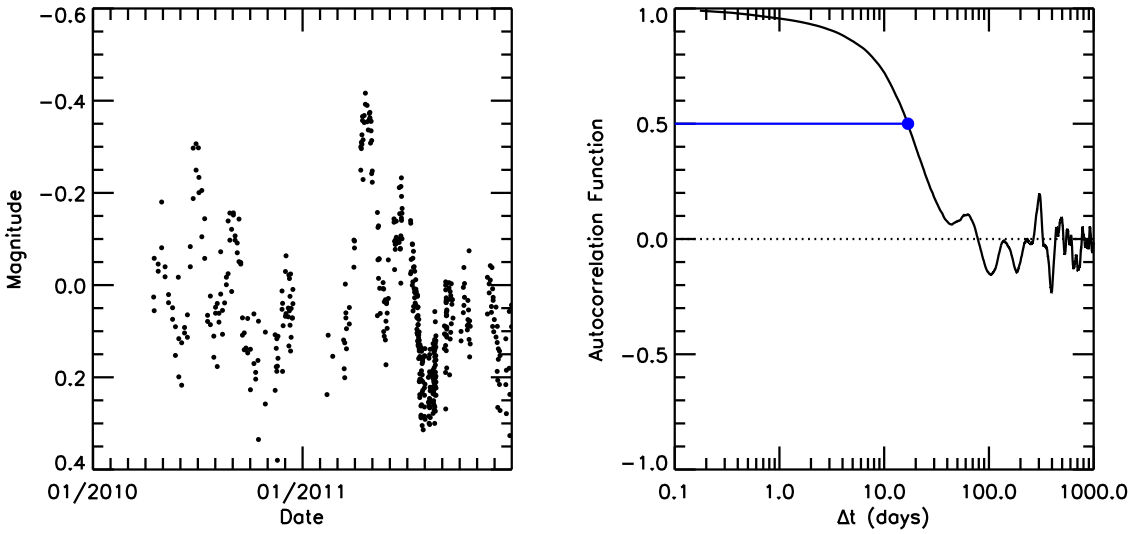


**(a)** Original Lightcurve **(b)** Interpolated ACF

**Figure 5.1:** An example of a damped random walk lightcurve with a damping time of 16 days (left) and an interpolated ACF derived from it (right). The blue line illustrates the exercise of defining the timescale as the point at which the ACF crosses a threshold (1/2, in this example).

The fixed time lag grid quantizes the output timescale to a multiple of 0.1 days. While this is adequate precision for our science goals, the quantization has the side effect that, in some simulation runs, the output timescale has zero variance. Were the variance not corrected, plots of the variance or the timescale discrimination would give the misleading impression that the timescale metric is *infinitely* precise. To give a more representative measure, I add $\frac{1}{\sqrt{12}}$ of the grid spacing of 0.1 days, in quadrature, to the standard deviation of all ACF-based timescales. The factor of $\frac{1}{\sqrt{12}}$ comes from

the fact that the standard deviation of a uniformly distributed random variable is $\frac{1}{\sqrt{12}}$ the length of the interval in which the variable may be found.

### 5.3.1 Semi-Ideal ACFs as a Comparison Standard

Section 4.5 derived the expected autocorrelation functions in the case of an infinite time series with no noise. To allow a more relevant comparison to the simulation results, we applied two corrections to the theoretical ACFs before presenting them in Figures 5.2 and 5.3.

We corrected the ACFs for the finite observing interval by multiplying ACF($\Delta t$) by $(1-\Delta t/\Delta T)$, where $\Delta t$ is the lag at which the ACF was measured and $\Delta T$ is the time baseline of the observations. This reproduces the effect of having fewer points from which to estimate the ACF at long lags. It does not correct for secondary systematic effects, such as errors in estimating the lightcurve mean propagating into the ACF.

We corrected for non-negligible noise by noting that, given a noisy signal $m'(t) = m(t) + \epsilon(t)$, with $\epsilon(t)$ an independent white noise process with mean zero, the autocovariance function is:

$$\begin{aligned} ACF'(\Delta t) &= E(m'(t)m'(t+\Delta t)) \\ &= E(m(t)m(t+\Delta t) + m(t)\epsilon(t+\Delta t) + \epsilon(t)m(t+\Delta t) + \epsilon(t)\epsilon(t+\Delta t)) \end{aligned}$$

Since $\epsilon(t)$ is, by assumption, uncorrelated with either the underlying signal or with the error process at any other time, the $\epsilon$ terms cancel out for $\Delta t \neq 0$:

$$\begin{aligned} ACF'(\Delta t) &= \begin{cases} E(m(t)m(t+\Delta t)) & \text{if } \Delta t \neq 0 \\ E(m(t)^2 + 2m(t)\epsilon(t) + \epsilon(t)^2) & \text{if } \Delta t = 0 \end{cases} \\ &= \begin{cases} ACF(\Delta t) & \text{if } \Delta t \neq 0 \\ ACF(\Delta t) + V(\epsilon) & \text{if } \Delta t = 0 \end{cases} \end{aligned} \tag{5.1}$$

Since the autocorrelation function is $ACF(\Delta t)/ACF(0) = ACF(\Delta t)/V(m)$, we can account for the noise contribution by multiplying the autocorrelation function by $1/\left(1+\frac{V(\epsilon)}{V(m)}\right)$.

### 5.3.2 Example Results

#### 5.3.2.1 Sinusoid

I present in Figure 5.2 the average interpolated ACF for a set of 1,000 simulations of a sinusoidal lightcurve with different periods, along with the theoretical prediction derived in the previous chapter. For short-period signals, the interpolation over our data gaps introduces a spurious correlation that washes out the expected sinusoidal signal. For long-period signals, the interpolated ACF resembles the theoretical ACF, although the amplitude of the correlation is slightly lower than in the

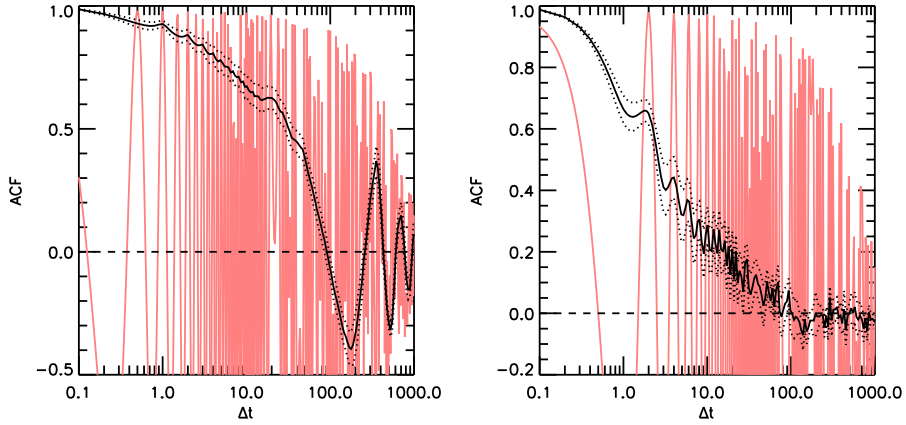


**(a)** Period 0.5 days




**(b)** Period 2.0 days

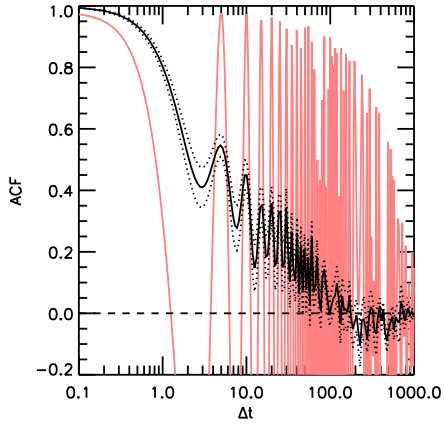


**(c)** Period 5 days

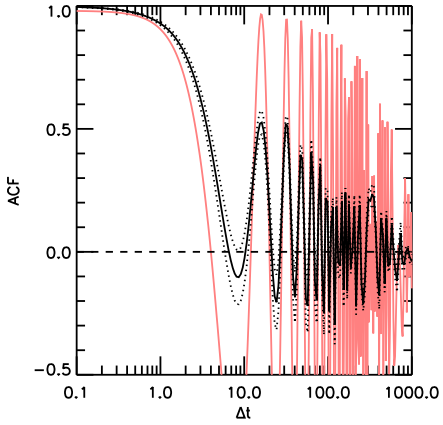


**(d)** Period 16 days

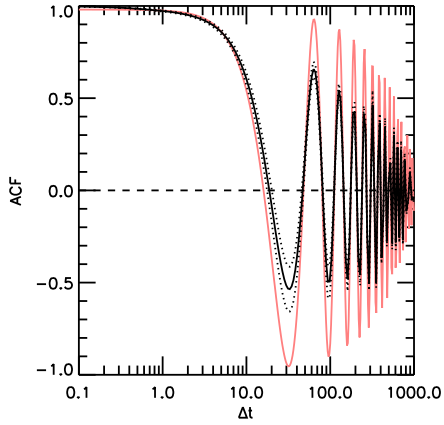


**(e)** Period 64 days

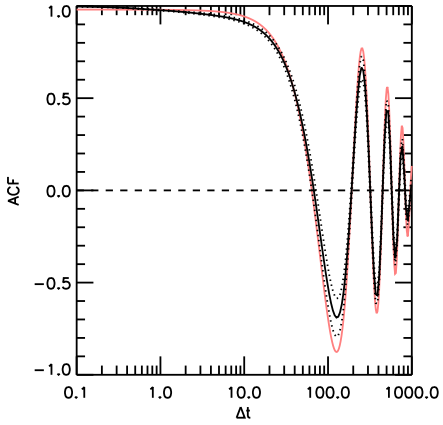


**(f)** Period 256 days

**Figure 5.2:** The mean interpolated autocorrelation function from 1,000 simulations of a sine wave at several representative periods. Dotted lines represent the standard deviation of the ACF at each time lag. The red curve shows the ACF predicted from Equation 4.24, after correcting for noise and for the finite observing window as described in subsection 5.3.1.

ideal case. The timescale of the spurious correlation decreases as the sine period increases.

#### 5.3.2.2 Damped Random Walk

I present in Figure 5.3 the average interpolated ACF for a set of 1,000 simulations of a damped random walk with different correlation times, along with the theoretical prediction derived in the previous chapter. As with the sinusoidal signal, there is a spurious autocorrelation introduced by the interpolation. However, this autocorrelation is significant at all input timescales, leading to timescale estimates that vary little with the underlying timescale of the data.

#### 5.3.2.3 Other Lightcurves

I also tested the performance of the interpolated ACF for simulations of squared exponential Gaussian processes and random walks. The ACF for a squared exponential Gaussian process looks qualitatively similar to that for a damped random walk, although the shape of the ACF varies more with input timescale than the damped random walk ACF does. The shape of the ACF for a random walk has a characteristic shape that does not depend on the walk's diffusion constant, and depends little on the details of the cadence: a ACF that falls smoothly with increasing time lag, crosses zero at roughly one quarter of the survey's time baseline, and then remains negative for all longer periods.

### 5.3.3 Performance

#### 5.3.3.1 Qualitative Behavior

In Figure 5.4, I compare the performance of three different timescales, all derived by finding the time lag at which the autocorrelation function first drops below a particular threshold. In the top two panels, the timescale calculated from simulations is divided by the corresponding timescale from section 4.5; the dotted line across the middle of the plot represents behavior consistent with analytical theory.

For sinusoidal signals with periods shorter than 16 days, the calculated timescale is an order of magnitude too large; for longer periods, the bias is much smaller, a few tens of percent. All three thresholds have similar performance in this case. For damped random walks, the calculated timescale varies little with the true timescale, so the ratio is high at short timescales and low at long timescales. The timescale from cutting the autocorrelation function at 1/2 shows a slightly shallower slope in this plot, indicating it scales more strongly with the true timescale.

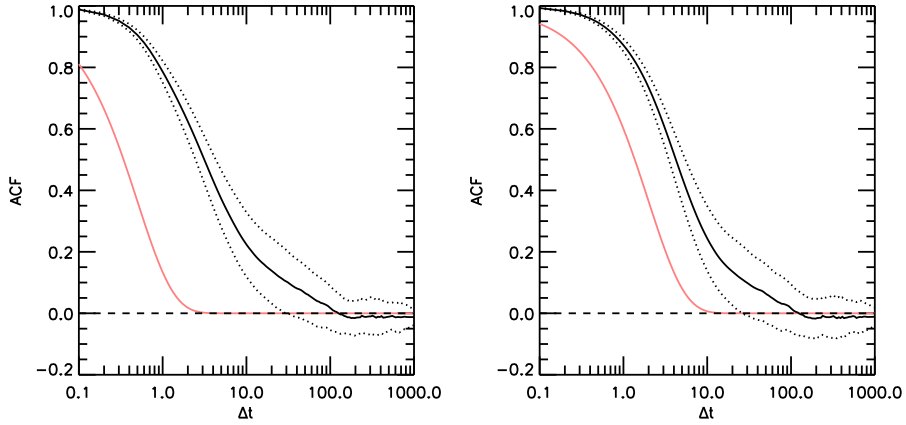


**(a)** Damping Time 0.5 days




**(b)** Damping Time 2.0 days

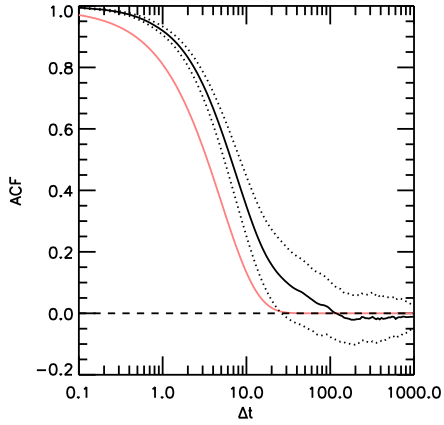


**(c)** Damping Time 5 days

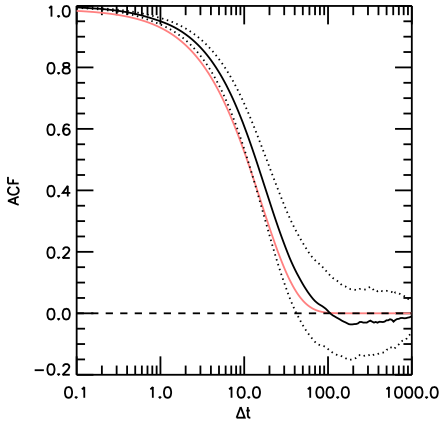


**(d)** Damping Time 16 days

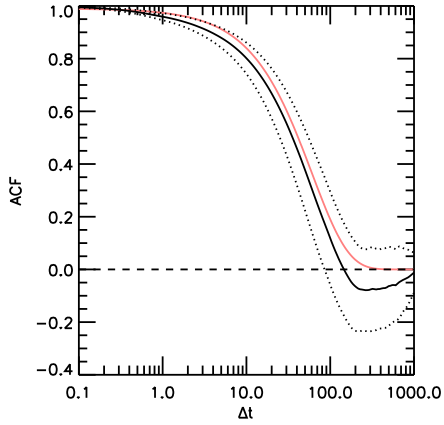


**(e)** Damping Time 64 days

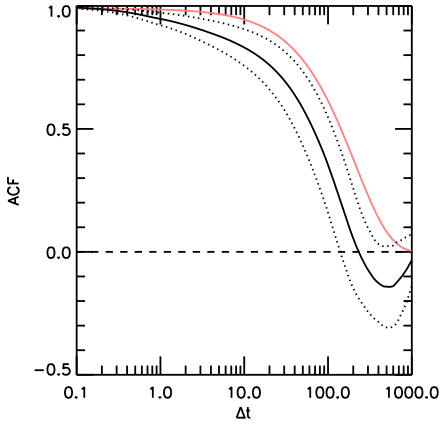


**(f)** Damping Time 256 days

**Figure 5.3:** The mean interpolated autocorrelation function from 1,000 simulations of a damped random walk at several representative timescales. Dotted lines represent the standard deviation of the ACF at each time lag. The red curve shows the ACF predicted from subsubsection 4.5.3.4, after correcting for noise and for the finite observing window as described in subsection 5.3.1.

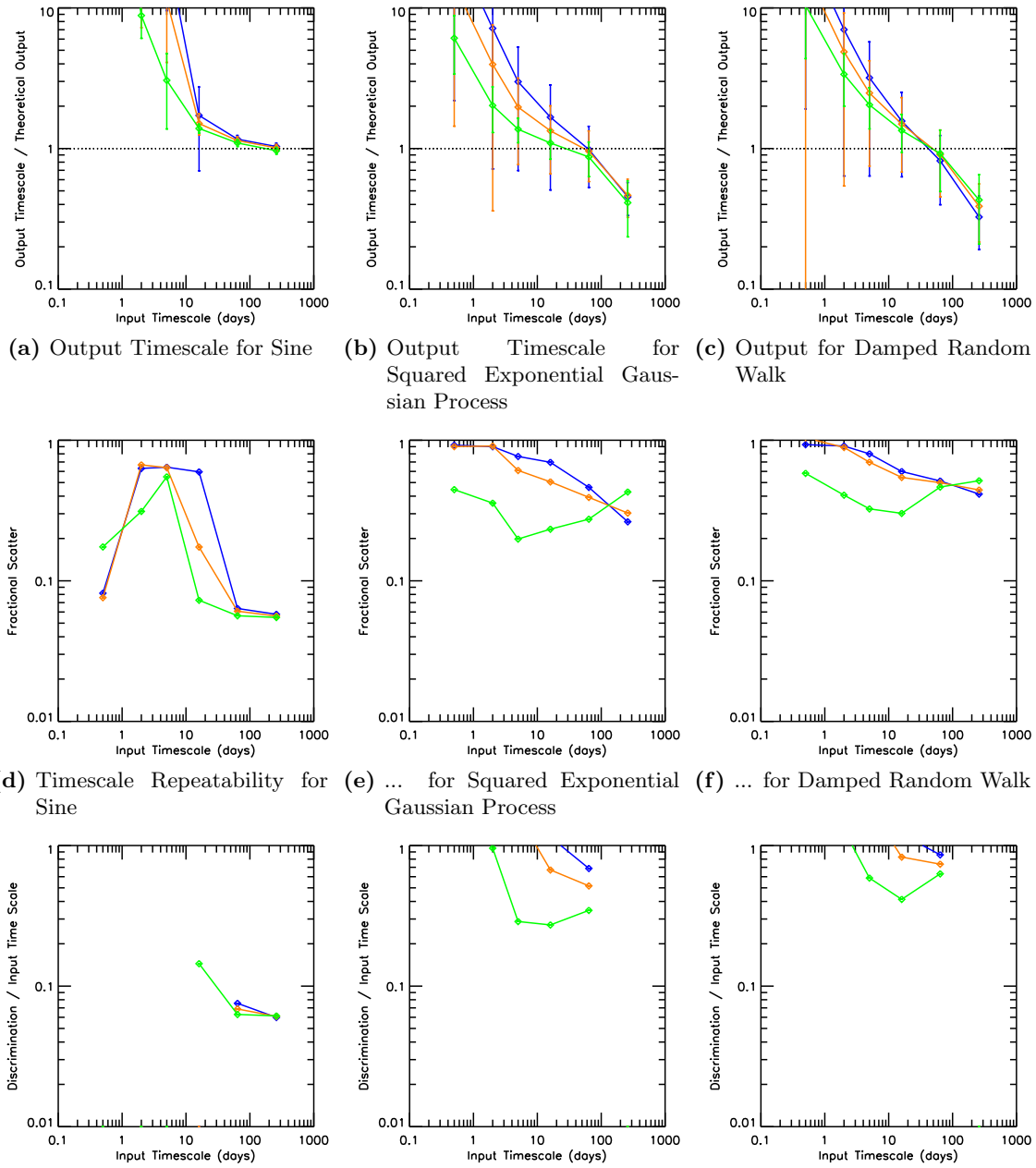


**(a)** Output Timescale for Sine

**(b)** Output Timescale for Squared Exponential Gaussian Process

**(c)** Output for Damped Random Walk

**(d)** Timescale Repeatability for Sine

**(e)** ... for Squared Exponential Gaussian Process

**(f)** ... for Damped Random Walk

**(g)** Timescale Discrimination for Sine

**(h)** ... for Squared Exponential Gaussian Process

**(i)** ... for Damped Random Walk

**Figure 5.4:** The timescale calculated from the autocorrelation function, plotted as a function of the true underlying timescale. Only simulations with no measurement noise are shown. Top panels show the ratio of the output timescale to the value predicted in section 4.5. Middle panels show the ratio of the standard deviation to the mean output timescale. Bottom panels show the degree by which the input timescale has to change to significantly affect the output timescale. In all plots, blue represents the time at which the autocorrelation function first falls below 1/9, orange the time at which it falls below 1/4, and green the time at which it falls below 1/2.

#### 5.3.3.2 Precision

In the middle two panels of Figure 5.4, the scatter in the estimated timescale across multiple simulation runs is plotted for three different timescale metrics. For both sinusoidal and damped random walk lightcurves, cutting the autocorrelation function at 1/2 generally yields less scatter than cutting at 1/4 or 1/9.

#### 5.3.3.3 Discrimination

Discrimination is a measure of how well the inferred timescale correlates with the true lightcurve timescale. Good discrimination requires both a strong dependence of output on input timescale and high repeatability for individual timescale measurements. Poor discrimination means a timescale metric cannot be used to separate short- and long-timescale lightcurves with any fidelity.

In the bottom two panels of Figure 5.4, the scatter in the estimated timescale across multiple simulation runs is plotted for three different timescale metrics. The discrimination is not defined at short sine periods because the output timescale *decreases* with the true period (cf. Figure 5.2). At longer sine periods, the inferred timescale correlates well with the period and the discriminatory power is comparable to the scatter in the individual measurements. For the damped random walk, the inferred timescale correlates poorly with the true timescale, so the discrimination is much poorer than the scatter alone would imply. While the true timescale of a long-period sinusoidal signal can be inferred to 10% or better, the accuracy of the same estimate for a damped random walk is only 70-80% at best.

#### 5.3.3.4 Sensitivity to Noise

The average value of the autocorrelation timescale changes very little between an effectively infinite signal-to-noise and a signal-to-noise ratio of 10. At a signal-to-noise ratio of 4, on the other hand, the calculated timescale shows much less variation with the true timescale. This is particularly dramatic for the sine wave (upper left panel), since for signal-to-noise of 10 or greater, the calculated timescale is proportional to the period for periods of 16 days or longer, while for signal-to-noise of 4 the proportionality disappears.

The scatter in individual measurements is more sensitive to signal-to-noise. The degree to which noise degrades measurement precision is independent of the true timescale. Again, signal-to-noise of 4 is significantly different from signal-to-noise of 10 or higher.

The discriminating power of timescales based on autocorrelation functions shows a similar dependence on signal-to-noise as the scatter. Discrimination gets poorer at low signal-to-noise in a manner independent of the true timescale.

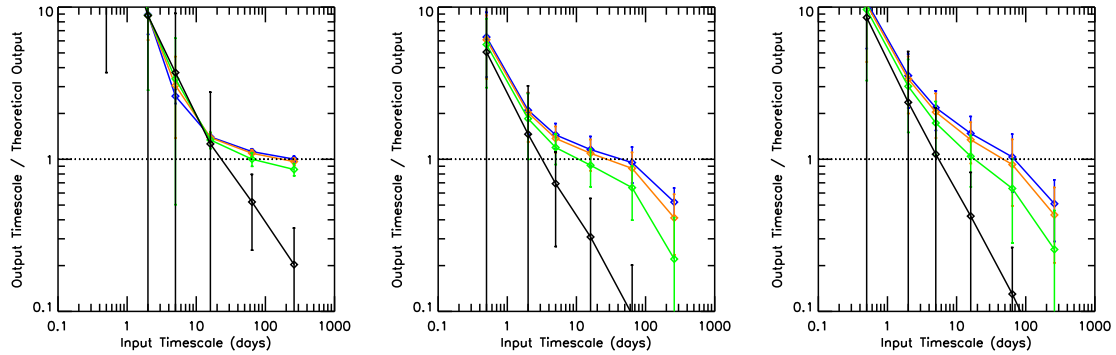


**(a)** Output Timescale for Sine




**(b)** Output Timescale for Squared Exponential Gaussian Process




**(c)** Output Timescale for Damped Random Walk

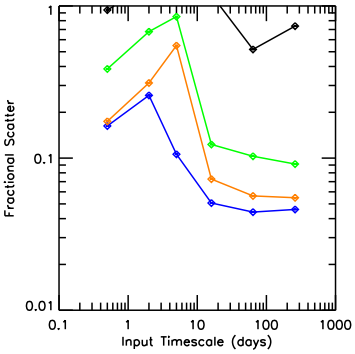


**(d)** Timescale Repeatability for Sine

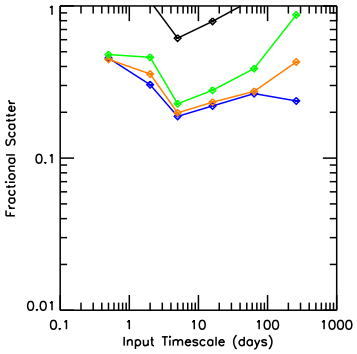


**(e)** Timescale Repeatability for Squared Exponential Gaussian Process

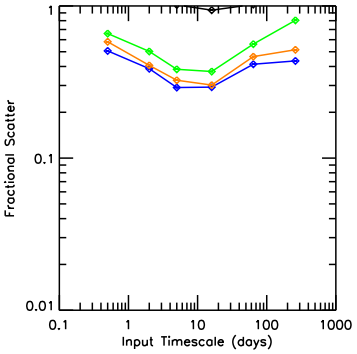


**(f)** Timescale Repeatability for Damped Random Walk

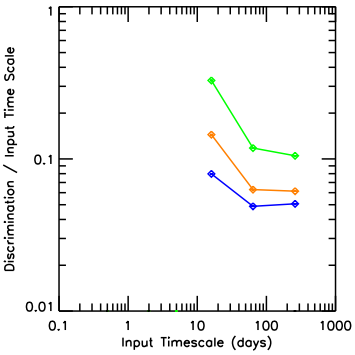


**(g)** Timescale Discrimination for Sine

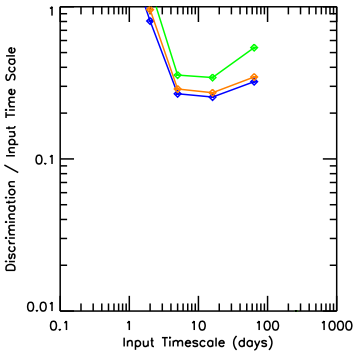


**(h)** Timescale Discrimination for Squared Exponential Gaussian Process

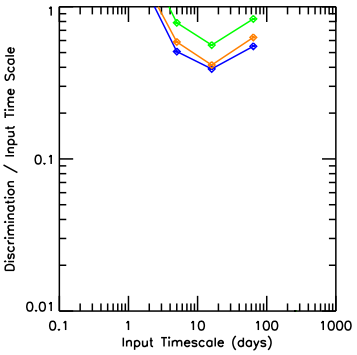


**(i)** Timescale Discrimination for Damped Random Walk

**Figure 5.5:** As Figure 5.4, but plotting only the timescale at which the autocorrelation function first falls below 1/2. Blue represents zero noise, orange represents a signal-to-noise ratio of 20, green a signal-to-noise ratio of 10, and black a signal-to-noise ratio of 4. All lightcurves have an expected 5-95% amplitude of 0.5 magnitudes.

#### 5.3.3.5 Sensitivity to Cadence

The behavior of the interpolated autocorrelation function is similar for the two PTF cadences and the YSOVAR cadence (Figure 5.6), except in their characteristic scales. Timescales calculated for lightcurves sampled with the full PTF cadence are systematically higher than those calculated for the PTF cadence in 2010, which are in turn higher than those for lightcurves sampled at the YSOVAR cadence.

For sinusoidal lightcurves sampled at either PTF cadence, the autocorrelation timescale correlates with the period for periods larger than or comparable to 16 days. For the YSOVAR sampling, the timescale is reliable for periods of 5 days or longer. The autocorrelation timescale is never well correlated with the period for a damped random walk, regardless of sampling. The fractional scatter shows no strong trends with the input timescale for either sampling or for either type of lightcurve. The discriminating power is best at long timescales for a sinusoidal signal, but is best at intermediate timescales (relative to the cadence and time baseline of the observations) for a damped random walk.

In general, the interpolated autocorrelation function performs best at the YSOVAR cadence, worse at the 2010-only PTF cadence, and worst of all at the full PTF cadence, as measured by output timescale bias or discriminating power. In Table 5.1, the YSOVAR cadence has the smallest maximum gap in the data, the smallest time base line, and the fewest points of the three cadences; the full PTF cadence has the largest maximum gap, the longest base line, and the most points. Of these properties, the maximum gap is most likely the one that controls ACF performance: after interpolation, the gap will be filled with a perfectly linear time series that an autocorrelation solver cannot distinguish from real data.

Neither characteristic cadence nor, surprisingly, linearity of the time series correlates with ACF performance; the YSOVAR cadence is intermediate between the two PTF cadences in both metrics.

### 5.3.4 Summary

In Chapter 4, I showed that the autocorrelation function can be converted into a timescale by finding the time lag at which it crosses some threshold. The resulting timescales are consistent to within a few tens of percent across different types of lightcurves, and they are, at least in the ideal case, proportional to the true timescale, making them versatile and accurate as defined in section 5.1.

To estimate the autocorrelation function for real, irregularly sampled data, I considered in this section interpolating the data to a high-cadence, regular grid. This interpolation introduces significant artifacts into the autocorrelation function. These artifacts dominate the inferred timescale, giving results that correlate weakly with the true period except in the case of a long-period sinusoidal signal. The performance depends little on signal-to-noise but is extremely sensitive to the cadence.

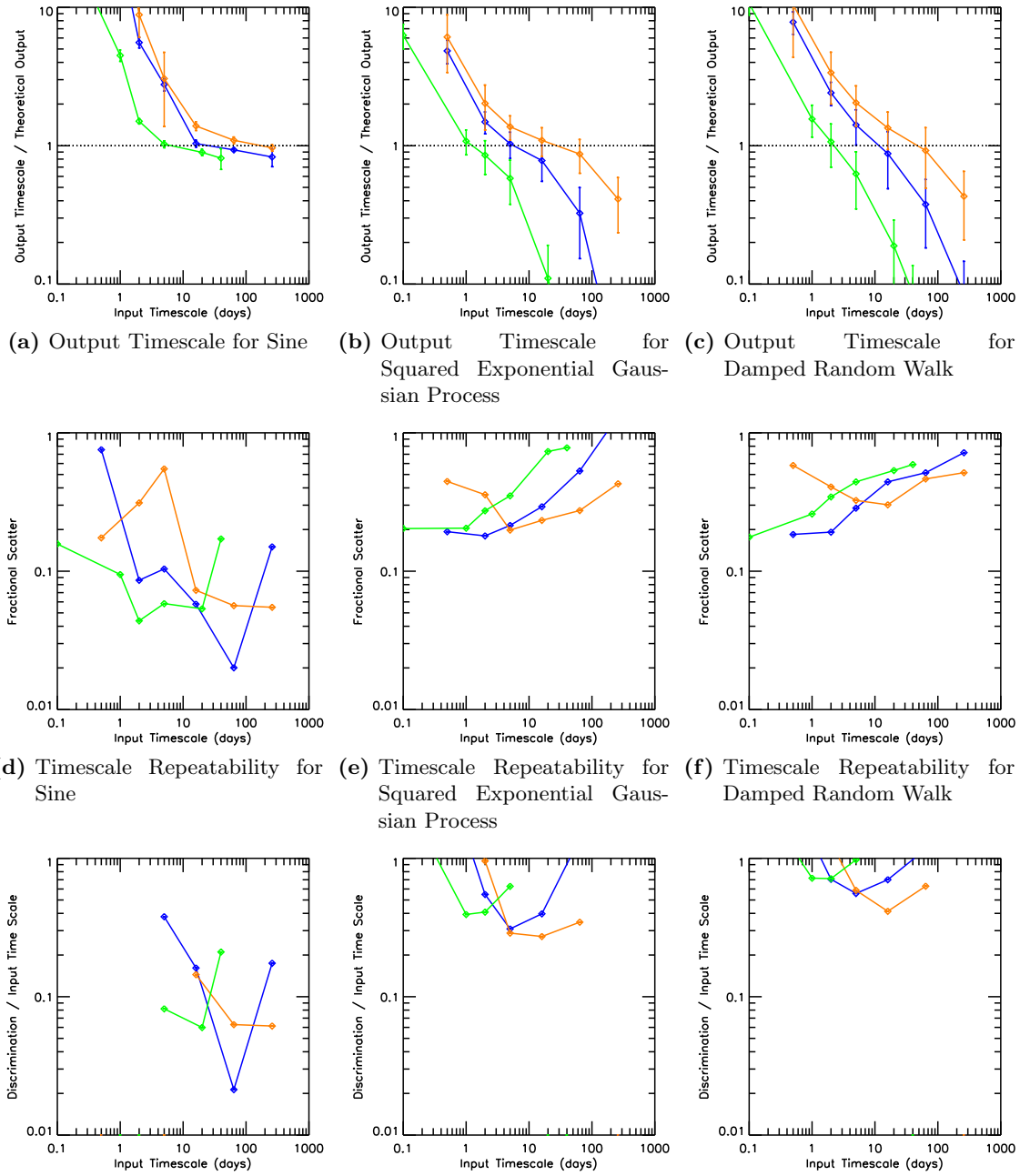


**(a)** Output Timescale for Sine

**(b)** Output Timescale for Squared Exponential Gaussian Process

**(c)** Output Timescale for Damped Random Walk

**(d)** Timescale Repeatability for Sine

**(e)** Timescale Repeatability for Squared Exponential Gaussian Process

**(f)** Timescale Repeatability for Damped Random Walk

**(g)** Timescale Discrimination for Sine

**(h)** Timescale Discrimination for Squared Exponential Gaussian Process

**(i)** Timescale Discrimination for Damped Random Walk

**Figure 5.6:** As Figure 5.4, but plotting only the timescale at which the autocorrelation function first falls below 1/2. Orange represents the full PTF cadence, blue the PTF cadence in 2010 alone, and green the YSOVAR cadence.

I do not recommend the use of autocorrelation functions as a timescale metric, except possibly in cases where the cadence has no gaps on timescales comparable to or larger than the variability. For irregular cadences, this metric is neither accurate nor dependable.

## 5.4 Scargle Autocorrelation Functions

We attempted to implement an autocorrelation function for irregular sampling in terms of the power spectrum, following Scargle (1989). While we were able to use the discrete Fourier transform to estimate the power spectrum of the data for arbitrary sampling, we found that the resulting autocorrelation function had severe systematics such as high-frequency oscillations. These appear to be an artifact of computing the power spectrum over a limited frequency range, usually neglecting high frequencies, and of aliases in the power spectrum.

We were unable to determine either an appropriate frequency cutoff or a way to apodize the frequencies naturally, so we did not run the grid of lightcurve tests described elsewhere in this chapter. While the Scargle (1989) ACF is a mathematically well-justified approach to calculating ACFs, the problem of how to correctly filter the frequency spectrum must be addressed before its robustness may be tested.

## 5.5 $\Delta m$-$\Delta t$ Plots

The general properties of $\Delta m$-$\Delta t$ plots were presented in section 4.6. For $\Delta m$-$\Delta t$ plots with a finite number of samples, I estimated the quantiles of $\Delta m$ as a function of $\Delta t$ by binning the $(\Delta t, \Delta m)$ pairs in $\Delta t$, and calculating the appropriate quantile within each bin. This is effectively taking a histogram of the data in $\Delta m$-$\Delta t$ space, with all the disadvantages thereof, but it is the simplest implementation. Timescales are then defined by finding the low end of the first $\Delta t$ bin in which a particular quantile of $\Delta m$ exceeds a set threshold.

In the analysis presented here, the first bin edge was set at $10^{-1.97}$ days, with subsequent bins at increments of 0.15 dex up to the full lightcurve baseline. This choice of bins allowed all possible timescales to be probed, even in the highest-cadence portions of our data, while our nightly observing gap would only deplete points from two bins, from $10^{-0.47}$ days to $10^{-0.32}$ days and from $10^{-0.32}$ days to $10^{-0.17}$ days.

In practice, the variance in timescales across different realizations of the same lightcurve generator usually exceeds the $\sim 40\%$ quantization introduced by 0.15 dex bins. Therefore, finer bins would not improve performance, and are likely to worsen it by increasing the scatter in each bin.

The use of $\Delta t$ bins in analyzing the $\Delta m$-$\Delta t$ plot quantizes the output timescale to one of the bin edges. While the scatter in most simulation runs exceeds the bin width, in some runs enough of

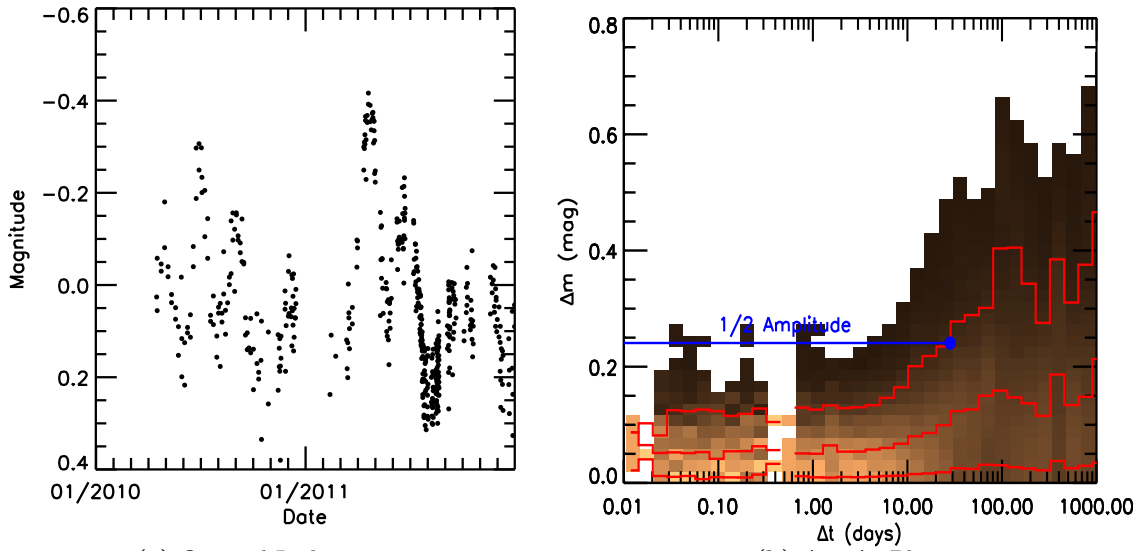


**(a)** Original Lightcurve **(b)** $\Delta m$-$\Delta t$ Plot

**Figure 5.7:** An example of a damped random walk lightcurve with a damping time of 16 days (left) and a binned version of the corresponding $\Delta m$-$\Delta t$ plot (right). The blue line illustrates the exercise of defining the timescale as the point at which the quantiles of $\Delta m$ (red lines) cross a threshold (half the 5-95% amplitude, in this example).

the observations fall into the same bin to bias the scatter downward. To give a more representative measure of the precision of $\Delta m$-$\Delta t$ analysis, I add $\frac{1}{\sqrt{12}}$ of the bin width in quadrature to the standard deviation of all $\Delta m$-$\Delta t$-based timescales. The factor of $\frac{1}{\sqrt{12}}$ comes from the fact that the standard deviation of a uniformly distributed random variable is $\frac{1}{\sqrt{12}}$ the length of the interval in which the variable may be found. With no constraint on where within a bin the true timescale lies, its position is effectively a uniform random variable in log space.

### 5.5.1 Semi-Ideal $\Delta m$-$\Delta t$ Plots as a Comparison Standard

Section 4.6 derived the expected behavior of $\Delta m$-$\Delta t$ plots in the case of an infinite time series with no noise. To allow a more relevant comparison to the simulation results, we corrected the theoretical $\Delta m$ medians before presenting them in Figures 5.8 and 5.9.

We corrected for non-negligible noise by observing that, for a Gaussian process, the magnitude difference $\Delta m_{\text{true}}$ between the intrinsic signal at two points separated by a fixed interval $\Delta t$ follows a normal distribution with some width $\sigma_{\text{true}}(\Delta t)$. If the signal is observed with some white noise with RMS amplitude $\epsilon$, then for $\Delta t \neq 0$ the difference between the noisy signals is the sum of two uncorrelated normal distributions, or a normal distribution with width $\sqrt{\sigma^2_{\text{true}}(\Delta t) + 2\epsilon^2}$. Therefore, the theoretical formulas in subsection 4.6.3 can be used in the noisy case by substituting $\sigma(\Delta t) \rightarrow \sqrt{\sigma^2(\Delta t) + 2\epsilon^2}$.

For the median $\Delta m$ quantile, which is presented in Figures 5.8 and 5.9, an equivalent substitution

is $\Delta m \rightarrow \sqrt{\Delta m^2 + (0.67449\sqrt{2}\epsilon)^2}$, where the expression in parentheses is the median $\Delta m$ for a white noise process with variance $2\epsilon^2$. While this expression is correct only for Gaussian process lightcurves, we also used it to transform the theoretical expectations for a sine in Figures 5.8, since it at least has the correct behavior in the limiting cases where the noise is much more than or much less than the expected variation.

## 5.5.2 Example Results

### 5.5.2.1 Sinusoid

I present in Figure 5.8 the average value of the $\Delta m$ median for a set of 1,000 simulations of a sinusoidal lightcurve with different periods, along with the theoretical prediction derived in the previous chapter. The values of $\Delta m$ in each bin generally follow the predictions, although in most bins $\Delta m$ is averaged over multiple cycles.

### 5.5.2.2 Damped Random Walk

I present in Figure 5.9 the average value of the $\Delta m$ median for a set of 1,000 simulations of a damped random walk with different correlation times, along with the theoretical prediction derived in the previous chapter. The average behavior of the $\Delta m$ median is close to the prediction, but there is a large amount of scatter from run to run.

### 5.5.2.3 Other Lightcurves

$\Delta m$-$\Delta t$ plots for a squared exponential Gaussian process qualitatively resemble those for a damped random walk, in that they resemble theoretical predictions on average but have a large degree of scatter from run to run. The $\Delta m$-$\Delta t$ plots for a random walk also resemble predicted behavior on average, but with nearly 100% scatter for bins probing timescales longer than 200 days. The rise in scatter suggests that $\Delta m$-$\Delta t$ plots cannot accurately represent variability on large fractions ($\sim$ 1/5) of the observing baseline; the lightcurve provides an unrepresentative snapshot of variability on longer timescales, and the $\Delta m$-$\Delta t$ plot cannot present information that is not in the data.

## 5.5.3 Performance

### 5.5.3.1 Qualitative Behavior

In Figure 5.10, I compare the performance of two different timescales, both derived by finding the value of $\Delta t$ at which the 90th percentile of $\Delta m$ first rises above a particular threshold. In the top two panels, the timescale calculated from simulations is divided by the corresponding timescale

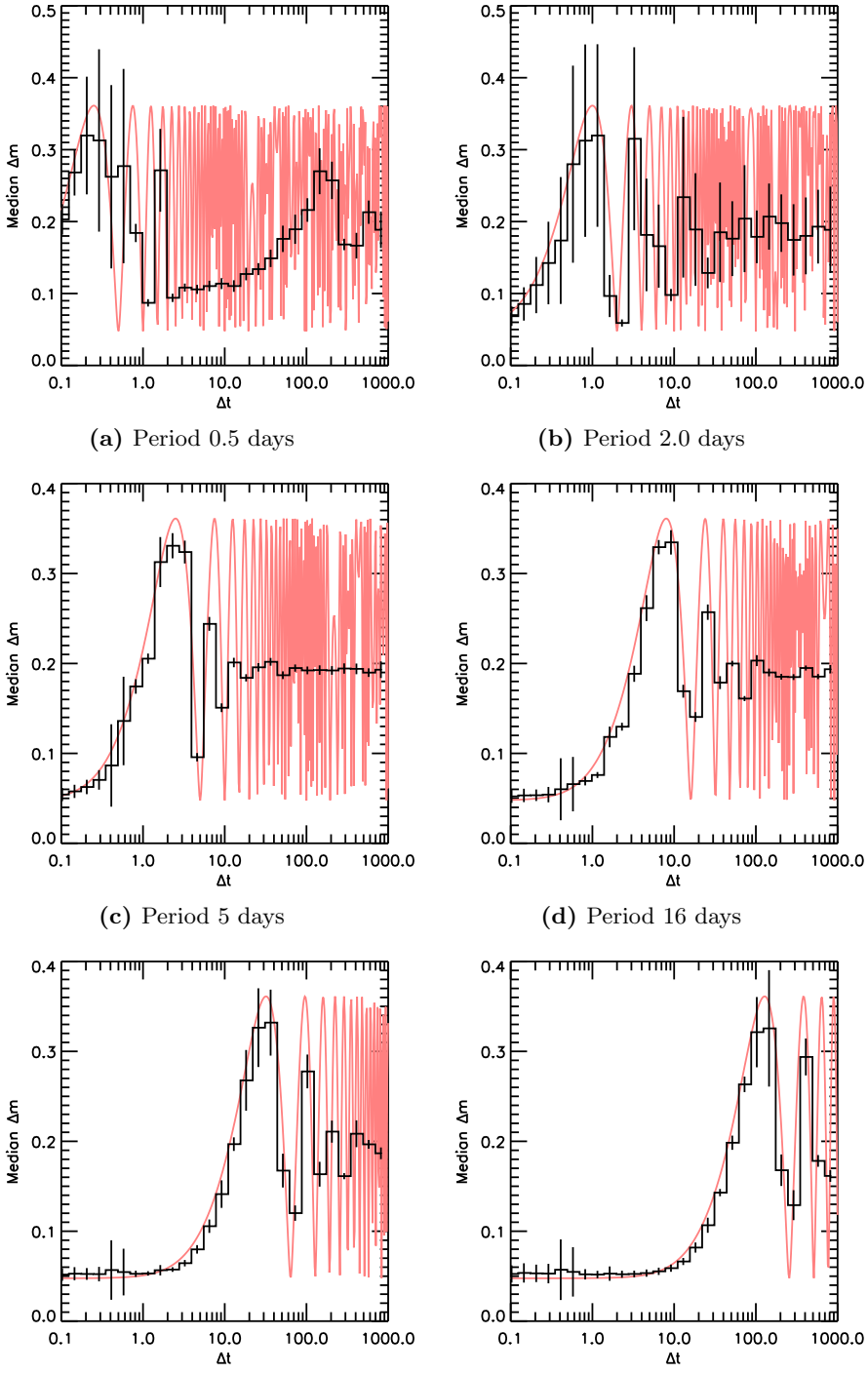


**(a)** Period 0.5 days

**(b)** Period 2.0 days

**(c)** Period 5 days

**(d)** Period 16 days

**(e)** Period 64 days

**(f)** Period 256 days

**Figure 5.8:** The average value of the $\Delta m$ median from 1,000 simulations of a sine wave at several representative periods. Error bars represent the standard deviation of the $\Delta m$ median in each $\Delta t$ bin. The red curve shows the $\Delta m$ median predicted from Equation 4.31, after correcting for noise and for the finite observing window as described in subsection 5.5.1.

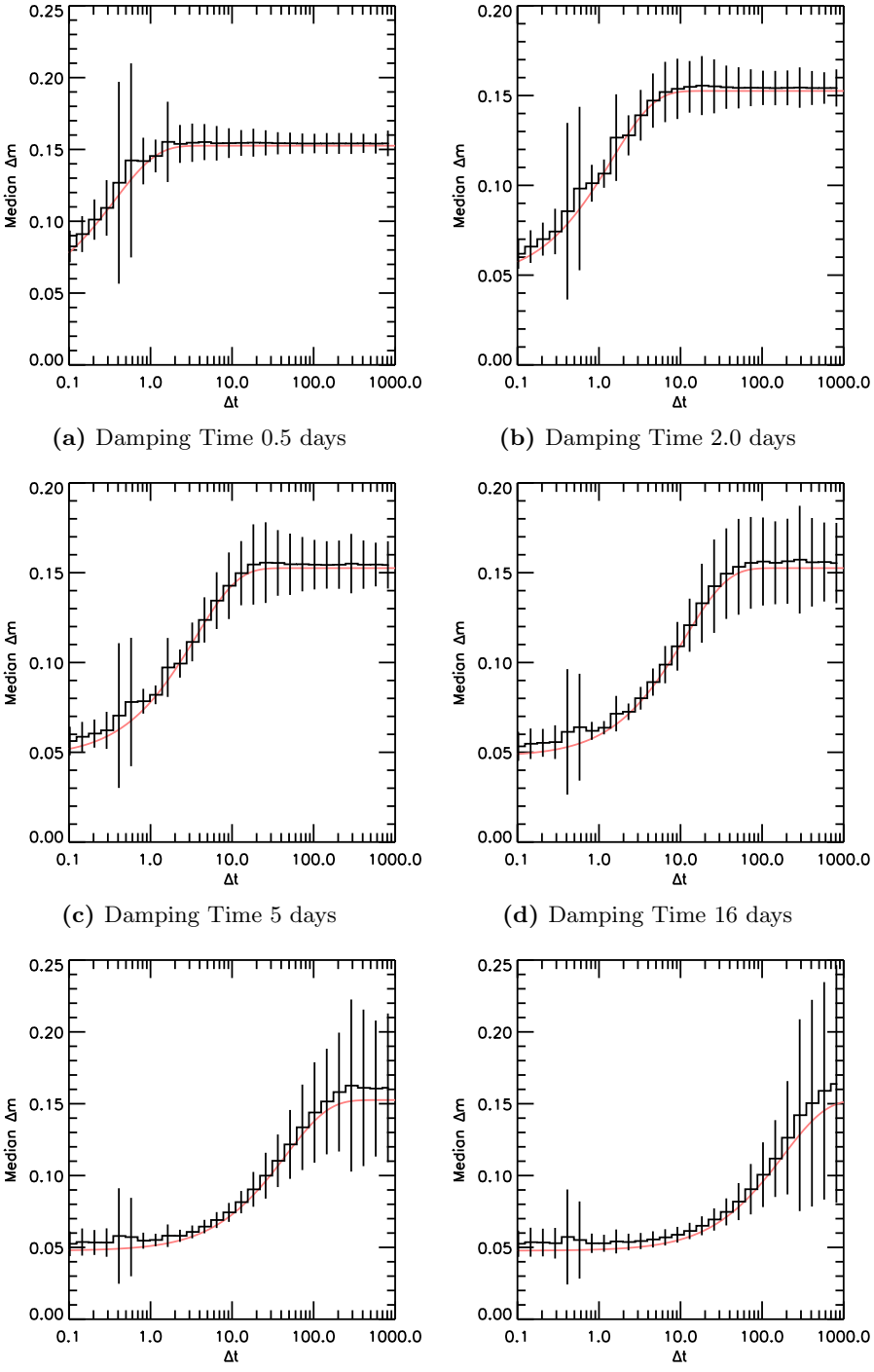


**(a)** Damping Time 0.5 days

**(b)** Damping Time 2.0 days

**(c)** Damping Time 5 days

**(d)** Damping Time 16 days

**(e)** Damping Time 64 days

**(f)** Damping Time 256 days

**Figure 5.9:** The average value of the $\Delta m$ median from 1,000 simulations of a damped random walk at several representative timescales. Error bars represent the standard deviation of the $\Delta m$ median in each $\Delta t$ bin. The red curve shows the $\Delta m$ median predicted from Equation 4.47, after correcting for noise and for the finite observing window as described in subsection 5.5.1.

from section 4.6; the dotted line across the middle of the plot represents behavior consistent with analytical theory.

For sinusoidal signals, the calculated timescale is in general consistent with analytical results. For damped random walks, the calculated timescale is consistent with theory for damping times up to 16 days; walks with timescales of 64 days or longer see a fall-off of up to a factor of three as the $\Delta m$-$\Delta t$ plot no longer has a representative sampling of the variability.

#### 5.5.3.2 Precision

The middle two panels of Figure 5.10 show the scatter in the estimated timescale multiple simulation runs. For sinusoidal signals, the scatter is of order 10%. For 2-day periods the scatter is much higher because at that period the largest change in the signal is over time intervals from half a day to a day, which our nightly cadence samples very poorly. For the damped random walk, the scatter is of order 40% for short timescale variables, and 50% or larger at long timescales. The timescale defined as the point where $\Delta m$ crosses one half of the lightcurve amplitude has slightly less scatter than the analogous timescale defined at one third of the amplitude.

#### 5.5.3.3 Discrimination

The bottom two panels of Figure 5.10 show the smallest difference in input timescale that can be distinguished using the output timescale. Since the $\Delta m$-$\Delta t$ timescale is, in general, proportional to the true timescale, the discrimination is set by the scatter in the estimated timescale. For long timescale damped random walks, the drop-off in output timescale is reflected in a reduced ability to discriminate between timescales differing by less than a factor of two.

#### 5.5.3.4 Sensitivity to Noise

Figure 5.11 shows the performance of a $\Delta m$-$\Delta t$ timescale as a function of the signal-to-noise ratio of the lightcurve. The average value of the timescale changes very little between an effectively infinite signal-to-noise and a signal-to-noise ratio of 20, particularly for a sinusoidal signal. At a signal-to-noise ratio of 4, on the other hand, the calculated timescale is always close to the smallest timescale sampled, suggesting that the $\Delta m$-$\Delta t$ plot is dominated by noise.

The scatter in individual measurements rises smoothly with decreasing signal-to-noise. The degree to which noise degrades measurement precision is independent of both the lightcurve shape and the true timescale. The discriminating power of the timescale metric degrades similarly, although for a damped random walk the power is more sensitive to signal-to-noise at short timescales than at long timescales.

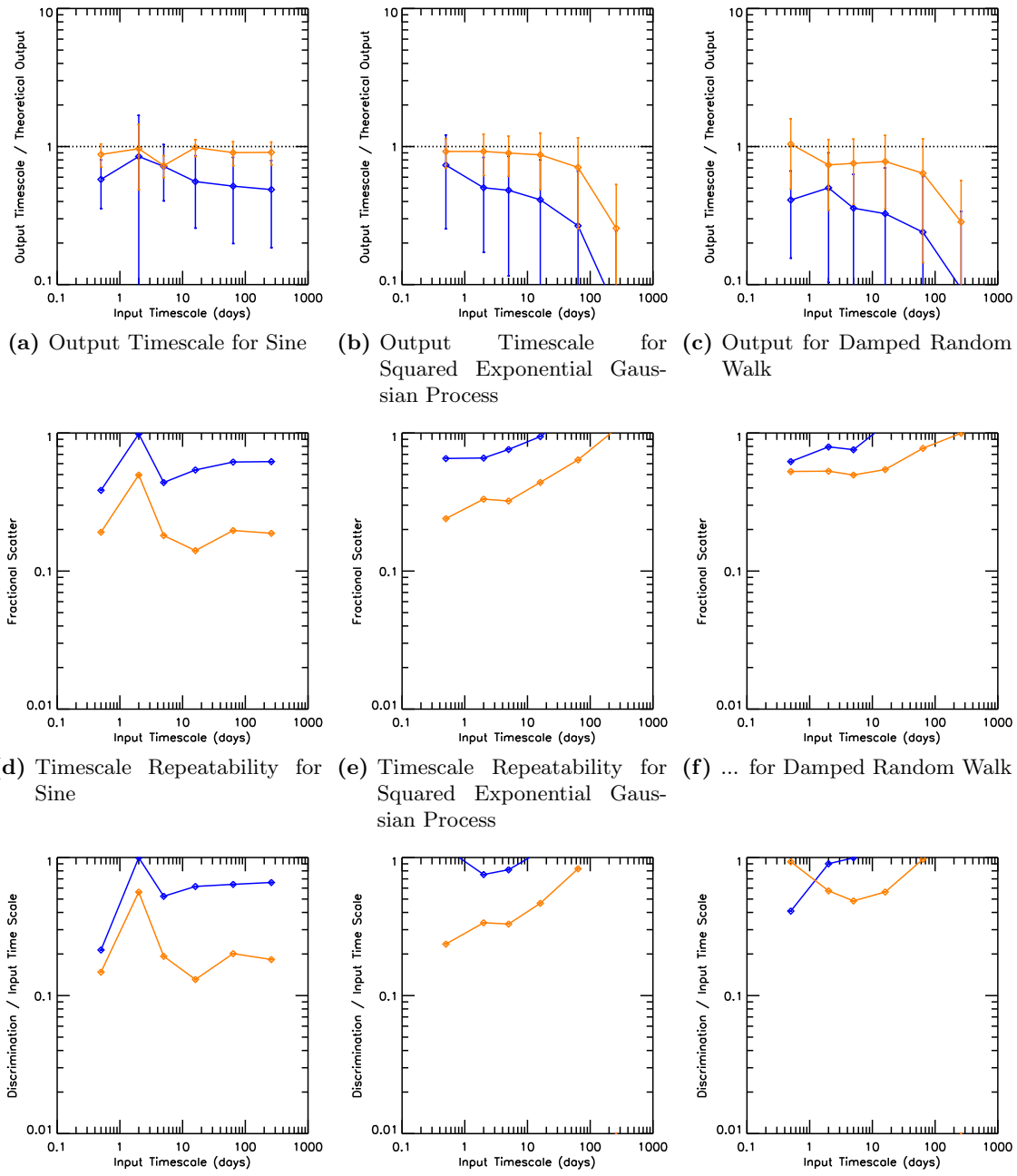


**(a)** Output Timescale for Sine

**(b)** Output Timescale for Squared Exponential Gaussian Process

**(c)** Output for Damped Random Walk

**(d)** Timescale Repeatability for Sine

**(e)** Timescale Repeatability for Squared Exponential Gaussian Process

**(f)** ... for Damped Random Walk

**(g)** Timescale Discrimination for Sine

**(h)** Timescale Discrimination for Squared Exponential Gaussian Process

**(i)** ... for Damped Random Walk

**Figure 5.10:** The timescale calculated from a $\Delta m$-$\Delta t$ plot, plotted as a function of the true underlying timescale. Only simulations with no measurement noise are shown. Top panels show the ratio of the output timescale to the value predicted in section 4.6. Middle panels show the ratio of the standard deviation to the mean output timescale. Bottom panels show the degree by which the input timescale has to change to significantly affect the output timescale. In all plots, blue represents the time at which the 90th percentile of $\Delta m$ first rises above one third the lightcurve amplitude, and orange the time at which it first rises above one half the amplitude.

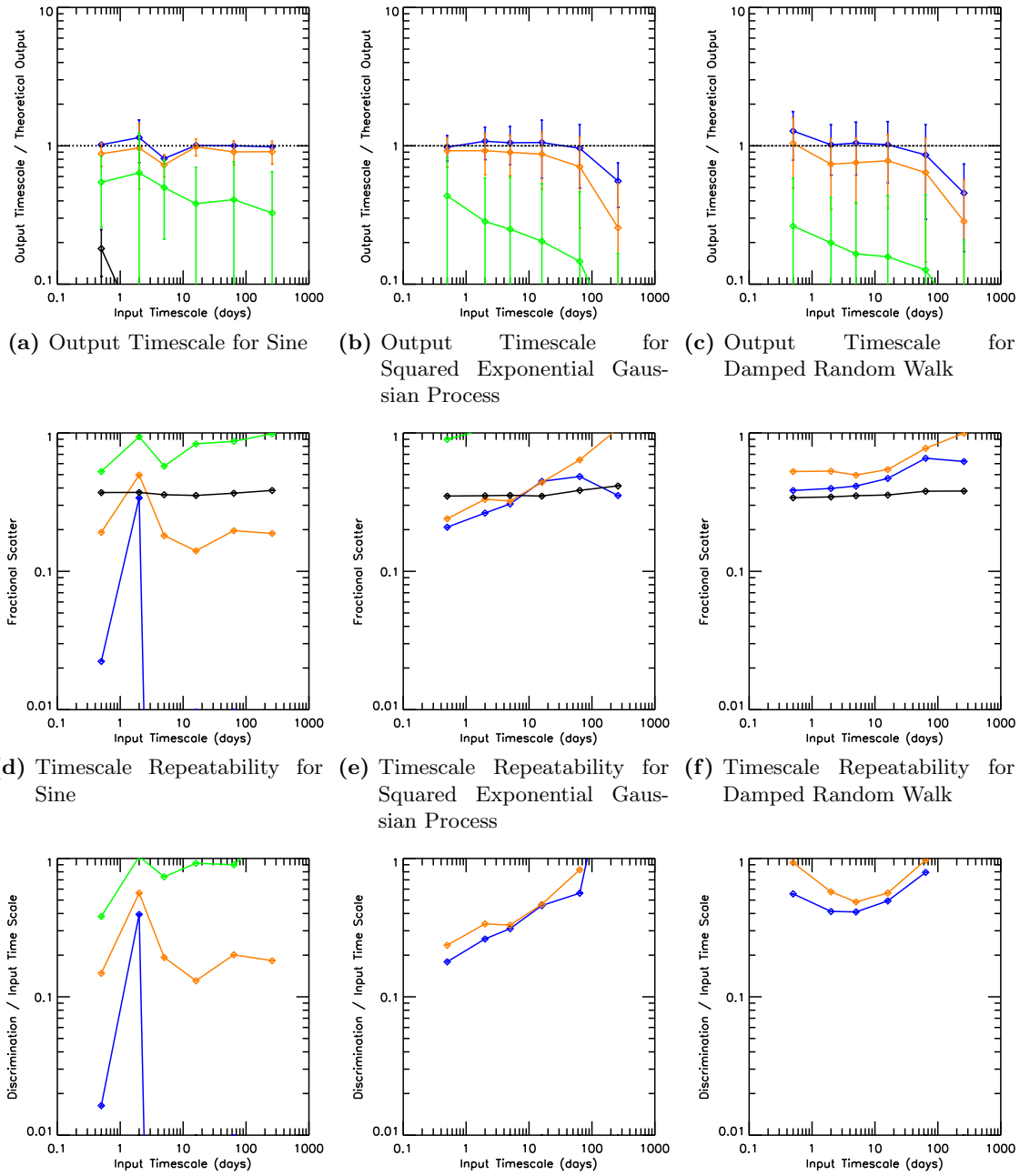


**(a)** Output Timescale for Sine

**(b)** Output Timescale for Squared Exponential Gaussian Process

**(c)** Output Timescale for Damped Random Walk

**(d)** Timescale Repeatability for Sine

**(e)** Timescale Repeatability for Squared Exponential Gaussian Process

**(f)** Timescale Repeatability for Damped Random Walk

**(g)** Timescale Discrimination for Sine

**(h)** Timescale Discrimination for Squared Exponential Gaussian Process

**(i)** Timescale Discrimination for Damped Random Walk

**Figure 5.11:** As Figure 5.10, but plotting only the timescale at which the 90th percentile of $\Delta m$ first rises above half the lightcurve amplitude. Blue represents zero noise, orange represents a signal-to-noise ratio of 20, green a signal-to-noise ratio of 10, and black a signal-to-noise ratio of 4. All lightcurves have an expected 5-95% amplitude of 0.5 magnitudes.

#### 5.5.3.5 Sensitivity to Cadence

In Figure 5.12, I compare the behavior of a $\Delta m$-$\Delta t$ timescale for the two PTF cadences and the YSOVAR cadence. For sinusoidal signals sampled at the full PTF cadence, the timescale is proportional to the period for periods from half a day to 256 days. At the 2010 only cadence, the timescale is well behaved for periods of 6 days or longer, but systematically too high for periods of 2 days or shorter. At the YSOVAR cadence, the timescale is proportional to the period for periods of two days and longer, but not for one day or shorter. For all three cases, the "turnoff" in the plot appears to happen at around the characteristic cadence (see Table 5.1.2 for a definition) or by at most twice this value; the grid is too coarse to make a precise assessment. This suggests that the $\Delta m$-$\Delta t$ timescale cannot properly assess timescales that are not well sampled by the data.

The $\Delta m$-$\Delta t$ timescale shows a somewhat different behavior for damped random walks. At the full PTF cadence, the timescale is proportional to the damping time for timescales between half a day and 64 days. At the 2010 PTF cadence and at the YSOVAR cadence, there is no obvious interval over which the $\Delta m$-$\Delta t$ timescale is proportional to the true timescale. At short timescales, the timescale is overestimated, possibly for the same reasons as for short periods in the sinusoidal case. At long timescales, the timescale is underestimated, because the observed lightcurve no longer probes the slowest variability in the system (cf. the $\Delta m$-$\Delta t$ plots in Figure 5.9).

When applied to a sinusoidal signal, a $\Delta m$-$\Delta t$ timescale has slightly more scatter on the YSOVAR cadence ($\sim 30\%$) than on either of the PTF cadences ($\sim 20\%$). When applied to a damped random walk, the timescale has the most scatter on the YSOVAR cadence ($\sim 100\%$) and the least on the full PTF cadence ($\sim 50\%$). The ability to discriminate input timescales follows a similar pattern. This scaling is most likely driven by either the number of points or the time baseline of each lightcurve, which is worst for the YSOVAR cadence and best for the full PTF cadence.

### 5.5.4 Summary

In Chapter 4, I showed that a $\Delta m$-$\Delta t$ plot can be converted to a scalar timescale by finding the $\Delta t$ bin in which a predetermined quantile of $\Delta m$ first rises above some threshold. The resulting timescales vary by roughly a factor of two across different types of lightcurves, but they are proportional to the true timescale, at least in the ideal case. As a result, $\Delta m$-$\Delta t$ plots are accurate but not versatile, in the sense defined in section 5.1.

I considered in this section the behavior of the $\Delta m$-$\Delta t$ plot and associated timescales when applied to finite, noisy data sets. Even when given imperfect data, the $\Delta m$-$\Delta t$ timescale correlates well with the true timescale of the lightcurve, confirming that it remains accurate even under realistic conditions. However, the behavior of individual lightcurves introduces a lot of scatter into the $\Delta m$-$\Delta t$ timescale, with a typical standard deviation as high as 50-70%. Therefore, $\Delta m$-$\Delta t$ timescales

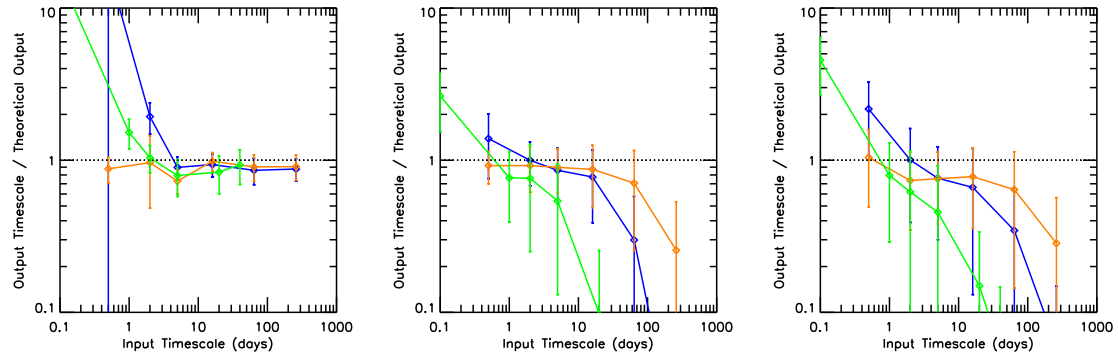


**(a)** Output Timescale for Sine **(b)** Output Timescale for Squared Exponential Gaussian Process **(c)** Output Timescale for Damped Random Walk

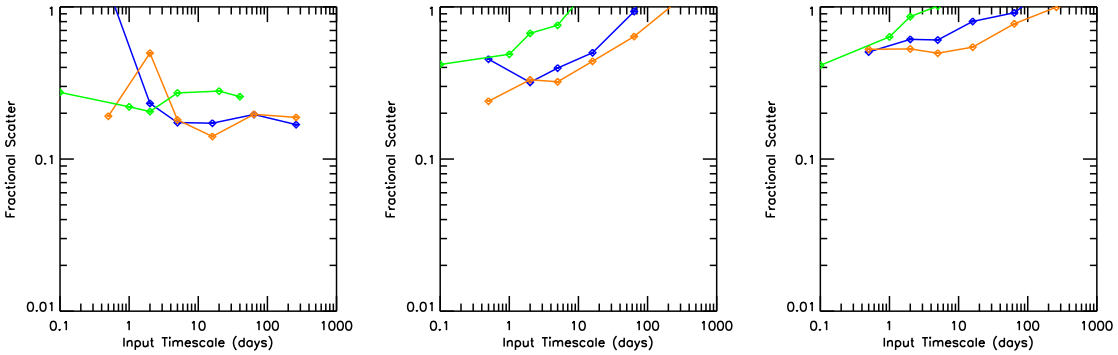


**(d)** Timescale Repeatability for Sine **(e)** Timescale Repeatability for Squared Exponential Gaussian Process **(f)** Timescale Repeatability for Damped Random Walk

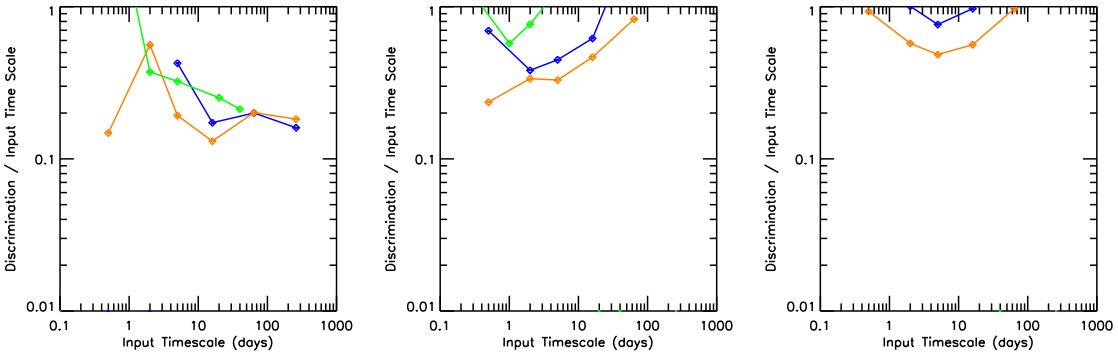


**(g)** Timescale Discrimination for Sine **(h)** Timescale Discrimination for Squared Exponential Gaussian Process **(i)** Timescale Discrimination for Damped Random Walk

**Figure 5.12:** As Figure 5.10, but plotting only the timescale at which the 90th percentile of $\Delta m$ first rises above half the lightcurve amplitude. Orange represents the full PTF cadence, blue the 2010-only PTF cadence, and green the YSOVAR cadence.

are not precise.

The $\Delta m$-$\Delta t$ timescales are moderately sensitive to the presence of noise in the lightcurve. Noise biases the inferred timescale downward; the effect is moderate if the noise RMS is at most one tenth the lightcurve amplitude, but quickly grows more severe at higher noise levels. The $\Delta m$-$\Delta t$ timescale also requires a cadence with a high dynamic range of sampling; it will overestimate the timescale for sources varying faster than about $\sim 1-2$ times the characteristic cadence, and will underestimate the timescale if the true timescale is greater than about 1/15 of the monitoring base line (Figure 5.12c). While the $\Delta m$-$\Delta t$ timescale keeps rising with input timescale past this point, "saturating" only at about 1/5 the base line (the case represented by the undamped random walk model), the discriminating power of the $\Delta m$-$\Delta t$ timescale is worse than a factor of two at these long timescales. Therefore, the $\Delta m$-$\Delta t$ timescale is only dependable in a limited sense.

The $\Delta m$-$\Delta t$ timescale is a potentially useful timescale metric if the data are observed with a high dynamic range cadence, with a coverage window at least $\sim 30$ times the sampling interval, and if the 5-95% amplitude of the variability is at least ten times the RMS of the noise. However, even then the timescales should be assumed to have a $1\sigma$ uncertainty of $\sim 50\%$. The $\Delta m$-$\Delta t$ timescale may be more appropriate for ensemble studies than for characterizing individual lightcurves.

## 5.6 Peak-Finding

Peak-finding is a timescale metric developed by Cody et al. (2014) for well-sampled aperiodic lightcurves. We use a slightly older version of the method from that presented by Cody et al., which begins with the first point on the lightcurve, then identifies the first local minimum or maximum that differs from the first point by a predetermined magnitude threshold. After each local minimum it finds the first local maximum differing from it by the threshold, and vice versa. In this way, the method builds up a list of alternating minima and maxima, discarding low-amplitude fluctuations. The mean time between minima and maxima separated by a given amplitude threshold is a measure of the speed of fluctuations of that amplitude. By repeating the process for a variety of thresholds, one builds up a plot (Figure 5.13) of timescale as a function of magnitude scale, from the level of measurement noise up to the full lightcurve amplitude.

For this study we have altered the algorithm of Cody et al. (2014) by considering the median separation between fluctuations, rather than the mean. The mean separation would be biased high by the large seasonal gaps in our data set. The median separation is much more robust to coverage gaps provided that most of the variability is on timescales shorter than the length of a season, because then the many minima and maxima within each season's coverage dominate the median.

In the analysis presented here, the median peak separation was calculated at each multiple of 0.01 mag, up to the full lightcurve amplitude. The resulting peak-finding plot was converted into a

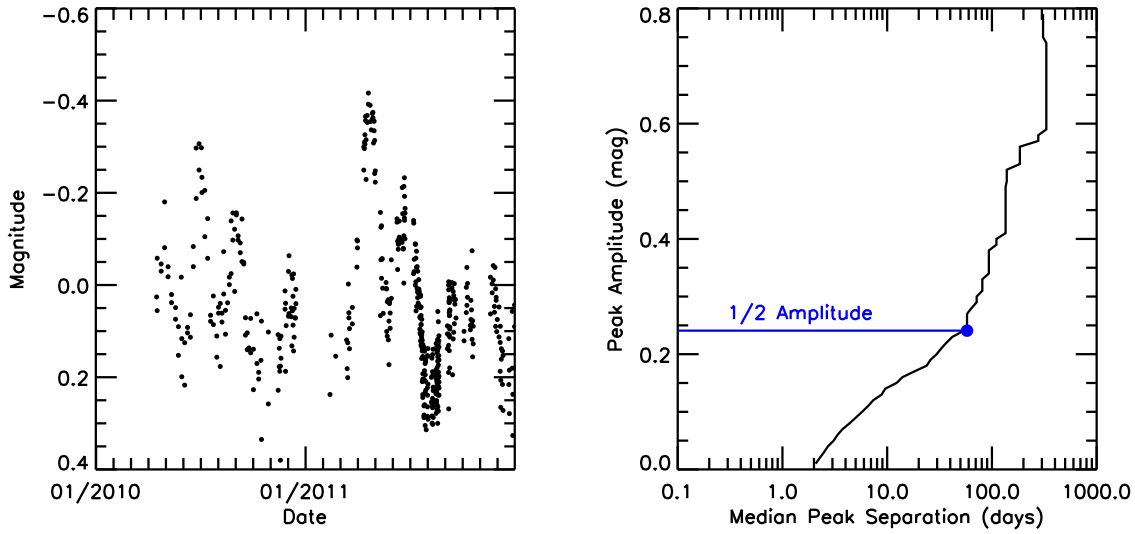


**(a)** Original Lightcurve **(b)** Peak-Finding Plot

**Figure 5.13:** An example of a damped random walk lightcurve with a damping time of 16 days (left) and a peak-finding plot derived from it (right). The blue line illustrates the exercise of defining the timescale as the point at which the peak-finding curve crosses a threshold (half the 5-95% amplitude, in this example).

single timescale by identifying the highest magnitude threshold at which at least one minimum and one maximum were found, and adopting the median separation at 80% of that highest threshold. Two alternative timescales were considered: the median separation between minima and maxima differing by at least one third the amplitude, and the median separation between extrema separated by at least half the amplitude.

### 5.6.1 Example Results

#### 5.6.1.1 Sinusoid

I present in Figure 5.14 the average value of the peak-finding curve for a set of 1,000 simulations of a sinusoidal lightcurve with different periods. A common feature to all curves is a steep rise at half the period. This rise makes timescales based on the peak-finding curve highly consistent for sinusoids, regardless of the magnitude threshold used.

#### 5.6.1.2 Damped Random Walk

Figure 5.15 shows the average peak-finding curve for simulations of a damped random walk. Except for a knee at 2-3 times the noise level, the peak-finding curves show no distinct features. The curves corresponding to long timescale variables rise more slowly than those corresponding to short timescale variables.

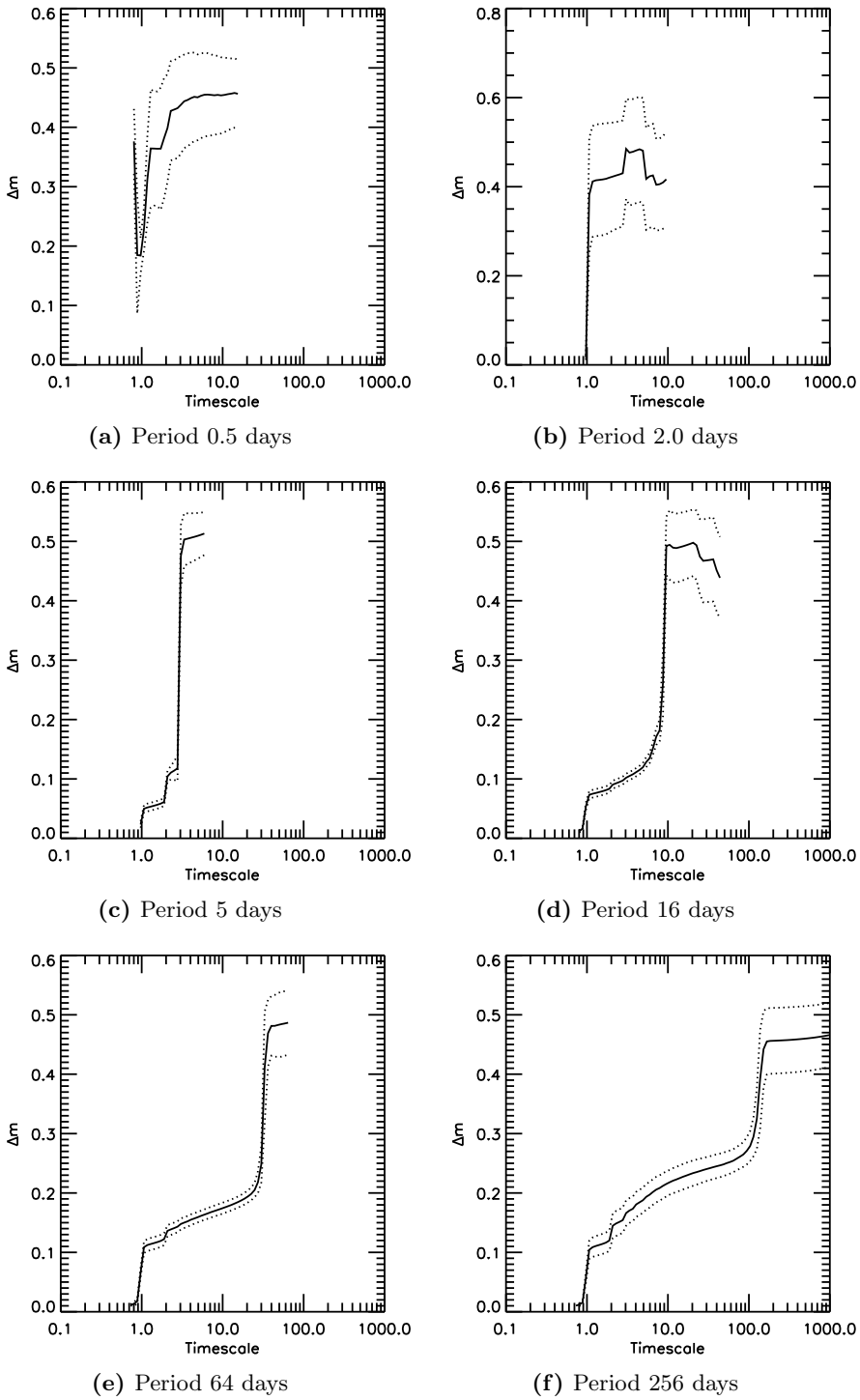


**(a)** Period 0.5 days

**(b)** Period 2.0 days

**(c)** Period 5 days

**(d)** Period 16 days

**(e)** Period 64 days

**(f)** Period 256 days

**Figure 5.14:** The mean peak-finding function from 1,000 simulations of a sine wave at several representative periods. Dotted lines represent the standard deviation of the peak-finding function at each time lag.

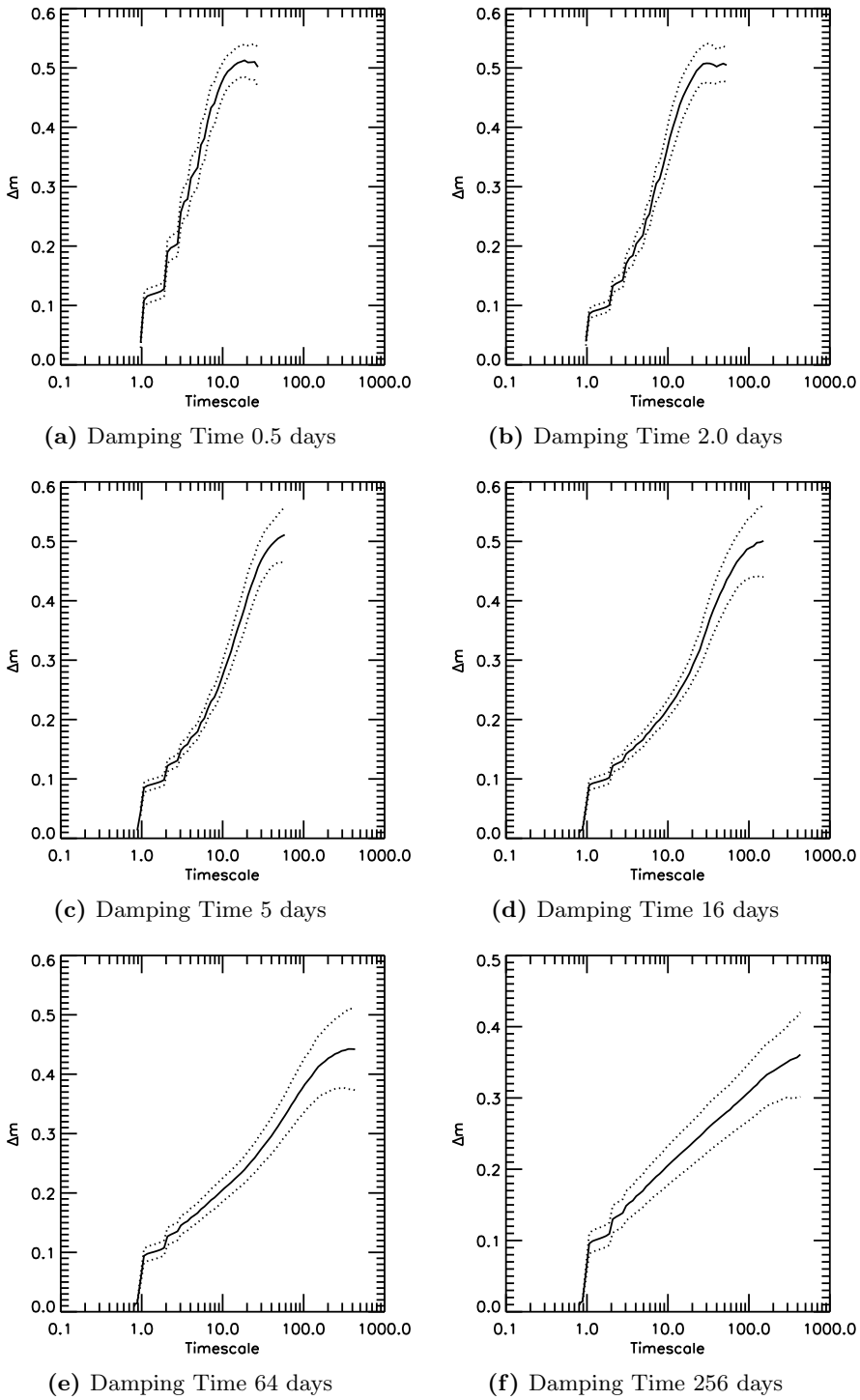


**(a)** Damping Time 0.5 days

**(b)** Damping Time 2.0 days

**(c)** Damping Time 5 days

**(d)** Damping Time 16 days

**(e)** Damping Time 64 days

**(f)** Damping Time 256 days

**Figure 5.15:** The mean peak-finding function from 1,000 simulations of a damped random walk at several representative timescales. Dotted lines represent the standard deviation of the peak-finding function at each time lag.

#### 5.6.1.3 Other Lightcurves

On a squared exponential Gaussian process, a peak-finding plot shows a leveling out on long timescales, indicating that high-amplitude minima and maxima rapidly become rare for these lightcurves. However, the peak-finding plot varies too much from lightcurve to lightcurve for this feature to serve as a useful timescale metric. On a random walk, which has no characteristic timescale, the peak-finding plot generally slopes upward, as it does for a damped random walk. However, the peak-finding plot for a random walk has many irregularities, including areas where it levels out.

### 5.6.2 Performance

#### 5.6.2.1 Qualitative Behavior

In Figure 5.16, I compare the performance of three different timescales, each defined as the time separation at which the peak-finding curve crosses a different threshold: one third the lightcurve amplitude, one half the lightcurve amplitude, or 80% of the highest $\Delta m$ in the peak-finding curve. The highest $\Delta m$ can be anywhere between half the lightcurve amplitude and its full amplitude, depending on the phase at which the lightcurve is initially observed.

For sinusoidal signals, the calculated timescale is proportional to the period for periods of two days or longer, and varies little with the choice of cutoff value. One exception is the time at which the peak-finding curve crosses one third the amplitude, which is biased low by a "bump" at timescales of two days (visible in Figure 5.14f) that may be the result of high-$\sigma$ outliers in the noise. For damped random walks, the calculated timescale increases with the damping time, but at a slower rate than a strict proportionality. The time at which the peak-finding curve crosses 80% of its maximum comes closest to a linear dependence on the true timescale. In neither case do the inferred timescales ever fall below one day; the median separation between peaks is always at least one day even if the magnitude threshold is lowered far enough to probe noise.

#### 5.6.2.2 Precision

The middle two panels of Figure 5.16 show the scatter in the estimated timescale over multiple simulation runs. For sinusoidal signals, the scatter is negligible for all but the shortest and longest periods. The scatter in the timescale is much larger for damped random walks; it is on the order of 20% for short timescale lightcurves, but grows to over 100% at longer timescales. The times at which the peak-finding curve crosses one third and one half the amplitude have consistently less scatter than timescales based on 80% of the tip of the peak-finding plot.

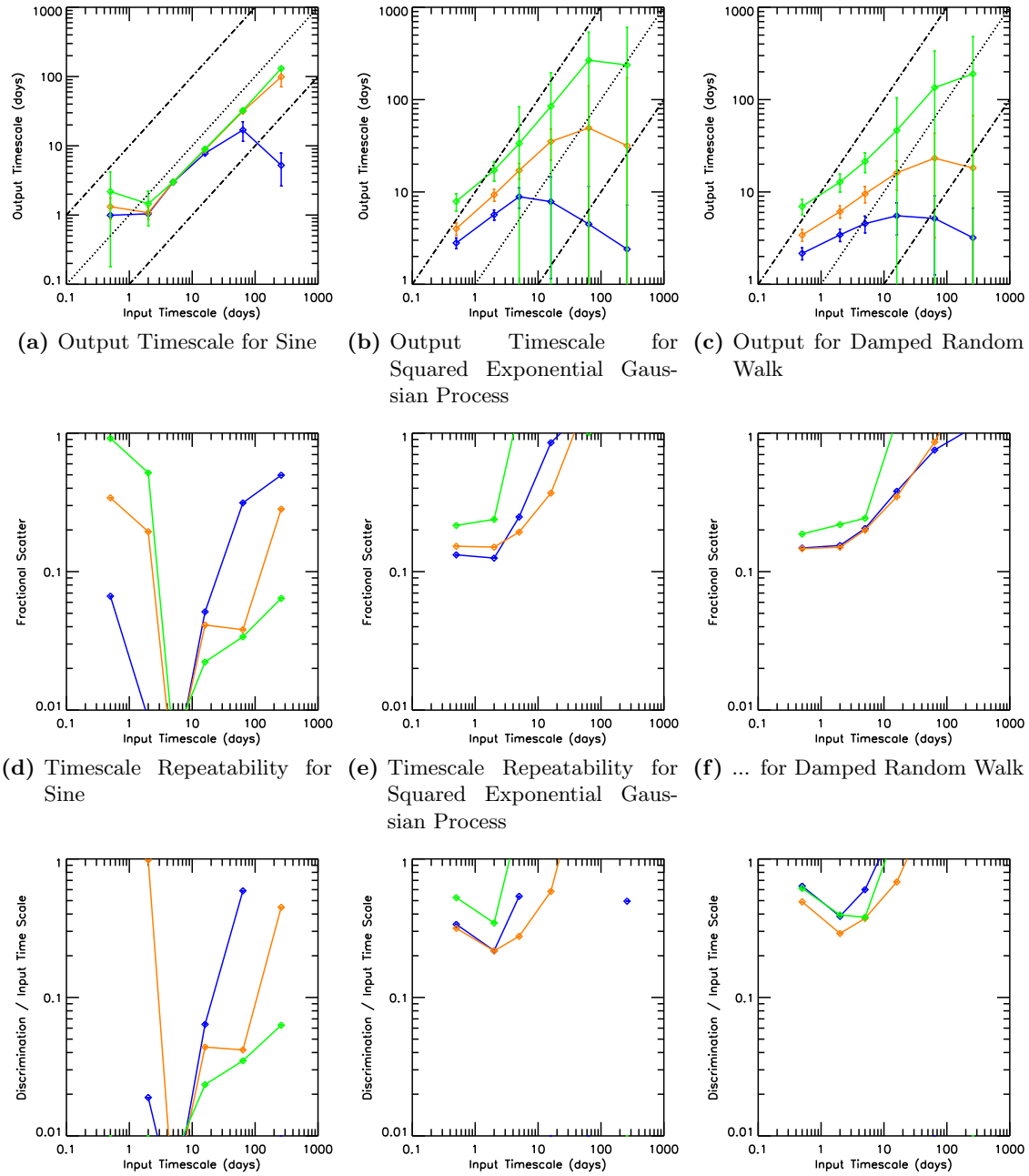


**(a)** Output Timescale for Sine

**(b)** Output Timescale for Squared Exponential Gaussian Process

**(c)** Output for Damped Random Walk

**(d)** Timescale Repeatability for Sine

**(e)** Timescale Repeatability for Squared Exponential Gaussian Process

**(f)** ... for Damped Random Walk

**(g)** Timescale Discrimination for Sine

**(h)** Timescale Discrimination for Squared Exponential Gaussian Process

**(i)** ... for Damped Random Walk

**Figure 5.16:** The timescale calculated from a peak-finding plot, plotted as a function of the true underlying timescale. Only simulations with no measurement noise are shown. Top panels show the average value of the output timescale. Middle panels show the ratio of the standard deviation to the mean output timescale. Bottom panels show the degree by which the input timescale has to change to significantly affect the output timescale. In all plots, blue represents the time at which the peak-finding curve first rises above one third the lightcurve amplitude, orange the time at which it rises above one half the amplitude, and green the time at which the peak-finding curve crosses 80% of its highest value.

#### 5.6.2.3 Discrimination

Because the peak-finding timescale is linear with the period for a sine, the discrimination shows the same behavior as the scatter. Because the peak-finding timescale grows more slowly than the damping time for a damped random walk, and even levels out for long timescale signals, the discriminating power of the peak-finding plot is never better than 40%. The discriminatory power does not depend on how the peak-finding plot is converted to a timescale: timescales based on 80% of the highest point in the plot show more scatter but also scale better with the lightcurve timescale on average, and the advantage and disadvantage compared to timescales measured at a fixed fraction of the amplitude cancel out.

#### 5.6.2.4 Sensitivity to Noise

Figure 5.17 shows the performance of a peak-finding timescale as a function of the signal-to-noise ratio of the lightcurve. The average value of the timescale changes very little between an effectively infinite signal-to-noise and a signal-to-noise ratio of 20 in the case of a sinusoidal signal, but decreases systematically with signal-to-noise in the case of a damped random walk. In both cases, at signal-to-noise of 10 or less the peak-finding timescale is barely correlated with the true timescale.

The precision of timescale measurements of a sinusoidal signal generally increases with signal-to-noise, as one might expect. The precision of timescale measurements of a damped random walk, on the other hand, decreases with signal-to-noise. This may indicate that at low signal-to-noise the timescale is strongly affected by a fixed systematic term.

The discriminating power of the peak-finding timescale roughly follows the precision for a sine wave, but is substantially poorer — no better than 30% — than the precision for a damped random walk. As noted above, for signal-to-noise of 10 or less the peak-finding timescale cannot discriminate between short- and long-timescale signals.

#### 5.6.2.5 Sensitivity to Cadence

In Figure 5.18, I compare the behavior of a peak-finding timescale for both PTF cadences and the YSOVAR cadence. For sinusoidal signals sampled at either the full PTF cadence or the YSOVAR cadence, the timescale is proportional to the period for periods of two days or more. For the more sparsely sampled 2010-only PTF cadence, peak-finding overestimates the period for a 2-day sine by nearly a factor of two. The average behavior of the peak-finding timescale, when applied to a damped random walk, is qualitatively similar regardless of the lightcurve cadence.

The peak-finding timescale shows the least scatter for lightcurves observed with the full PTF cadence, more for lightcurves observed with the 2010-only PTF cadence, and the highest amount of scatter for the YSOVAR cadence. This is true regardless of whether the timescale is measured

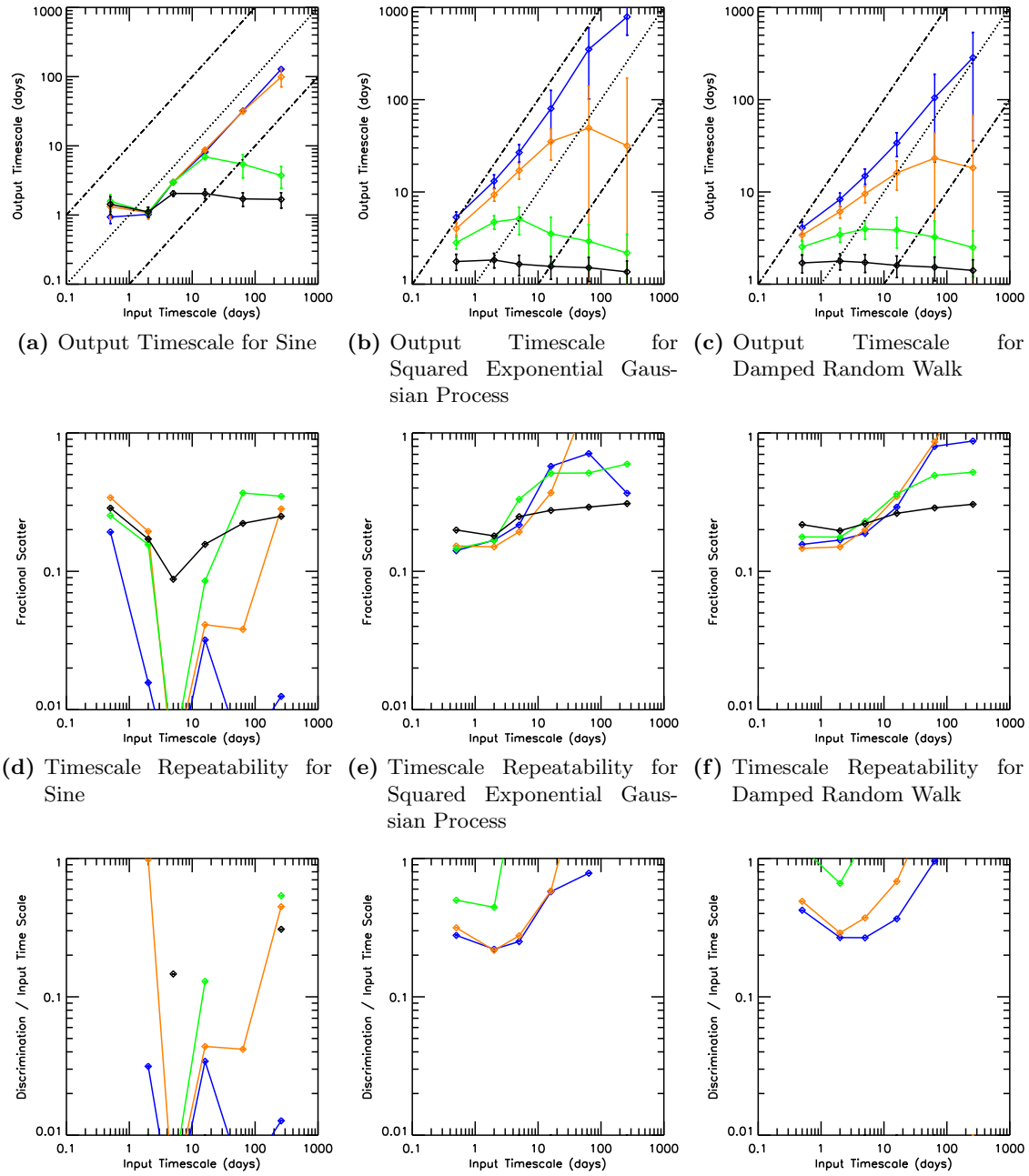


**(a)** Output Timescale for Sine

**(b)** Output Timescale for Squared Exponential Gaussian Process

**(c)** Output Timescale for Damped Random Walk

**(d)** Timescale Repeatability for Sine

**(e)** Timescale Repeatability for Squared Exponential Gaussian Process

**(f)** Timescale Repeatability for Damped Random Walk

**(g)** Timescale Discrimination for Sine

**(h)** Timescale Discrimination for Squared Exponential Gaussian Process

**(i)** Timescale Discrimination for Damped Random Walk

**Figure 5.17:** As Figure 5.16, but plotting only the timescale at which the peak-finding curve first reaches one half the lightcurve amplitude. Blue represents zero noise, orange represents a signal-to-noise ratio of 20, green a signal-to-noise ratio of 10, and black a signal-to-noise ratio of 4. All lightcurves have an expected 5-95% amplitude of 0.5 magnitudes.

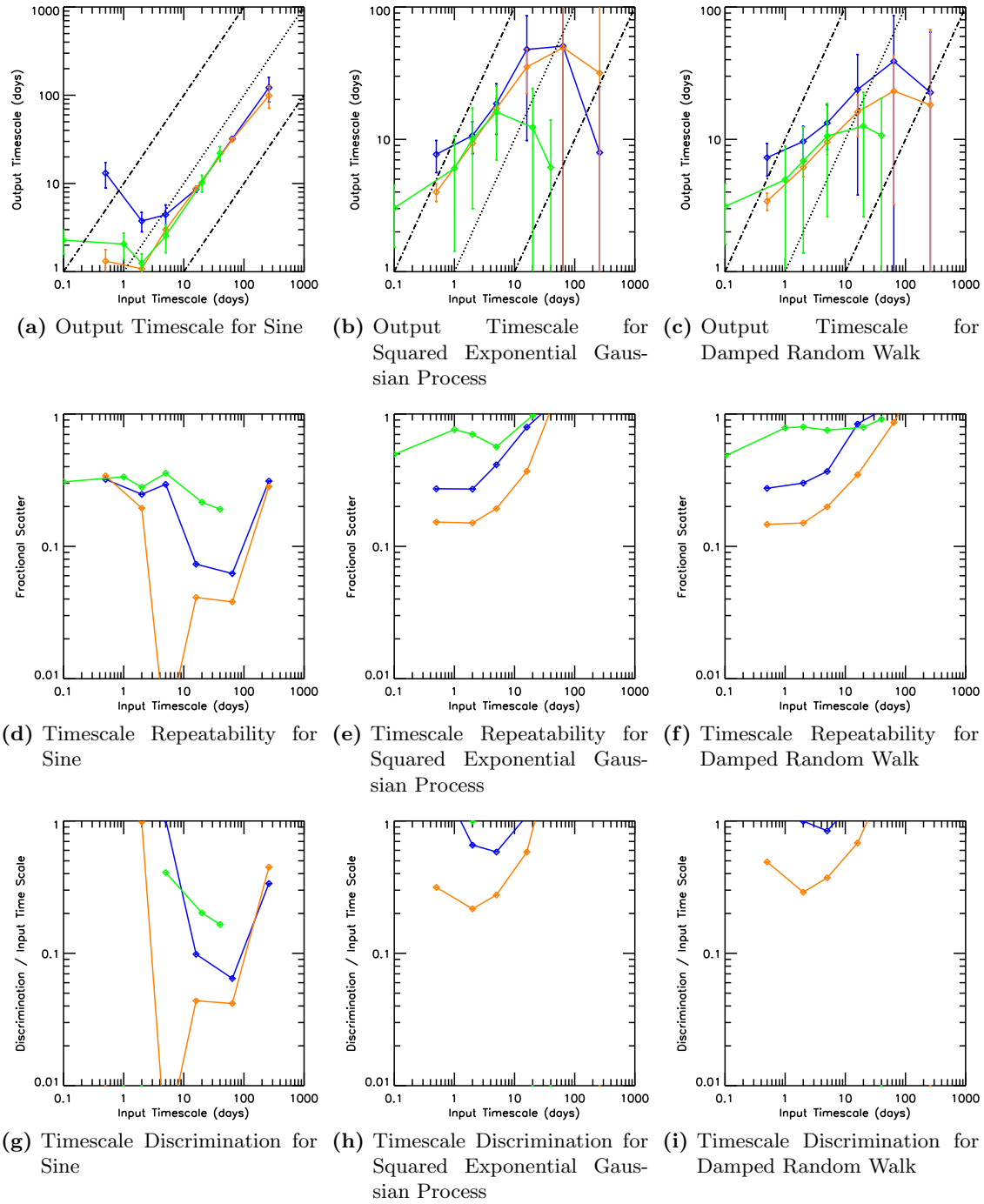


**(a)** Output Timescale for Sine

**(b)** Output Timescale for Squared Exponential Gaussian Process

**(c)** Output Timescale for Damped Random Walk

**(d)** Timescale Repeatability for Sine

**(e)** Timescale Repeatability for Squared Exponential Gaussian Process

**(f)** Timescale Repeatability for Damped Random Walk

**(g)** Timescale Discrimination for Sine

**(h)** Timescale Discrimination for Squared Exponential Gaussian Process

**(i)** Timescale Discrimination for Damped Random Walk

**Figure 5.18:** As Figure 5.16, but plotting only the timescale at which the peak-finding curve first reaches one half the lightcurve amplitude. Orange represents the full PTF cadence, blue the 2010-only PTF cadence, and green the YSOVAR cadence.

for sinusoidal signals or for damped random walks. The discriminating power shows a similar trend with signal-to-noise ratio.

### 5.6.3 Summary

Because it is based on extrema of a lightcurve rather than its average behavior, peak-finding does not lend itself easily to analytical treatment and was not studied in Chapter 4. The numerical simulations presented in this section suggest that, while the peak-finding timescale correlates with the input timescale for a variety of lightcurves, the shape of the scaling is sensitive to the type of lightcurve. In the sense of section 5.1, it is accurate but not versatile.

For rapidly varying signals the peak-finding timescale shows a scatter of ∼10-20% for long time series such as the PTF cadences, but somewhat more scatter (∼ 40%) for lightcurves observed with the YSOVAR cadence. Regardless of cadence, the scatter grows to a factor of two for aperiodic lightcurves with timescales longer than 1/15 to 1/20 the observing base line. Therefore, peak-finding timescales are not precise except for time series many times longer than the signals of interest.

The peak-finding timescales are moderately sensitive to the presence of noise in the lightcurve. Noise biases the inferred timescale downward; the effect is moderate if the noise RMS is at most one tenth the lightcurve amplitude, but quickly grows more severe at higher noise levels. The average behavior of the lightcurve seems to depend little on the cadence adopted, showing a similar slope (Figure 5.18c) up to timescales of order the time series base line. As noted above, the timescale needs a long time series to provide precise measurements. The timescale therefore is not dependable: its performance depends on both signal-to-noise and the cadence.

The peak-finding timescale is best suited for long-term monitoring of short-timescale variability. The 5-95% amplitude of the variability should be at least ten times the RMS of the noise to ensure that noise does not confuse the peak-finding algorithm. Even then, the peak-finding timescale should be interpreted only in an ordinal sense; it can determine which lightcurves vary more rapidly than others, but may get the absolute timescale wrong by as much as an order of magnitude.

## 5.7 Gaussian Process Modeling

Gaussian process regression is an increasingly popular analysis tool for modeling aperiodic time series that are assumed to consist of a smooth (but unknown) function plus noise. Since a Gaussian process has no specific functional form, a good fit is instead characterized by a high likelihood that the data were drawn from a Gaussian distribution with a particular covariance matrix.

In the most common case, the one I use here, the covariance matrix $K$ is assumed to be the sum of a squared exponential Gaussian process, characterized by an amplitude $\sigma$ and a coherence time

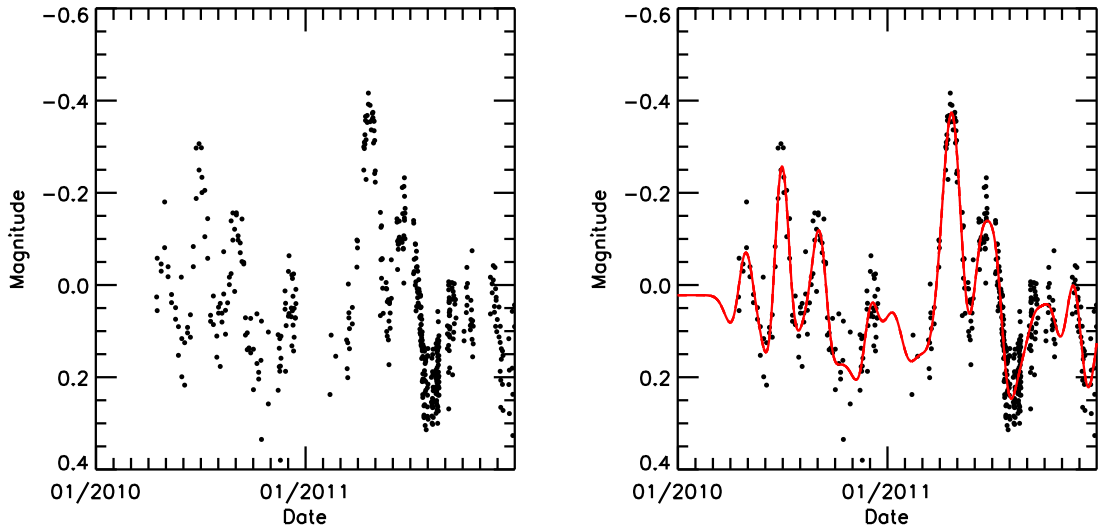


**(a)** Original Lightcurve **(b)** Gaussian Process Fit

**Figure 5.19:** An example of a damped random walk lightcurve with a damping time of 16 days (left) and the best GP fit (right). Formal errors in the model are far smaller than the scatter of actual data points. The timescale is one of the model parameters, but cannot be directly read from the plot.

$\tau$, and a white noise process, characterized by an amplitude $\sigma_n$:

$$K_{ij} = K(t_i, t_j) = \sigma^2 \exp\left(-\frac{(t_i - t_j)^2}{2\tau^2}\right) + \sigma_n^2 \delta(t_i, t_j)$$

where $\delta$ denotes the Kronecker delta. For the purposes of this study, the two amplitudes $\sigma$ and $\sigma_n$ are nuisance parameters, and only the best fit coherence time $\tau$ is reported. The fitting package we used (`gptk`) used conjugate gradient descent to maximize the likelihood

$$L(\sigma, \tau, \sigma_n | \vec{m}) = -\frac{1}{2}\vec{m}^{\mathrm{T}} K^{-1} \vec{m} - \frac{1}{2}\log|K| - \frac{n}{2}\log 2\pi$$

given the vector of observed magnitudes $\vec{m}$.

Because the likelihood function for Gaussian process regression involves the inverse of the $N \times N$ covariance matrix $K$, where $N$ is the number of data points, computing the likelihood function is a cubic operation in $N$. Since conjugate gradient descent may require up to $N$ iterations to converge, the overall task of fitting a lightcurve is *quartic* in $N$. To keep running times reasonable, I only attempted Gaussian process regression on lightcurves simulated on the YSOVAR cadence ($N = 39$), and only generated 30 lightcurves per grid point rather than the usual 1,000. The lightcurve parameter grid was the same as before, except that the noise-free case was replaced with a signal-to-noise ratio of 300. Since the amount of noise in the data is one of the free parameters, and since `gptk` fits the parameters in log space, attempting to fit a noise-free squared exponential

Gaussian process ($\ln \sigma_n = -\infty$) with a noisy squared exponential Gaussian process would never converge.

### 5.7.1 Performance

#### 5.7.1.1 Qualitative Behavior

Figure 5.21 shows the performance of timescales derived from Gaussian process fitting as a function of the signal-to-noise ratio of the magnitude measurements. In many cases the fit failed to converge at all, with the fraction of times in which the fit succeeded shown in Figure 5.20. The curves in Figure 5.21 are only for those modeling attempts that returned a valid solution.

For sinusoidal signals, the calculated timescale is proportional to the period for periods of two days or longer, while timescales for shorter sine periods tend to be higher than those for longer periods. For squared exponential random walks, the timescale generally increases with the true timescale except in low signal-to-noise simulations. For damped random walks, on the other hand, the calculated timescale is always 1-4 days, with only a weak dependence on underlying timescale. This might be because the damped random walk has substantial structure on timescales shorter than the characteristic timescale, and Gaussian process fitting is reported to be dominated by the most rapidly varying component (Miller, priv. comm. (2012)).

For all three types of lightcurves, the best fit timescale has a systematic trend in the sense that the timescale is lower for lower signal-to-noise lightcurves. The same behavior was observed for $\Delta m$-$\Delta t$ plots and for peak-finding, and just as in those cases the likely cause is that the noise (which, by construction, has an infinitesimal timescale) is being mistaken for real variability. Why this confusion should happen when fitting a model that explicitly includes a white noise term, however, is unclear. It may be a bias introduced by the use of maximum-likelihood methods, combined with a partial degeneracy in the model between a short timescale for the main process and a strong white noise component. Choi et al. (2014) also encountered a bias towards short timescales when fitting damped random walk models to noisy lightcurves; we may be seeing a related issue here.

Unlike the other timescale metrics described in this chapter, Gaussian process fitting provides an uncertainty for the best fit timescale. The accuracy of these uncertainties is tested in Figure 5.20, which plots

$$\chi^2 = \sum_i \frac{(\hat{\tau}_i - \langle \hat{\tau}_i \rangle)^2}{\sigma^2_{\hat{\tau}_i}}$$

where $i$ denotes one of the 30 lightcurves in each run, $\hat{\tau}_i$ is the timescale returned by the fit, and $\sigma_{\hat{\tau}_i}$ is the error returned by the fit. In general, the formal errors reflect the true uncertainty in $\hat{\tau}$ for short timescale lightcurves, but grossly underestimate it for longer timescale lightcurves, with the discrepancy growing at decreasing signal-to-noise. Curiously, even when the lightcurve is a squared exponential process with noise — in other words, the model being fitted is perfectly accurate — the

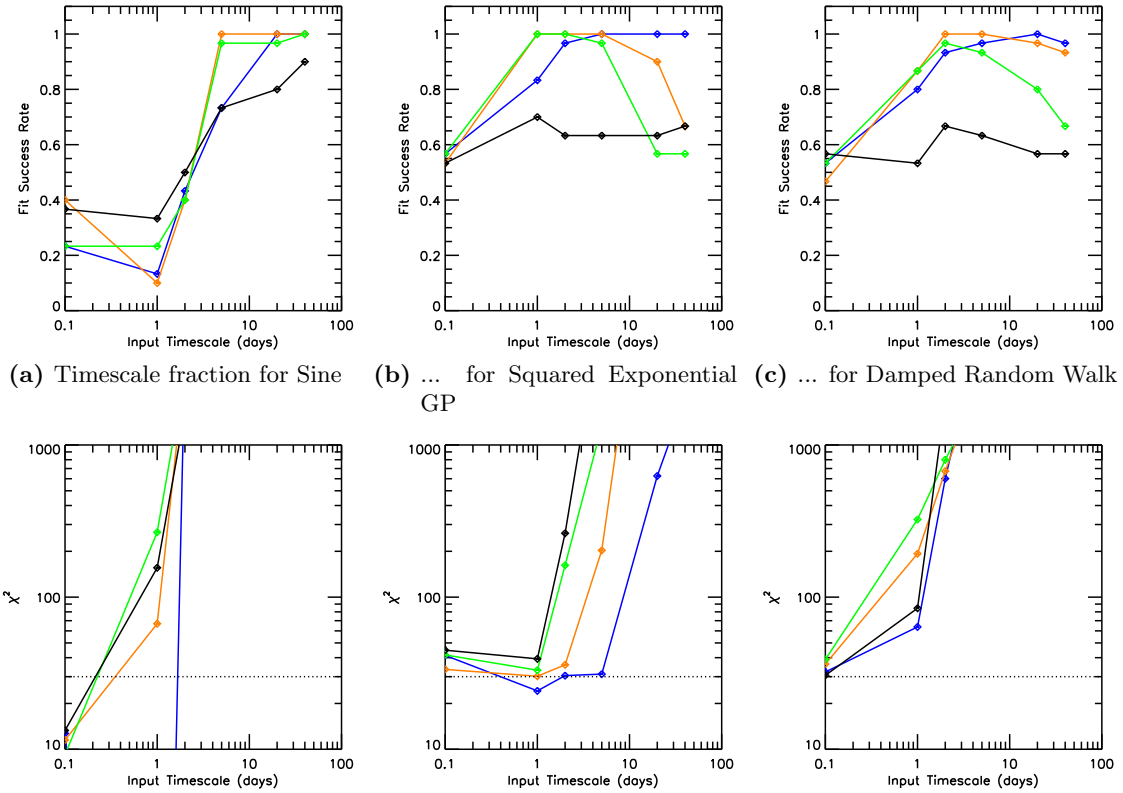


**(a)** Timescale fraction for Sine **(b)** ... for Squared Exponential GP **(c)** ... for Damped Random Walk

**(d)** GP $\chi^2$ for Sine **(e)** ... for Squared Exponential GP **(f)** ... for Damped Random Walk

**Figure 5.20:** In the top row, the fraction out of 30 simulations for which the Gaussian process fit converged. All runs are with an expected 5-95% amplitude of 0.5 mag. In the bottom row, the $\chi^2$ statistic for each set of 30 simulations, defined as the total squared deviation of individual measurements from their mean, normalized by their formal errors. The dotted line at $\chi^2 = 30$ represents the expected value if the formal errors are accurate.

scatter in $\hat{\tau}$ still exceeds that predicted by the formal uncertainties. The excess scatter at long input timescales may indicate that the time series no longer covers a long enough interval to sample the full variability; given the steep dependence of running time on lightcurve length, we did not test any extensions of the YSOVAR cadence.

#### 5.7.1.2 Precision

The middle two panels of Figure 5.21 show the scatter in the estimated timescale over multiple simulation runs. For sinusoidal signals and squared exponential Gaussian process signals, the scatter is typically a few tens of percent. The scatter in the timescale is much larger for damped random walks, on the order of 80% or more.

#### 5.7.1.3 Discrimination

Because the Gaussian process fitting timescale is linear with the period for a sine, the discrimination shows the same behavior as the scatter. Because the timescale grows very slowly with the damping time for a damped random walk, the discriminating power of Gaussian process regression is never better than a factor of two. The simulations with squared exponential Gaussian process lightcurves are intermediate between these two cases, with good discriminating power at high signal-to-noise but rapid degradation as the data get noisier.

#### 5.7.1.4 Completeness

The Gaussian process fit rarely converges when applied to sines with periods shorter than 2 days, has a roughly 40% convergence rate at 2 days, and has a high ($> 90\%$) convergence rate at longer periods. This threshold roughly corresponds to the period at which the timescale begins to show a linear dependence on the period. There is no clear trend with signal-to-noise.

When applied to a short timescale squared exponential Gaussian process lightcurve, the fit converges roughly 50% of the time, with higher rates for longer true timescales. Curiously, while for timescales of 10 or 20 days the convergence rate is maximized at high signal-to-noise, for timescales of 1 or 2 days the convergence rate is higher for a signal-to-noise ratio of 10 or 20 than at signal-to-noise of 300. As with the sines, the change between these two regimes corresponds to a change in the behavior of the timescale itself: at long periods, the timescale is systematically underestimated at low signal-to-noise, just when the fraction of successful fits falls.

The rate of successful convergence is qualitatively the same for a damped random walk as for a squared Gaussian process, except with a weaker dependence on signal-to-noise. There is no obvious change in the behavior of the timescales at 5 days, when the convergence rate for low signal-to-noise lightcurves begins to fall.

#### 5.7.1.5 Sensitivity to Noise

Figure 5.21 shows the performance of Gaussian process fitting as a function of the signal-to-noise ratio of the lightcurve. When applied to either sinusoidal or squared exponential Gaussian processes, the timescale inferred from Gaussian process fitting decreases systematically with signal-to-noise. When applied to a damped random walk, the timescale shows no obvious trend with signal-to-noise, but also seems to depend little on the intrinsic properties of the lightcurve.

The precision of timescale measurements of a sinusoidal signal or a squared exponential Gaussian process signal generally increases with signal-to-noise, as one might expect. The fractional uncertainty is 10-30% for mid-range timescales (1-10 days), but rises to 100% at timescales of 1 day or shorter, and 20 days or longer for the Gaussian process. The scatter in timescale measurements also increases at low signal-to-noise for a damped random walk, but to a much lesser degree than in the other two cases.

The discriminating power of the Gaussian process timescale roughly follows the precision for a sine wave and for a squared exponential Gaussian process, although in the latter case the degradation with signal-to-noise is much steeper than for the precision. The Gaussian process has almost no discriminating power when applied to a damped random walk, thanks to the combination of weak average dependence on the damping timescale and high scatter from lightcurve to lightcurve.

### 5.7.2 Summary

While in principle Gaussian process models can be treated analytically, doing so in the limit of infinite sampling as required by Chapter 4 would have been prohibitively complex. The numerical simulations presented in this section suggest that the Gaussian process timescale is correlated with the true timescale for some kinds of lightcurves but not others, so the metric is not accurate in the sense of section 5.1. In addition, the fit does not always converge, for reasons unknown; it is, strictly speaking, not universal.

I do not recommend the use of Gaussian process models as a timescale metric, unless the data are known in advance to have only a small number of frequency components. For complex lightcurves, such as damped random walks, the model results are inaccurate as well as computationally expensive.

## 5.8 Revisiting Bursters and Faders

Earlier in this chapter, I tested how well several candidate timescale metrics could reproduce the known timescales of synthetic lightcurves. While informative, this test has the limitation that it cannot be applied to real data, where the "true timescale" is necessarily unknown. A test that *does* work for real data is desirable, if only for reassurance that the results of Chapter 4 and this chapter

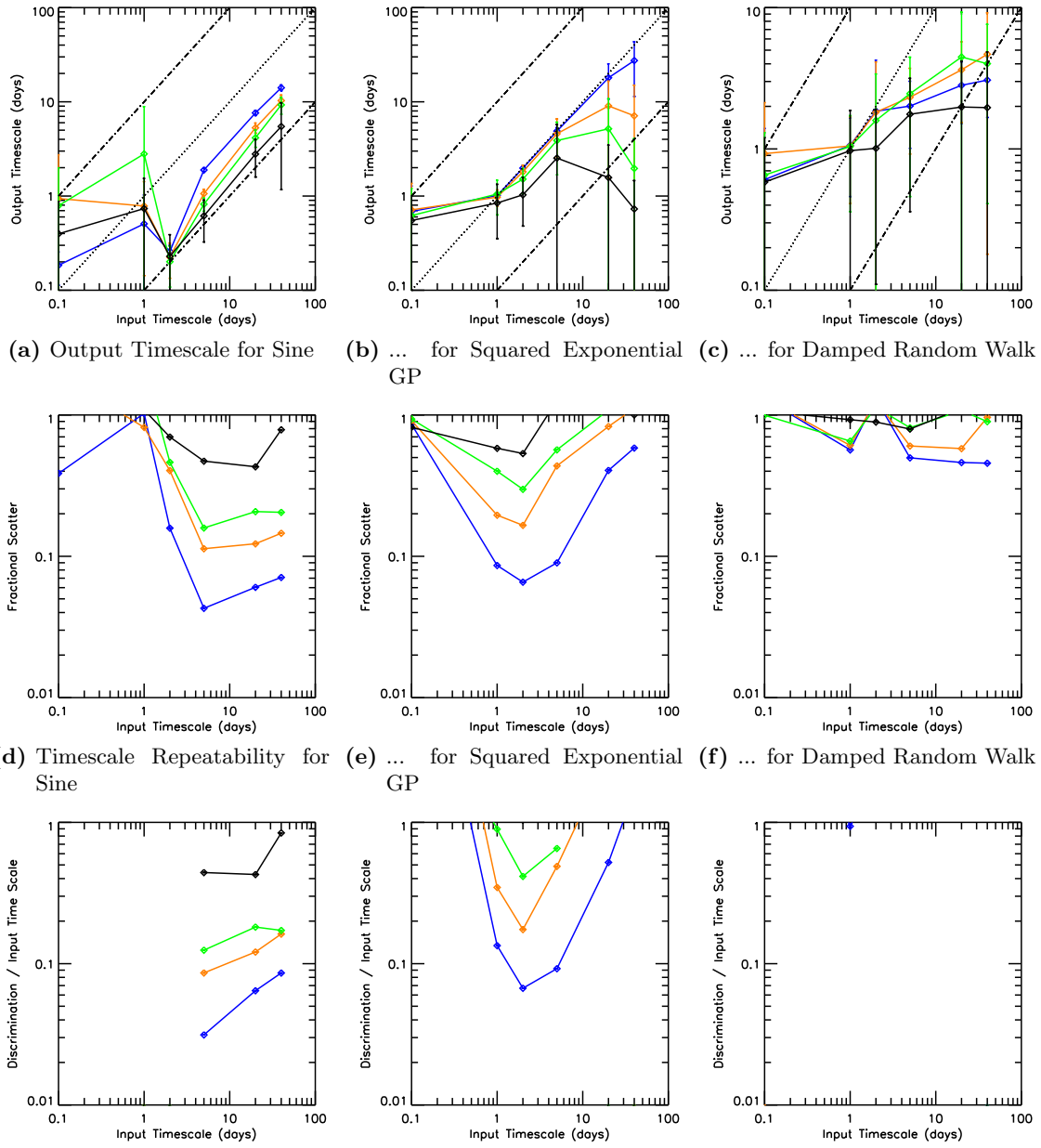


**(a)** Output Timescale for Sine **(b)** ... for Squared Exponential GP **(c)** ... for Damped Random Walk

**(d)** Timescale Repeatability for Sine **(e)** ... for Squared Exponential GP **(f)** ... for Damped Random Walk

**(g)** Timescale Discrimination for Sine **(h)** ... for Squared Exponential GP **(i)** ... for Damped Random Walk

**Figure 5.21:** The timescale calculated from a squared exponential Gaussian process model, plotted as a function of the true underlying timescale. Only runs with an expected 5-95% amplitude of 0.5 mag are shown. Top panels show the average value of the output timescale. Middle panels show the ratio of the standard deviation to the mean output timescale. Bottom panels show the degree by which the input timescale has to change to significantly affect the output timescale. In all plots, blue represents a signal-to-noise ratio of 300, orange represents a signal-to-noise ratio of 20, green a signal-to-noise ratio of 10, and black a signal-to-noise ratio of 4.

do not apply only to mathematically tractable signals.

Another criterion a good timescale metric should satisfy is that its output looks plausible under visual inspection of the corresponding lightcurve. This is necessarily a subjective criterion, as confirmation bias (Nickerson, 1998, and references therein) ensures that there will be multiple, possibly very different, values for a timescale that all look "reasonable" when a lightcurve is compared to them *a posteriori*. Therefore, plausibility is a necessary but insufficient criterion, and should be treated only as a supplement to the more objective tests presented in Chapter 4 and earlier in this chapter.

For this test, I selected the 41 sources listed in Table 3.3 as having bursting or fading behavior. I tested three timescale metrics on this set of lightcurves. The first was a $\Delta m$-$\Delta t$ plot with $\Delta t$ bins in steps of 0.15 dex from $10^{-1.97}$ days to the maximum length of the lightcurve. The characteristic timescale was defined to be the time bin in which the 90th percentile of the $\Delta m$ values first exceeds half the lightcurve's amplitude, itself defined as the difference between 5th and 95th percentiles. The second metric was a peak-finding plot, with the characteristic timescale defined to be the separation between peaks differing by at least half the lightcurve amplitude. The third metric was a Gaussian process fit. The results are presented in Table 5.3.

Correlations between the computed and by-eye timescales are shown in Figures 5.22 and 5.23. The $\Delta m$-$\Delta t$ timescale shows a weak correlation with both burst and fade width, but not with burst or fade separation. The peak-finding timescale may be very weakly correlated with event width, but it is not correlated with event separation. The Gaussian process timescale is not correlated at all with any of the by-eye timescales.

I also inspected several lightcurves — those for LkH$\alpha$ 139, LkH$\alpha$ 174, FHO 15, FHO 19, FHO 25, and FHO 26 — by eye to confirm whether the computed timescale metrics corresponded to real structure in the lightcurve. For the lightcurve of FHO 26, I refer the reader to subsection 3.6.1. For $\Delta m$-$\Delta t$ timescales, the comparison was made by estimating the lightcurve amplitude by eye, then searching for pairs of observations (not necessarily associated with bursting or fading) separated by half that amplitude. The range of time separations between such pairs tended to include the $\Delta m$-$\Delta t$ timescale, indicating that the timescale is at least roughly consistent with visual inspection of the lightcurve. For peak-finding timescales, I estimated the lightcurve amplitude by eye, then searched for local minima and maxima (again, not necessarily distinct bursting or fading events) separated by at least half that amplitude. Depending on the lightcurve, the separations between these manually identified peaks tended to be 2-3 times longer or 2-3 times shorter than the peak-finding timescale, leaving the peak-finding results difficult to interpret.

$\Delta m$-$\Delta t$ timescales seem easiest to relate to specific variations within the corresponding lightcurve. Peak-finding timescales are harder to associate with specific structures, and the best-fit timescales produced by Gaussian process models appear to have no correlation at all with any intuitive measure

| Source | Burst Width(s) | Burst Separation(s) | Fade Width(s) | Fade Separation(s) | $\Delta m$-$\Delta t$ | Peak-Finding | Gaussian Process |
|---|---|---|---|---|---|---|---|
| 205032.32+442617.4 | 0.1-0.5 | 5-40 | | | 0.03 | 2 | 1.9 ± 0.5 |
| 205036.93+442140.8 | | | >352 | >640 | 80 | 1,100 | 8.7 ± 0.4 |
| 205040.29+443049.0 | 3.0 | >165 | | | 1.8 | 11 | 0.48 ± 0.04 |
| 205042.78+442155.8 | 0.04-0.12 | 1-313 | | | 0.02 | 3 | 26 ± 4 |
| 205100.90+443149.8 | | | 2-3 | 13-39 | 1.3 | 10 | 1.06 ± 0.04 |
| 205114.80+424819.8 | 47-56 | 96-334 | | | 10 | 100 | 10.2 ± 0.6 |
| 205115.14+441817.4 | | | 120 | >930 | 10 | 18 | |
| 205119.43+441930.5 | | | 1-2 | 4-7 | 0.3 | 5 | |
| 205120.99+442619.6 | 0.5-2.0 | 14-80 | | | 0.9 | 6 | |
| 205123.59+441542.5 | 43 | 560 | | | 1.8 | 4 | 1.04 ± 0.05 |
| 205124.70+441818.5 | | | 1-3 | 7-10 | 0.6 | 5 | 0.38 ± 0.03 |
| 205139.26+442428.0 | | | 6-7 | 22-50 | 2.5 | 18 | |
| 205139.93+443314.1 | | | 50-150 | 129-264 | 30 | 50 | |
| 205145.99+442835.1 | | | 100 | >630 | 3 | 9 | 0.85 ± 0.05 |
| 205155.70+443352.6 | | | 4-6 | 9-25 | 1.3 | 12 | |
| 205158.63+441456.7 | 0.5-3.0 | 7.0 | 4-16 | 83-327 | 1.3 | 8 | 0.52 ± 0.04 |
| 205203.65+442838.1 | | | 36-119 | 685 | 0.01 | 9 | 2.1 ± 0.2 |
| 205228.33+442114.7 | | | 1.5 | 5.78 | | | |
| 205230.89+442011.3 | | | 3 | 7.71 | 0.6 | 5 | 0.52 ± 0.02 |
| 205252.48+441424.9 | | | 2-6 | 11-21 | 1.8 | 9 | 0.96 ± 0.04 |
| 205253.43+441936.3 | | | 2-4 | 11-28 | 4 | 8 | 1.16 ± 0.09 |
| 205254.30+435216.3 | | | 30-100 | 298-348 | 7 | 13 | 0.82 ± 0.05 |
| 205314.00+441257.8 | | | 2-80 | 29-337 | 0.9 | 6 | 0.59 ± 0.04 |
| 205315.62+434422.8 | 0.5-150 | 25-610 | | | 40 | 17 | 1.05 ± 0.03 |
| 205340.13+441045.6 | 2-20 | 11-31 | 3-10 | 11-80 | 1.8 | 10 | 0.90 ± 0.04 |
| 205410.15+443103.0 | | | 3 | 8-10 | 0.9 | 6 | 0.64 ± 0.04 |
| 205413.74+442432.4 | | | 2-5 | 2-19 | 1.3 | 7 | |
| 205424.41+444817.3 | | | 5-11 | 250-330 | 0.6 | 6 | |
| 205445.66+444341.8 | | | 3-20 | 45-300 | 0.9 | 6 | 0.75 ± 0.06 |
| 205446.61+441205.7 | | | 2-6 | 13-62 | 1.8 | 6 | 0.96 ± 0.05 |
| 205451.27+430622.6 | 5-30 | 30-250 | | | 7 | 50 | 4.0 ± 0.3 |
| 205503.01+441051.9 | | | 6 | >57 | 4 | 12 | 1.17 ± 0.04 |
| 205534.30+432637.1 | | | 65 | >680 | 7 | 4 | 13.3 ± 1.8 |
| 205659.32+434752.9 | 3-4 | 11-12 | | | 3 | 11 | 1.06 ± 0.05 |
| 205759.84+435326.5 | 2.2-18 | >100 | | | 0.9 | 5 | 0.51 ± 0.04 |
| 205801.36+434520.5 | | | 14-37 | 29-90 | 80 | 71 | 1.24 ± 0.03 |
| 205806.10+435301.4 | 1.5-5.0 | 35 | | | 1.3 | 6 | 0.94 ± 0.06 |
| 205825.55+435328.6 | | | 2-6 | 8-123 | 0.9 | 6 | 0.72 ± 0.04 |
| 205839.73+440132.8 | 0.5-4.0 | 8-210 | | | 14 | 19 | |
| 205905.98+442655.9 | | | 10-15 | 27-47 | 1.3 | 14 | |
| 205906.69+441823.7 | | | 2-3 | 8-63 | 0.9 | 4 | 0.43 ± 0.05 |

**Table 5.3:** The results of applying several timescale metrics to the sample of Table 3.3. All timescales are in days. The first four columns after the source name are the timescales estimated by eye as described in Figure 3.4.1. The last three columns are the timescales returned by $\Delta m$-$\Delta t$ plots, peak-finding, and Gaussian process fitting, as described in the text.

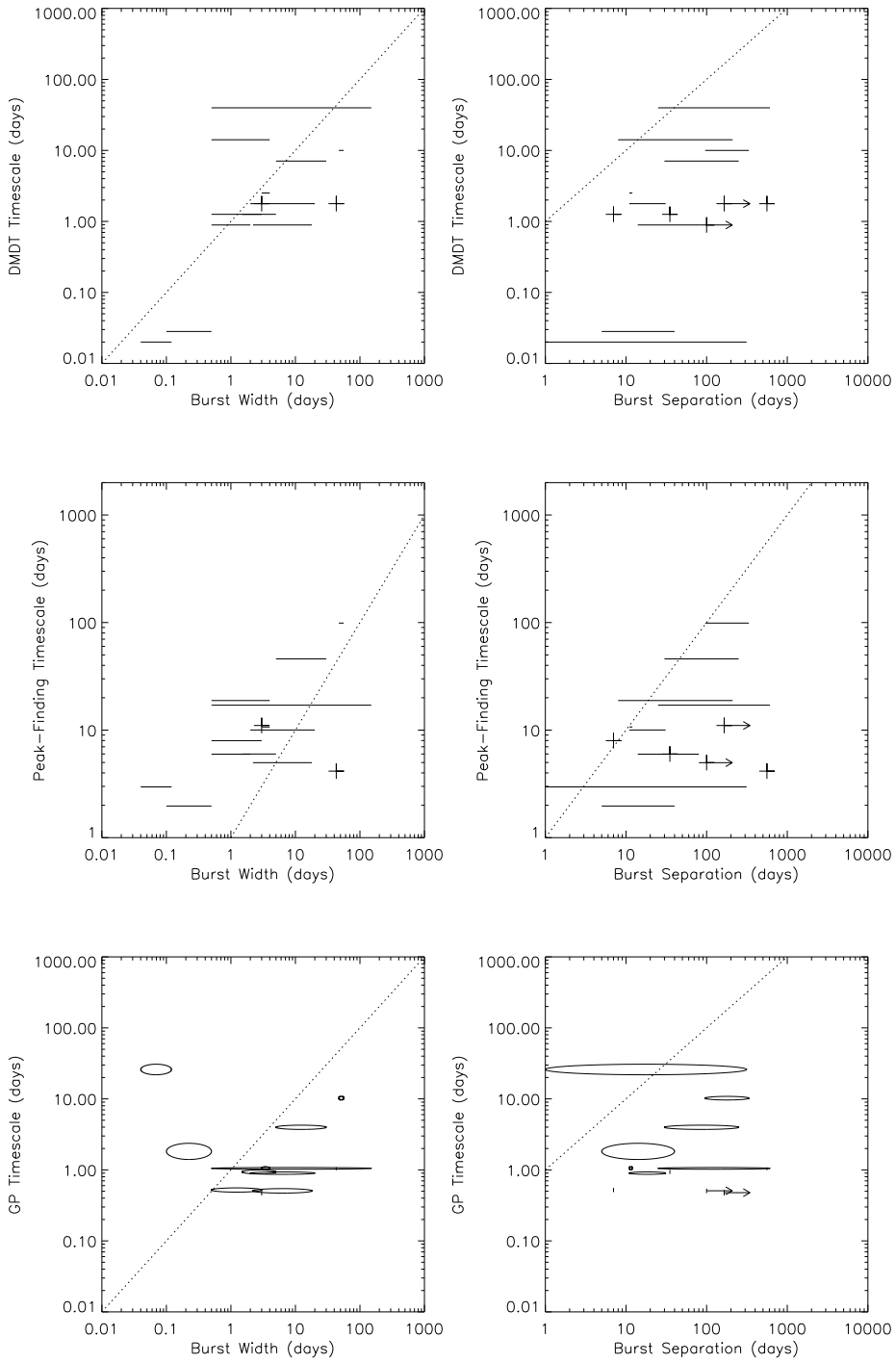


**Figure 5.22:** Comparison of the computed timescale metrics with timescales determined by eye, for sources showing bursting behavior. The dotted line indicates where the timescales on the two axes are equal. The vertical axis shows a timescale derived from $\Delta m$-$\Delta t$ plots in the top row, from peak-finding in the middle row, and from a Gaussian process fit in the bottom row. The spread in values along the Gaussian process axis represents the formal $1\sigma$ uncertainty. The horizontal axis shows the full width at baseline of each bursting event in the left column, and the separation between consecutive peaks in the right column. The spread in values along the horizontal axis represents variation in properties among different bursting events in the same lightcurve.

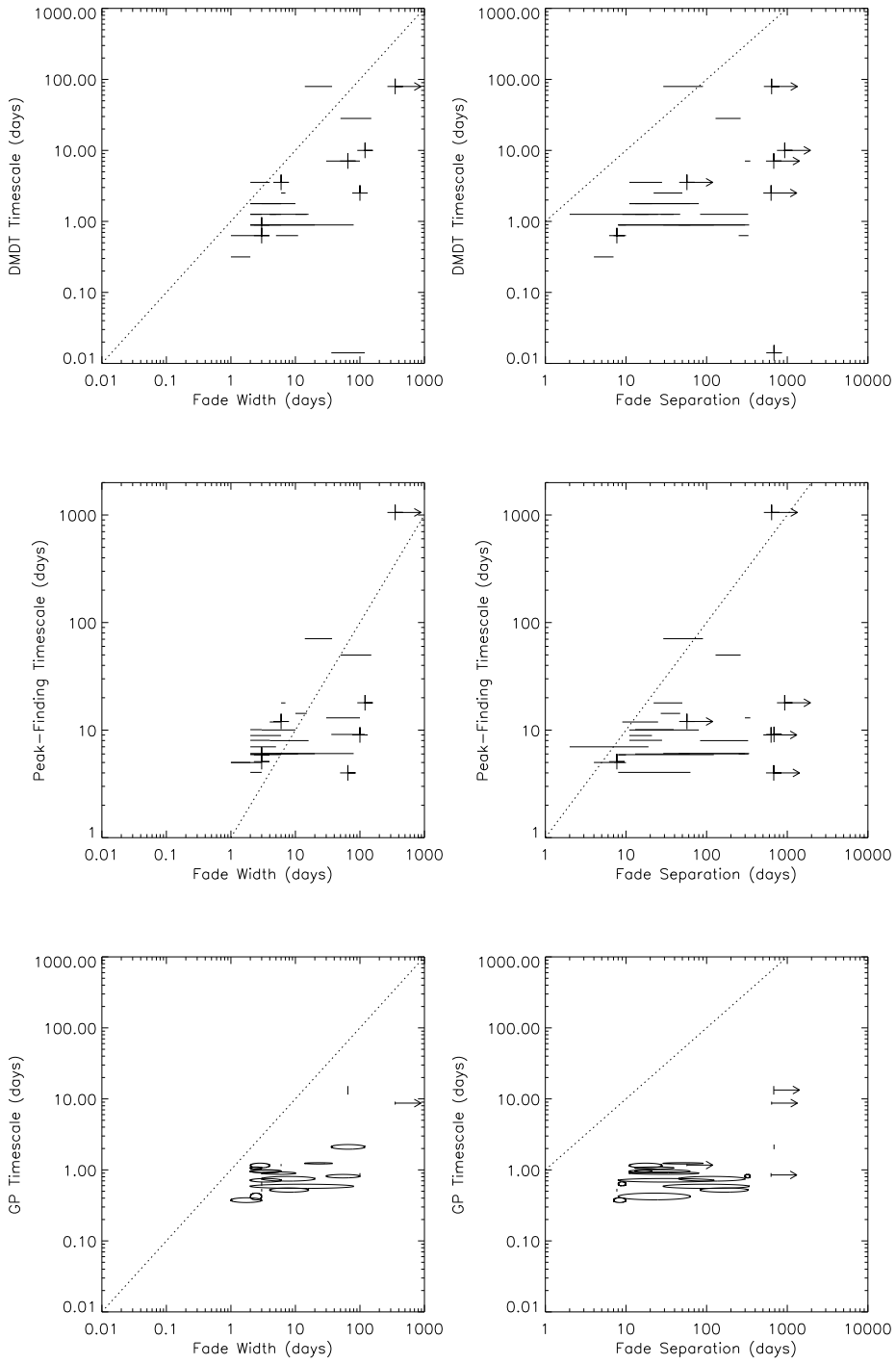


**Figure 5.23:** As Figure 5.22, but for sources showing fading behavior.

of timescale. Although these results must be interpreted with caution, since I had preconceptions about the effectiveness of the timescale metrics at the time I tested them on specific lightcurves, the results are broadly consistent with the conclusion of section 5.9 that $\Delta m$-$\Delta t$ plots are the most appropriate tool for this thesis.

## 5.9 Summary of Numerical Results

I present in Table 5.4 the simulated performance of each timescale metric according to the criteria provided in section 5.1. This table is, to my knowledge, the first of its kind. While no single metric satisfies all the criteria, $\Delta m$-$\Delta t$ Plots and Peak-Finding both perform well enough to warrant *careful* use in real applications. Both metrics suffer from high variance, and both are sensitive to the cadence: $\Delta m$-$\Delta t$ plots are only sensitive to timescales between the survey's characteristic cadence and 1/15 of the survey time base line, while peak-finding shows high scatter above 1/20-1/15 the base line. In addition, no four of the metrics work well with signals with multiple timescales (see Chapter 4), and none offer a significance test for the existence of a characteristic timescale.

I recommend the use of peak-finding for signals whose statistical properties are known *a priori* (e.g., they are all well described by a particular model) as well as timescales much shorter than the monitoring base line, and the use of $\Delta m$-$\Delta t$ plots for signals of unknown form but with timescales known to be intermediate between the cadence and the maximum base line.

| Criterion | Interpolated ACF | $\Delta m$-$\Delta t$ Plots | Peak-Finding | GP Modeling |
|---|---|---|---|---|
| Universal | Yes | Yes | Yes | No |
| Data-Driven | Tuning Param. | Tuning Param. | Yes | Yes |
| Versatile | to $\sim 20\%$ | to factor of 2 | to factor of 2.5 | to factor of 2.5 |
| Accurate | 25-300% | 20-100% | 25-100% | 6-600% |
| Precise | 10-60% | 20-80% | 10-100% | 10-100% |
| Dependable vs. Noise | Yes | Up to 1/10 amp. | Up to 1/10 amp. | No |
| Dependable vs. Cadence | No | No | No | |
| Robust vs. Outliers | | | | |
| Robust vs. Appended Data | | | | |
| Significance Test | No | No | No | No |

**Table 5.4:** Performance of timescale metrics according to the criteria from section 5.1. See the individual sections of this chapter for more details. A blank means the criterion was not tested.

Because they probe different parts of the lightcurve, timescales based on competing metrics cannot be directly converted to each other; the conversion factor depends on the statistical properties of a signal, which for a real lightcurve are usually unknown *a priori*. The distinction is similar to the varying conversion factor between RMS amplitude and peak-to-peak amplitude for lightcurves with different properties.

In Table 5.5, I show the ratio of all simulated timescales to $\Delta m$-$\Delta t$ timescales, which we use extensively in Chapter 6, for each lightcurve model considered here. Simulated ACF timescales or

| Timescale Metric | Sinusoid | Squared Exponential GP | Damped Random Walk |
|---|---|---|---|
| Period | $\sim 7\tau_{\Delta m\text{-}\Delta t}$ | N / A | N / A |
| Simulated $\Delta m$-$\Delta t$ 90% quantile crosses 1/2 amp | $\tau_{\Delta m\text{-}\Delta t}$ | $\tau_{\Delta m\text{-}\Delta t}$ | $\tau_{\Delta m\text{-}\Delta t}$ |
| Simulated peak-finding crosses 1/2 amp | $\sim 3\tau_{\Delta m\text{-}\Delta t}$ | $\sim 2\tau_{\Delta m\text{-}\Delta t}$ | $\sim 2\tau_{\Delta m\text{-}\Delta t}$ |
| Simulated peak-finding crosses 80% of peak-finding max | $\sim 3\tau_{\Delta m\text{-}\Delta t}$ | $\sim 6\tau_{\Delta m\text{-}\Delta t}$ | $\sim 6\tau_{\Delta m\text{-}\Delta t}$ |

**Table 5.5:** Output of each timescale metric, normalized by the $\Delta m$-$\Delta t$ timescale for ease of comparison in Chapter 6. This table can be used to convert between different timescale metrics by dividing each column by the timescale to be converted *from*. For example, the period is usually around twice (7/3, at one significant figure) the peak-finding timescale for a periodic signal. Two variants of the peak-finding timescale are listed: finding the time at which the peak-finding curve crosses 80% of its maximum is the approach adopted by Cody et al. (2014), while we prefer to find the time at which it crosses half the lightcurve amplitude, which gives less scatter in measurements at the cost of systematically lower results at long timescales. All results are for a 0.5 mag peak-to-peak lightcurve observed at a median signal-to-noise ratio of 20 using the full PTF cadence.

Gaussian process timescales are not listed because neither metric shows a clear correlation with lightcurve properties. While most definitions of timescale are within an order of magnitude of each other, they can still differ by a factor of several. These conversions need to be kept in mind while comparing results from different papers.

The timescale conversion factors between peak-finding and $\Delta m$-$\Delta t$ timescales differ greatly between the sinusoid and the aperiodic models we considered. This difference in scale arises because peak-finding characterizes the most extreme variations in a lightcurve, while $\Delta m$-$\Delta t$ timescales characterize the most typical variations. For a sinusoidal model, we showed in section 4.6 that the $\Delta m$-$\Delta t$ timescale is 1/6 the period, consistent with a factor of seven difference between peak-finding and $\Delta m$-$\Delta t$ plots after allowing for errors introduced by noise and cadence. For either flavor of Gaussian process model, the probability of an extremum falls faster than exponentially as one moves away from the model mean, so the peaks selected by peak-finding become proportionally rarer.

## 5.10 References

Choi, Y., Gibson, R. R., Becker, A. C., Ivezić, Ž., Connolly, A. J., MacLeod, C. L., Ruan, J. J., & Anderson, S. F. 2014, ApJ, 782, 37, arXiv:1312.4957

Cody, A. M. et al. 2014, AJ, 147, 82, arXiv:1401.6582

Findeisen, K. 2014, LightcurveMC: An extensible lightcurve simulation program, ascl:1408.012, astrophysics Source Code Library

Morales-Calderón, M. et al. 2011, ApJ, 733, 50, arXiv:1103.5238

Nickerson, R. S. 1998, Review of General Psychology, 2, 175

Scargle, J. D. 1989, ApJ, 343, 874

# Chapter 6

# Variability and Population Statistics in the North America Nebula

## 6.1 Introduction

With the groundwork laid in Chapter 4 and Chapter 5, we can now use the PTF-NAN data set to characterize aperiodic variables in the North America Nebula complex. Our goals are both to select previously unknown candidate members of the complex, and to use the timescales of aperiodic variability to constrain the range of physics responsible for the variability. In this work we focus on the bulk properties of the candidate member population; a more detailed study of specific variability mechanisms or individual sources will be deferred to a later paper.

## 6.2 Previous Work in the North America Nebula

The state of known membership in the North America Nebula Complex has been reviewed by Reipurth & Schneider (2008), Guieu et al. (2009), and Rebull et al. (2011). Prior to Guieu et al. (2009), most candidate members of the region had been selected as H$\alpha$ emission objects; Guieu et al. (2009) and Rebull et al. (2011) also added infrared excess as a selection criterion. Both criteria are likely to have missed members that have lost their disks. Infrared excess surveys directly test for the presence of a circumstellar disk, and as such are insensitive to more evolved members. Emission-line surveys are usually only sensitive to very strong emission lines, and therefore have low yields: of the final Rebull et al. (2011) membership list, only 201 out of 2,196 candidates had been selected by previous work. By using variability properties to identify young stars, we can achieve both the high yield of infrared excess surveys as well as the sensitivity to nonaccreting members of emission-line surveys.

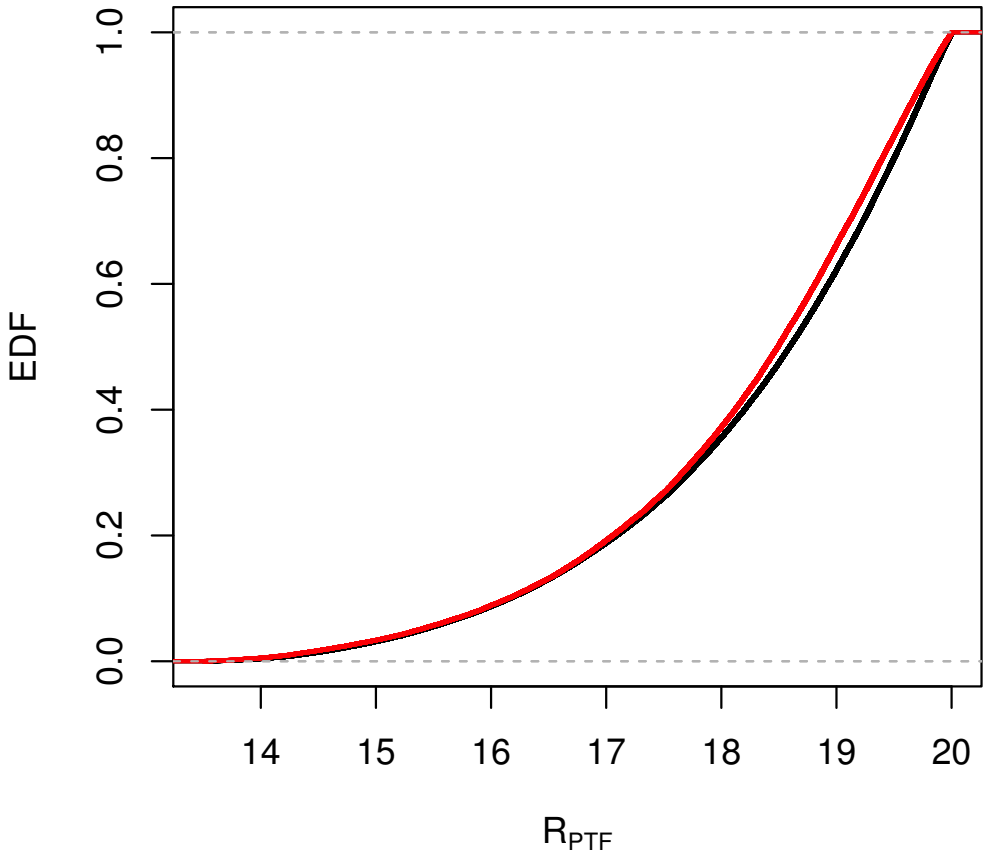


**Figure 6.1:** The empirical cumulative distribution function (EDF) of PTF magnitude for all 58,616 high quality sources (black curve) and the subset with 2MASS counterparts (red curve), showing that the latter are slightly brighter but that the distributions are very similar. The distributions of sources with Spitzer or IPHAS counterparts are not shown, but would fall on top of the black curve in this plot.

## 6.3 Source Statistics

The PTF Photometric Pipeline reports 142,648 sources in the six chips covering the NAN Complex (see Figure 2.1 for the sky coverage of these six chips). Considering only sources with $13.5 \leq R_{\rm PTF} \leq 20.0$ and with unflagged detections in more than half the survey epochs lowers this number to 58,616. Of the 53,983 sources in areas covered by both Spitzer's IRAC and MIPS instruments, 52,062, or 96%, are detected by Spitzer. 54,498 of the variables (93%) appear in the 2MASS Point Source Catalog, 49,098 (84%) in the USNO-B1.0 catalog, and 51,729 (88% of variables, or 99% of sources with Spitzer counterparts) in the IPHAS Initial Data Release. The sources with 2MASS counterparts tend to be slightly brighter on average than the full sample of 58,616 PTF sources, as shown in Figure 6.1, but there is no strong correlation between the presence or absence of a counterpart and PTF magnitude.

## 6.4 Candidate Member Selection

### 6.4.1 Identifying the Variables

We identified variable sources following the same procedure as in subsection 3.2.1, so the detection statistics summarized in Table 3.1 apply. As in subsection 3.2.1, we considered only the western six chips of the PTF field. We found 2,705 variable sources on these six chips.

### 6.4.2 Spectroscopic Candidates

We observed 2,185 spectra of PTF sources toward the North America Nebula complex, selecting stars that were either variable or had infrared excess. Another 11 spectra from the region were taken by the PTF collaboration. Due to time constraints, we focused on a subsample of 782 spectra corresponding to sources brighter than $R_{\rm PTF} = 18.5$ with significant variability as defined in subsection 3.2.1. Spectra from fainter sources will be presented in future work. The focus on stars of 18th magnitude or brighter may have introduced a bias away from lower mass or more embedded members.

After reducing the spectra, we measured equivalent widths for the key youth indicators H$\alpha$ 6563 Å, Ca II 8542 Å, and Li I 6708 Å, as well as the qualitative presence of Ca II 8498,8662 Å and He I 6678 Å, using the splot command in IRAF 2.12.2a. We attempted to measure [O I] 6300,6363 Å as well, but found significant sky contamination, particularly in the MMT spectra. Therefore, we did not use [O I] as a youth indicator.

For consistency, all spectra hotter than type M had their continuum normalized to 1 before having their equivalent widths measured. The continuum fit was done with a 20th order cubic spline function, rejecting points more than $2\sigma$ below or $5\sigma$ above the fit over 10 iterations. Type M spectra were left unaltered, since we could not find settings that led to a consistent treatment of molecular absorption bands.

Equivalent widths were nominally calculated using direct integration (splot 'e' command) over a 20 Å window centered on the line, forcing the continuum to 1 (or to a by-eye estimate, for M stars). In cases where a prominent line interfered, particularly the [N II] lines near H$\alpha$, the edge of the integration window was instead taken to be the local minimum or maximum between the intended line and the interfering line. For a handful of stars where broad line profiles made direct integration impossible, the equivalent width was instead calculated by deblending a series of Gaussian components, leaving the depth and width of each component, as well as a linear background term, as free parameters.

A spectrum was identified as a high-confidence membership candidate if it had net Ca II emission (i.e., the equivalent width, as measured above, was negative), He I emission, or Li I absorption in excess of 0.1 Å equivalent width (any apparent feature at 6708 Å with a smaller equivalent width was deemed too likely to be noise). Ca II emission and He I emission almost always originate with

accretion, while Li I absorption is almost always a sign of youth. In addition, spectra with both H$\alpha$ emission and at least some emission in the cores of the Ca II lines were interpreted as accreting young stars. Spectra with only H$\alpha$ emission, but no other youth indicators, were identified as low-confidence candidates, as H$\alpha$ emission can also be associated with stellar activity in stars up to 20 Myr (Gondoin et al., 2012) to 1 Gyr old (Gizis et al., 2002), depending on the star's mass. Stars with neither line emission nor Li absorption were treated as likely non-members, although future work may reveal them to be associated with the North America Nebula complex.

If a source had multiple spectra at different epochs, the highest membership confidence of all the spectra was adopted as the membership confidence for the source. For example, a source with Ca II emission at one epoch but not another was classified as a high-confidence member.

Of 2,705 variable sources with good PTF photometry, 619 had spectra examined for youth indicators. Of these, 156 were high-confidence members, 162 low-confidence members, and 301 likely non-members.

### 6.4.3 Revisiting Infrared Excess Assessment

Because Rebull et al. (2011) used the presence of infrared excess, indicating warm circumstellar dust, as their primary membership criterion, they had to be careful to avoid selecting red sources that were not young stars. In particular, several of their criteria were designed to reject galaxies at the expense of fainter young stars.

This work selects young stars on the basis of variability, so background galaxies, with the exception of active galactic nuclei, are unlikely to be a major contaminant. When classifying sources on the basis of their infrared properties, therefore, we broadened the criteria of Rebull et al. (2011) to include sources that, were they not variable, would be likely galaxies. This gave us a more complete assessment of which stars still had circumstellar disks.

We considered a source to show an infrared excess if it met *any* of the following criteria:

1. $[3.6]-[24] > 1.25$ and $[3.6]-[24]$ differing from $-0.13$ by more than $5\sigma$ (if $[3.6] \geq 10.0$) or $10\sigma$ (if $[3.6] < 10.0$). This is condition 1 in section 4.2 of Rebull et al. (2011).

2. $K_s < 14$ and $K_s - [24] > 1$ (condition 3 in section 4.2 of Rebull et al. (2011))

3. a detection at 70 $\mu$m (condition 4 in section 4.2 of Rebull et al. (2011))

4. $[4.5]-[8.0] > 0.5$ and $[3.6-5.8] > 0.35$ and $[3.6]-[5.8] \leq 3.5([4.5]-[8]-0.5)+0.5$ (Equation 3 of Guieu et al. (2009)) but colors consistent with an AGN (Equation 2 of Guieu et al. (2009)) or shock-dominated sources (Equation 4 of Guieu et al. (2009))

These criteria differ from those of Rebull et al. (2011) in that we allowed sources to have colors similar to those of galaxies (i.e., sources could satisfy Equation 1 of Guieu et al. (2009)), we allowed

sources to have $[3.6] \geq 14$ (condition 2 in section 4.2 of Rebull et al. (2011)), and we ignored non-infrared data (conditions 6-11 in section 4.2 of Rebull et al. (2011)).

Of the 2,705 variable sources with good PTF photometry, we had Spitzer counterparts for 2,512. Of these, 208 have an infrared excess by at least one of the above criteria, 33 fail all the criteria, and 2,271 lack sufficient data to tell. Of the last group, all but four sources lack a Spitzer detection at 24 $\mu$m, so criterion 1 could not be checked. In addition, criterion 3 can only confirm the presence of an infrared excess, but not reject it. Thus, while it is likely that most of these 2,271 sources lack an infrared excess, and they are treated as such in the remainder of the chapter, we lack the data to demonstrate that only the photosphere contributes to these stars' 24 $\mu$m flux.

### 6.4.4 Photometric Candidates

We made a preliminary selection of candidate members using ancillary optical photometric data, to reduce the number of false positives from variable field sources. Of the recent optical surveys that covered our field, the most complete was the INT Photometric H-alpha Survey (IPHAS). Since the IPHAS initial data release had been withdrawn from publication at the time of writing, we could only use IPHAS data that had been collected by Rebull et al. for sources with Spitzer counterparts. Nonetheless, we had both $r$ and $i$ photometry for 83% of our sample.

In Figure 6.2 we show the colors of our variable sources in the IPHAS bands. The area between the two red lines is where main sequence stars are expected to lie (Drew et al., 2005). Most sources fall in this region, indicating they have at most modest H$\alpha$ excesses. Sources above the region are emission-line stars, confirmed by spectra where we have them. We note that emission-line stars selected by Witham et al. (2008) were already included in the member list compiled by Rebull et al. (2011). We do *not* include them in the sample for variability statistics in subsection 6.5.1 and section 6.6, unless they were independently selected on the basis of variability.

The 128 sources below the main sequence locus appear to have poor photometry in either the IPHAS $r$ or H$\alpha$ bands; spectra show a mix of emission-line and nonemitting objects. Given the likelihood that the measurements are misleading, we do not exclude sources with low $r - H\alpha$ on the basis of their colors.

In Figure 6.3 we show a color-magnitude diagram of our sources. Sources are scattered over a broad swath of color-magnitude space. The empty region in the lower right is caused by our selection of $R_{\rm PTF} \leq 20$ sources. In Figure 6.3b we show only the variables whose spectra were examined for youth indicators. Nearly all the high-confidence members have $r - i < 2$; among $r - i > 3$ most sources are likely non-members (specifically, giants), although some have Balmer emission.

We use Figure 6.3 to reject sources that are too faint to be main-sequence or pre-main-sequence stars associated with the North America Nebula complex. The figure shows both isochrones and the main sequence at a distance of 600 pc; we adopt this distance rather than the 520 pc we assume

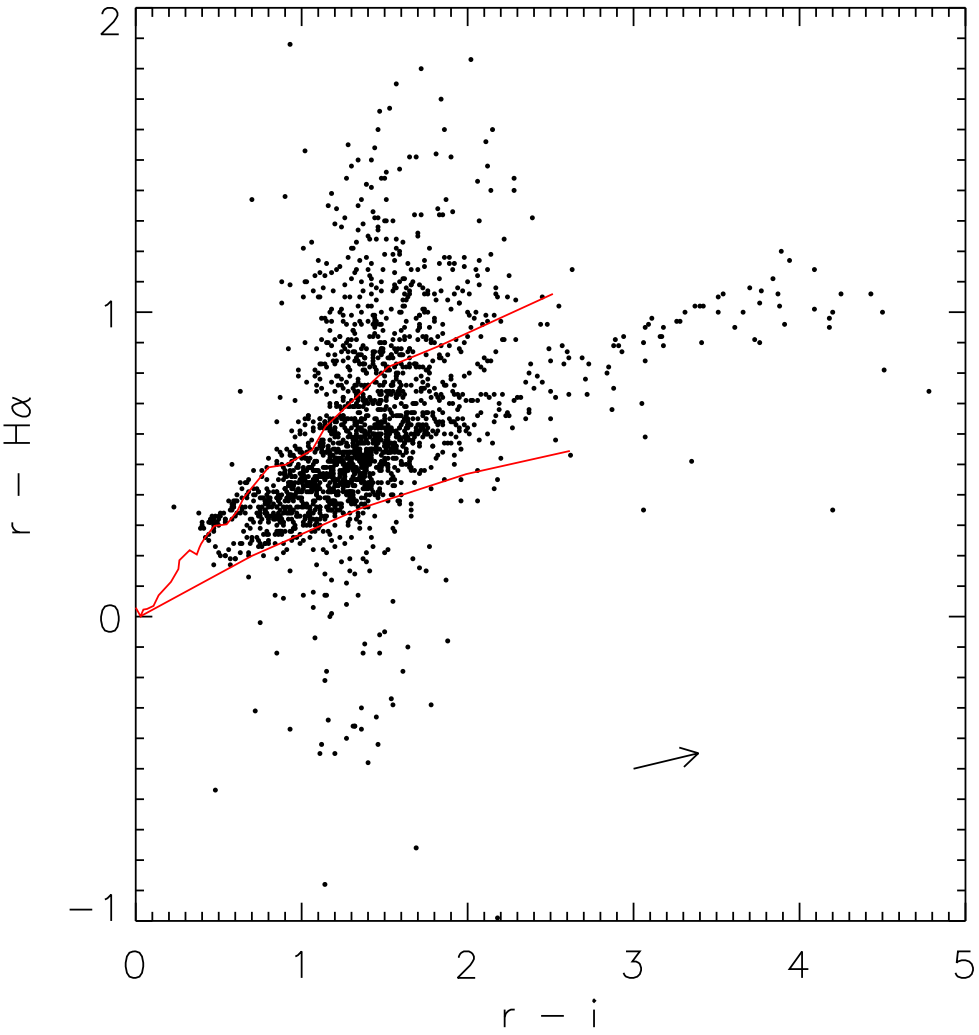


**Figure 6.2:** An $r - H\alpha$ vs. $r - i$ color-color plot. The solid red lines show the upper and lower boundaries of the region where main-sequence stars can be found, if the extinction to individual sources is allowed to take on arbitrary values (Drew et al., 2005). The black arrow shows the (approximate) extinction vector from Cardelli et al. (1989), assuming $R_V = 3.1$.

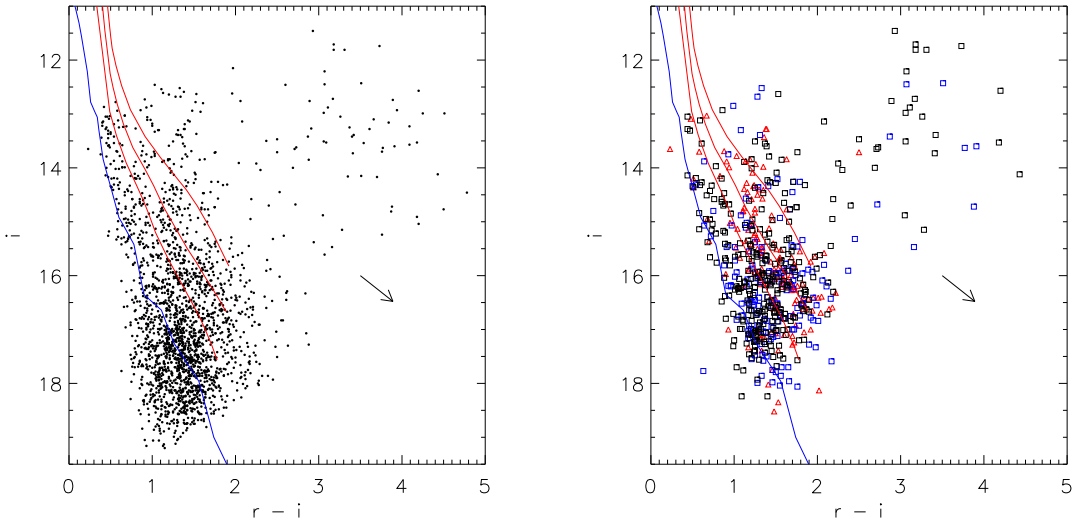


**(a)** All variables **(b)** Spectroscopic targets only

**Figure 6.3:** An $i$ vs. $r-i$ color-magnitude plot. The red curves show, from top to bottom, synthetic photometry of D'Antona & Mazzitelli (1997) isochrones at 1 Myr, 3 Myr, and 10 Myr at a distance of 600 pc. The blue curve is the empirical main sequence from Kraus & Hillenbrand (2007) at the same distance. The black arrow shows the extinction vector from Cardelli et al. (1989), assuming $R_V = 3.1$. Extinction tends to shift sources onto younger isochrones. In the right panel, red triangles are high-confidence members, blue squares low-confidence members, and black squares likely non-members, as defined in subsection 6.4.2. Very red sources $r-i \gtrsim 1$ tend to be much more luminous than other sources in the field, indicating that they are background giants.

throughout the rest of this chapter to allow for a more conservative rejection of background sources. The reddening vector tends to raise sources above the main sequence, so any sources below it should be non-members with high probability, regardless of their extinction.

Since many IPHAS sources in the region have $i$ photometry but not $r$, and cannot be placed on the color-magnitude diagram directly, we also reject sources with $i > 18.7$. Sources that have $i > 18.7$ but fall within our detection limit of $R_{\rm PTF} \leq 20$ are assumed too blue to fall above the main sequence, although we caution that the IPHAS $i$ photometry is unlikely to have been taken while the source was near its median PTF magnitude.

There are five sources that are well below the main sequence line, yet are high-confidence spectroscopic members. These sources are:

**FHO 89** ($i = 18.0, r-i = 1.41$) The IPHAS $r$ magnitude of 19.4 is considerably fainter than the observed range $R_{\rm PTF} \sim$ 17.7-18.4. However, this source is clearly blended in the PTF image, so likely neither the IPHAS nor PTF photometry are reliable.

**FHO 299** ($i = 18.4, r-i = 1.53$) is a source with a 3-magnitude peak-to-peak amplitude that appears to have been observed by IPHAS close to minimum light. The source would spend most of its time above our background source cutoff.

**FHO 558** ($i = 13.7, r-i = 0.23$) is V751 Cyg, a known cataclysmic variable. This source illustrates that even high-confidence members are not necessarily young stars.

**FHO 568** ($i = 18.5, r - i = 1.48$) The IPHAS $r$ magnitude of 20.0 is considerably fainter than the observed range $R_{\rm PTF} \sim$ 17.3-18.7. However, this source is a close double in SDSS images, so likely neither the IPHAS nor PTF photometry are reliable.

**FHO 1891** ($i = 17.0, r - i = 0.93$) is a young star with both a strong emission-line spectrum and a strong infrared excess. Variability cannot account for its position in the IPHAS color-magnitude diagram.

Of the five sources, then, only two, FHO 299 and FHO 1891, represent high-quality detections of young stars. This supports the idea that most of the sources below the blue line in Figure 6.3 are likely non-members. Therefore, we can remove sources below the main sequence line from our sample without significantly sacrificing completeness.

Of 2,705 variable sources with good PTF photometry, 1,822 are sufficiently bright (above the main sequence line) to be plausible members of the North America Nebula complex. Of those, we exclude the 68 sources in the region with $r - i > 2$ and $i < 10 + 2(r - i)$, including 24 of the 33 sources where we could rule out an infrared excess, as probable giants. This leaves 1,754 variables with photometry consistent with North America Nebula membership.

### 6.4.5 Variability as a Youth Indicator

In Figure 6.4, I show the RMS amplitudes for sources whose spectra were examined for youth indicators, according to their membership confidence. Here, and throughout the chapter, I use the observed RMS of the lightcurve, rather than the RMS in excess of that expected from the source magnitude as in Figure 3.1. The problem of correcting the RMS amplitude of a signal for a fixed noise contribution is ill-posed: the relationship between signal RMS, noise RMS, and combined RMS depends on the distribution of both signal and noise; in addition, the simplest solution (subtraction of the noise estimate in quadrature) carries the risk of returning imaginary results. I choose to use the observed RMS, which is a well-understood quantity despite its magnitude dependence.

While high-confidence members to tend to have higher RMS than low-confidence or likely non-members, there is still heavy overlap among the samples: RMS, taken by itself, cannot be used to select members. This is consistent with the results of the spectroscopic analysis, which showed that half our sample, selected by a combination of variability and infrared excess, had no youth indicators. We may be able to revisit variability amplitude as a selection criteria once we are certain which high-confidence members are genuine members and which likely non-members are genuine non-members.

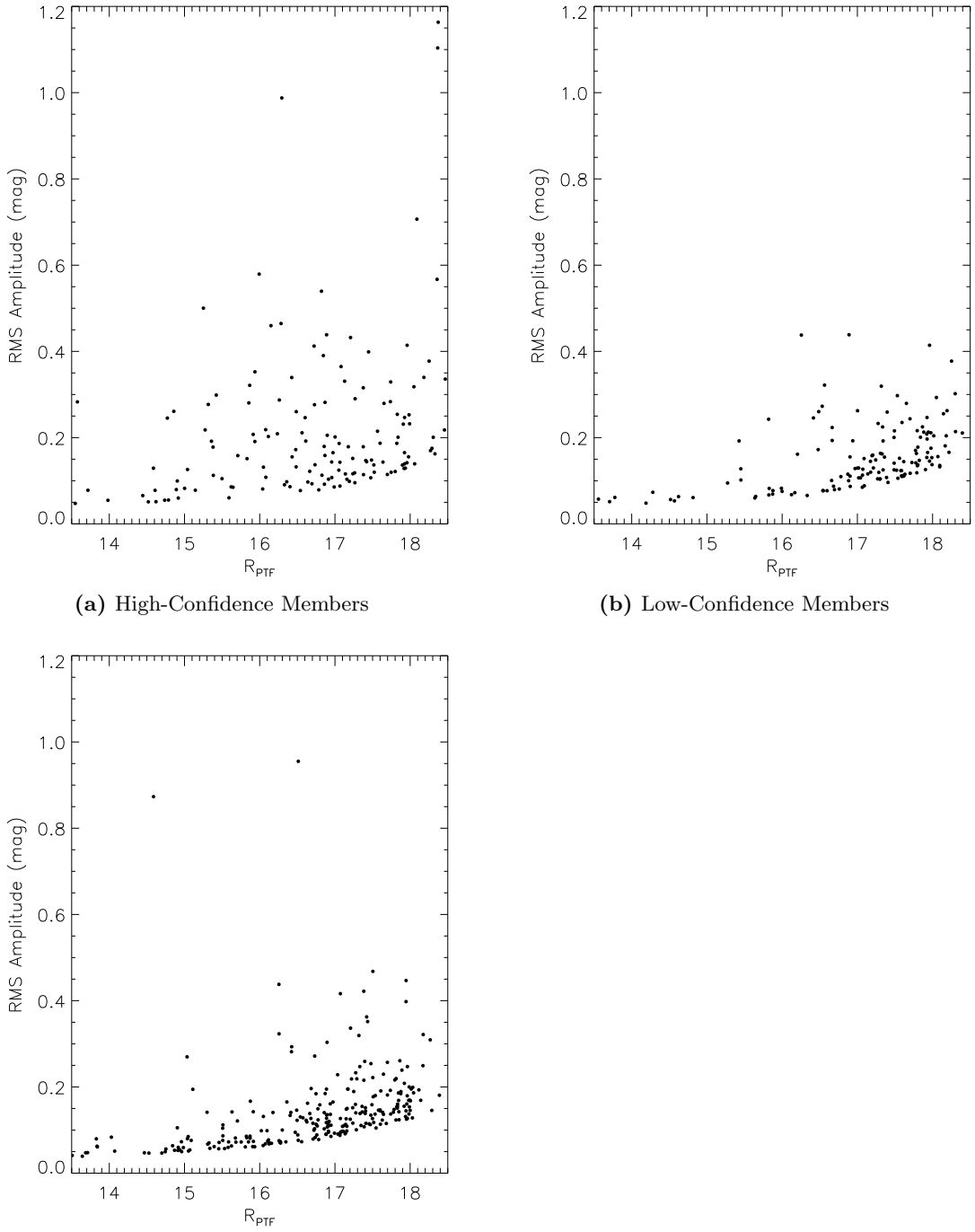


**(a)** High-Confidence Members

**(b)** Low-Confidence Members

**(c)** Likely Non-Members

**Figure 6.4:** RMS vs. magnitude distributions for sources with different degrees of membership confidence. High-confidence members have slightly higher RMS amplitudes than other sources, but otherwise there is no correlation with the sources' spectroscopic properties. The lower density of sources for $18 \leq R_{\rm PTF} \leq 18.5$ is an artifact of us primarily choosing sources brighter than 18th magnitude as spectroscopic targets.

| Category | Number | Notes |
|---|---|---|
| Previous candidates from Rebull et al. (2011) | 2,082 | |
| Rebull et al. candidates detected by PTF pipeline | 588 | 28% of candidates |
| Rebull et al. candidates with reliable photometry | 354 | 60% of PTF sources |
| Rebull et al. candidates recovered as variable sources | 177 | 50% of reliable lightcurves |
| Rebull et al. candidates rejected as members based on our spectra | 6 | |
| New variability-selected candidates | 1,359 | |
| New candidates with Spitzer counterpart | 1,173 | 86% of candidates |
| Candidates with IPHAS $r$ and $i$ | 897 | 76% of Spitzer sources |
| New candidates with high-confidence membership spectrum | 54 | |
| New candidates with low-confidence membership spectrum | 128 | |
| New candidates with no spectrum | 1,177 | 87% of new variable candidates |

**Table 6.1:** Summary statistics for our sample of 3,441 candidate members, including candidates first identified here and candidates selected by Rebull et al. (2011). Only PTF sources on the westernmost 6 chips of the field are considered. "Reliable photometry" is defined as $13.5 \leq R_{\rm PTF} \leq 20.0$ and unflagged observations in at least half of all epochs.

Given the probable high contamination of a variability selected-sample, section 6.5 and later will focus on the 282 spectroscopic candidate members except where otherwise stated.

### 6.4.6 New Candidate Members in the North America Nebula Complex

Our final membership list is based on a large number of partially overlapping samples. In addition to the infrared-excess selected list of Rebull et al. (2011), we have Spitzer photometry for many other sources in the field. We have the PTF source catalog for our field, including sources that appear to be variable. We have follow-up spectra of a subset of the infrared-excess sources and the variables, and we have IPHAS photometry for a subset of the Spitzer sources, both with and without infrared excess.

We begin with the list of 2,082 candidate members from Rebull et al. (2011), of which only 629 are optically visible according to IPHAS. To this list, we add the sources we selected in this section on the basis of optical variability and follow-up spectroscopy. These two samples are complementary: the Rebull et al. (2011) sources are dominated by infrared excess sources, while our variability-selected sample is more sensitive to sources with little to no infrared excess. We define a source as a candidate member of the North America Nebula complex if it was identified as a candidate member by Rebull et al. (2011), or if it meets all of the following criteria:

1. it is variable
2. it does not have a spectrum indicating likely non-membership
3. it either has a position in the IPHAS color-magnitude diagram consistent with membership or is missing IPHAS photometry

These criteria produce a list of 3,441 candidate members, 1,359 of them not selected by Rebull et al. (2011), which are listed in Table 6.2. Some more details of the candidate selection are listed in Table 6.1. The variability selected candidates overlap only slightly with the infrared excess selected

| [RGS2011] ID | FHO Number | $R_{med}$ (mag) | RMS (mag) | [RGS 2011] Class | Spectroscopic Membership | Photometric Membership |
|---|---|---|---|---|---|---|
| 205009.17+445518.7 | 31 | 17.7 | 0.17 | | | Possible Member |
| 205011.62+445522.7 | 33 | 18.9 | 0.28 | | | |
| 205015.00+441741.9 | 34 | 19.3 | 0.35 | | | |
| 205018.20+440402.2 | 39 | 18.0 | 0.15 | | Possible | Possible Member |
| 205019.86+440221.2 | 40 | 17.1 | 0.09 | | Likely | Possible Member |

**Table 6.2:** All 3,441 candidate members identified by this study. Only a portion of the table is shown for reference; all 3,441 rows may be downloaded online. $R_{med}$ is the median PTF magnitude of the lightcurve. RMS denotes the root-mean-square scatter of the lightcurve. The [RGS 2011] Class is the spectral class (I, flat, II, or III) assigned by Rebull et al. (2011). Spectroscopic membership is "Likely" for high-confidence members, "Possible" for low-confidence members, and "Non-Member" for likely non-members. Photometric membership is "Background" for sources that fell below the main sequence in Figure 6.3, "Giant" for sources that are likely giants, and "Possible Member" for sources whose color-magnitude diagram position is consistent with North America Nebula Complex membership.

candidates of Rebull et al. (2011); only 154 out of the 3,441 candidate members were selected by both methods. Some of the limited overlap can be attributed to the different wavelength regimes probed by PTF and Spitzer: while 88% of the PTF-selected candidates are detected by Spitzer, only 17% of the Spitzer-selected candidates fall in the PTF photometric sample.

Many of the 1,359 new variability-selected candidates have neither sufficient optical photometry to place them on an $i$ vs. $r-i$ color-magnitude diagram, nor a spectrum to test their membership. Therefore, it is likely that some will be classified as likely non-members on further investigation. We can obtain a rough estimate of the number of members that will remain by examining the source statistics. Of the 398 sources with a good position in the color-magnitude diagram and a spectrum available, 171 (43%) show youth indicators in their spectrum. Of the 23 sources with no color-magnitude information but a spectrum available, 11 (48%) show youth indicators. Of the 202 sources with color-magnitude information and a spectrum consistent with youth, 171 (85%) have a CMD position consistent with membership. Of the 1,463 sources with color-magnitude information but no spectrum, 726 (50%) have a CMD position consistent with membership. Of the 1,359 new candidates, 171 have both a spectrum and a CMD position available, 11 have only a spectrum, 726 have only a CMD position, and 451 have neither a spectrum nor a CMD position. Assuming for simplicity that there are no biases between the samples with and without CMD or spectrum information, the number of sources that are expected to remain in the sample of new candidates after obtaining photometry and spectra for all variable sources is $171+11\times0.85+726\times0.43+451\times(0.43\times0.50$ OR $0.85\times0.48)$, for a total of 590-680 vetted candidates, depending on the highly uncertain confirmation rate for the 451 sources with no supplementary data.

Therefore, our catalog of 3,441 candidate members is expected to correspond to an expected population of 2,600-2,700 likely members after additional followup work. This is a significant expansion over the $\sim 2,000$ sources associated with the region by Rebull et al. (2011). In addition, since our

variability survey is amplitude limited (as discussed in subsection 6.6.1, particularly Figure 6.13), it is likely that improvements to the PTF pipeline that lower our detection thresholds will uncover additional candidates.

## 6.5 Applying Timescale Metrics

### 6.5.1 Characterizing the Full Variability-Selected Sample of NAN Candidate Members

For each of the 2,705 variables in the PTF sample, I calculated the $\Delta m$-$\Delta t$ plot with $\Delta t$ bins in steps of 0.15 dex from $10^{-1.97}$ days to the maximum length of the lightcurve. This is the same binning used in Chapter 5 when testing the performance of $\Delta m$-$\Delta t$ plots; while somewhat coarse, it ensures a statistically significant number of points in most bins, and allows the coverage gap at time intervals of 8-16 hours to be isolated to just two bins, from $10^{-0.43}$ days to $10^{-0.17}$ days.

The two $\Delta t$ bins on either side of this gap will be well-populated by intranight observations on the short end and by observations on consecutive nights on the long end. The clean contrast minimizes systematic errors: the two undersampled bins from $10^{-0.47}$ days to $10^{-0.17}$ days have very few points "spilling over" from adjacent, better-populated, bins, while the adjacent bins have a roughly uniform sampling across their $\Delta t$ width. As an additional safeguard, we ignored the small number of points falling within the two undersampled bins from $10^{-0.47}$ days to $10^{-0.17}$ days.

For each $\Delta m$-$\Delta t$ plot, the $\Delta t$ bin in which the 90th percentile of $\Delta m$ first exceeded half the lightcurve amplitude was defined as the timescale of the lightcurve, as the simulations summarized in section 5.9 show this timescale metric performs well in the parameter space occupied by the PTF North America Nebula survey. Timescales were calculated both by considering all points in the lightcurve and by considering only points with photometric errors smaller than 0.1 mag. A comparison is shown in Figure 6.5. It is more common for a timescale with high-error points to be less than the corresponding timescale without those points than for the reverse to be true, which is consistent with expectations if the timescale is biased downward by noisy points. Deviations between the two measurements are most common if at least one timescale is shorter than 0.1 day.

A large fraction of our sources are aperiodic, and characterizing these sources is a major goal of our survey. Therefore, the most relevant simulations from Chapter 5 are those for a squared exponential Gaussian process and for a damped random walk. In Figure 5.11, these simulations typically have timescales characterized to 20-50%, depending on the choice of lightcurve model and on the value of the timescale. Since, as shown in the next section, many lightcurves have timescales of order a day but complex structures more similar to a damped random walk than to a squared exponential Gaussian process, I adopt 50% as the typical timescale uncertainty in this sample.

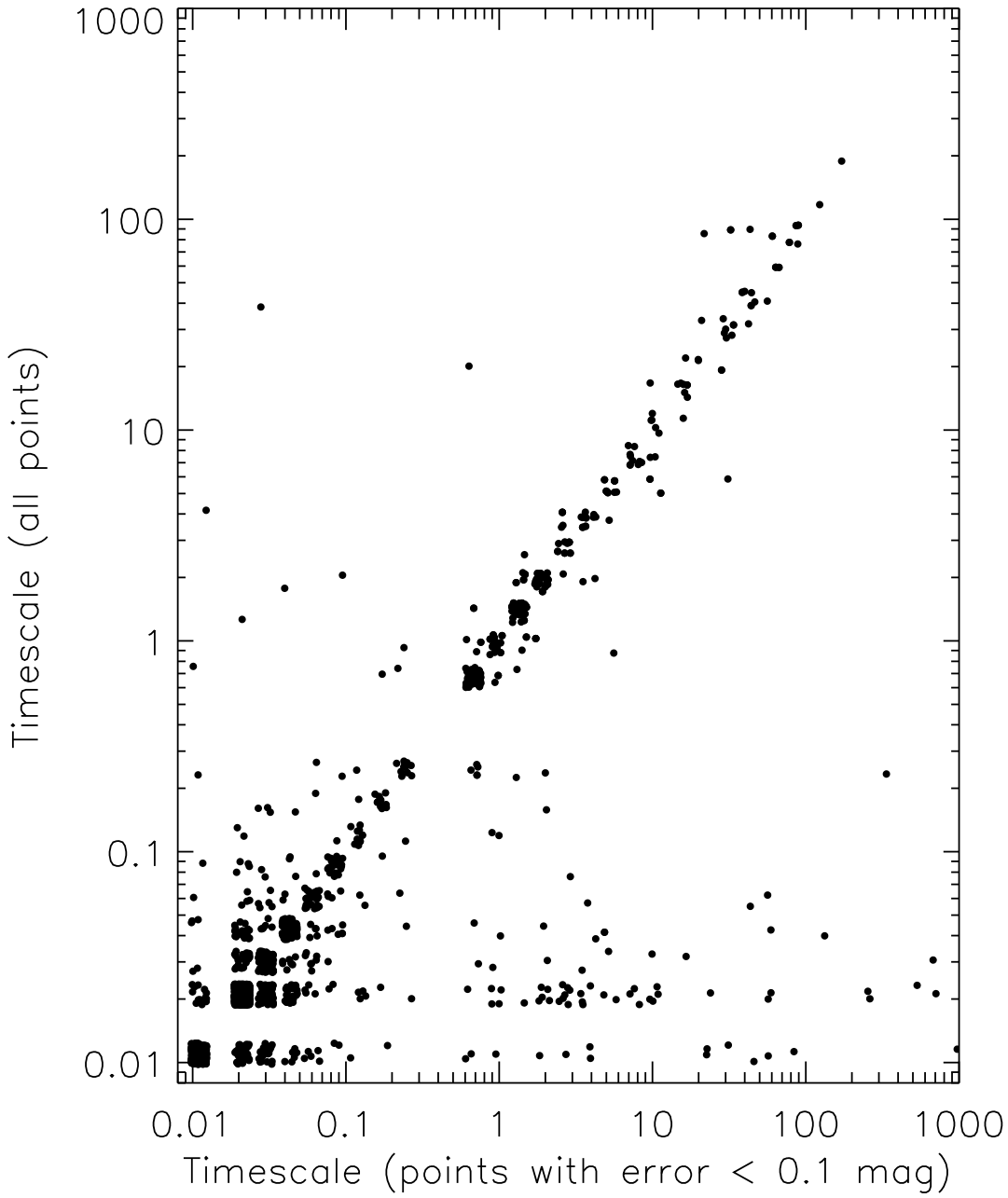


**Figure 6.5:** Timescales for variable PTF sources calculated including (vertical axis) and ignoring (horizontal axis) points with photometric errors exceeding 0.1 mag. Only the 1,845 sources for which both timescales could be calculated are shown. Timescales have been randomized by $\pm 0.05$ dex to clarify the number of points in each bin. The gap at $\sim 0.5$ days is imposed by our nightly cadence. For most sources, the two timescales fall in the same bin, or differ by at most one bin.

Inspection of sources with timescales shorter than 0.1 day reveals no single cause for the short values. Some lightcurves appear to simply be noisier than the majority of stars with the same median magnitude, leading to their false classification as variables on the basis of their RMS. Some lightcurves have unflagged artifacts in the photometry, particularly blended sources or bad CCD columns. Others are lightcurves with 0.1-0.2 day variability that fell below 0.1 day due to timescale uncertainty.

In the remainder of this chapter I use timescales excluding points with 0.1 mag or larger errors, and discard values below 0.1 day as invalid. This leaves 515 sources with timescale measurements, 207 of which have spectra.

### 6.5.2 Timescales in the North America Nebula Complex

The $\Delta m$-$\Delta t$ plots for the 2,705 PTF variables show a wide variety of behaviors. I show some typical examples of high-confidence candidates in Figure 6.6, low-confidence candidates in Figure 6.7, and likely non-members in Figure 6.8. As these figures show, $\Delta m$-$\Delta t$ plots provide information about lightcurve structure regardless of magnitude, noise level, and membership probability.

As a further illustration, Figure 6.9 shows examples as a function of timescale across two and a half orders of magnitude. The timescale definition adopted in subsection 6.5.1 represents the time one must wait to see a large change in magnitude, relative to the overall lightcurve amplitude. For periodic sources, for example, the timescale as defined here should never exceed half the period and may be considerably shorter, depending on the shape of the lightcurve.

While we cannot directly measure the amount of variability occurring in the nightly gap at $10^{-0.47}$-$10^{-0.17}$ days, the $\Delta m$-$\Delta t$ plots suggest that this is an important time interval to characterize. Many sources have significantly higher $\Delta m$ values in the $10^{-0.17}$-$10^{-0.02}$ day bin than in the $10^{-0.62}$-$10^{-0.47}$ day bin, suggesting that you can see significant changes on time intervals of less than a day. This does not appear to be a bias related to the one-day average cadence, as the simulations of Chapter 5 showed no predisposition for the $10^{-0.17}$-$10^{-0.02}$ day bin to be *substantially* higher than the $10^{-0.62}$-$10^{-0.47}$ day bin. Time intervals in the nightly gap have been probed by Cody et al. (2013) and Cody et al. (2014) using space-based data, but the lightcurves illustrated in either publication show relatively little variation over time intervals of less than a day. A more thorough statistical analysis will be published at a later date.

Some lightcurves also show substantial variation on time intervals of 0.1 day or less. In Figures 6.6b, 6.7b, and 6.8c, a smaller fraction of point pairs show a large magnitude change at short time intervals than at long ones; this can be seen from the coloring of the low-amplitude ($\Delta m \lesssim 0.1$ mag) bins in those plots, which contain most of the sources at short time intervals but not at long ones. For these, the short timescale is somewhat misleading, and choosing a lower percentile than the 90th as the basis of the timescale should raise the result. In Figures 6.8a, 6.8h, 6.8e, and 6.8i, on the other

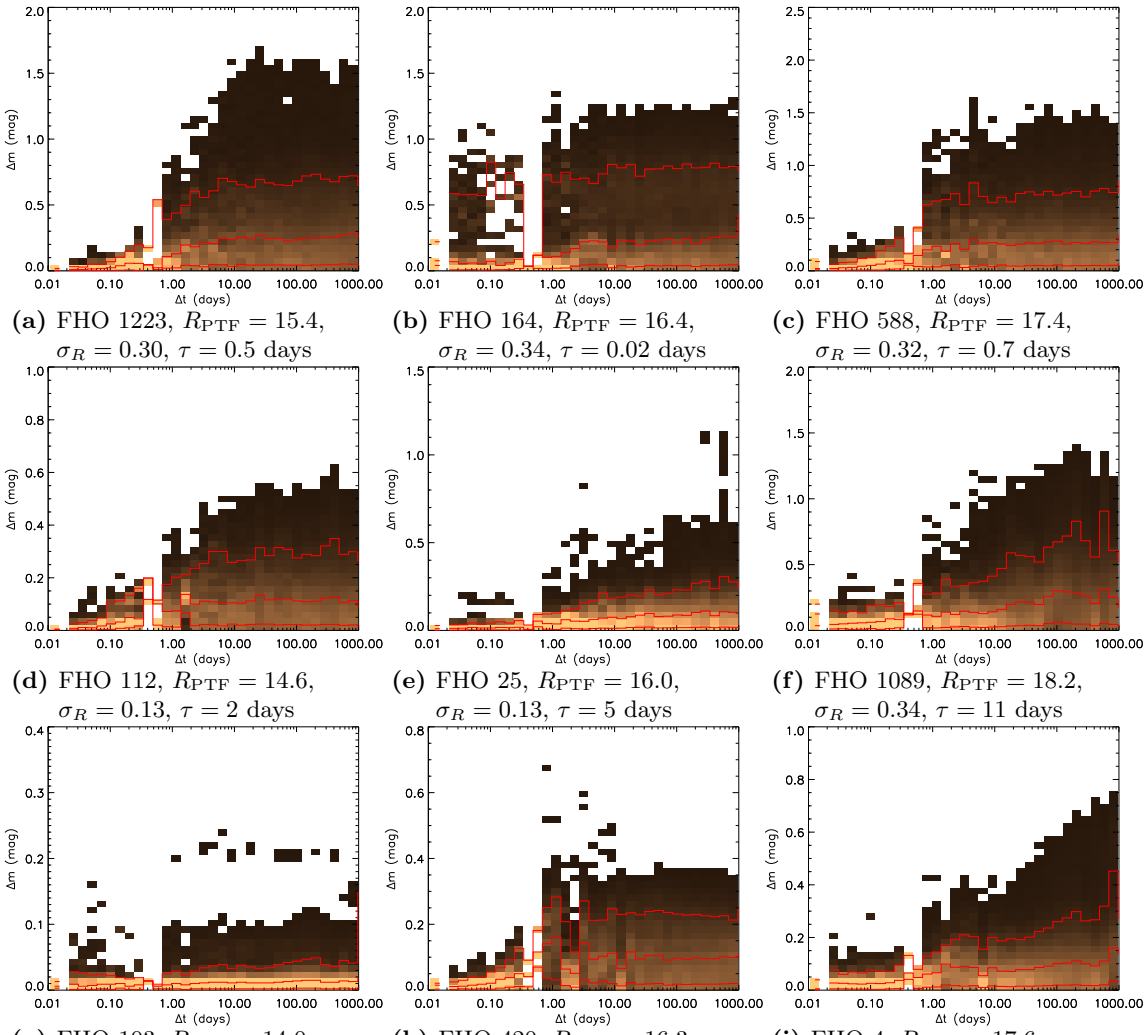


**(a)** FHO 1223, $R_{\rm PTF} = 15.4$, $\sigma_R = 0.30$, $\tau = 0.5$ days

**(b)** FHO 164, $R_{\rm PTF} = 16.4$, $\sigma_R = 0.34$, $\tau = 0.02$ days

**(c)** FHO 588, $R_{\rm PTF} = 17.4$, $\sigma_R = 0.32$, $\tau = 0.7$ days

**(d)** FHO 112, $R_{\rm PTF} = 14.6$, $\sigma_R = 0.13$, $\tau = 2$ days

**(e)** FHO 25, $R_{\rm PTF} = 16.0$, $\sigma_R = 0.13$, $\tau = 5$ days

**(f)** FHO 1089, $R_{\rm PTF} = 18.2$, $\sigma_R = 0.34$, $\tau = 11$ days

**(g)** FHO 103, $R_{\rm PTF} = 14.0$, $\sigma_R = 0.05$, $\tau = 0.02$ days

**(h)** FHO 420, $R_{\rm PTF} = 16.3$, $\sigma_R = 0.09$, $\tau = 0.5$ days

**(i)** FHO 4, $R_{\rm PTF} = 17.6$, $\sigma_R = 0.14$, $\tau = 2$ days

**Figure 6.6:** Typical $\Delta m$-$\Delta t$ examples for high-confidence candidates, showing that $\Delta m$-$\Delta t$ plots work at all magnitudes, noise levels, and amplitudes. Sources get fainter moving from left to right, and lower-amplitude (relative to the noise level, see subsection 3.2.1) moving from top to bottom. Light shading indicates a high fraction of points in a $\Delta t$ bin (column) fall in a particular cell; dark shading indicates a sparsely populated cell. Red lines are, from top to bottom, the 90th, 50th, and 10th percentiles of $\Delta m$ in each $\Delta t$ column. A variety of timescales are represented, from 0.02 days (Figure 6.6b) to 11 days (Figure 6.6f).

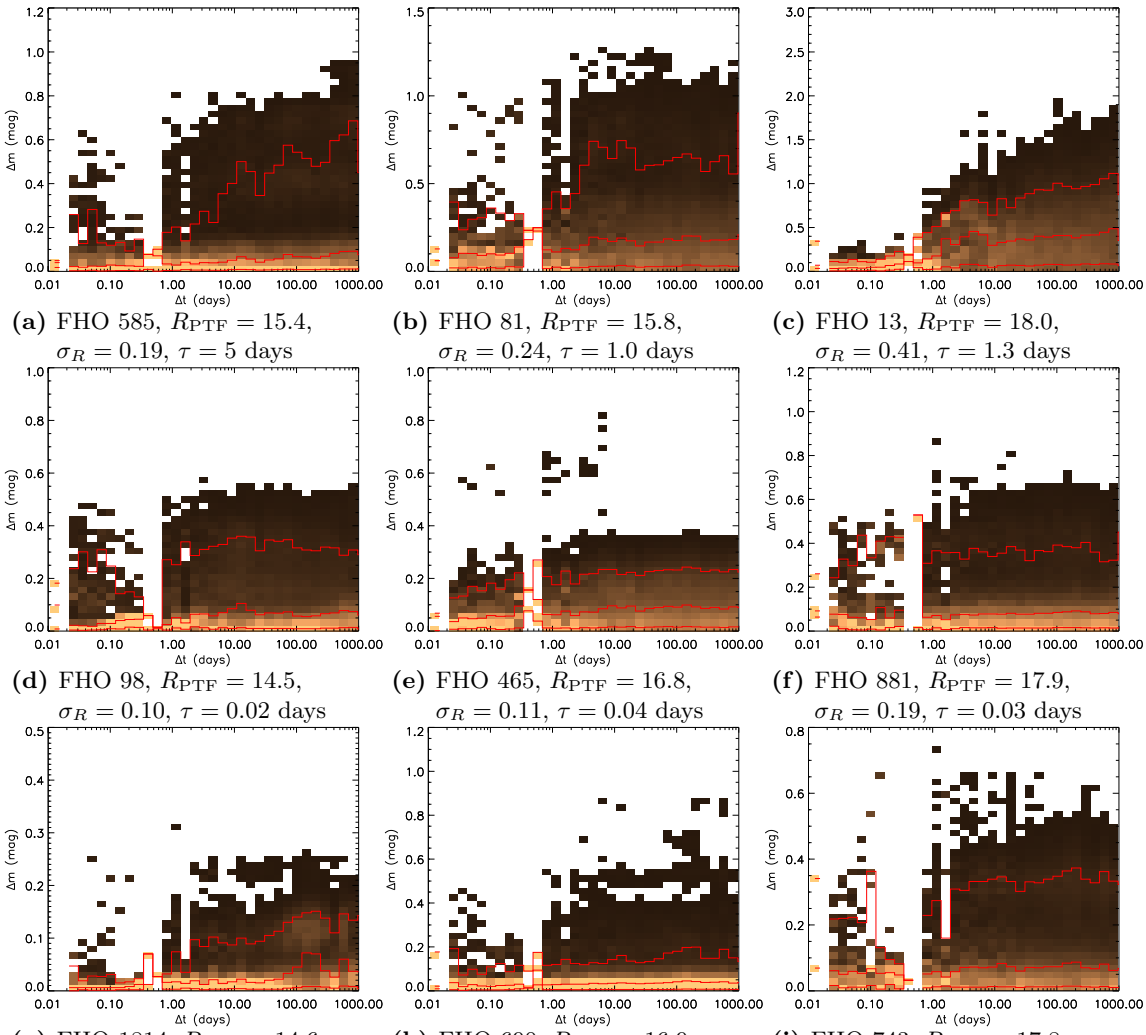


**(a)** FHO 585, $R_{\rm PTF} = 15.4$, $\sigma_R = 0.19$, $\tau = 5$ days

**(b)** FHO 81, $R_{\rm PTF} = 15.8$, $\sigma_R = 0.24$, $\tau = 1.0$ days

**(c)** FHO 13, $R_{\rm PTF} = 18.0$, $\sigma_R = 0.41$, $\tau = 1.3$ days

**(d)** FHO 98, $R_{\rm PTF} = 14.5$, $\sigma_R = 0.10$, $\tau = 0.02$ days

**(e)** FHO 465, $R_{\rm PTF} = 16.8$, $\sigma_R = 0.11$, $\tau = 0.04$ days

**(f)** FHO 881, $R_{\rm PTF} = 17.9$, $\sigma_R = 0.19$, $\tau = 0.03$ days

**(g)** FHO 1814, $R_{\rm PTF} = 14.6$, $\sigma_R = 0.05$, $\tau = 2$ days

**(h)** FHO 690, $R_{\rm PTF} = 16.9$, $\sigma_R = 0.09$, $\tau = 0.011$ days

**(i)** FHO 743, $R_{\rm PTF} = 17.8$, $\sigma_R = 0.13$, $\tau = 0.011$ days

**Figure 6.7:** As Figure 6.6, but for low-confidence candidates. Timescales range from 0.011 days (Figures 6.7h and 6.7i) to 5 days (Figure 6.7a).

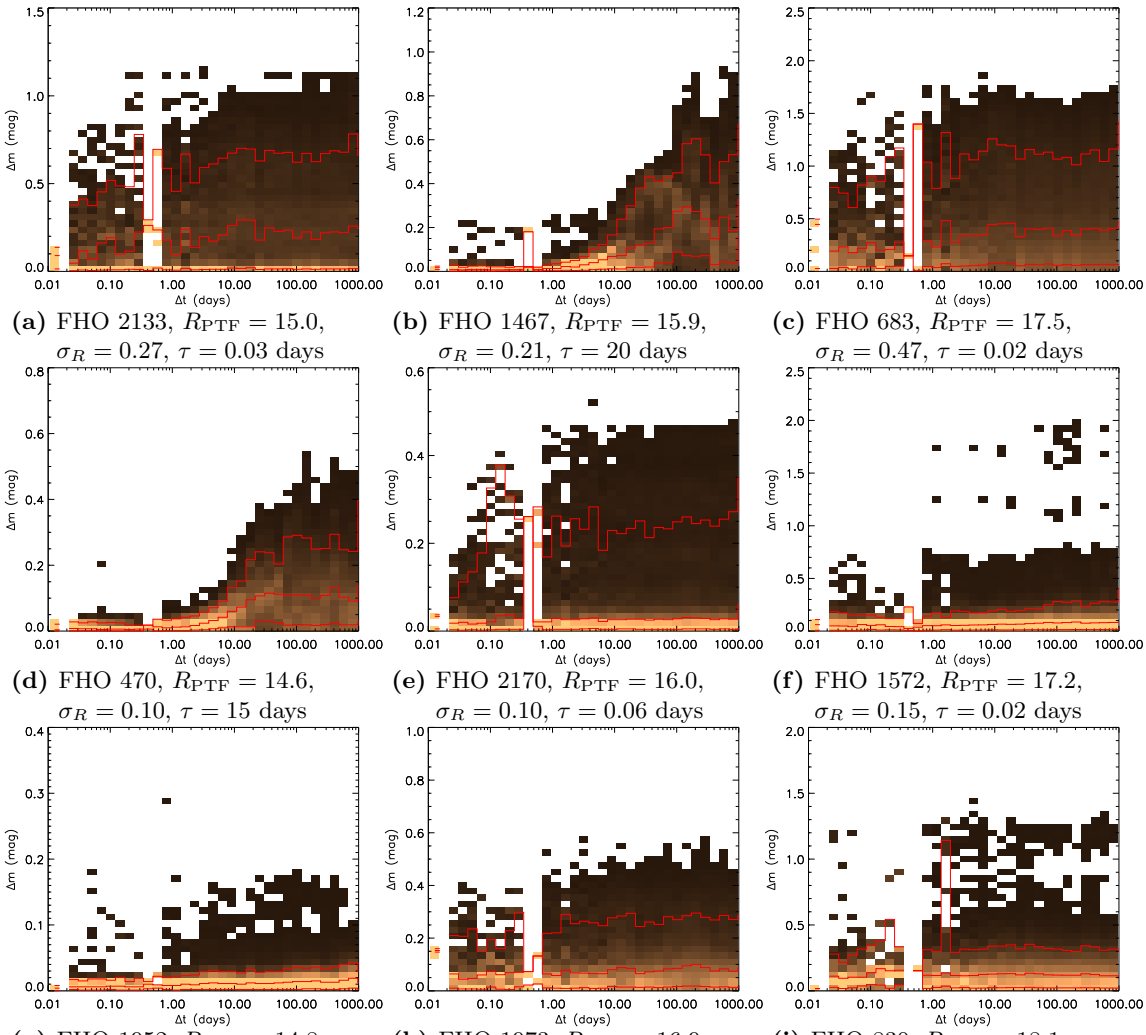


**(a)** FHO 2133, $R_{\rm PTF} = 15.0$, $\sigma_R = 0.27$, $\tau = 0.03$ days

**(b)** FHO 1467, $R_{\rm PTF} = 15.9$, $\sigma_R = 0.21$, $\tau = 20$ days

**(c)** FHO 683, $R_{\rm PTF} = 17.5$, $\sigma_R = 0.47$, $\tau = 0.02$ days

**(d)** FHO 470, $R_{\rm PTF} = 14.6$, $\sigma_R = 0.10$, $\tau = 15$ days

**(e)** FHO 2170, $R_{\rm PTF} = 16.0$, $\sigma_R = 0.10$, $\tau = 0.06$ days

**(f)** FHO 1572, $R_{\rm PTF} = 17.2$, $\sigma_R = 0.15$, $\tau = 0.02$ days

**(g)** FHO 1952, $R_{\rm PTF} = 14.8$, $\sigma_R = 0.06$, $\tau = 2$ days

**(h)** FHO 1973, $R_{\rm PTF} = 16.9$, $\sigma_R = 0.11$, $\tau = 0.02$ days

**(i)** FHO 830, $R_{\rm PTF} = 18.1$, $\sigma_R = 0.17$, $\tau = 0.02$ days

**Figure 6.8:** As Figure 6.6, but for likely non-members. Timescales range from 0.02 days (Figures 6.8a, 6.8c, and 6.8h) to 20 days (Figure 6.8b).

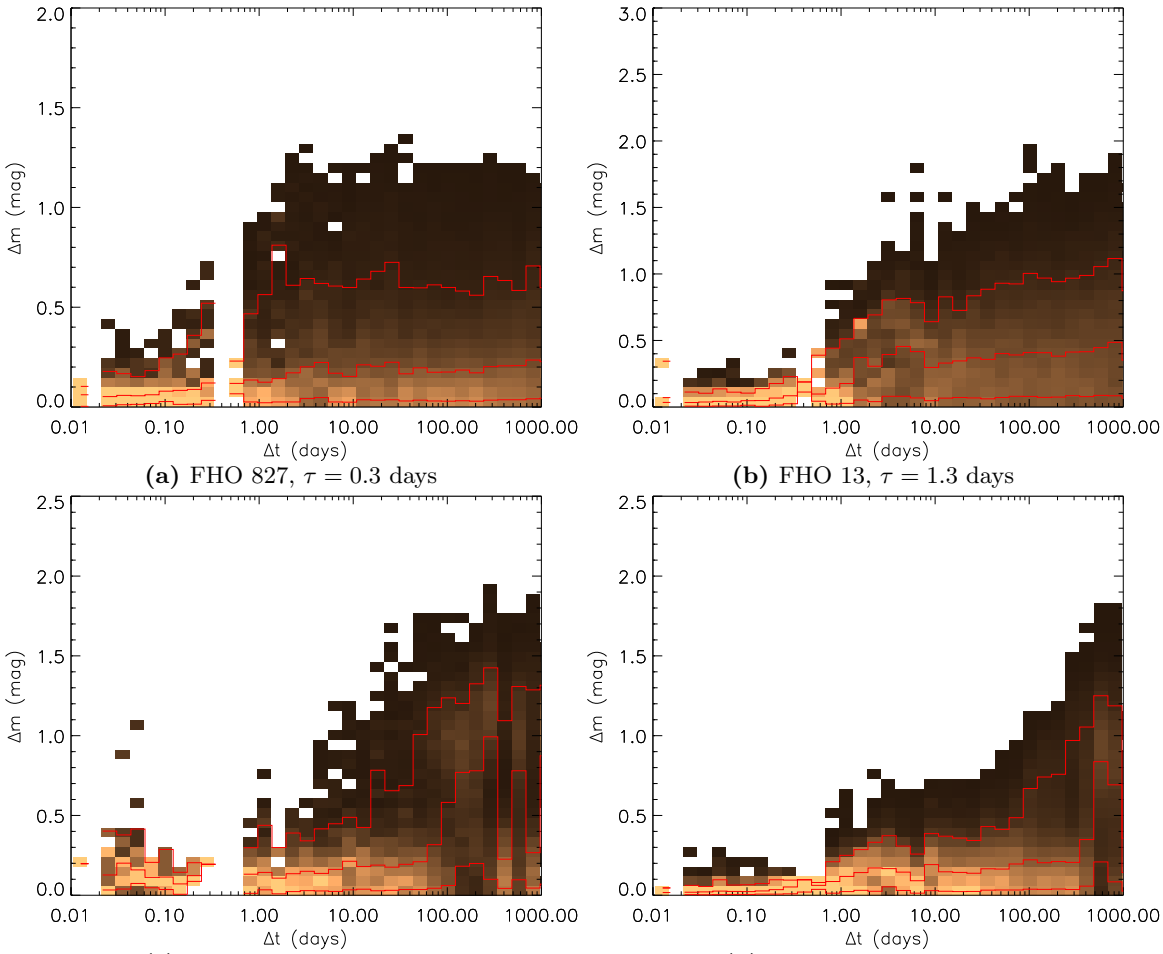


**(a)** FHO 827, $\tau = 0.3$ days

**(b)** FHO 13, $\tau = 1.3$ days

**(c)** FHO 1039, $\tau = 15$ days

**(d)** FHO 2175, $\tau = 85$ days

**Figure 6.9:** Typical $\Delta m$-$\Delta t$ examples for high-amplitude sources at a variety of timescales. Light shading indicates a high fraction of points in a $\Delta t$ bin (column) fall in a particular cell; dark shading indicates a sparsely populated cell. Red lines are, from top to bottom, the 90th, 50th, and 10th percentiles of $\Delta m$ in each $\Delta t$ column.

hand, the $\Delta m$ distribution seems to be nearly independent of the time interval on which observations are compared. At face value, this distribution means that the source experiences 0.2 mag or greater changes in 30 minutes or less, but no additional variability at longer time intervals; inspection of the lightcurves confirms that they show no correlation even in high cadence data. While we find it implausible that a star would have such rapid and short timescale variability, we cannot find a specific systematic error affecting these stars but not others. Any conclusions regarding variability on very short timescales will require further study.

The distribution of timescales is shown in Figure 6.10. Values range from our cutoff at 0.1 days to timescales just over 100 days, where simulations show that $\Delta m$-$\Delta t$ timescales have an average ceiling set by our observing cadence (see Figure 5.12 and accompanying text). The $10^{-0.17}$-$10^{-0.02}$ day bin has a disproportionately large number of sources, because it includes sources whose true timescale would lie within the poorly sampled gap at $\sim 0.5$ days: in effect, the bin contains sources with a timescale anywhere between $10^{-0.47}$ days and $10^{-0.02}$ days.

Even ignoring the inflated $10^{-0.17}$-$10^{-0.02}$ day bin, the timescale distributions for all sources and for high-confidence members are inconsistent with a log-uniform distribution over [1, 100], with a two-sided Kolmogorov-Smirnov (K-S) test returning a p-value smaller than $2 \times 10^{-16}$ for all sources and a p-value of $8 \times 10^{-14}$ for high-confidence members. The plot for high-confidence members shows a pronounced excess of sources with characteristic timescales between 1 day and 2 days, separate from the artificially enhanced $10^{-0.17}$-$10^{-0.02}$ day bin. We see no tendency for $\Delta m$-$\Delta t$ timescales to cluster between 1 day and 2 days in the simulations of Chapter 5, so this is unlikely to be a systematic effect related to either the cadence or the $\Delta m$-$\Delta t$ method.

This result is broadly consistent with previous results finding periods of order a week for periodically varying young stars. According to Table 4.3, the characteristic timescale of a sinusoidal signal should be 1/6 its period. The periods for T Tauri stars are typically in the 2-15 day range, peaking at 6-8 days (Herbst et al., 2000; Cohen et al., 2004); any periodic T Tauri stars in our sample should therefore either be part of the $\sim 1$ day peak or fall in our $\sim 0.5$ day gap.

With a K-S p-value of 0.009, the timescale distribution for low-confidence members is marginally inconsistent with a log-uniform distribution; there are hints that it may also have a peak at 1-2 days. The timescale distribution for likely nonmembers, on the other hand, is marginally consistent with a log-uniform distribution, with a p-value of 0.02. However, since these samples have only 26 and 17 sources, respectively, with timescales of 1 day or longer, any tests of their distributions are necessarily imprecise.

The timescale distribution with magnitude is shown in Figure 6.11. There is no change in the measured timescales with respect to magnitude. This suggests that the same timescales are relevant for high- and low-luminosity sources (with the important caveat that only some variables are North America Nebula members, and therefore at the same distance), and reassures us that timescales

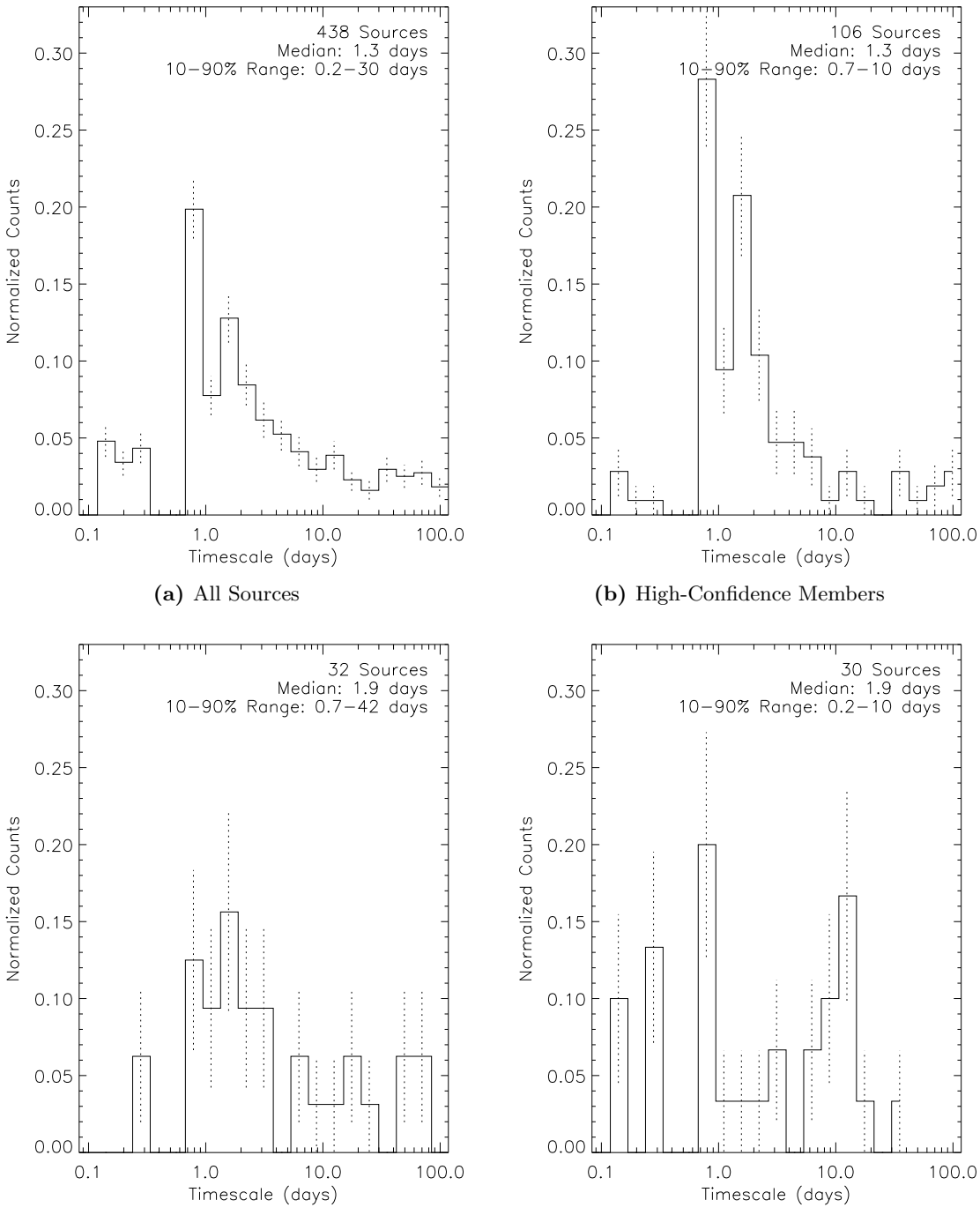


**(a)** All Sources

**(b)** High-Confidence Members

**(c)** Low-Confidence Members

**(d)** Likely Non-Members

**Figure 6.10:** Distribution of timescales for all sources, whether or not they have a spectrum, and for high-confidence members, low-confidence members, and likely non-members, as defined in subsection 6.4.2. High-confidence members are likely to have timescales around $\sim 1$ day, while both low-confidence members and likely non-members have a flat timescale distribution to within the limitations of the small number statistics.

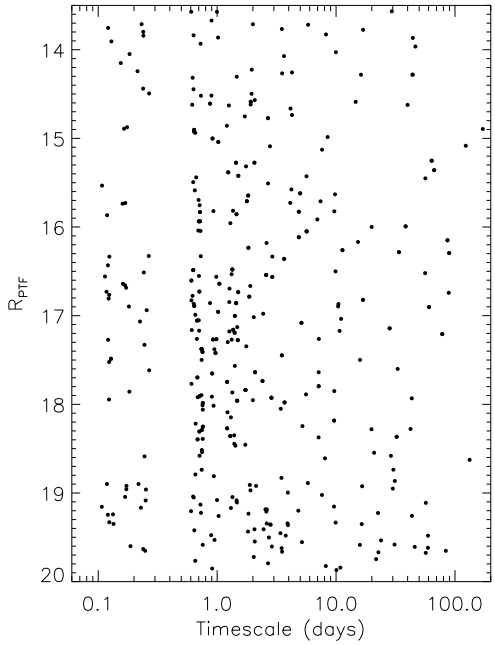


**Figure 6.11:** The distribution of timescales as a function of median PTF magnitude. There is little to no correlation between timescale and magnitude; sources both bright and faint can have any timescale in the sample.

for faint sources are not dominated by photometric noise, which would produce an excess of short timescales.

The data set therefore contains aperiodic variability on timescales from just under a day to the longest scales detectable with our data. There appears to be a large number of sources with timescales of 1-2 days, consistent with variability from stellar rotation or dynamical changes at the inner disk edge. We see a sharp increase in variability between the longest intranight time baselines and the shortest baselines between consecutive nights, suggesting that variability on baselines of half a day may be worth following up with more appropriate data sets.

## 6.6 Variability Properties

### 6.6.1 Timescales and Amplitudes

I show the distribution of timescales and amplitudes for all sources in the sample of 2,705 variables, whether or not they had spectra, in Figure 6.12 and Figure 6.13, respectively. The two figures divide sources according to the detection or non-detection of an infrared excess, as described in subsection 6.4.3. The sources without a detected infrared excess are expected to be dominated by sources that genuinely lack an excess above their photosphere, but many of these sources were also too faint to be detected by Spitzer at 24 $\mu$m, so a weak long-wavelength excess cannot be ruled out.

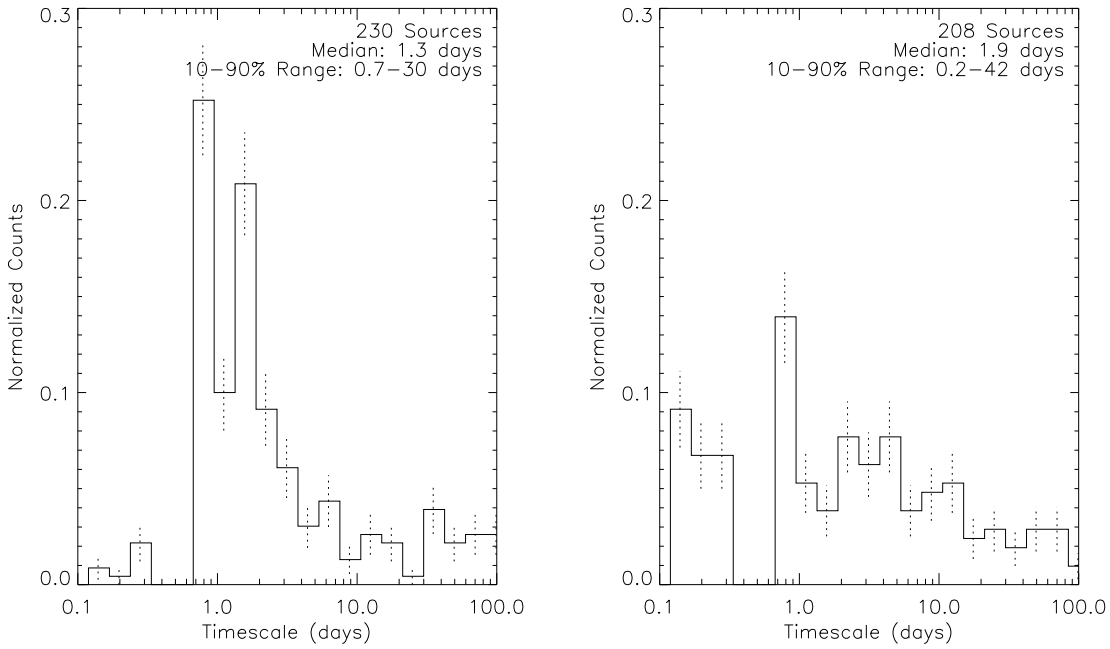


**(a)** Infrared Excess **(b)** No Infrared Excess

**Figure 6.12:** Distribution of timescales for sources with and without an infrared excess. Sources with an infrared excess tend to cluster around timescales of $\sim$ 1-2 days.

The distribution of timescales for infrared excess sources, shown in Figure 6.12a, resembles that for high-confidence spectroscopic candidates (Figure 6.10b), in that the distribution reaches a maximum on timescales of 1-2 days. This is in large part due to the overlap between the samples: 78% of infrared excess sources with spectra are high-confidence candidates, while 63% of high-confidence candidates with a Spitzer counterpart have an infrared excess.

The distribution for sources that were not identified in subsection 6.4.3 as having an infrared excess appears much flatter than that for infrared excess sources. Despite the apparent even distribution, a two-sided Kolmogorov-Smirnov (K-S) test finds that the data for timescales longer than 1 day are inconsistent with a log-uniform distribution over [1, 100], with a p-value of 0.0003. The current data suggest these sources have a slight preference towards timescales of 3-5 days, but a larger sample will be needed to confirm.

The amplitude distributions in Figure 6.13 for sources with and without a detected infrared excess are similar to each other, except that the infrared excess sources tend to have slightly higher amplitudes on average as well as a longer tail to high amplitudes. The differences between the two samples are significant; a two-sided Kolmogorov-Smirnov test comparing the two samples finds a p-value of $2 \times 10^{-5}$.

Both distributions peak at around 0.1-0.2 mag, somewhat higher than our detection threshold of 0.07-0.1 mag (see Figure 3.1 for detection thresholds as a function of chip and magnitude). Because

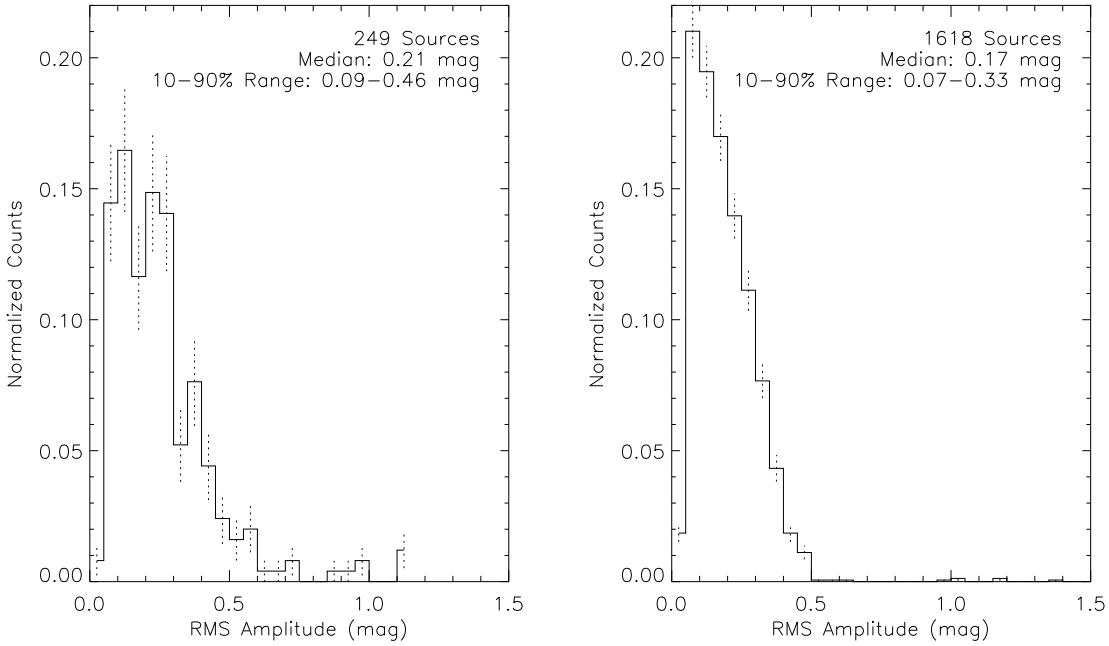


**(a)** Infrared Excess **(b)** No Infrared Excess

**Figure 6.13:** Distribution of amplitudes for sources with and without a detected infrared excess. The distribution for infrared excess sources is somewhat broader, and both rise upward to our detection threshold at $\sim 0.1$ mag.

our survey is amplitude-limited, the similarity in peaks does not necessarily indicate a similarity between the infrared-excess and non-infrared-excess sources; we may merely be probing the high-amplitude tail of either distribution.

The *joint* distribution of timescale and amplitude is shown in Figure 6.14. Many of the results from Figure 6.12 and Figure 6.13 can be seen here, including the concentration of sources toward short timescales and the scarcity of sources with higher RMS amplitudes than 0.5 mag.

The most striking property of the joint distribution of timescale and amplitude is that there is no strong trend between amplitude and timescale. Sources below 0.4-0.5 mag may have almost any combination of amplitude and timescale. In particular, we see a handful of sources with timescales of $\sim$ 100 days, but amplitudes of only $\sim$ 0.1 mag; to our knowledge, this is the first time that low-amplitude, long-timescale variability has been identified. Sources above 0.5 mag are too sparse to constrain the timescale distribution.

### 6.6.2 High-Amplitude Sources

We individually examined the lightcurves and spectra of all candidate members with RMS amplitudes exceeding 0.6 mag. Of 17 sources with high amplitudes, four (FHO 222, FHO 1176, FHO 1346, and FHO 1951) have pulsating lightcurves, and of those FHO 1176 and FHO 1346 also have spectra

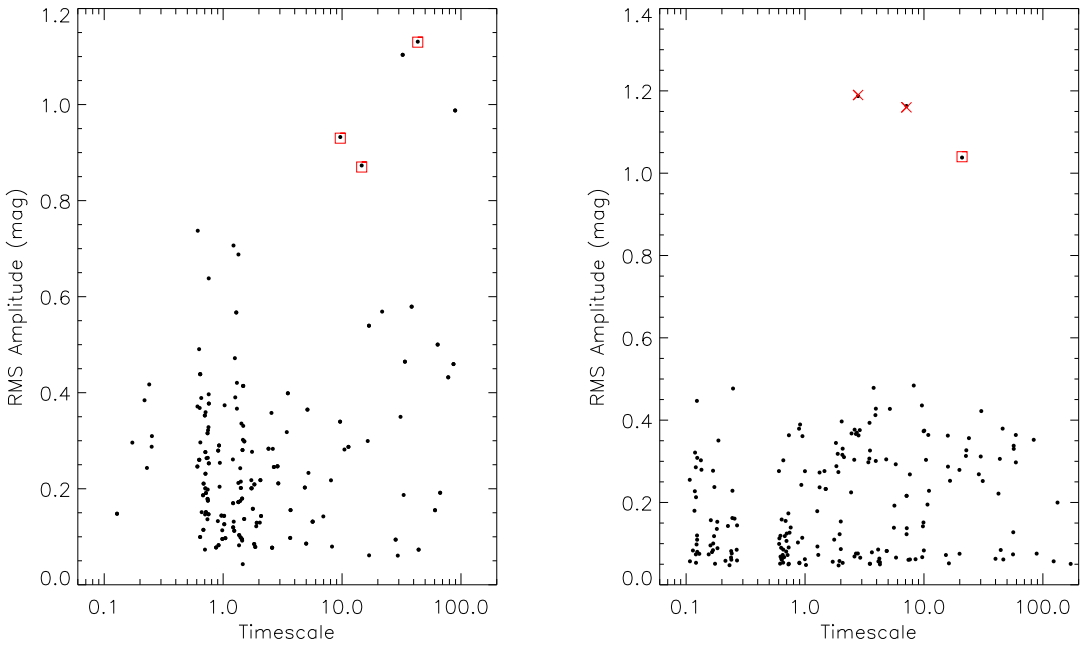


**(a)** Infrared Excess **(b)** No Infrared Excess

**Figure 6.14:** RMS vs. timescale distributions for sources with and without a detected infrared excess from subsection 6.4.3. Timescales have been randomized by ±0.05 dex for clarity. While sources with infrared excess tend to have slightly higher amplitudes and timescales around ∼ 1 day, there are few clear groups within the amplitude-time parameter space. Sources above 0.6 mag RMS marked by red boxes are giants, while those marked by X's are dominated by pipeline problems; see subsection 6.6.2 for more details. Sources above 0.6 mag that are not marked appear to be genuine young stars on closer inspection.

consistent with late-type stars. We believe these four sources to be background giants; none have IPHAS photometry, and they could not be rejected using a color-magnitude diagram. Another six sources (FHO 180, FHO 232, FHO 444, FHO 1351, FHO 1518, and FHO 2348) have no apparent structure in the lightcurve or have obvious unflagged artifacts.

The remaining seven (FHO 105, FHO 455, FHO 561, FHO 598, FHO 618, FHO 781, and FHO 2359) appear to be genuine high-amplitude variables that do not behave like giants. Of the seven, all except FHO 618 have a detected infrared excess, and all except FHO 598 and FHO 2359 have spectra (all of which show youth indicators).

While there is some giant contamination in our sample, a large number of sources appear to be genuine young stars. We mark giants in Figure 6.14 with boxes, and stars with suspect photometry with crosses. Unmarked high-amplitude sources in Figure 6.14 are likely candidate members.

### 6.6.3 Correlation with Infrared and Emission Line Properties

The amplitude and timescale for all 2,705 PTF variables is plotted against 2MASS/Spitzer infrared color in Figure 6.15. Point colors indicate the infrared source class from Rebull et al. (2011); black points are sources that either had insufficient photometric data for Rebull et al. to classify, or, on the left side of either panel, that were not found to have an infrared excess by Guieu et al. (2009) or Rebull et al. (2011).

The black curve in either panel shows the median $K - [8.0]$ color for stars of a given amplitude or timescale. Variables with RMS amplitudes below 0.3 mag are predominantly sources with blue infrared colors, which may or may not be young stars; the majority of variables with amplitudes above 0.3 mag have a clear excess. A majority of variables with timescales between 0.7 days and 6 days have an infrared excess, while most variables with either longer or shorter timescales do not. There is a hint that variables with timescales of $\sim 80$ days or longer are also predominantly infrared excess sources, but more examples of long-timescale variables will be needed to confirm this.

The variability properties of the sources with spectra are shown in Figures 6.16 and 6.17 as a function of the equivalent widths of the H$\alpha$ 6563 Å, Ca II 8542 Å, and Li I 6708 Å lines. H$\alpha$ and Ca II are both accretion indicators, and show similar behavior in both figures. The strongest H$\alpha$ and Ca II emitters have amplitudes of 0.4-0.5 mag, and the strongest H$\alpha$ emitters also have timescales of 0.7-1 days. The strongest Ca II emitters show no preference for a particular timescale. For weaker emitters, there seems to be no trend between either H$\alpha$ or Ca II strength and timescale.

The highest-amplitude sources in Figure 6.16 tend to be only modest H$\alpha$ and Ca II emitters, with H$\alpha$ equivalent widths of a few tens of Å and Ca II widths of around 10 Å. While line equivalent width is only a crude measure of accretion rate, these results suggest that the highest-amplitude variables may not be (directly) accretion-powered. A comparison with accretion rate measurements for these stars may clarify these results.

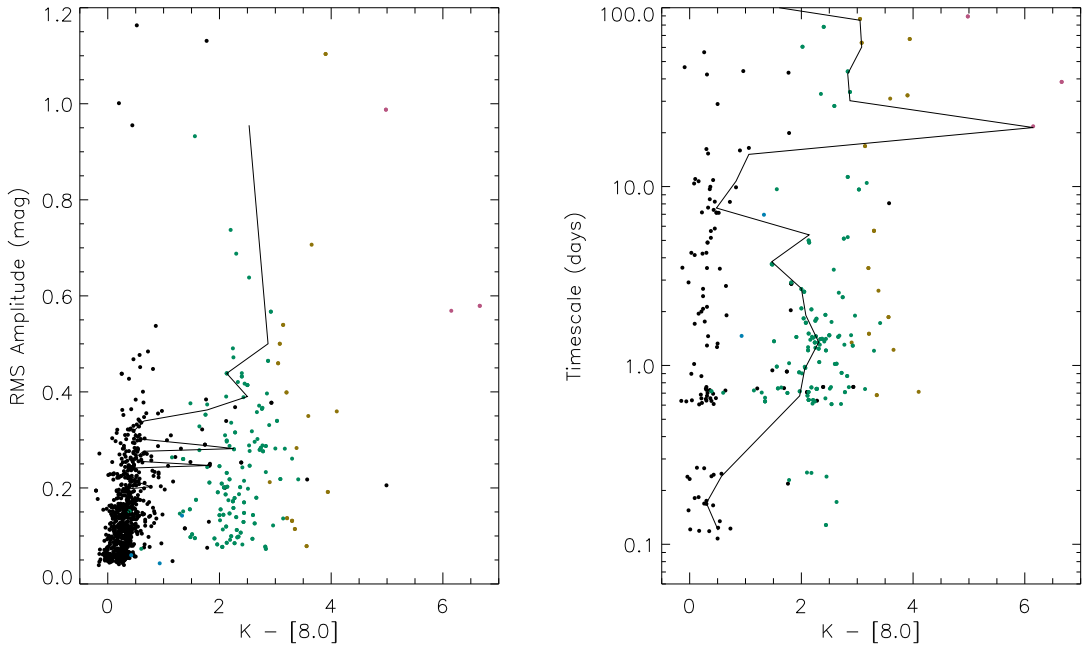


**Figure 6.15:** Optical lightcurve properties as a function of infrared class and color for variable PTF sources whose lightcurves have flags (listed in subsection 2.2.2) in fewer than half the epochs. Both amplitude and timescale are weakly correlated with the source's infrared properties; one can find a range of colors at any amplitude or timescale and a range of amplitudes and timescales at any color. Timescales have been randomized by ±0.05 dex for clarity. The solid line indicates the median color in 15-point bins (left) or in the $\Delta t$ bins used for the $\Delta m$-$\Delta t$ plot (right). The color of the dots indicates the degree of infrared excess: blue dots are class III sources, green ones class II, yellow ones have a flat IR spectrum, while magenta sources are class I sources. Black sources were not assigned an IR excess class by Rebull et al. (2011), either because they did not have an excess or because they were too faint to classify definitively.

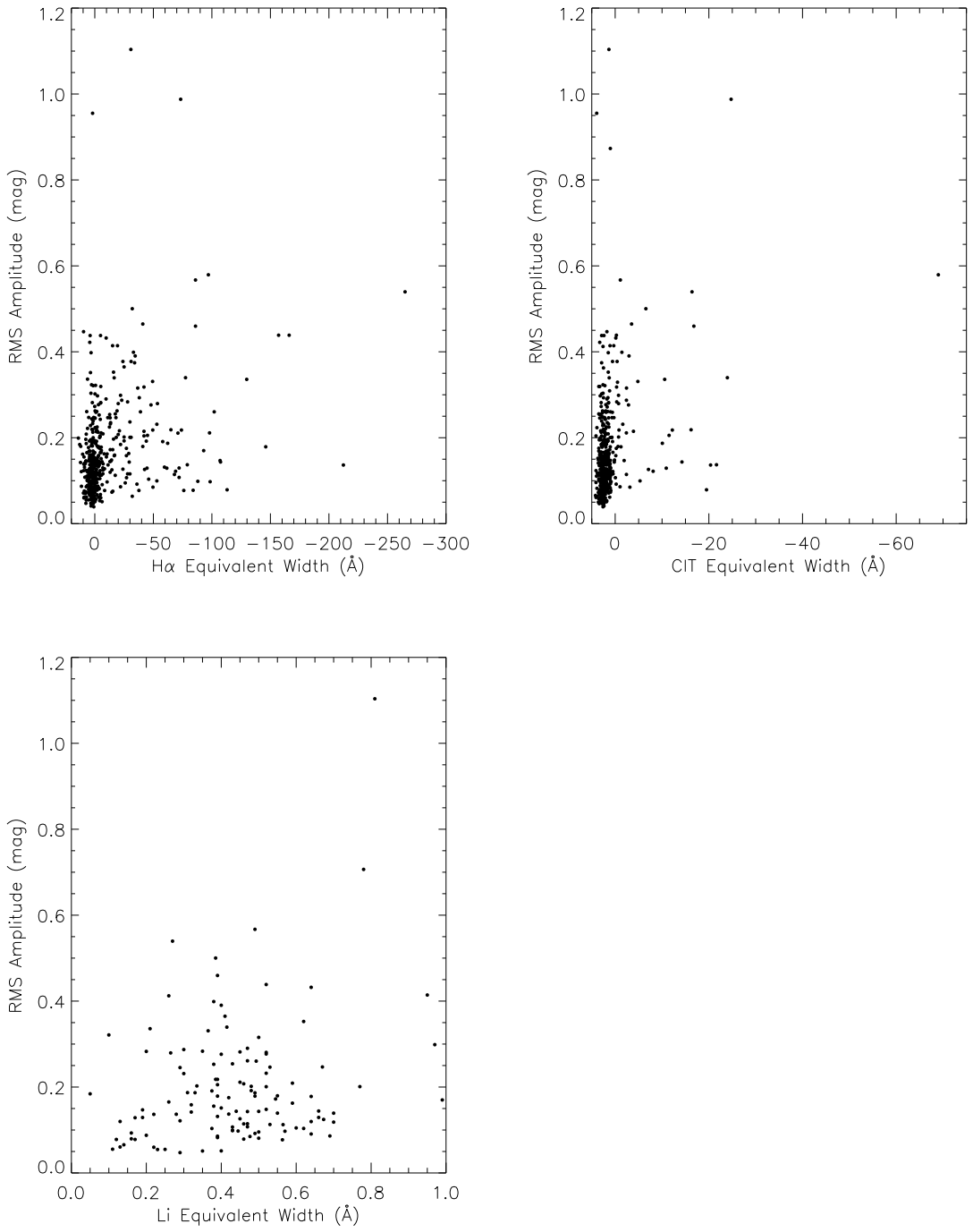


**Figure 6.16:** The variability amplitude vs. the strength of the H$\alpha$ 6563 Å and Ca II 8542 Å lines, which probe accretion onto the star, and Li I 6708 Å, which probes stellar age. Strong H$\alpha$ and Ca II emitters, and presumably rapidly accreting stars, do not have the highest amplitudes, but strong Li I absorbers, presumably the youngest stars, do.

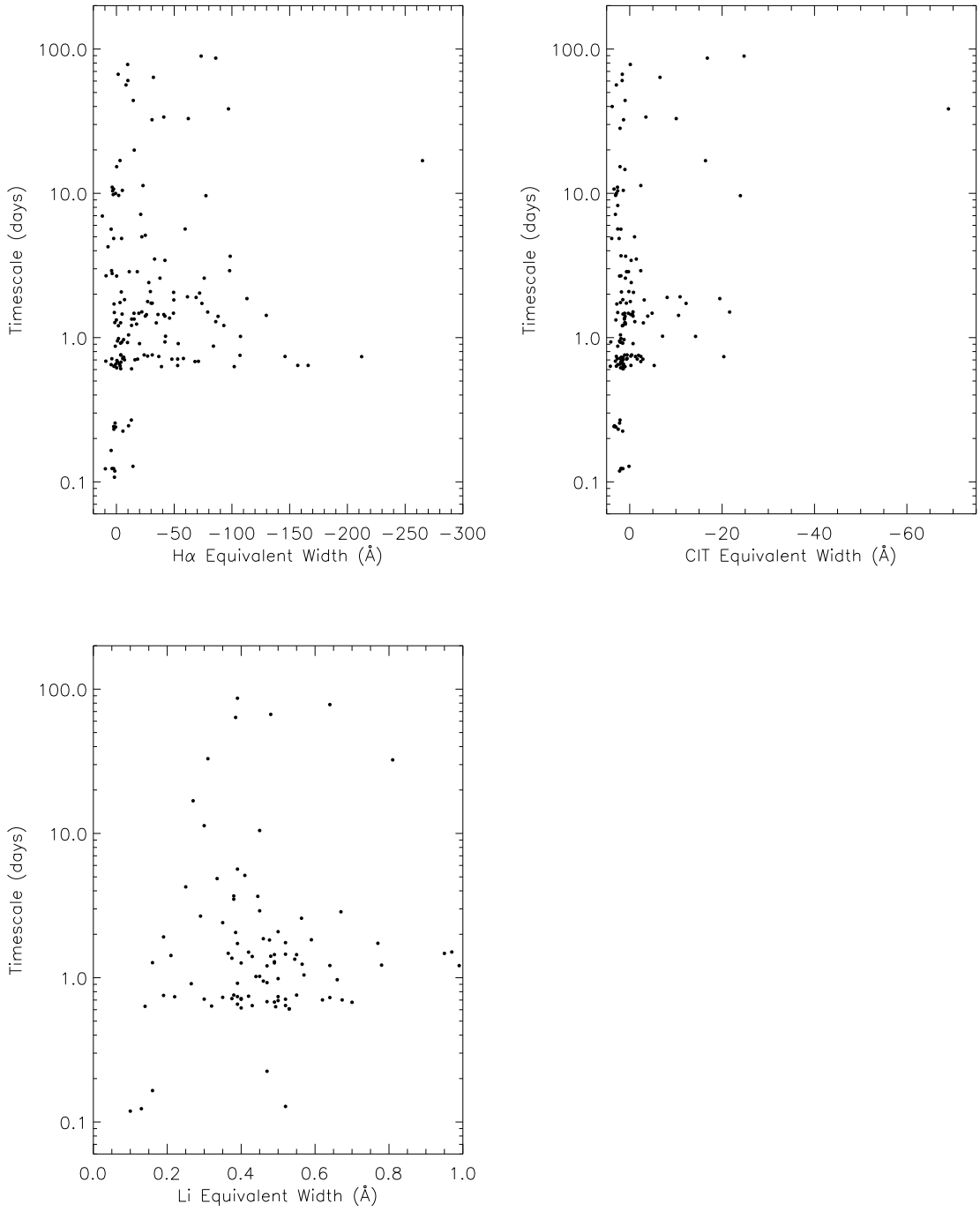


**Figure 6.17:** H$\alpha$ and Ca II infrared triplet emission and Li absorption for variables with different timescales. There is no systematic trend of line strength with timescale. Timescales have been randomized by $\pm 0.05$ dex for clarity.

While there is no significant correlation between variability amplitude and Li I equivalent width in Figure 6.16, we do find that the two highest-amplitude sources with lithium measurements also have among the strongest equivalent widths. Two sources are not, however, statistically significant.

While stars with Li I equivalent widths exceeding 0.3 Å appear to have no preference for timescale in Figure 6.16, stars with weaker lithium detections tend to have short timescales. It is not clear whether this is a genuine trend in stellar properties, or whether we are insensitive to weak lithium lines in longer-term variables. Long-term variables are no more likely to be faint than short-term variables (Figure 6.11), so this is not simply a matter of long-term variables having noisier spectra.

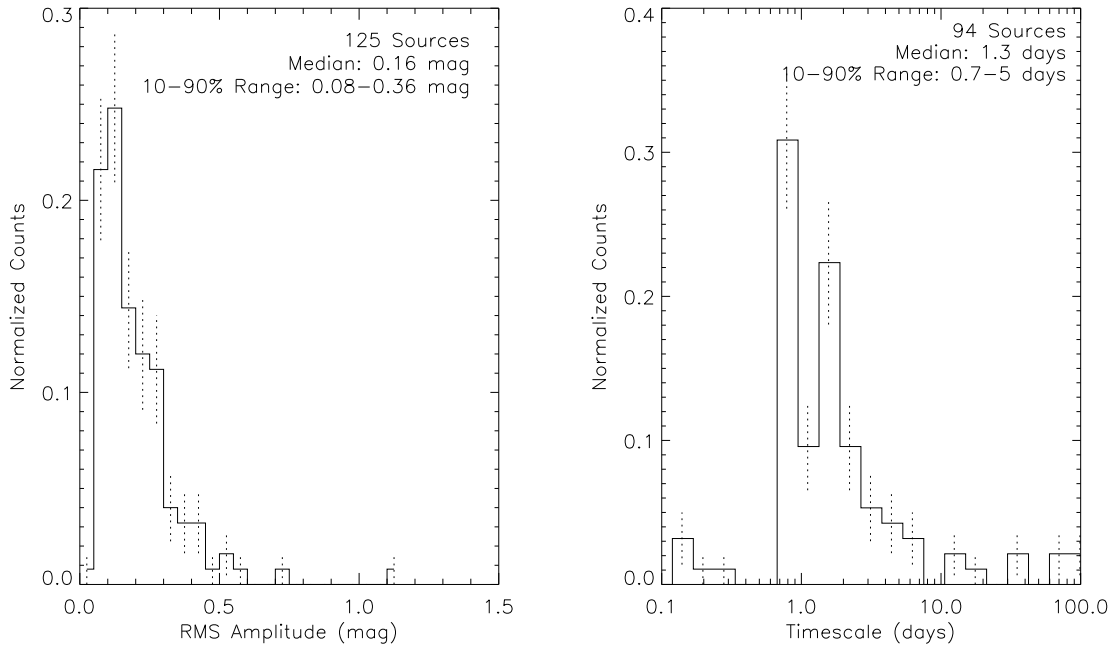


**Figure 6.18:** Distribution of amplitudes and timescales for sources with lithium absorption. As with the infrared excess sources, timescales tend to cluster around timescales of $\sim$ 1 day. Only stars with lithium detections are shown, so the plot is incomplete, and in particular biased toward sources with low veiling — only 45% of variable sources with an infrared excess show detectable lithium absorption.

In Figure 6.18, I show the amplitude and timescale distributions of all sources with Li I detections, regardless of the strength of the line. These distributions closely resemble those for high-confidence members (Figure 6.10b; all lithium sources are high-confidence members by definition, while 82% of high-confidence members have lithium detections) and infrared excess sources (Figure 6.13a and Figure 6.12a; 63% of all lithium sources have an infrared excess, while 73% of all infrared excess sources with spectra have detectable lithium absorption).

There appears to be no strong correlation between variability timescale and infrared color, emission line equivalent width, or lithium absorption equivalent width. The lack of a correlation suggests

that neither short- nor long-term variables represent a homogeneous group, but instead probe a blend of all physical mechanisms consistent with that timescale. We discuss the breadth of such mechanisms in the following section.

### 6.6.4 Evidence for Multiple Dominant Variability Mechanisms

As discussed in subsection 1.2.1, the timescale of a young star's variability should be tied to the region of the star or circumstellar environment responsible for the variability. The only processes that should be able to produce variability on timescales of hours are inside the inner disk edge, for example in funnel flows. Changes on the order of days can be caused by dynamical processes at the inner edge of the disk or by rotation of the star. Timescales on the order of weeks may be associated with changes in the stellar magnetosphere, or with phenomena in the inner disk beyond the disk edge, while timescales of months or years may be probed by dynamical processes farther out, or by viscous processes at the disk edge. On timescales of years, stellar activity cycles may also come into play.

Many of the infrared excess sources change brightness significantly within one or two days, consistent with previous observations and with expectations that the variability should be associated with stellar rotation or with processes at the inner disk edge. However, the presence of both high- and low-amplitude variability on timescales from $\sim$ 0.7 days to $\sim$ 100 days suggests that we are seeing a variety of physical processes in the disk, not merely dynamical changes at the disk rim. Figure 6.14a may be used to select targets dominated by particular variability mechanisms; for example, large-amplitude variations on timescales of months may correspond to large accretion or extinction events in the inner disk.

However, we also see variations on timescales of up to several months in sources that do not have a detected circumstellar disk. Of the 23 candidate members with no detected infrared excess and a timescale above 20 days, 11 can be placed on Figure 6.2, where their colors and magnitudes are inconsistent with being giants. Some of these sources appear to be unflagged systematics in the photometry. Some (FHO 2084, FHO 2402) show signs of accretion, and may have a very weak, undetected infrared excess. Others (FHO 755, FHO 1574) show irregular variability typically associated with young stars, but do not yet have spectra we can use to constrain the presence or absence of accretion. It is possible that these are diskless members of the North America Nebula complex, and that an unforeseen mechanism is responsible for the variability. Future spectroscopy will determine if this is the case.

## 6.7 Discussion

### 6.7.1 Comparison with Other State-of-the-Art Data Sets

#### 6.7.1.1 Peak-Finding Timescales from CSI 2264

The CSI 2264 survey (Stauffer et al., 2014) of the NGC 2264 region combined infrared time series photometry from Spitzer with optical time series photometry from CoRoT to investigate the variability of young stars in both wavelength regimes. Cody et al. (2014) calculated timescales for CoRoT lightcurves from the survey using the peak-finding method, which we described in section 5.6 and illustrated in Figure 5.13. Since their lightcurves covered an interval of 39 days at a roughly 10 minute cadence, the optical data set of Cody et al. (2014) is complementary to ours, probing shorter timescales than is practical with PTF.

Because peak-finding uses a different definition of timescale than $\Delta m$-$\Delta t$ plots do, care must be taken when comparing our results to those of Cody et al. (2014). We have carried out simulations similar to those presented in section 5.6 for the cadence used by CSI 2264, at a signal-to-noise ratio of 100, a value typical of the lightcurves studied by Cody et al.. In these simulations we defined the peak-finding timescale to be the timescale of variations 80% as tall as the tip of the peak-finding curve, like Cody et al. did.

We present the simulation results in Figure 6.19. The top row of panels, which compares the timescale found by peak-finding to the timescale parameter used in the simulations, show that the peak-finding timescale is proportional to the timescale input to the simulation (the "true timescale") for true timescales between 0.1 and 10 days. For longer-term variables, the timescale from the peak-finding analysis appears to level out at roughly 20 days. The middle row of panels shows that, for aperiodic signals, the scatter in timescales is of the same order as the timescale itself, or a factor of two error. This is comparable scatter to that found in Chapter 5 for both peak-finding and $\Delta m$-$\Delta t$ plots run on the PTF cadence.

Cody et al. (2014) normalized their peak-finding timescale to twice the value used in Table 5.5 or plotted in Figure 6.19 so that it would agree with the period for periodic sources. After we correct for this convention, introduced after the simulations were carried out, our simulations indeed show that the peak-finding timescale found for simulated sinusoidal signals equals the period on average. Multiplying the peak-finding rows of Table 5.5 by two, we find that timescales computed by peak-finding for CSI 2264 lightcurves are expected to be 6-12 times larger than timescales computed from $\Delta m$-$\Delta t$ timescales for PTF-NAN lightcurves, given the same underlying process for generating lightcurves. The ratio between peak-finding and $\Delta m$-$\Delta t$ timescales depends on the statistical properties of the lightcurve, and the figure of 6-12 times should be taken as representative values only. However, since any individual measurement of either timescale metric may be uncertain by up to a factor of two,

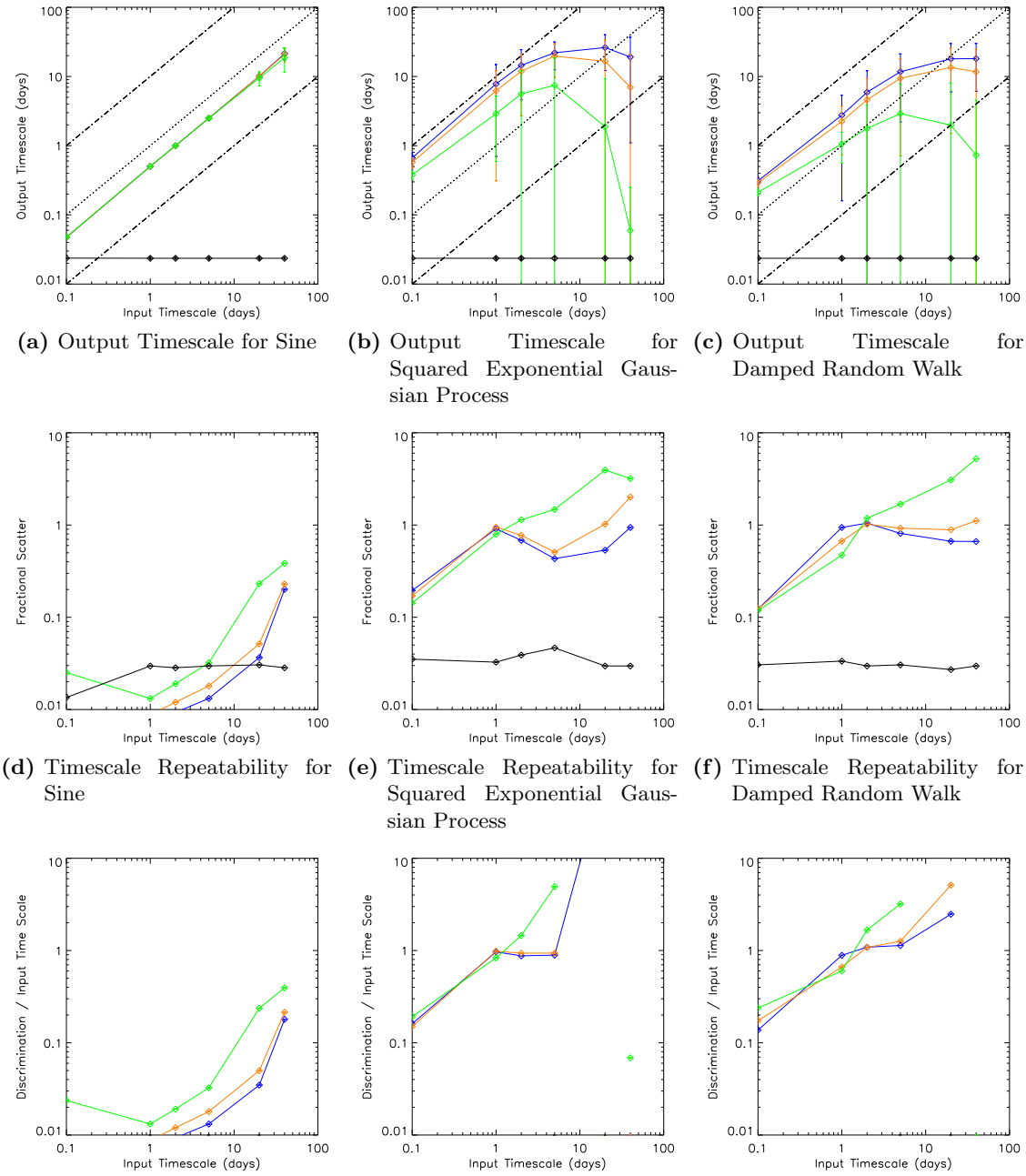


**(a)** Output Timescale for Sine

**(b)** Output Timescale for Squared Exponential Gaussian Process

**(c)** Output Timescale for Damped Random Walk

**(d)** Timescale Repeatability for Sine

**(e)** Timescale Repeatability for Squared Exponential Gaussian Process

**(f)** Timescale Repeatability for Damped Random Walk

**(g)** Timescale Discrimination for Sine

**(h)** Timescale Discrimination for Squared Exponential Gaussian Process

**(i)** Timescale Discrimination for Damped Random Walk

**Figure 6.19:** The timescale calculated from a peak-finding plot in simulated CoRoT observations, plotted as a function of the underlying timescale of the simulated lightcurve. Top panels show the average value of the output timescale, which increases linearly with the true timescale before deviating from linearity at $\sim 10$ days. Middle panels show the ratio of the standard deviation to the mean output timescale; the uncertainty is typically a factor of two for the two aperiodic models. Bottom panels show the degree by which the input timescale has to change to significantly affect the output timescale. In all plots, blue represents lightcurves with an expected 5th to 9th percentile amplitude of 0.5 mag, orange an amplitude of 0.25 mag, green an amplitude of 0.1 mag, and black an amplitude of 0.01 mag. All runs have a signal-to-noise ratio of 100.

the variation in the conversion factor does not affect our comparisons.

Cody et al. (2014) find a distribution of timescales that is quite broad, from $\sim$ 4 days to 40 days. This is equivalent to $\sim$ 0.4-6 days by our definition, corresponding to the broad peak seen in Figure 6.12. Figure 6.12a shows a substantial decrease in the number of variables with timescales from 2 days to 6 days; Figure 33 from Cody et al. (2014) shows no such trend between 15 days and 40 days. It is possible that the number of sources they count having timescales between 20 and 40 days is being inflated by longer-term (e.g., 100 day) variables, as the authors note.

#### 6.7.1.2 H$\alpha$ Emission Timescales from LAMP

The LAMP survey (Costigan et al., 2012) and follow-up work (Costigan et al., 2014) carried out time series spectroscopy of selected accreting pre-main-sequence stars on time intervals ranging from minutes to weeks. They characterized the variability of the H$\alpha$ emission line, expressing the H$\alpha$ equivalent widths in terms of accretion rates using empirical relations.

Figures A17 and A18 in Costigan et al. (2014) are analogous to our $\Delta m$-$\Delta t$ plots, only with $\Delta \log \dot{M}$ in place of $\Delta m$, while Figure 11 from Costigan et al. (2012) can be compared to the median curves in our $\Delta m$-$\Delta t$ plots. The main difference between our figures and theirs is that the figures of Costigan et al. (2014) show very few pairs of points with no change in H$\alpha$ flux. The lack of pairs of observations with similar measurements in the Costigan et al. data is likely an artifact of their limited time sampling. Costigan et al. (2014) find that H$\alpha$ flux differences rise from short time intervals to time intervals of 2-3 days, and then remain constant at longer time intervals. Since the definition of lightcurve timescale adopted in subsection 6.5.1 only requires that a $\Delta m$ quantile exceed half the overall lightcurve amplitude, Costigan et al. (2014) observe accretion variability with characteristic timescales of $\sim$ 1 day in our formalism. This is consistent with the 1-2 day peak we find for infrared excess sources.

Costigan et al. (2014) find that H$\alpha$ variability on time intervals of hours is rare, occurring in roughly 10% of observations. Likewise, Cody et al. (2014) found that variability rarely has timescales of less than 0.4 days (in our $\Delta m$-$\Delta t$ convention). Based on these two studies, it appears that we do not miss important variability classes by ignoring hour-scale variability in our own survey.

### 6.7.2 Systematic Errors in Non-Coeval Studies

While valuable, time series data requires a considerable investment of observing time. Single-epoch photometry in multiple bands will remain an important tool for characterizing young stars for the foreseeable future. However, when photometry from different epochs is combined to estimate source colors or SEDs, variability introduces a systematic error that (for aperiodic variability) grows monotonically with the length of the time span separating the combined observations. With the $\Delta m$-$\Delta t$ data from the PTF-NAN survey, we can quantify this error for the first time.

More formally, let an observer have photometric measurements $m_i$ in bands $B_i$ measured at epochs $t_i$. I assume that the observer does *not* have any constraints on the variability of the source, other than that it is a young star, and possibly the presence or absence of an infrared excess. The calculation of source colors or SEDs from such a data set implicitly assumes that the magnitudes $m_0$ at some common epoch $t_0$ (where the index 0 can be chosen arbitrarily without loss of generality) equal the observed magnitudes $m_i$. If $t_i \neq t_0$ and the source is variable, using $m_i$ as an estimator introduces an error in $m_0$, in addition to any (photometric) error in measuring $m_i$.

Without prior knowledge of any systematic trends in source brightness, and without prior knowledge of whether any of the observed magnitudes are unusually high or low, the expected value of $m_i - m_0$ is zero. The variance in estimating $m_0$ is therefore $E((m_i - m_0)^2)$. In the $\Delta m$-$\Delta t$ formalism, if $\Delta t = t_i - t_0$, then this is $E((\Delta m)^2)$. This average needs to be taken over not only all possible values of $t_0$ and $t_i$, but also over the distribution of variability properties in the sample. The expectation value can be factored:

$$\begin{aligned} E((\Delta m)^2) &= \sum_{\text{sources}} \sum_{\text{obs}} (\Delta m)^2 p(\text{data}, \text{src}) \\ &= \sum_{\text{sources}} \sum_{\text{obs}} (\Delta m)^2 p(\text{data}|\text{src}) p(\text{src}) \\ &= \frac{1}{N} \sum_{\text{sources}} \left( \sum_{\text{obs}} (\Delta m)^2 p(\text{data}|\text{src}) \right) \\ &= \frac{1}{N} \sum_{\text{sources}} E((\Delta m)^2|\text{src}) \end{aligned}$$

This is simply the average across the sample of the structure function $E((\Delta m)^2)$ for each source. Taking the square root yields the error introduced in the estimation of the magnitude $m_0$ at one epoch using the magnitude $m_i$ at another.

In Figure 6.20 we show plots of the variability-induced error for all candidate members brighter than $R_{\rm PTF} = 18.5$, as well as the subsets with and without a detected infrared excess. The restriction to sources brighter than 18.5th magnitude is to prevent the high noise levels of faint sources from washing out the signal. For infrared excess sources, an observation one night old constrains the source's current magnitude to $\sim 0.1$ mag. If observations in different bands are taken two weeks apart, on the other hand, the delay introduces an error of $\sim 0.2$ mag in translating the data to a common epoch. When combining data from different *years*, the error on colors or SEDs grows to be a substantial $\sim 0.5$ mag. SEDs published using such widely separated photometry should be interpreted with great caution.

If a young star has little to no infrared excess, on the other hand, coeval photometry is much less important. Measurements separated by long timescales show little more scatter than measurements separated by short timescales. Readers should use caution when interpreting Figure 6.20c,

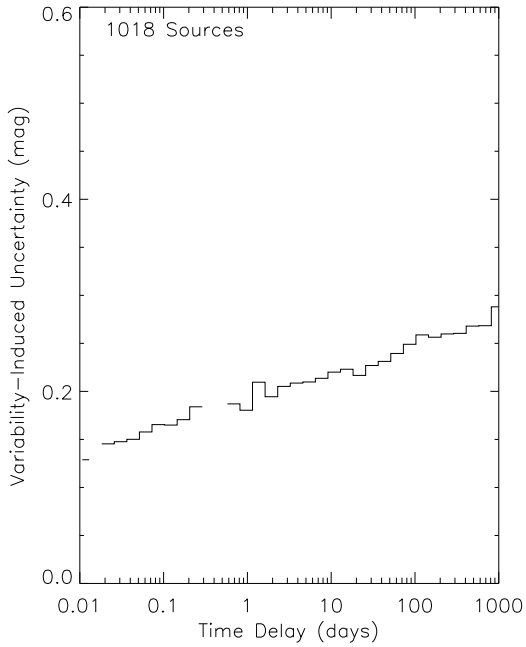


**(a)** All Candidates

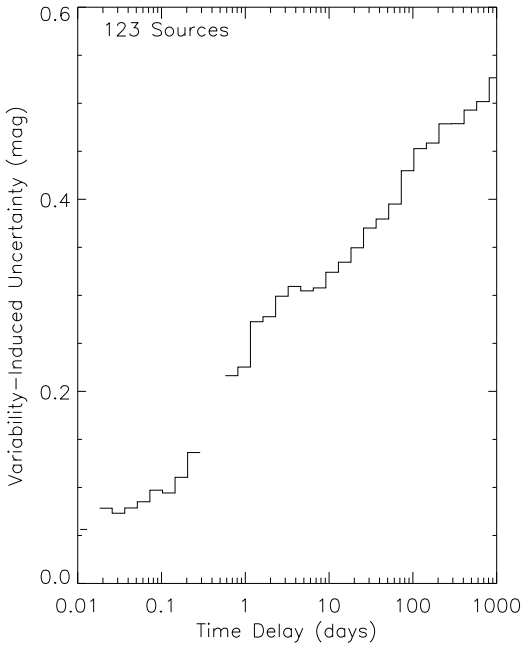


**(b)** Infrared Excess Detected

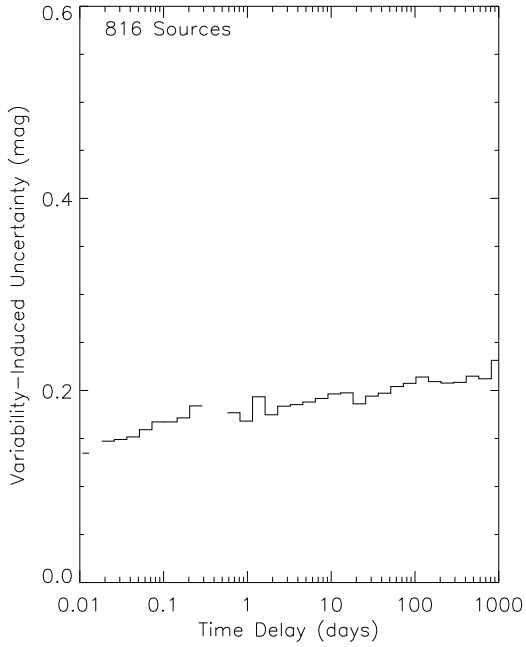


**(c)** No Infrared Excess Detected

**Figure 6.20:** The error introduced by using the magnitude at one epoch to estimate that at another, as a function of the time interval separating the two epochs. These calculations assume no knowledge of either the amplitude or the timescale of the source. Results are shown for any young star, for stars known to have an infrared excess, and stars that either are known to lack an infrared excess or that have strong limits on any excess.

however; sources reported to have significant variability over time intervals below $\sim$ 0.1 day may have otherwise undetected photometric errors.

## 6.8 Summary

We have used the presence of variability, combined with ancillary data, to identify 1,359 new candidate members of the North America Nebula complex. From our current source statistics, we expect that 600-700 of these candidates will survive vetting. These are candidates that could not have been selected using either of the previous two methods, namely emission-line and infrared excess surveys, and may represent a population of nonaccreting stars in the region.

We have used newly developed timescale metrics to characterize the timescales of aperiodic variability among both the newly and the previously identified candidates for the first time. We adopt a definition of timescale that tends to be shorter than both periods (e.g., Cohen et al., 2004) and peak-finding timescales (Cody et al., 2014), so our results need to be converted to equivalent peak-finding times or periods before they can be compared to timescales found in previous work. The calculations of Chapter 4 and the simulations of Chapter 5 provide guidance on how to do such conversions. The exact conversion factor depends on the shape and statistical properties of the lightcurves in a given sample, but conversions good to within a factor of a few can be done without making any assumptions about the lightcurves being studied.

We see a large number of variables whose magnitude changes significantly on time intervals of 1-2 days, and a broader distribution from just under a day to $\sim$ 100 days, the longest timescale characterizable with our data. We do not see any evidence, based on the simulations of Chapter 5, that this peak is a systematic effect. We interpret the 1-2 day peak as variability arising from stellar rotation or dynamical changes at the inner disk edge, but note that a wide range of variability mechanisms must be invoked to explain the full range of timescales. We see no correlation between the timescale and variability amplitude, infrared colors, or spectroscopic properties of a source, suggesting that the factors that determine a star's variability properties are more complex than assumed by us or by previous authors.

Since we see a sharp increase in variability between the longest intranight time baselines and the shortest baselines between consecutive nights, we believe that many sources undergo important changes on time intervals of a large fraction of a day. Variability on time intervals of half a day may be worth investigating in CoRoT, LCOGT, or other appropriate data sets. In addition, only part of our sample has had spectra taken or analyzed for youth indicators; expanding the set of analyzed spectra will help refine our membership list and constrain some of the ambiguities in the preceding discussion.

## 6.9 References

Cardelli, J. A., Clayton, G. C., & Mathis, J. S. 1989, ApJ, 345, 245

Cody, A. M. et al. 2014, AJ, 147, 82, arXiv:1401.6582

Cody, A. M., Tayar, J., Hillenbrand, L. A., Matthews, J. M., & Kallinger, T. 2013, AJ, 145, 79, arXiv:1302.0018

Cohen, R. E., Herbst, W., & Williams, E. C. 2004, AJ, 127, 1602, arXiv:astro-ph/0312066

Costigan, G., Scholz, A., Stelzer, B., Ray, T., Vink, J. S., & Mohanty, S. 2012, MNRAS, 427, 1344, arXiv:1209.0462

Costigan, G., Vink, J. S., Scholz, A., Ray, T., & Testi, L. 2014, MNRAS, 440, 3444, arXiv:1403.4088

D'Antona, F., & Mazzitelli, I. 1997, Mem. Soc. Astron. Italiana, 68, 807

Drew, J. E. et al. 2005, MNRAS, 362, 753, astro-ph/0506726

Gizis, J. E., Reid, I. N., & Hawley, S. L. 2002, AJ, 123, 3356, astro-ph/0203499

Gondoin, P. et al. 2012, A&A, 548, A15, arXiv:1210.3221

Guieu, S. et al. 2009, ApJ, 697, 787, arXiv:0904.0279

Herbst, W., Maley, J. A., & Williams, E. C. 2000, AJ, 120, 349, arXiv:astro-ph/0003307

Kraus, A. L., & Hillenbrand, L. A. 2007, AJ, 134, 2340, arXiv:0708.2719

Rebull, L. M. et al. 2011, ApJS, 193, 25, arXiv:1102.0573

Reipurth, B., & Schneider, N. 2008, in Handbook of Star Forming Regions, ed. B. Reipurth, Vol. 1 (Astronomical Society of the Pacific), 36

Stauffer, J. et al. 2014, AJ, 147, 83, arXiv:1401.6600

Witham, A. R., Knigge, C., Drew, J. E., Greimel, R., Steeghs, D., Gänsicke, B. T., Groot, P. J., & Mampaso, A. 2008, MNRAS, 384, 1277, arXiv:0712.0988

# Chapter 7

# The Promise of Aperiodic Variability

## 7.1 Review of Thesis Goals

My thesis research focused on characterizing the timescales of aperiodic variability in young stars, particularly variability occurring over intervals of days to years. Despite being relatively poorly characterized, aperiodic and long-term variability are valuable tools because they can constrain accretion changes or larger circumstellar disk structures, while short-term periodic variability mainly constrains stellar rotation or stable structures at the disk inner rim. While the work in this thesis was not intended to extract such physical constraints directly from lightcurves, it does lay essential groundwork by developing new ways to quantify time series data and by defining the bulk properties of variability in a young stellar population.

A secondary goal of this work was taking a new census of young stars in the nearby (5-600 pc) North America Nebula complex. The complex's location in the Galactic plane, combined with its negligible proper motion, had historically made membership in the complex difficult to determine. Variability is the most effective way to identify weak-lined T Tauri stars (WTTS) associated with the complex, so we carried out a blind survey to identify new candidate members.

## 7.2 New Techniques and Results

In this work I have carried out the PTF North America Nebula (PTF-NAN) Survey, a young star variability survey of unprecedented scope and temporal dynamic range. The wide field of view of PTF, combined with the richness of the North America Nebula field, has allowed us to observe optical lightcurves of 243,392 sources, of which 148,778 are free from gross artifacts such as saturation or blending in at least half the survey epochs. Many of these sources are part of the general Galactic disk, rather than the North America Nebula, and lie outside the scope of this thesis. In addition,

the availability of almost nightly monitoring from late 2010 through 2012, with sparser coverage starting in late 2009 and with an as yet unreduced 2013 extension, makes this a nearly unique data set for simultaneously studying variability on timescales of days to years. Only Kepler offers a higher cadence for as long a baseline for a comparable number of stars. The result is a data set whose scientific value extends far beyond this thesis, enabling detailed study of Galactic variables of all types.

In addition, we have made a significant addition to our knowledge of membership in the North America Nebula complex. Applying cuts on sky position, color, magnitude, and variability amplitude, we identified 1,359 new candidate members, in addition to acquiring variability data for 354 out of $\sim 2000$ previously identified candidate members. A catalog of the new members will be presented online. Since the sample of 1,359 new candidates is not yet completely vetted, the final tally of new candidates is likely to be closer to 600-700.

In addition to 203 spectra of variables in the North America Nebula field previously observed by Lynne Hillenbrand, our follow-up survey took 644 new spectra of variables in the field. Including spectra of sources in the field without detected variability, we have 1,875 spectra from Lynne Hillenbrand's previous work and 793 new spectra. The targets for these spectra include both variables and infrared excess sources, and only the spectra of 782 variables brighter than 18th magnitude have been studied in this thesis. The full set of spectra will prove a valuable resource for understanding the population of the North America Nebula complex.

Thanks to the exceptional time sampling and time coverage of the PTF-NAN survey, we were able to clearly see the behavior of aperiodic variables of a variety of shapes and timescales. To lay the groundwork for future quantitative study of aperiodic variables, and to put our own preliminary analysis into context, we carefully examined the effectiveness of five candidate metrics for differentiating slowly- from rapidly-varying aperiodic signals: autocorrelation functions, structure functions, Gaussian process regression, $\Delta m$-$\Delta t$ plots, and peak-finding. Of these, the $\Delta m$-$\Delta t$ plot is a new metric I developed. To simulate the light curve performance, I developed an extensible lightcurve simulation program, LightcurveMC (Findeisen, 2014). This program can generate data sets at any cadence over a grid of amplitudes, signal-to-noise ratios, and lightcurve parameters. In addition, it was designed to handle both alternative lightcurve models and alternative timescale metrics in a uniform manner, allowing new examples of either to be added as needed. The software is open source, and I plan to continue to maintain it in the future.

We found that both autocorrelation functions and Gaussian process regression have difficulty giving accurate results when gaps are present in the data, in the former case despite precautions developed by other authors to minimize the effect. Of the metrics covered, $\Delta m$-$\Delta t$ plots and peak-finding perform the best, but are reproducible only to a factor of two and require time coverage an order of magnitude longer than the longest timescales of interest to ensure a representative

sample of long-timescale baselines. Of the two, $\Delta m$-$\Delta t$ plots seemed to agree slightly better with by-eye assessments of real lightcurves. Despite their limitations, both timescale measures are already enabling new work that would have been impossible with earlier metrics such as periodograms. Peak-finding was used to characterize short-timescale variability of young stars by Cody et al. (2014), while based on the results of our tests we adopted $\Delta m$-$\Delta t$ plots as our timescale tool for studying the PTF-NAN data set.

The differing statistical properties of the models we simulated mean that timescales from different metrics cannot be converted to each other directly, just as the relationship between root-mean-square (RMS) amplitude and peak-to-peak amplitude depends on the shape of the lightcurve in question. I showed that $\Delta m$-$\Delta t$ timescales tend to be shorter than periods (by a factor of four to six, depending on the lightcurve shape) or peak-finding timescales (by a factor of five to ten, depending on the specific definition of peak-finding adopted), because the $\Delta m$-$\Delta t$ timescale represents the time one must wait to see a change of (for our choice of parameters) roughly half the lightcurve amplitude. Periods and peak-finding timescales can both be defined in terms of the minima and maxima of the lightcurve, and represent the time intervals between the most extreme changes in the source magnitude. More specific conversion factors between alternative timescale metrics are presented in Table 5.5.

Having adopted $\Delta m$-$\Delta t$ timescales as the metric of choice, based on the simulation work, we inferred the timescale distribution for candidate North America Nebula members, treating periodic and aperiodic variables on an equal footing. Our time coverage, combined with our simulation results on how an observing cadence affects the validity of $\Delta m$-$\Delta t$ plots, allowed us to characterize timescales from fractions of a day to $\sim$ 90 days. While we observed sources with timescales throughout this range, we found that the timescales of our sample, particularly our spectroscopically identified high-confidence membership candidates, tended to peak around 1-2 days. This is consistent with both informal observers' experience that young stars change their brightness significantly from night to night, and with published results indicating that periodic young stars (which surely compose some fraction of our sample) have a maximum in their periods at 6-8 days (Herbst et al., 2000; Cohen et al., 2004), after allowing for $\Delta m$-$\Delta t$ timescales always being smaller than periods for the same lightcurve. However, it is the first time a peak in the timescale distribution of aperiodic variables has been quantitatively demonstrated.

Because we only observed sources at night, we had no constraints on variability on time baselines of 8-16 hours. However, we did find that most sources showed much more variation from night-to-night than within a night. This suggests that much of the variation in source magnitude is first introduced at the poorly probed timescales of half a day, rising towards the 1-2 day peak we identified. We propose that future investigations focus on characterizing this range of short timescales using LCOGT or similar facilities. Filling in the gap at timescales shorter than one day will help us

understand the shape and significance of the 1-2 day peak.

We also examined the joint distribution between amplitude and timescale to attempt to constrain the underlying physics, as outlined in the introduction. We found that our sources show no correlation between the amplitude and the timescale of their variability — long timescale variables were just as likely to have high amplitudes and low amplitudes, and likewise for short- and intermediate-timescale variables. We infer that a wide range of physical processes must be responsible for both high- and low-amplitude variables, and that we cannot attribute all high-amplitude variables to, for example, accretion fluctuations.

As a practical application of the variability distribution, we quantified the error introduced when a researcher combines observations taken at different epochs while neglecting variability. We found that if a star has significant circumstellar material (as indicated by an infrared excess), the error is $\sim 0.2$ mag if observations are taken within a day of each other, but can grow up to $\sim 0.5$ mag if observations from different years are combined carelessly. However, our analysis also indicates a noise floor at $\sim 0.15$ mag that is likely caused by imperfections specific to the PTF data, so these results need to be interpreted with caution for now.

Taken together, the individual results of this thesis represent the most systematic exploration of aperiodic variability among young stars to date. I have constructed the distribution of all young variables, periodic or not, on timescales from less than a day to $\sim 100$ days. I have shown that aperiodic variability is rarely dominated by long-term trends, and have provided recommendations on how to quantify aperiodic variability in other time series data sets. I have measured the error introduced into colors or SEDs from combining photometry of variable sources taken at different epochs. However, even with this new data, the causes of young stellar variability remain poorly characterized. In the final section of this thesis, I outline possible directions for future work to address the physics underlying variability in young stars.

## 7.3 Publications

The work presented in this thesis has so far resulted in only one publication, Findeisen et al. (2013), on the properties of bursting and fading events within otherwise lower-amplitude variables. However, we intend to publish two more in the next year, covering our study of aperiodic timescale metrics (Chapter 4 and Chapter 5) and the $\Delta m$-$\Delta t$ analysis of the North America Nebula data (Chapter 6).

In addition, two projects I undertook during my early graduate student career resulted in one publication each. In the first, I used UV photometry from GALEX to search for a distributed population of older members around the Taurus and Upper Scorpius regions (Findeisen & Hillenbrand, 2010). In the second, I characterized the use of UV photometry as a measure of stellar activity (Findeisen et al., 2011).

## 7.4 Future Work

The work presented in this thesis represents only the first steps toward using the full power of aperiodic variability to understand young stars. Many of the conclusions presented here can be improved by more careful analysis of spectra, by confirming membership for our candidate members, and, most of all, by improving the quality of the photometry. In less crowded fields, PTF photometry is regularly repeatable to 1% or better; achieving the same precision in the North America Nebula complex would allow us to discover lower-amplitude variables, while eliminating systematic errors from crowding and nebula emission would reduce the incidence of instrumental contaminants.

In addition, I would like to use the newly developed $\Delta m$-$\Delta t$ technique to study other data sets, particularly higher-cadence observations that do not have nightly gaps. A study of behavior at these timescales would complement the results of this thesis, which focused on long-timescale variability but was less sensitive to changes within a single night.

Finally, while $\Delta m$-$\Delta t$ plots and peak-finding are the most reliable of the aperiodic timescale metrics we have tested, there are many more proposed algorithms that may work even better. I would like to extend the analysis of Chapter 5 to these methods to determine if, and when, they are appropriate additions to the astronomer's toolbox. Time series studies may be the next frontier of observational astronomy, but without well-understood tools we will not be able to achieve the full promise of aperiodic variability.

## 7.5 References

Cody, A. M. et al. 2014, AJ, 147, 82, arXiv:1401.6582

Cohen, R. E., Herbst, W., & Williams, E. C. 2004, AJ, 127, 1602, arXiv:astro-ph/0312066

Findeisen, K. 2014, LightcurveMC: An extensible lightcurve simulation program, ascl:1408.012, astrophysics Source Code Library

Findeisen, K., & Hillenbrand, L. 2010, AJ, 139, 1338, arXiv:1001.3684

Findeisen, K., Hillenbrand, L., Ofek, E., Levitan, D., Sesar, B., Laher, R., & Surace, J. 2013, ApJ, 768, 93, arXiv:1303.3629

Findeisen, K., Hillenbrand, L., & Soderblom, D. 2011, AJ, 142, 23, arXiv:1105.1377

Herbst, W., Maley, J. A., & Williams, E. C. 2000, AJ, 120, 349, arXiv:astro-ph/0003307